Lateral-torsional buckling resistance of pultruded fibre reinforced polymer shapes

by

Tien Thuy Nguyen

A thesis presented for the degree of

Doctor of Philosophy in Engineering

University of Warwick

May 2014

CONTENTS

LIST OF TABLES

LIST OF FIGURES

x

NOTATIONS

a buckling half-wave length, mm

A cross-section area, mm^2

$A_{flanges}$ area of flanges in a section, mm^2

A_{web} area of the web in a section, mm^2

A_v shear area, mm^2

α modification factor for a closed-form equation

α_c correction factor for the calculation of torsional constant

α_{rt} weighting factor for Q_{rt}

α_δ weighting factor for Q_δ

α_{LT} imperfection factor

b_m mean of correction factor for test results

b_l distance from the flange outstand to the middle vertical axis of the web in a channel section, mm

b_f	breadth of a cros-section, mm
β	target reliability factor
β_s	shear coefficient
c_w	warping spring, $kN.mm^3$
C_1	factor to account for the type of moment distribution and support condition
C_2	factor to account for the vertical position of the load with respect to the shear centre
C_b	moment modification factor for non-uniform moment distribution for laterally unsupported span when both ends of the beam are braced
χ_{LT}	reduction factor
D	maximum allowance of out-of-straightness imperfection in standards, mm
D_c	diameter of the largest inscribed circle, mm
$\left.\begin{array}{l} D_L \\ D_T \\ D_{LT} \\ D_s \end{array}\right\}$	flexural rigidities for the orthotropic plate, kN.mm
$\delta,\ \delta_x$	initial minor out-of-straightness along beam's length, mm
δ_e	vertical deflection in column test, mm

δ_e	elongation on the tensile load direction of test specimen, mm
δ_i	error term
δ_{max}	maximum initial minor out-of-straightness of a beam, mm
Δ	logarithm of the error term δ $[\Delta_i = \ln(\delta_i)]$
$\overline{\Delta}$	estimated value for $E(\Delta)$
Δ_{cr}	difference between critical LTB loads
$\Delta_{cr,FEA}$	difference between critical buckling loads
Δ_{Limit}	difference between limiting buckling loads
$\Delta_{Limit,FEA}$	difference between limiting buckling loads from FEA
e_s	distance from the vertical centre line of the web plate to the shear centre in a channel section, mm
e_{s1}	distance from the outer surface of web to the shear centre in a channel section, mm
e_y	load eccentricity, mm
E	modulus of elasticity, kN/mm^2 (GPa)
E_1 E_2 E_3	three moduli in orthotropic material, kN/mm^2 (GPa)

E_L longitudinal modulus of elasticity, kN/mm^2 (GPa)

$E_{L,m}$ mean longitudinal of elasticity, kN/mm^2 (GPa)

$(E_L)_f$ longitudinal modulus of elasticity of the flange, kN/mm^2 (GPa)

$(E_L)_w$ longitudinal modulus of elasticity of the web, kN/mm^2 (GPa)

E_T transverse modulus of elasticity, kN/mm^2 (GPa)

EI_y flexural rigidity about major axis, kN.mm^2

EI_z flexural rigidity about minor axis, kN.mm^2

$\left.\begin{matrix} \varepsilon_0 \\ \varepsilon_{45} \\ \varepsilon_{90} \end{matrix}\right\}$ or $\left.\begin{matrix} \varepsilon_{0,r} \\ \varepsilon_{45,r} \\ \varepsilon_{90,r} \end{matrix}\right\}$ three strains measured with rosette strain gauge with '0' , '45' and '90' as the angle between the strain gauges and the tensile load

$\left.\begin{matrix} \varepsilon_{11} \\ \varepsilon_{12} \\ \gamma_{12} \end{matrix}\right\}$ three plane strains of orthotropic material with 1-1 taken along fibre direction

ε_L longitudinal strain

$\varepsilon_{LTB,max}$ maximum strain in the LTB testing

ε_T transverse strain

η_{LT} generalized imperfection factor

f_y yield strength, MPa

f_{ym} mean value for yield strength, MPa

$g_{rt}(\underline{X})$	resistance function of the basic variables $\underline{X}$ used as the design model
G	shear modulus, kN/mm^2 (GPa)
$\left.\begin{array}{l} G_{12} \\ G_{13} \\ G_{23} \end{array}\right\}$	three shear moduli in orthotropic material, kN/mm^2 (GPa)
G_{LTm}	mean in-plane shear modulus, kN/mm^2 (GPa)
G_{LT}	in-plane shear modulus, kN/mm^2 (GPa)
GI_t	torsional rigidity, kN.mm^2
γ_{max}	maximum shear strain in LTB testing
γ_M	partial safety factor for lateral-torsional buckling mode of failure
h	depth of a cross-section, mm
h_w	depth of web panel (distance from mid-depth of top flange to mid-depth of bottom flange), mm
H	height of column, mm
I_t	torsional rigidity, mm^4
I_w	warping rigidity, mm^6
I_y	second moment of area for flexure about the beam's major axis, mm^4
I_z	second moment of area for flexure about the beam's minor axis, mm^4

k	restraint factor for lateral flexural bending at end supports; 0.5 for full restraint to 1.0 for fully unrestrained
$k_{d,n}$	design fractile factor for the case "V_X unknown"
$k_{d,\infty}$	design fractile factor of $k_{d,n}$ for $n \rightarrow \infty$
k_n	characteristic fractile factor for the case V_X unknown
k_w	restrain factor for warping at end supports
$k_{I\text{-flange}}$	spring constant for flange of I section
$k_{I\text{-web}}$	spring constant for web of I section
k_{∞}	value of k_n for $n \rightarrow \infty$
K_t	transverse sensitivity factor of the strain gauges
κ_F	flexural stiffness, kN.mm^2
κ_S	shear stiffness, kN
L	major axis flexural span of beam, mm
L_b	lateral unrestrained span of beam, mm
L_c	critical length, mm
L_p	limiting laterally unrestrained span for limit state of yielding, mm
L_r	limiting laterally unrestrained span for limit state of inelastic lateral-torsional buckling, mm

L_{Overall}	overall span of beam including the overhang lengths, mm
λ	time effect factor
λ_{LT}	non-dimensional slenderness or generalised slenderness
$\lambda_{\text{LT,0}}$	plateau length
$M_{\text{b,Rd}}$	design buckling resistance moment of a laterally unrestrained beam, kN.mm
M_{cr}	elastic critical buckling moment of resistance, kN.m
M_{e}	latetal-torsional buckling moment from LTB testing, kN.m
$M_{\text{pl,y}}$	plastic moment of resistance, kN.m
M_{y}	moment resistance at first yield, kN.m
M_{Ed}	design value of moment, kN.m
M_{Loc}	local buckling moment, kN.m
$M_{\text{LTB,max}}$	maximum moment in the LTB testing, kN.m
M_{n}	nominal flexural strength of member, kN.m
M_{u}	required flexural due to factored loads of member, kN.m
n	number of experiment results
$N_{\text{cr,z}}$	elastic critical Euler buckling load, kN

ν	Poission's ratio for steel
ν_0	Poission's ratio of the material on which the gauge factor was measured
$\left.\begin{array}{l}\nu_{12}\\\nu_{13}\\\nu_{23}\end{array}\right\}$	three Poission's ratios in orthotropic material
ν_{LT}	major Poission's ratio
P	central point load, kN
P_3	point load applied at 3 mm lateral eccentricity from the shear centre vertical plane, kN
P_{-3}	point load applied at -3 mm lateral eccentricity from the shear centre vertical plane, kN
P_5	point load applied at 5 mm lateral eccentricity from the shear centre vertical plane, kN
P_{-5}	point load applied at -5 mm lateral eccentricity from the shear centre vertical plane, kN
P_{10}	point load applied at 10 mm lateral eccentricity from the shear centre vertical plane, kN
P_{-10}	point load applied at -10 mm lateral eccentricity from the shear centre vertical plane, kN
P_{15}	point load applied at 15 mm lateral eccentricity from the shear centre

vertical plane, kN

P_{-15}	point load applied at -15 mm lateral eccentricity from the shear centre vertical plane, kN
P_{cr}	elastic critical lateral torsional buckling load, kN
P_{cr1}	elastic critical buckling load obtained using geometric properties that ignored the fillet radius areas, kN
P_{cr2}	elastic critical buckling load obtained using geometric properties that accounted for the fillet radius areas, kN
$P_{cr,e}$	elastic critical lateral torsional buckling load from experiment, kN
$P_{cr,FEA}$	elastic critical lateral torsional buckling load from finite element analysis, kN
$P_{cr,FEA,1}$	elastic critical lateral torsional buckling load from finite element analysis for case 1 of load position, kN
$P_{cr,FEA,2}$	elastic critical lateral torsional buckling load from finite element analysis for case 2 of load position, kN
$P_{cr,FEA,base}$	a base value for critical buckling load from finite element analysis, kN
$P_{cr,TF}$	elastic critical buckling load obtained for Top Flange loading, kN
$P_{cr,SC}$	elastic critical buckling load obtained for Shear Centre loading, kN
$P_{cr,BF}$	elastic critical buckling load obtained for Bottom Flange loading, kN

P_u	ultimate failure load in column local buckling test, kN
$P_{Limit,e}$	limiting buckling load from experiment, kN
$P_{Limit,FEA}$	limiting buckling load from finite element analysis, kN
$P_{Loc,FEA}$	local buckling load of a concentric loaded column obtained using finite element analysis, kN
$P_{LTB,\,max}$	maximum LTB loads in testing, kN
φ_0	initial twist imperfection, rad
ϕ	rotation at mid-span, degree
ϕ_b	resistance factor in structural design
Ψ	warping function, mm^2
Ψ_{max}	maximum of warping function, mm^2
Φ_{LT}	value to determine the reduction factor χ_{LT}
r	resistance value, kN.mm
r_c	radius of the fillet corner in a section, mm
r_d	design value of the resistance, kN.mm
r_e	experimental resistance value, kN.mm
r_k	characteristic value of the resistance, kN.mm

r_{t} theoretical resistance value, kN.mm

s estimated value of the standard deviation σ

s_{Δ} estimated value of σ_{Δ}

s_{δ} estimated value of σ_{δ}

$\left.\begin{array}{l} \sigma_{11} \\ \sigma_{12} \\ \sigma_{12} \end{array}\right\}$ three plane stresses of orthotropic material with 1-1 taken along fibre direction, MPa

$\sigma_{\mathrm{u,e}}$ compression stress at ultimate failure in the local buckling test, MPa

$\left.\begin{array}{l} \sigma_{xx} \\ \sigma_{yy} \\ \sigma_{xy} \end{array}\right\}$ Three plane stresses with x-x taken along the tensile load direction and y-y perpendicular to x-x, MPa

$\sigma_{\mathrm{L,t}}$ longitudinal tensile strength, MPa

σ_{Loc} local buckling stress, MPa

σ_{Locm} mean value of local buckling stress, MPa

$\sigma_{\mathrm{Loc,a}}$ local buckling stress obtained from analytical solution, MPa

$\sigma_{\mathrm{Loc,e}}$ local buckling stress obtained from experiment, MPa

$\sigma_{\mathrm{Loc,flange}}$ local buckling stress of flange, MPa

$\sigma_{\mathrm{Loc,web}}$ local buckling stress of web, MPa

$\sigma_{\mathrm{Loc,FEA}}$ local buckling stress obtained from finite element analysis, MPa

t_f	flange thickness, mm
t_p	thickness of the panel, mm
t_w	web thickness, mm
τ_{max}	maximum shear stress in LTB testing, MPa
τ_u	shear strength, MPa
θ	angle between the tensile loading direction and fibre direction, Degree
θ_1	angle between the loading axis x with strain gauge SG#1, Degree
θ_2	angle between the loading axis x strain gauge SG#3, Degree
θ_3	angle between the loading axis x with strain gauge SG#2, Degree
U_x	displacement in X-direction, mm
U_y	displacement in Y-direction, mm
U_z	displacement in Z-direction, mm
UR_x	rotation about X-direction, Degree
UR_y	rotation about Y-direction, Degree
UR_z	rotation about Z-direction, Degree
v_0	initial minor axis out-of-straightness imperfection, mm
V_{fy}	coefficient of variation of f_y

V_{max}	maximum shear forces in LTB testing, kN
V_{r}	coefficient of variation of r
V_{rt}	coefficient of variation of r_{t}
V_{EL}	coefficient of variation of E_{L}
V_{GLT}	coefficient of variation of G_{LT}
V_X	coefficient of variation of X
V_{Xi}	coefficients of variation of the basic variables X_i
$V_{\hat{\delta}}$	estimator for the coefficient of variation of the error term δ
$V_{\sigma\text{Loc}}$	coefficient of variation of σ_{Loc}
w	vertical deflection of shear centre at mid-span, mm
W_{y}	elastic section modulus about the major axis, mm^3
W_{z}	elastic section modulus about the minor axis, mm^2
W_{w}	elastic warping section modulus, mm^3
X_0	horizontal distance to the centroid from the outer surface of the web in a channel section, mm
$\underline{X}_{\text{m}}$	array of mean values of the basic variables
z_{g}	distance from the shear centre to the point of load application, mm

ACKNOWLEDGEMENTS

DECLARATION

This thesis is submitted to the University of Warwick in support of my application for the degree of Doctor of Philosophy. It has been composed by myself and has not been submitted in any previous application for any degree.

Tien Thuy Nguyen

Parts of this thesis have been published by the author:

NGUYEN, T.T., CHAN, T.M. and MOTTRAM, J. T. (2012). Coupled buckling of simply supported fiber reinforced polymer I-beams: A finite element parametric study. *In Proceedings of CIMS2012 Conference*, Glasgow, UK, 407-414.

NGUYEN, T.T., CHAN, T.M. and MOTTRAM, J.T. (2013). Influence of boundary conditions and geometric imperfections on lateral–torsional buckling resistance of a pultruded FRP I beam by FEA. *Composite Structures*, 100, 233-242.

NGUYEN, T.T. CHAN, T.M. and MOTTRAM, J.T. (2013). Experimental determination of the resistance of pultruded FRP beams failing by lateral-torsional buckling, *In Proc. 6th Inter. Conf. on Advanced Composites in Construction*, NetComposites Ltd., Chesterfield, UK, 2013, 252-263.

NGUYEN, T.T., CHAN T.M. and MOTTRAM, J. T. (2014). Lateral-torsional buckling resistance by testing of pultruded FRP beams under different loading ad displacement boundary conditions. *Composites Part B: Engineering*, 60, 306-318.

ABSTRACT

The currently lack of design guidance for pultruded fibre-reinforced polymer member requires more study on their structural behaviours in order to provide structural designer with confidence when applying this material into civil engineering. Elastic lateral-torsional buckling is an important global instability mode of failure for flexure about the major axis of open sections which is characterised by a coupled elastic deformation of lateral deflection and twist about beam's longitudinal axis.

The key elements of this study are laboratory testing, finite element analysis and development of design guidance that is compatible with Eurocode 3 design procedure. 94 tests have been carried out on tensile coupons to characterise the four key material properties for longitudinal, transverse, shear moduli of elasticity and major Poission's ratio that are required for the prediction of the buckling resistance using closed-form equations and by finite element analysis. 114 tests on the elastic lateral-torsional buckling of I and channel beams under various loading and displacement boundary conditions have been carried out to determine the buckling resistance. Finite element modelling methodology has been developed and both linear and nonlinear numerical analyses have been performed to show that the methodology is suitable. Further sensitivity analysis has been conducted to demonstrate that the buckling resistance is highly influenced by the combination of material, geometric and loading imperfection. A calibration has been implemented, based on the new test results, following the Eurocode 0's approach to establish the material partial factor for the investigated instability mode of failure

CHAPTER 1

INTRODUCTION

Produced by the continuous composite material process known as '*pultrusion*', the Pultruded Fibre-Reinforced Polymers (PFRP) shapes consist of thin walls of glass or carbon fibre reinforcement embedded in a thermoset resin based matrix. This process is cost-effective and can be employed to produce a wide range of uniform cross-section from the conventional shapes as shown in Figure 1.1(a) that can substitute steel beams and columns in frame construction, to a more complex one in Figure 1.1(b) that serves as bridge decking. The applications of PFRP shapes and systems in construction are growing because of their distinct advantages such as: lightweight, high fatigue resistance, corrosion resistance and electromagnetic transparency (Bank, 2006).

 (a)   (b)

Figure 1.1 PFRP shapes: (a) conventional shape; (b) bespoke shape

Figure 1.2 PFRP frame structure (http://www.strongwell.com/markets/building-and-construction/)

Figure 1.3 Multistorey building (http://www.fiberline.com/structures/case-stories-other-structures/-eyecatcher-building/eyecatcher-building)

Figure 1.4 Startlink test house (Zafari, 2012)

The first application of PFRP shape (Figure 1.2) into the field of building system is a single-story frame using for computer and electronic laboratories (Bank, 2006). As this type of building requires electromagnetic transparency to avoid the interference between the building materials (above the ground level) and the computer or electronic systems, PFRP shape is shown to be one of the best solutions. Fiberline composites A/S built a five-storey frame building (Figure 1.3) with height of 15 metres in 1999 to show the potential application of this new material in building.

A two-storey residential trial house was built in Lincolnshire in 2012 with an aim to bring energy efficient and low cost living space to future housing in the UK. It is certain that application of this newly emerged material into commercial and residential constructions will grow quickly in the future.

3

Figure 1.5 Railway pedestrian bridge (www.apatech.ru/chertanovo_eng.html)

Figure 1.6 Road bridge over highway (http://www.fiberline.com)

Applications were also found in bridge engineering. Hundreds of short span light-truss pedestrian bridges have been constructed worldwide since 1970s (Bank, 2006). Figure 1.5 is a picture of the Russian first ever PFRP bridge during installation. The bridge has span of 41.4 metres and wide of 3 metres. It was constructed by three parts with centre part is 13 metres and the two others are each 15 metres. The installation took only one hour. Figure 1.6 presents a composite-steel hybrid bridge with span of 27 metres and width of 5 metres. The bridge comprises of two steel I beams above which a bespoke PFRP deckling was adhesively bounded. These two examples have shown that advantages of light-weight and noncorrosive properties made PFRP bridge become the first choice for places where short construction time and low maintenance cost are required.

Having the shape that can be similar to structural steel, the mechanical properties of PFRP are not the same. Although the direct strength (tension or compression) in the direction of pultrusion of PFRP shape can be between 200 MPa to 400 MPa, which is comparable to structural graded steel, their modulus of elasticity is significant lower. The modulus in the longitudinal direction E_L is between 20 GPa and 30 GPa which is only 1/7 to 1/10 of steel. Because of the low stiffness-to-strength ratio, design of PFRP member (in frame construction) is normally controlled by elastic deflections and/or elastic buckling instabilities and rarely by strength (Clarke, 1996, Chambers, 1997). Research into the buckling behaviour becomes particularly important for PFRP material.

When a thin-walled open shaped beam is laterally unrestrained along the span a key ultimate mode of failure is that of Lateral-Torsional Buckling (LTB). This instability failure is for flexure about the major axis of open sections, and is characterised by a coupled elastic deformation of lateral deflection and twist about the beam's longitudinal

centroidal axis. The studies of the LTB behaviour of PFRP beams, especially by way of physical testing, are limited (Nguyen *et al.*, 2014).

This Ph.D. further the understanding of LTB response of PFRP I and channel beams under various loading and displacement boundary conditions by way of Finite Element Analysis (FEA) and physical testing as a step towards the development of a future Eurocode for PFRP material. All the sections adopted in this research were provided by Fiberline A/S, Denmark. They were pultruded with E-glass fibres and fire-retardant vinylester matrix. The fibre reinforcements are of the three main types for unidirectional rovings, woven and complex mats. The mass fraction of glass content in a PFRP shape is approximately 60% (Anon., 2014a). The detail architectures of the fibres were not given by the pultruder.

This thesis consists of seven chapters in which Chapter 2 provides a general review of the relevant literature covering mainly the testing from previous researchers.

Chapter 3 covers 94 tensile tests on longitudinal coupons, transverse coupons and 10-degree off-axis coupons of four different sections to determine their key material properties of PFRP.

Chapter 4 reports results from 114 LTB tests on four sections at five or four span lengths, two displacement boundary conditions and three vertical load positions. Test arrangement, procedure and comparison with closed-form predictions are described.

Chapter 5 presents the linear and nonlinear finite element analyses of PFRP beams. The modelling methodologies for material, element type, mesh size, geometric and boundary conditions are reported. The models are verified by the test results and sensitivity analyses are carried out.

Chapter 6 provides a preliminary study to develop a design method for beam in bending using 114 test data in Chapter 4 and following the calibration procedure given in Eurocode 0 (BSI, 2002a).

Chapter 7 summarizes the key findings and conclusions drawn from this thesis and the recommendation for further work.

CHAPTER 2

LITERATURE REVIEW

2.1.   Introduction

This chapter provides background information to the lateral-torsional buckling instability of thin-walled members and a general review of the previous experimental researches on this buckling behaviour of PFRP beams to show the need for further research on this particular topic with the pultruded profiles.

2.2.   Lateral-torsional buckling failure

To commence the review of background information the author will introduce the elastic failure mode of Lateral-Torsional Buckling (LTB) and explain how a beam's resistance for this mode is dependent on a number of parameters.

When a laterally unrestrained beam is subjected to flexure about its major axis (Figure 2.1) it may fail by a coupled combination of lateral deflection (v) and twist rotation (ϕ) along the length, at a load that is lower than the strength of the beam. This elastic instability behaviour of beam has been referred as "Lateral-Torsional Buckling" (Timoshenko and Gere, 1961). LTB resistance is influenced by the displacement

Boundary Condition (BC), the loading condition and the beam's geometrical and mechanical properties.
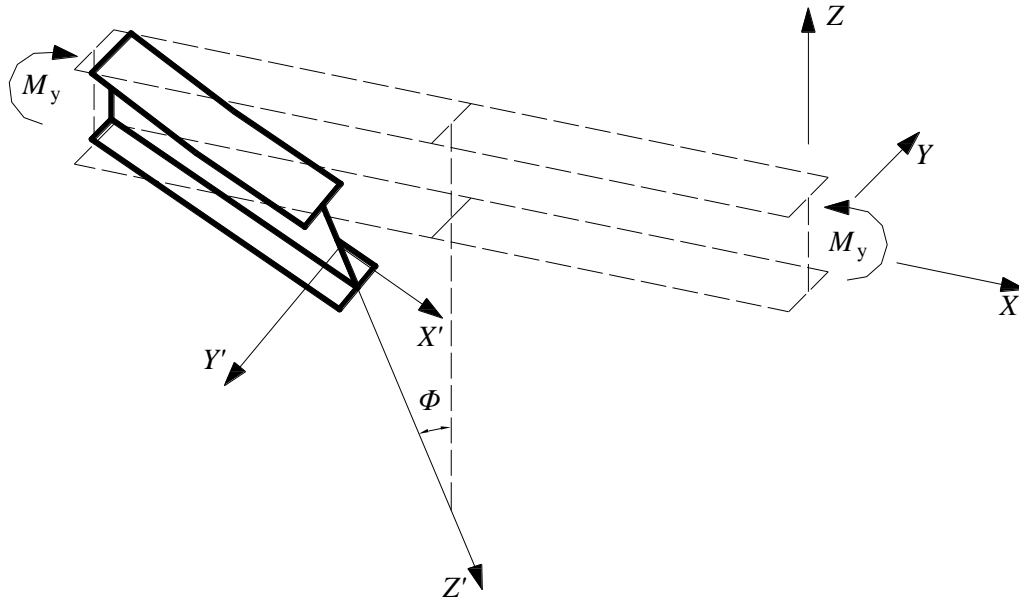
Figure 2.1 LTB of simply supported I-beam under pure bending

| (a) Narrow-flange I shape | (b) Wide-flange I shape | (c) Channel shape | (d) Square tube |
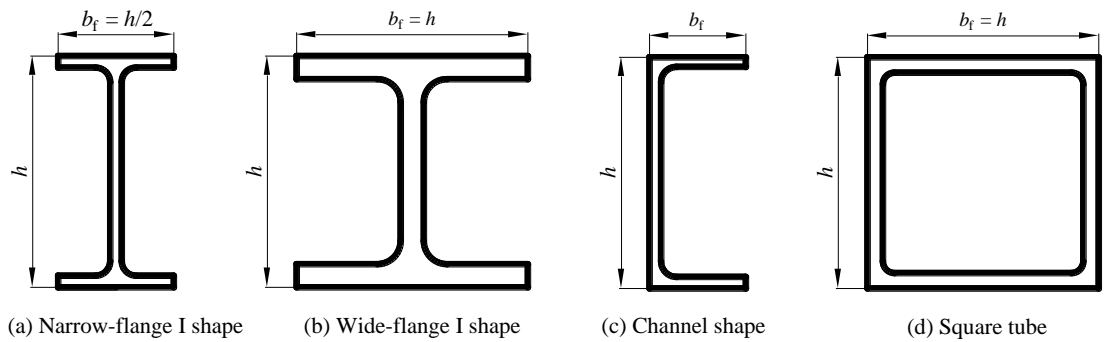
Figure 2.2 Standard structural shapes

Amongst the open cross-section as shown in Figures 2.2(a)-(c), the narrow-flange shape is most susceptible to the LTB due to its low lateral flexural rigidity (EI_z) and torsional rigidity (GI_t). The closed-section such as square tube in Figure 2.2(d) is rarely failed by

LTB thanks to its high EI_z and GI_t compared to the vertical flexural rigidity (EI_y). In terms of the displacement BC, the more restraints applied at ends, the higher is the LTB resistance. There are two main types of BC: (1) simply supported and (2) cantilever.

The instability theory (Timoshenko and Gere, 1961, Trahair, 1993) defines the simply supported (about major axis) condition as "beam to be fully restrained for translational displacement about major and minor axis and twist along the length, but is free to rotate about major and minor axis $(k = 1)$ and to warp $(k_w = 1)$". Here, k refers to the factor of effective length for restraint against lateral bending, while k_w is the equivalent factor for end warping. By changing the lateral flexural bending conditions (changing of k) or warping condition (changing of k_w) from free (k or $k_w = 1.0$) to fixed (k or $k_w = 0.5$) three other simply supported BCs are achieved. They are $k = 1$ and $k_w = 0.5$; $k = 0.5$ and $k_w = 1$ and $k = 0.5$ and $k_w = 0.5$.
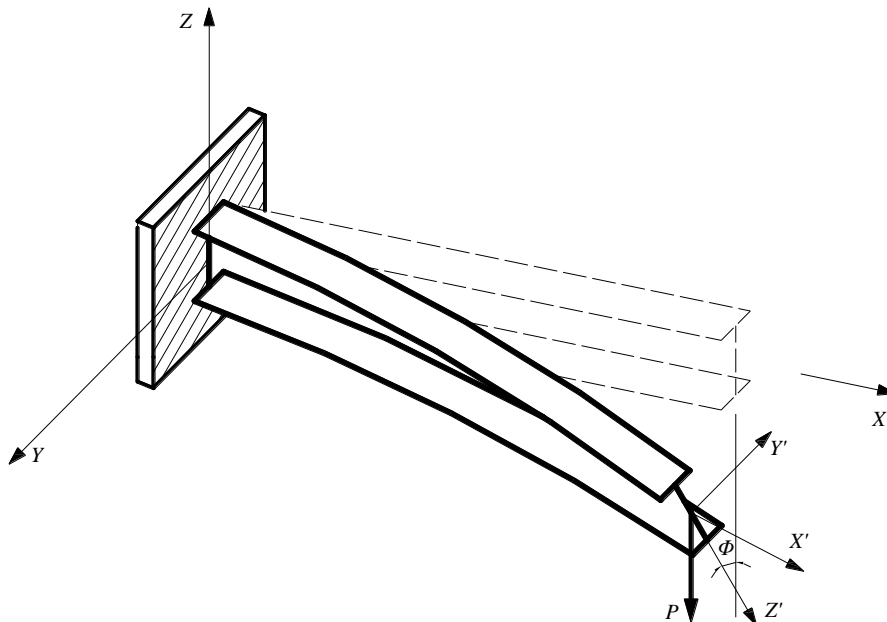
Figure 2.3 LTB of cantilever I beam under point load at free end

In the cantilever beam, one end is fully clamped whist other end is free. Figure 2.3 shows a cantilever I beam with dashed outline for undeformed and with LTB failure with a point load at the "free" end.

When a beam is subjected to a point load, LTB resistance is influenced by the vertical distances from the point of application (z_g) to the Shear Centre (SC) due to an additional torque about the longitudinal (centroidal) axis that is generated from the lateral movement of the vertical point load when instability happens (Trahair, 1993). Because the torque acts in the opposite sense to the LTB twist rotation when the load is applied below the SC (e.g. on Bottom Flange (BF)), the buckling resistance will increase. Likewise, when load acts above (e.g. on Top Flange (TF)), the torque applies to the same direction with the twisting of beam, buckling resistance will, therefore, decreases.
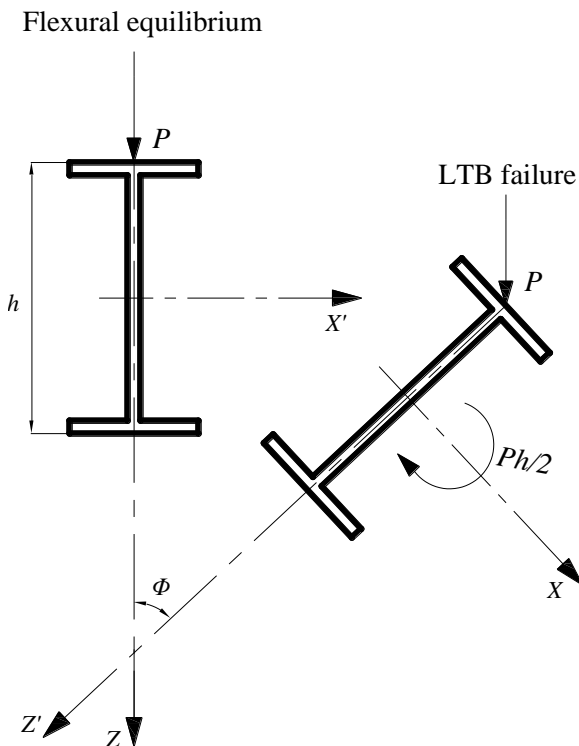
Figure 2.4 Flexural static equilibrium and LTB instability deformation (not to scale)

Theoretical investigations on this elastic buckling behaviour have been a subject of research for nearly a century (Timoshenko, 1936, Flint, 1948, Clark and Hill, 1960, Trahair, 1993, Bureau, 2006). These works have resulted in a general closed-form expression for the critical elastic LTB moment (M_{cr}) of an isotropic beam that is symmetrical about the major axis. This expression allows for different bending moment distributions, for changing end and warping restraints and for different height levels at which the loading is applied.

The expression can be written as (Clark and Hill, 1960, BSI, 1992, Bureau, 2006):

$$M_{cr} = C_1 \frac{\pi^2 E I_z}{(kL)^2} \left(\sqrt{ \left(\frac{k}{k_w} \right)^2 \frac{I_w}{I_z} + \frac{(kL)^2 G I_t}{\pi^2 E I_z} + \left(C_2 z_g \right)^2 } - C_2 z_g \right) \qquad (2.1)$$

In Eq. (2.1) L is the simply supported span. C_1 is the equivalent uniform moment factor that accounts for the shape of the bending moment distribution. C_2 is the factor to account for the vertical load height with respect to the SC. z_g is the height of the load from the SC. It is zero at the SC and positive when the load is located above (towards TF) and negative when placed below (towards BF). I_z, I_w and I_t is second moment of area for flexure about the beam's minor axis, warping rigidity and torsional rigidity, respectively.

This equation can be adopted in Eurocode 3 (BSI, 2005a) for the checking of LTB failure. The American standard for structural steel in buidings AISC 360-10 (AISC, 2010) adopts the same expression with $k = k_w = 1$. There is no consideration in this design standard for k being different from k_w. It is noted that Eq. (2.1) neglects the contribution of shear deformation whose presence decreases the buckling resistance of 1-5% for PFRP I shape (Roberts, 2002).

It is well-known that the solution giving Eq. (2.1) is based upon three sets of relationships for: equilibrium equations; strain-displacement relationship; force-strain relationship (Trahair, 1993). The difference between isotropic and orthotropic material property modelling is in the terms for the force-strain relationships (Kollár and Springer, 2003). By exchanging the isotropic stiffnesses in the relationships with the orthotropic equivalents (Allen and Bulson, 1980) and, when required, accounting for the influence of shear deformation, a solution for the orthotropic beam is obtained. The solution with shear deformation included gives slightly lower ($<5\%$) critical LTB load than that using Eq. (2.1) for the narrow-flange beam (e.g. $b_f = h/2$). This is mainly due to the presence of shear deformation is neglected in Eq. (2.1). Because it is also well-known that a PFRP beam can be treated as being consisted of orthotropic panels (Kollár and Springer, 2003), it is acceptable (Mottram, 1992a, Razzaq *et al.*, 1996, Trumpf, 2006) for Eq. (2.1) to be adopted on substituting the isotropic modulus of elasticity E and G with longitudinal elastic modulus E_L and in-plane shear modulus G_{LT} for the FRP material.

For the case of a cantilever beam, there are several solutions for the prediction of critical buckling load P_{cr}. One solution is the following formula developed by Timoshenko and Gere (1961):

$$P_{cr} = \frac{4.013\sqrt{EI_z GI_t}}{\left(L^2 - \sqrt{\dfrac{L^2 EI_w}{GI_t}}\right)} \tag{2.2}$$

P_{cr} can also be determined by adopting Eq. (2.1) with $k = k_w = 1$ and $z_g = 0$. By replacing C_1 with α, the expression is:

$$P_{cr} = \alpha \frac{\pi^2 EI_z}{L^3} \sqrt{\frac{I_w}{I_z} + \frac{L^2 GI_t}{\pi^2 EI_z}} \tag{2.3}$$

The formula to calculate α is given in Nethercot and Rockey (1973) Eqs. (2.1)-(2.3) were adopted in previous studies (Mottram, 1992a, Brooks and Turvey, 1995, Turvey, 1996, Trumpf, 2006) to predict the LTB resistance of PFRP beam. Reported herein is a general review of the key studies that informed the author's Ph.D. work.

2.3.   Lateral-torsional buckling of simply supported beam

The first experimental attempt is credited to Mottram (1992a), who conducted 35 tests on a single I beam having dimension of 101.6×50.8×6.4 mm (4×2×¼ in.) at a single span of 1500 mm. The simply supported beam (for major and minor axis flexure) was subjected to three-point bending with a 'test machine' compressive load, as seen in Figure 2.5, applied above the Top Flange (TF) through a steel fixture with freedom to displace laterally. The onset of instability failure was signalled when the base plate of the fixture had displaced sideways 2 mm from its zero-load position.
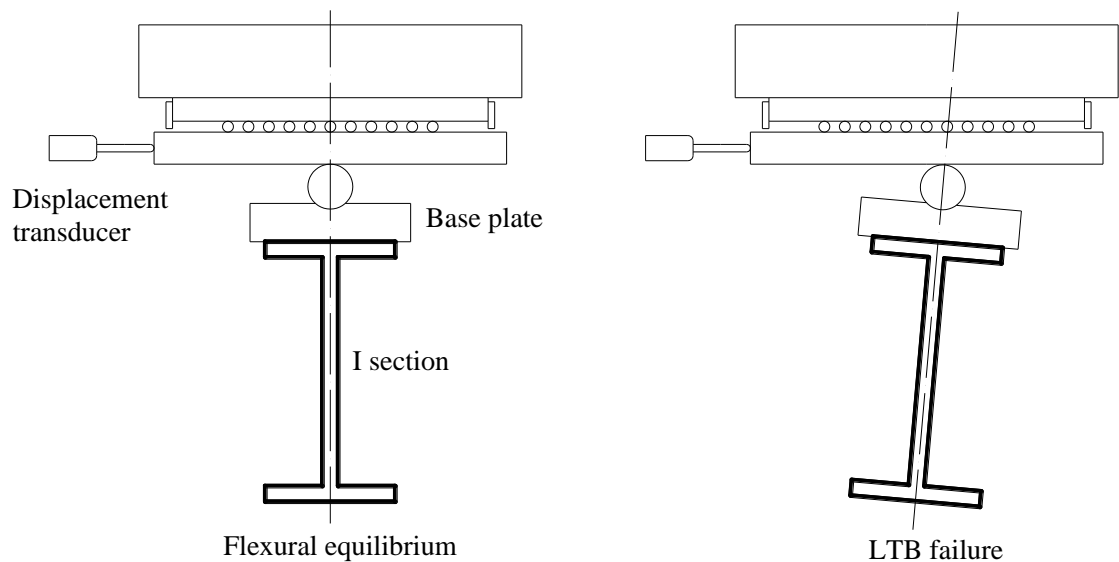
Figure 2.5 Test configuration in Mottram (1992a)

Mottram (1992a) attempted to create a bifurcation failure whereby the beam fails suddenly without any prior twist (and coupled lateral deflection). He observed a large range in the LTB resistance with P_{cr} = 2.8 kN to 5.75 kN. He argued that the presence of imperfections could be accounted for by taking the test results when the set-up allowed the beam to deform in the third mode, and later buckle suddenly with the first mode. It was observed that with this beam response the maximum buckling resistance was realized.

In the same year, Mottram (1992b) presented the solution to the governing differential equation for the LTB problem of PFRP beam. Comparing the numerical results obtained with predictions by Eq. (2.1), he showed that the differences were within 3% when the load was applied at SC. The difference between the predictions and the experimental measurements was found to be less than 30%. By plotting $P_{cr}L^2 / (4\sqrt{E_L I_z G_{LT} I_t})$ against $L^2 G_{LT} I_t / (E_L I_w)$, Mottram was able to illustrate the influence of load height and warping rigidity on the buckling resistance. It is found that due to the relative high ratio of E_L / G_{LT} , the contribution of warping to the torsional stiffness for a PFRP beam $L^2 G_{LT} I_t / (E_L I_w)$ is less than half of that for the identical steel I beam. This implies that the influence of warping rigidity is to be higher in PFRP beam. He also observed from that for a low value of $L^2 G_{LT} I_t / (E_L I_w)$ the buckling curves tend to diverge and that divergence is less obvious with steel. This indicates that the influence of load height is also more important for the PFRP beam.

The next study with simply supported PFRP beams was by Razzaq *et al*.(1996). They used the research to propose a Load and Resistance Factor Design (LRFD) approach to design for LTB strength based on a combined theoretical and experimental study using PFRP channel sections. Tests were conducted on four different cross-sections at spans ranging from 1524 mm to 2743 mm (5 ft. to 9 ft.). Beams were tested under four points

bending. Onset of failure was reported to be either when the instability suddenly happened or when lateral deflection (and integral rotation) increased without any increase in vertical load.
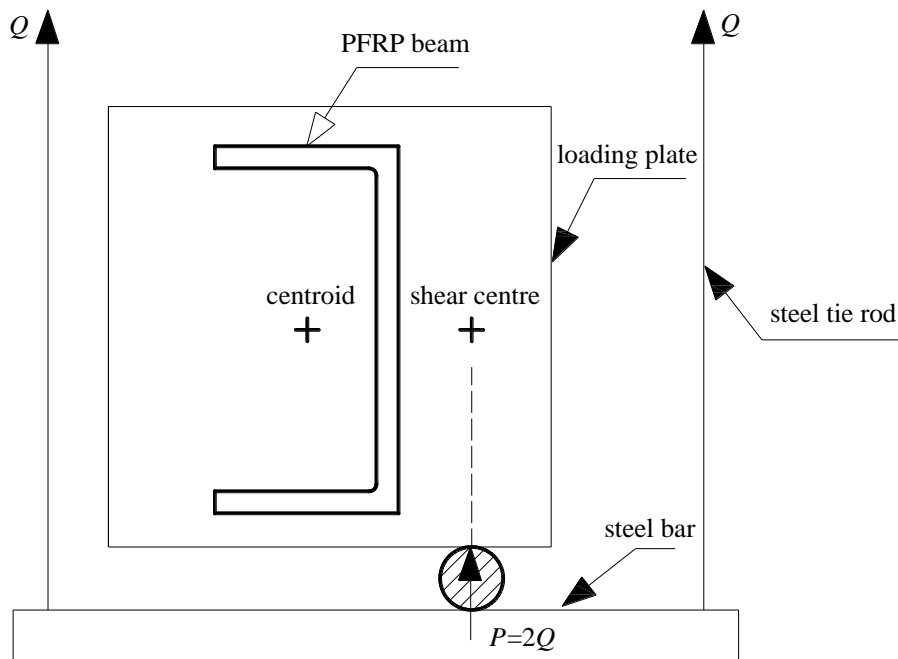
Figure 2.6 Loading configuration in Razzaq *et al.* (1996)
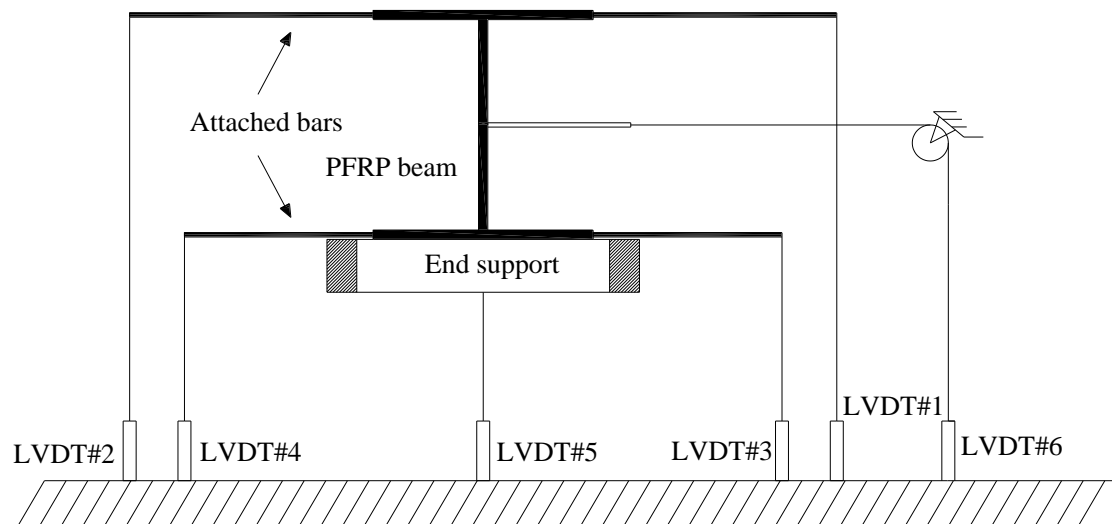
Figure 2.7 Arrangement of LVDTs at mid-span in Davalos *et al.* (1997)

One of the weaknesses of the test arrangement illustrated in Figure 2.6 is that where there is no "bifurcation" failure, the loading plate will not keep the line of action of P through the same application point (e.g. shear centre or beam centroid). This is because the point of load application changed as the beam started to twist and move sideways. This arrangement did not strictly satisfy the requirement in the fundamental theory of LTB (Timoshenko and Gere, 1961, Trahair, 1993) that the 'point' of concentrated load remain unchanged relative to the deforming cross-sections, and that their lines of action move parallel to their initial undeformed positions.

Davalos *et al.* (1997) reported two tests on two wide-flange I beams at span $L = 4.42$ m (or 14.5 ft). The PFRP sections had the same dimensions but different fiber architectures. The beams were subjected to three-point flexure with the load applied on TF through a hydraulic ram which was fixed to the supporting frame. It was admitted by Davalos *et al.* (1997) that their test arrangement would provide a restraining force to ultimately increase the apparent LTB load. A series of LVDTs (Figure 2.7) were arranged at mid-span to measure the rotation. Strain gauges were placed on top flange to measure the strain at failure. A comparison was made between an analytical solution, FEA and test results. The analytical solution gave similar results to the FEA and both were 25% higher than the established from testing.

Trumpf (2006) carried out 16 tests on four narrow-flange I sections, size of $120 \times 60 \times 6$ mm, $160 \times 80 \times 8$ mm, $200 \times 100 \times 10$ mm, and $240 \times 120 \times 12$ mm at spans $L = 613$ mm to 2400 mm. The sections were manufactured by Fiberline A/S, Dermark. As shown in Figure 2.8(a) the vertical point load was applied at a height of 62 mm above the top flange (i.e. $z_{\mathrm{g}} = h / 2 + 62$ mm) using a hydraulic jack. He recommended a partial safety

factor of $\gamma_M = 1.5$ for a LTB curve for the tested PFRP beams. This recommendation was based on the calibrated γ_M from 1.37 to 1.43 for 16 tests.

(a)   (b)
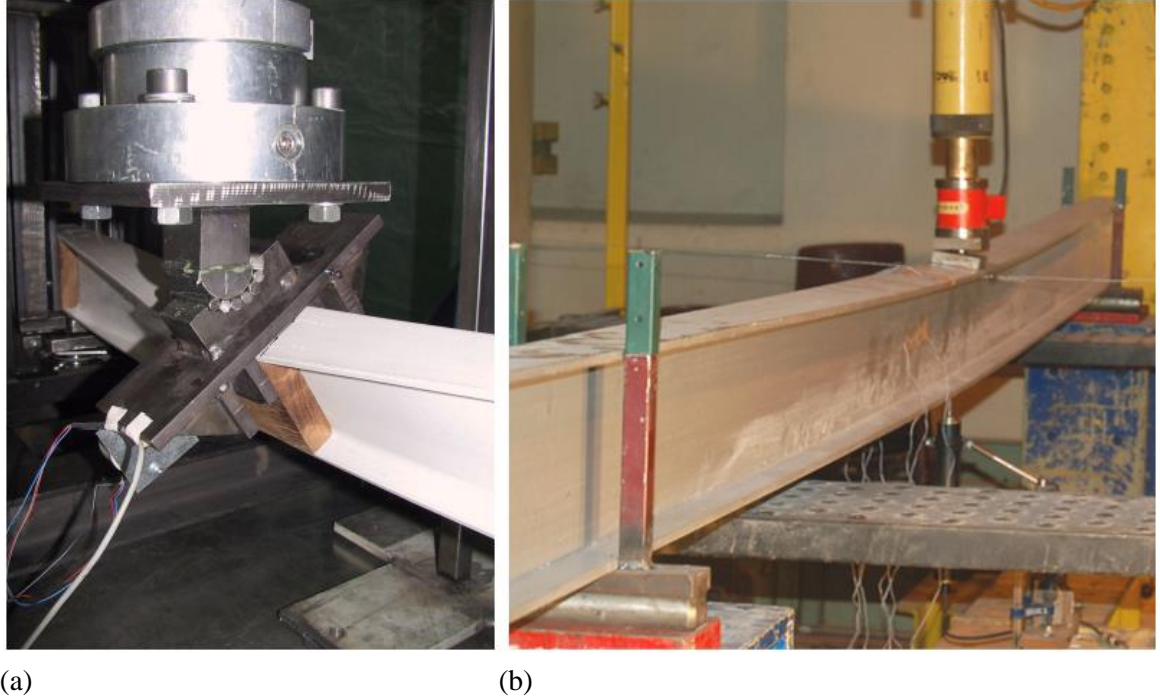
Figure 2.8 LTB testing on I beam: (a) in Trumpf (2006); (b) in Correia *et al.* (2011)

Recently, Correia *et al.* (2011) conducted lateral testing on a single I beam, size of $200 \times 100 \times 10$ mm, produced by Topglass firm, Italy. Figure 2.8(b) shows their test arrangement. It is observed that in both studies the TF is not free to move laterally and this additional restraint, which is not assumed in the formulation of Eq. (2.1), must have an influence on the LTB resistance. In addition, as the jack was rigidly fixed in one position, the load cannot follow the beam's deformation when it starts to buckle. Correia *et al.* (2011) found that when LTB failure happens the maximum direct stress is considerably below the direct tensile strength of PFRP material. This observation agrees with what observed by Mottram (1992b) who found the direct stress at LTB failure to be 30% of the material strength.

2.4. Lateral-torsional buckling of cantilever beam
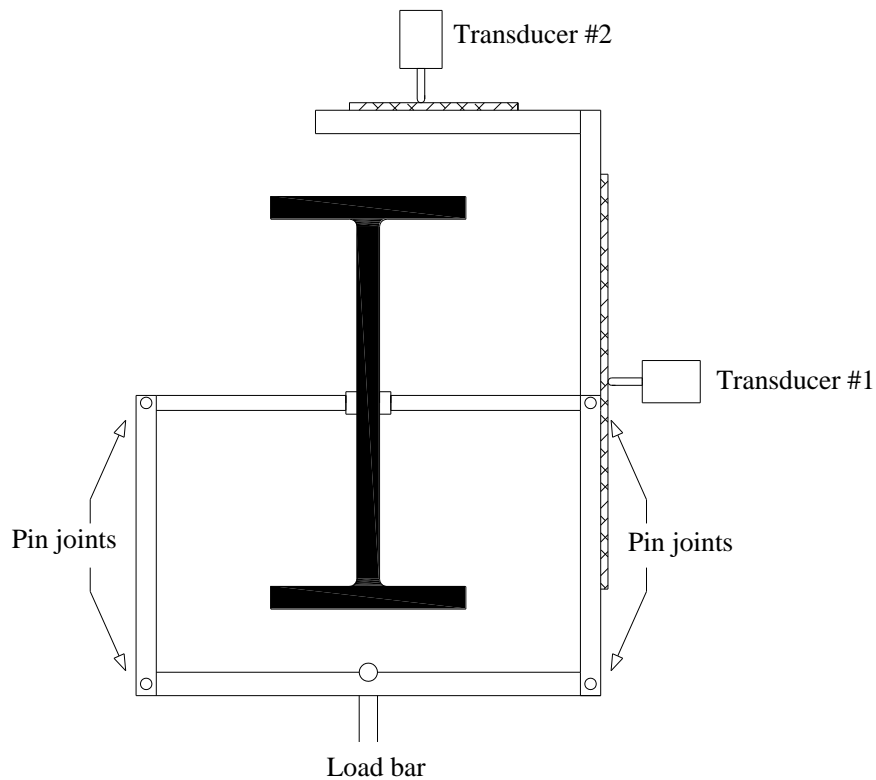
Figure 2.9 Measurement set-up in Brooks and Turvey (1995)

Brooks and Turvey (1995) conducted 10 tests on cantilever I beams size of $102 \times 51 \times 6.4$ mm with a four-bar fixture attached at mid-depth of the free end from which the load bar was hanged. This loading fixture seen in Figure 2.9 also allows transducers #1 and #2 to measure the vertical and horizontal displacement for the beam specimen. They compared the P_{cr} results with three prediction methods. The first method was by Eq. (2.3) and the second from Eq. (2.2). Their third prediction is eigenvalue FEA using the commercial coding ABAQUS®. Experimental P_{cr}s were found to be 30% lower than predictions. It is argued that the difference was because the shear modulus at 1.37 GPa in the three predictions must be considerably below the actual modulus. The comparison showed that the Eq. (2.2) is most suitable for cantilever beams failing by LTB.

Turvey (1996) later studied the effects of changing the height of loading with cantilever I-beams having spans from 500 mm to 1500 mm. The concentrated end point load was applied above, at, and below the shear centre using the same test arrangement as in Brooks and Turvey (1995). The new experimental results were also compared with the three numerical predictions. The differences of 25-55% were obtained when the in-plane shear modulus was taken as 0.7 GPa. This study suggested the influence of geometric imperfection and pre-buckling should not be neglected. Qiao *et al.* (2003) and Shan and Qiao (2005) added new test data on cantilever I and channel beams, respectively.

2.5. Aims and objectives

The review of previous experimental researches shows that there are limited numbers of test result for simply supported PFRP beam. The loading arrangement applied was often on or above the top flange. Response and resistance changes for vertical loading applied on TF, at SC, on BF have not been investigated. Load has been applied using a hydraulic jack and this introduces unwanted restraint to LTB. As a result, the chosen loading arrangement did not satisfy the theoretical assumption for LTB failure. The review has highlighted that there is lack of investigations on how resistance changes with changing displacement boundary conditions (e.g. free to rotate or fully restrained about minor axis). A comprehensive understanding of LTB failure by way of testing that simulates the closed-form resistance formulae (like Eq. 2.1) is essential to be able to provide structural designers with verified design guidance for members in bending.

This research project aims to investigate the LTB response of PFRP beams using both FEA and experimental studies leading to the construction of a design curve with

universal application. To meet this goal, new tests with I- and channel sections were conducted at different span lengths, and with changing vertical load heights and changing displacement boundary conditions. To overcome any restraint from loading, the central load was applied by dead weights. This was not practical when the load exceeded 2 kN and the fixture chosen minimised the restraint against free lateral and twisting deformations.

A large number of material tests have been carried out to characterize the material properties required to make numerical and analytical predictions. FEA of the beams with the BCs and from the test series was carried out to develop a modelling methodology that can be used to determine the LTB resistant of other beam section sizes that cannot be characterized by laboratory testing.

CHAPTER 3

MATERIAL CHARACTERIZATION

3.1. Introduction

Application of PFRP material in structural engineering requires knowledge of elastic constants. The two properties of elasticity modulus E and shear modulus G are crucial when the closed-form equation (Eq. 2.1) is applied to predict the Lateral-Torsional Buckling (LTB) resistance. These elastic constants can be those of the full-section (e.g. E and G approximates from three-point bending test on section) or the longitudinal (tension or compression) modulus E_L and in-plane shear modulus G_{LT} obtaining from coupon tests. To analyse the buckling behaviour of PFRP beams by FEA (Nguyen *et al.*, 2013), two more elastic constants are required. They are E_T and v_{LT}, where E_T is the transverse elastic modulus and v_{LT} is the major Poisson's ratio.

This chapter presents the test methods employed to characterize the abovementioned four elastic constants and experimental results for the four sections involves in the LTB tests (one I-section and three channel sections). The experimental programme includes the following three series of tensile coupon tests: 54 longitudinal tests for E_L and v_{LT}, 20 transverse tests for E_T and 20 ten-degree (10°) off-axis tests for G_{LT}. The coupons for the longitudinal tensile tests cut from flanges and web have different widths

depending on the size of the section. Those for transverse tensile tests and 10° off-axis tests could only be extracted from the webs since the width of flanges in the four sections are not wide enough. Local buckling tests with short columns are also reported in this chapter. The purpose of these tests is to determine the local buckling stress σ_{Loc} as it is required in the non-dimensional slenderness ratio λ_{LT} used in Chapters 4 and 6. Prior to the coupon tests, the full-section properties are determined by analysing the LTB experimental data (to be presented in Chapter 4) to approximate the full-section properties E and G.

3.2. Full-section properties

The full-section properties can be obtained by following method A in Annex G of the European standard EN 13706-2 (BSI, 2002b). It requires a number of three-point bending tests to be conducted on several span lengths. The data will then be plotted for each span as either w/PL vs. L^2 or w/PL^3 vs. $1/L^2$. The slopes of the two plots give approximations to the flexural and shear stiffnesses, respectively. From these stiffnesses, the full-section moduli E and G can be determined. The two plots are constructed upon rearranging the central deflection equation from Timoshenko beam theory:

$$w = \frac{PL^3}{48EI_{\mathrm{y}}} + \frac{PL}{4GA_{\mathrm{v}}}$$

(3.1)

Rearranging Eq. (3.1) gives the following relationship:

$$\frac{w}{PL} = \frac{1}{48EI_{\mathrm{y}}}L^2 + \frac{1}{4GA_{\mathrm{v}}}$$

(3.2)

and

$$\frac{w}{PL^3} = \frac{1}{4GA_{\mathrm{v}}}\frac{1}{L^2} + \frac{1}{48EI_{\mathrm{y}}}$$

(3.3)

23

Where $A_v = \beta_s A$ is the shear area whose approximation is associated with the shear coefficient β_s in the Timoshenko beam theory. When an I or channel beam is under bending about its major axis, the shear stress is intensively distributed over the web area. Therefore, the shear area A_v can be simply calculated as to be $(h - 2 \times t_f) \times t_w$. A more rigorous expression to approximate the A_v can be found in Bank (1987) and Omidvar (1998). Since the difference between the simple approximation and the rigorous expression is found to be insignificant (e.g. For I-section, A_v is 694 mm^2 when using Omidvar's expression and 684 mm^2 by the simple method), the former is adopted.

It is theoretically apparent that the gradient of L^2 vs. w/PL matches the intercept of w/PL^3 vs. $1/L^2$ and in reverse the intercept of w/PL vs. L^2 will be identical to the gradient of w/PL^3 vs. $1/L^2$. Therefore, each plot can be used to estimate both flexural and shear stiffness. This graphical technique requires two beams to be tested at a minimum of five different span lengths and the range of spans should cover short to long lengths (i.e. smaller and larger than the estimated critical length L_c). The critical length is established at which the contribution of shear deformation is about 12% of the deflection under flexure. From Eq. (3.1), the contribution of shear deformation is $PL/(4G_{LT}A_v)$, where the deflection from flexure is $PL^3/(48E_LI_y)$. Once the contribution of shear deformation is 12%, we have:

$$\frac{12}{100} = \frac{\dfrac{PL_c}{4G_{LT}A_v}}{\dfrac{PL_c^3}{48E_LI_y}} = \frac{12E_LI_y}{L_c^2G_{LT}A_v}$$

$$L_c = \sqrt{100E_LI_y/(G_{LT}A_v)} = 10\sqrt{\kappa_F/\kappa_S} \qquad (3.4)$$

where κ_F is the flexural stiffness (i.e. $\kappa_F = E_LI_y$) and κ_S is shear stiffness (i.e. $\kappa_S = G_{LT}A_v$).

The main LTB tests reported in Chapter 4 have been carried out using three-point bending configuration that is equivalent to what is required by this graphical method. Although the main test series are for beams failing by LTB, there will be stable flexural deformation during the first several load increments. Hence, it is feasible to utilize the data from these tests with the graphical technique. Buckling tests were conducted at four or five span lengths of 1828, 2438, 2844, 3454 and 4064 mm, depending on the section's cross-sectional dimensions.

All sections have a 6 mm nominal thickness for the web and the flange outstands. The I-beam is nominally 120 mm deep by 60 mm wide. The three channel sections have labels C1 to C3. Section C1 has a depth of 120 mm and flanges of breadth 50 mm (or 120×50 mm). C2 and C3 shapes have sizes with dimensions of 100×50 mm and 100×30 mm, respectively. The Fiberline Design Manual (2014a) gives in Tables 2.5 and 2.7 the property information for I and C1 sections, respectively. The nominal elastic constants (for design purpose) of these two shapes are given as $E = 23\,\text{GPa}$ and $G = 3\,\text{GPa}$. These properties for sections C2 and C3 are not tabulated in the design manual, they are available from the pultruder's website at http://www.fiberline.com. These two C-sections have the same elastic constants (E and G) as sections I and C1.

Table 3.1 Geometric properties and critical span lengths of the test sections

Section name	Nominal dimensions (mm)	I_y (mm^4)	A_v (mm^2)	L_c (mm)
(1)	(2)	(3)	(4)	(5)
I	$120 \times 60 \times 6$	2.97×10^6	684	1830
C1	$120 \times 50 \times 6$	2.58×10^6	684	1700
C2	$100 \times 50 \times 6$	1.66×10^6	564	1500
C3	$100 \times 30 \times 6$	1.14×10^6	564	1250

Applying these elastic constants into Eq. (3.4) the critical length of each section is listed in column (5) of Table 3.1. This table has in columns (1-4) the section name, the nominal dimensions, the nominal second moment of area about major axis (I_y) and the

shear area (A_v). It can be seen that the span lengths in the buckling tests do not strictly satisfy the requirement of EN 13706-2 that is to have span at length longer and shorter than L_c. In fact all sections are tested with the smallest span on the high side of L_c.

Table 3.2 w/PL data to obtain the full elastic constants

Span (mm)	1828	2438	2844	3454	4064
	w/PL (1/N)				
(1)	(2)	(3)	(4)	(5)	(6)
I	8.01×10^{-7}	1.33×10^{-6}	1.80×10^{-6}	2.60×10^{-6}	3.60×10^{-6}
C1	9.37×10^{-7}	1.60×10^{-6}	1.99×10^{-6}	3.02×10^{-6}	4.21×10^{-6}
C2	1.25×10^{-6}	2.42×10^{-6}	3.40×10^{-6}	4.76×10^{-6}	6.35×10^{-6}
C3	2.21×10^{-6}	3.40×10^{-6}	4.60×10^{-6}	7.10×10^{-6}	-

Table 3.2 summarizes the w/PL values taken from the main buckling tests when the beams are under in-plane bending with very small ($\phi < 0.5^\circ$) or no twist rotation. Column (1) gives the section name and columns (2-6) present the w/PL data with span length from the shortest $(L = 1828 \text{ mm})$ to the longest $(L = 4064 \text{ mm})$. There is no data for section C3 at the longest span as no buckling test was conducted at span of 4064 mm.
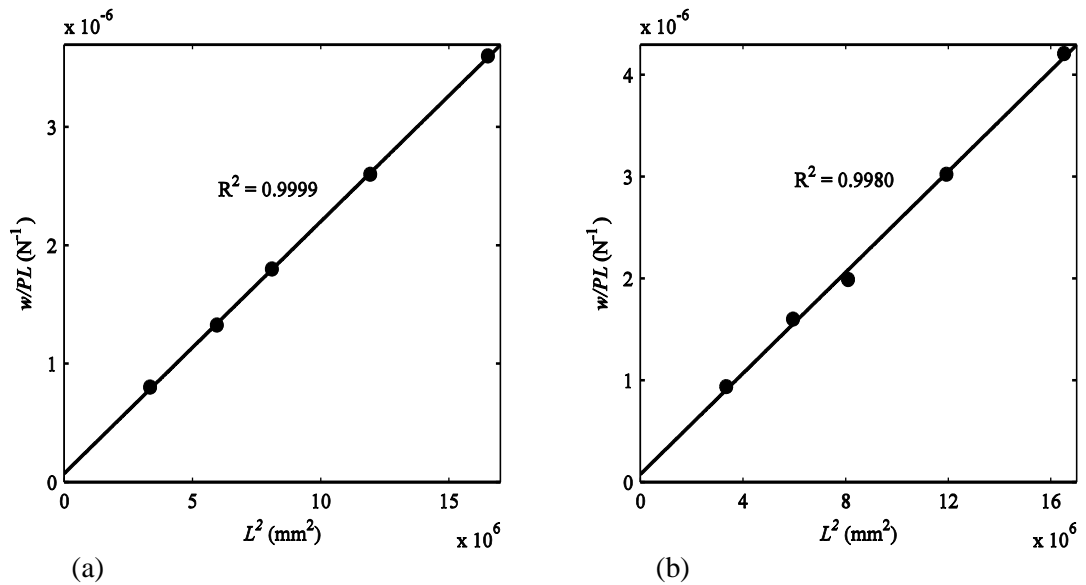
Figure 3.1 w/PL vs. L^2 for: (a) I beams; (b) C1 beams
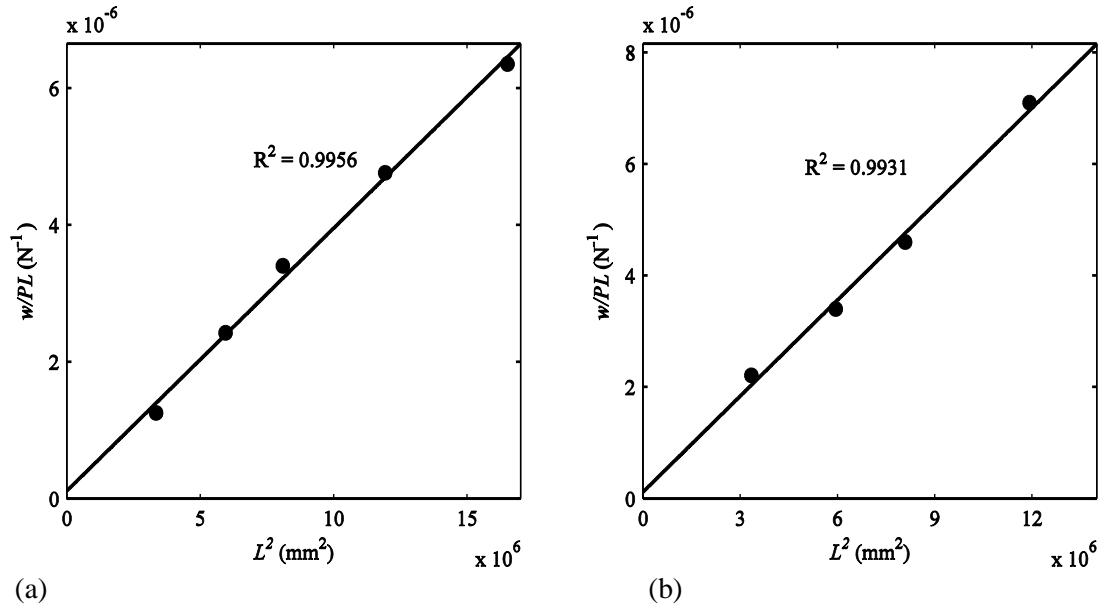
Figure 3.2 *w/PL* vs. L^2 for: (a) C2 beams; (b) C3 beams

Using the data in Table 3.2, four plots of w/PL vs. L^2 are presented in Figures 3.1(a) and 3.1(b) for sections I and C1 and Figures 3.2(a) and 3.2(b) for sections C2 and C3. The R-squared values on the figures in range from 0.993 to 0.999 shows a good fit between the data point and the least-squares linear trend line.

Table 3.3 presents the section moduli for I and three channel sections, with columns (1-3) giving the name of section, the gradient and the intercept of the straight line of the plots presented in Figures 3.1 and 3.2. Columns (4) and (5) give the predicted E and G.

Table 3.3 Prediction of section moduli of I- and channel sections

Section	Gradient $\dfrac{1}{48EI_y}$ (1/N.mm^2)	Intercept $\dfrac{1}{4G_{LT}A_v}$ (1/N)	E (GPa)	G (GPa)
(1)	(2)	(3)	(4)	(5)
I	2.13×10^{-13}	7.60×10^{-8}	33.0	4.8
C1	2.48×10^{-13}	8.04×10^{-8}	32.6	4.5
C2	3.84×10^{-13}	1.18×10^{-7}	32.5	3.8
C3	5.74×10^{-13}	1.26×10^{-7}	31.9	3.5

27

It can be seen that E is in range of 31.9 GPa to 33.0 GPa, and this is significantly higher (39-44%) than the nominal value 23 GPa in the Fiberline Design Manual (2014a). The shear moduli are in range of 3.5 GPa to 4.8 GPa and this shows a significant variation. This observation is well-known (Roberts and Al-Ubaidi, 2002) since the intercept in this graphical method is very sensitive to the change in the gradient. A minor change in the gradient will significantly alter the intercept of the line.

3.3.   Longitudinal elastic modulus

3.3.1.   Tensile test method

To determine E_L, tensile coupon testing was adopted that followed the British Standards for the determination of tensile properties of plastics BS EN 527-1 (BSI, 2012a) and BS EN 52-4 (BSI, 1997). This test method can give the tensile strength $\sigma_{L,t}$ too. Another standard test method that is equivalent to the BSs is ASTM D638 (ASTM, 2010). However, this standard requires a dog bone shaped coupon, which is not appropriate with PFRP material because of the undesirably loss of continuous fibres along the specimens. This loss creates stress concentration in the wasted regions that potentially leads to a premature failure. Further American test method is ASTM D3039 (ASTM, 2008) that is for the determination of tensile properties of polymer matrix composite materials. This standard is popular amongst American researchers when characterizing the tensile properties of PFRP. This study will follow the procedure and requirements in the BS EN standard. The elastic constants E_L and ν_{LT} will be determined using both BS EN 527 and ASTM D3039-08 to highlight the differences obtained.

3.3.2. Test specimens

Rectangular coupons were prepared by cutting the flange and web panels as shown in Figure 3.3. With the I-section there are four coupons from four outstand flanges and two from the web, making a total of six coupons. Specimens were given labels name I-1 to I-6, where I-1 and I-2 are from top flange, I-3 and I-4 are from bottom flange and I-5 and I-6 taken from the web. It is noted that the definition of 'top' or 'bottom' flange here only imply opposite flanges. For each of the three channels, two coupons were taken from the flanges and two were extracted from the web, giving a total of four coupons per section. These coupons have labels consisting of section name (e.g. C1, C2 and C3) and their position in the section (1 for top flange, 2 for bottom flange, 3 and 4 for web). For example C1-1 is the coupon from section C1 and top flange. The names and positions where coupons were extracted from are illustrated in Figure 3.3.

| I section | C1 section | C2 section | C3 section |
| (120×60×6 mm) | (120×50×6 mm) | (100×50×6 mm) | (100×30×6 mm) |
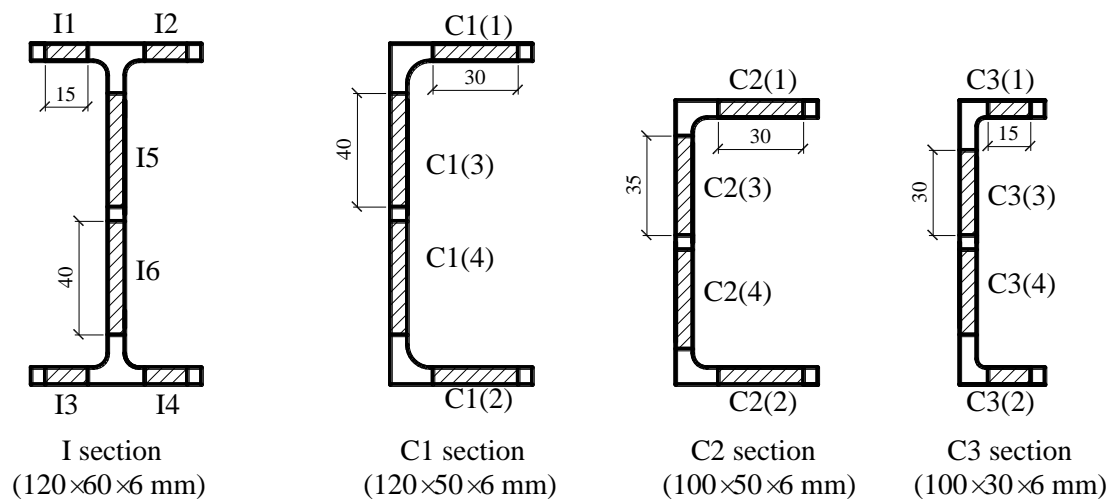
Figure 3.3 Positions where longitudinal coupons were extracted and their widths in millimetres

Outstand flanges are expected to have the same fibre architecture, while the web might have a higher amount of mat reinforcement to resist shearing force. Interestingly,

Stoddard (1997) found that the tensile elastic moduli of the flanges from a PFRP I-section size of $101.6 \times 50.8 \times 6.35$ mm from Strongwell (American) are actually not the same. The moduli on the same side (i.e. from top and bottom flanges) are relatively close together with a difference of 5-10%. The difference is nearly 20% when comparing these pair of moduli with the pair from the other side of the web. No further explanation was made on why such a significant deviation in E_L was measured. Following what was observed by Stoddard (1997), flange I-1 and I-3; flange I-2 and I-4; and web I-5 and I-6 are assumed to have the same material properties. For the channels, the two flanges and web are treated as two different materials. BS EN 527-4 suggests there should be a minimum of five specimens per batch (for each test direction). There are six specimens per patch in this investigation. The I-section has a total of 18 specimens separated into three groups of material (I-1 and I-3 in group 1; I-2 and I-4 in group 2; and I-5 and I-6 in group 3). Each position (e.g. I-1) will have three coupons for the longitudinal direction. Each channel has 12 specimens, separated into two groups for the flange and web material.

Coupon length is 290 mm and at both ends aluminium tabs were bonded to prevent local failure from stresses generated by gripping. It is to expect that failure would occur in the gauging length. The aluminium tabs have length of 70 mm and thicknesses of 2 mm. Tabs width are same as widths of the specimen. Coupons from I-section have the width of 15 mm from flange and 40 mm from the web. For C1, C2 and C3, the widths are 30 mm, 30 mm and 15 mm for flange material and for the web material, they are 40 mm, 35 mm and 30 mm respectively. These dimensions are shown in Figure 3.3.
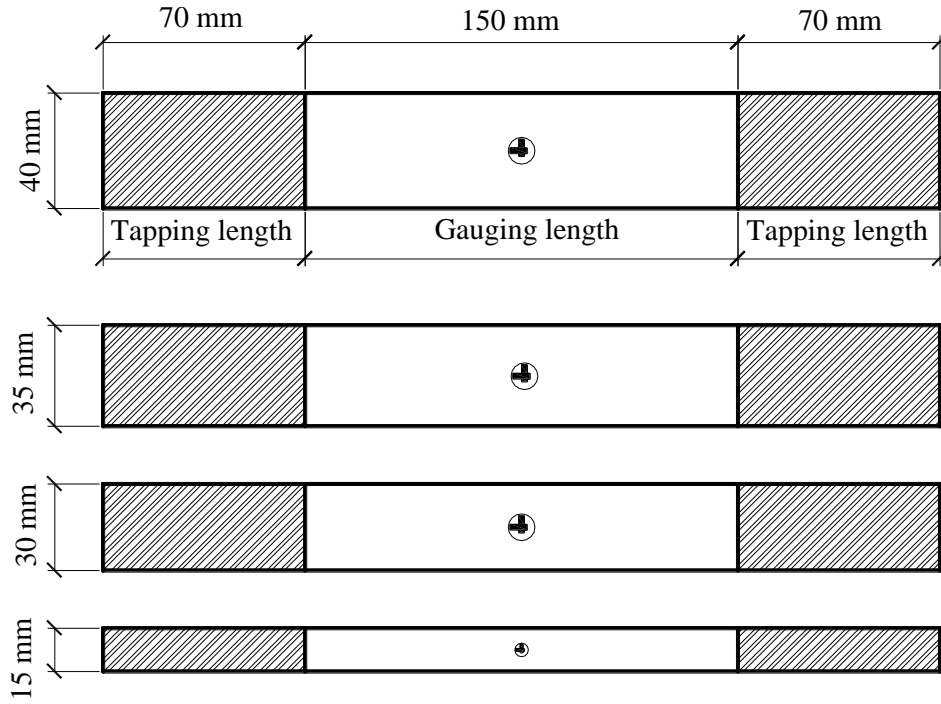
Figure 3.4 Dimension of longitudinal coupons and tabbing lengths

Figure 3.4 presents the four coupon sizes and their plan dimensions. It also shows where strain gauging was located. Two strain gauges were placed back-to-back at the centre at both sides to eliminate potential influence of undesirable flexure during the test. The actual tensile strain is taken by averaging the two readings.

Two types of strain gauge were used, with 36 coupons having unidirectional single-element foil strain gauges and other 18 coupons having bi-directional (two-element cross), stacked type foil strain gauges. The reason for using the bi-directional gauges was to determine ν_{LT}. By measuring strain in the longitudinal (ε_L) and transverse (ε_T) directions, ν_{LT} is obtained from the ratio $-\varepsilon_T / \varepsilon_L$. Before conducting tensile tests, the width and thickness of all specimens were measured using a digital calliper with repeatability to 0.01 mm.

Table 3.4 Measurements of specimen dimensions of I- and C1-sections

Specimen name	Mean width (mm)	Mean thickness (mm)	Specimen name	Mean width (mm)	Mean thickness (mm)
I-1-1	14.98	6.10	C1-1-1	29.93	6.14
I-1-2	15.03	6.04	C1-1-2	30.05	6.02
I-1-3	15.05	5.99	C1-1-3	29.95	6.13
I-2-1	15.01	6.08	C1-2-1	30.05	6.09
I-2-2	14.98	6.15	C1-2-2	29.94	6.10
I-2-3	14.98	6.02	C1-2-3	30.02	6.08
I-3-1	14.99	5.99	C1-3-1	40.04	5.96
I-3-2	15.03	6.11	C1-3-2	39.83	5.89
I-3-3	15.00	6.05	C1-3-3	39.85	6.01
I-4-1	15.07	6.01	C1-4-1	39.95	5.89
I-4-2	15.05	6.03	C1-4-2	40.21	5.98
I-4-3	14.83	5.89	C1-4-3	39.96	5.91
I-5-1	40.02	6.07	Mean of panel thickness		6.02
I-5-2	40.00	6.03	Standard Deviation		0.09
I-5-3	39.94	6.09	Coefficient of Variation		1.5%
I-6-1	39.95	6.04			
I-6-2	39.93	6.02			
I-6-3	39.65	6.05			
Mean of panel thickness		6.04			
Standard Deviation		0.55			
Coefficient of Variation		0.9%			

Table 3.5 Measurements of specimen dimensions of C2- and C3-sections

Specimen name	Mean width (mm)	Mean thickness (mm)	Specimen name	Mean width (mm)	Mean thickness (mm)
C2-1-1	29.99	6.00	C3-1-1	15.06	5.95
C2-1-2	29.96	6.07	C3-1-2	15.01	5.93
C2-1-3	29.95	5.96	C3-1-3	14.99	6.01
C2-2-1	29.80	6.03	C3-2-1	15.04	5.99
C2-2-2	29.79	6.03	C3-2-2	15.02	5.89
C2-2-3	29.89	6.01	C3-2-3	14.97	5.95
C2-3-1	35.01	5.97	C3-3-1	35.14	5.96
C2-3-2	34.92	5.97	C3-3-2	34.98	5.97
C2-3-3	35.05	6.04	C3-3-3	35.03	5.92
C2-4-1	34.95	6.04	C3-4-1	35.09	5.96
C2-4-2	34.96	5.92	C3-4-2	34.94	5.94
C2-4-3	35.30	6.16	C3-4-3	35.05	6.01
Mean of panel thickness		6.02	Mean of panel thickness		5.96
Standard Deviation		0.06	Standard Deviation		0.03
Coefficient of Variation		1.0%	Coefficient of Variation		0.6%

The measurements were taken at three different places (i.e. two ends and middle) for each dimension. Their mean values are summarized in Table 3.4 for I and C1 and in

Table 3.5 for C2 and C3. It is noted that name of the specimen has been modified by adding a digit number (i.e. 1, 2 and 3). This is to show the order of testing. For example, specimen I-1-**1** is the **1**st coupon, extracted from I-section at the "1" position for top left flange (see Figure 3.3). Specimens have a label ending in '1' are those with bi-directional strain gauges. All those ending with '2' or '3' only had unidirectional strain gauges. Tables 3.4 and 3.5 also present the mean thicknesses of all panels for each section. It is found that they are 6.04, 6.02, 6.02 and 5.96 mm for I, C1, C2 and C3 respectively. The Coefficient of Variations (CV) are from 0.6% to 1.5% which is insignificant.

3.3.3. Test procedure and results

In a typical test, the coupon was placed in the grips of a 100 kN Testometric screw-threaded test machine as shown in Figure 3.5(a). The machine operates in stroke control and the rate was set to 1 mm/minute. Load and strain gauge readings were recorded using a Orion data logger and the stroke displacement determined by the test machine software. Tensile force was applied until the specimen started to emit acoustic emission, followed soon afterwards by ultimate failure, generally in the central region. Figure 3.5 (b) shows the typical rupture failure when the axial strain is over 1%. In ten tests it was found that the aluminium tabs debonded before rupture. This generally leads to the premature failure at one end in Figure 3.5(c) or no failure. The testing had to be terminated as the applied tension started to reduce quickly. This uncommon outcome did not affect the determination of E_L and ν_{LT} but $\sigma_{L,t}$ with eight specimens was not obtained.
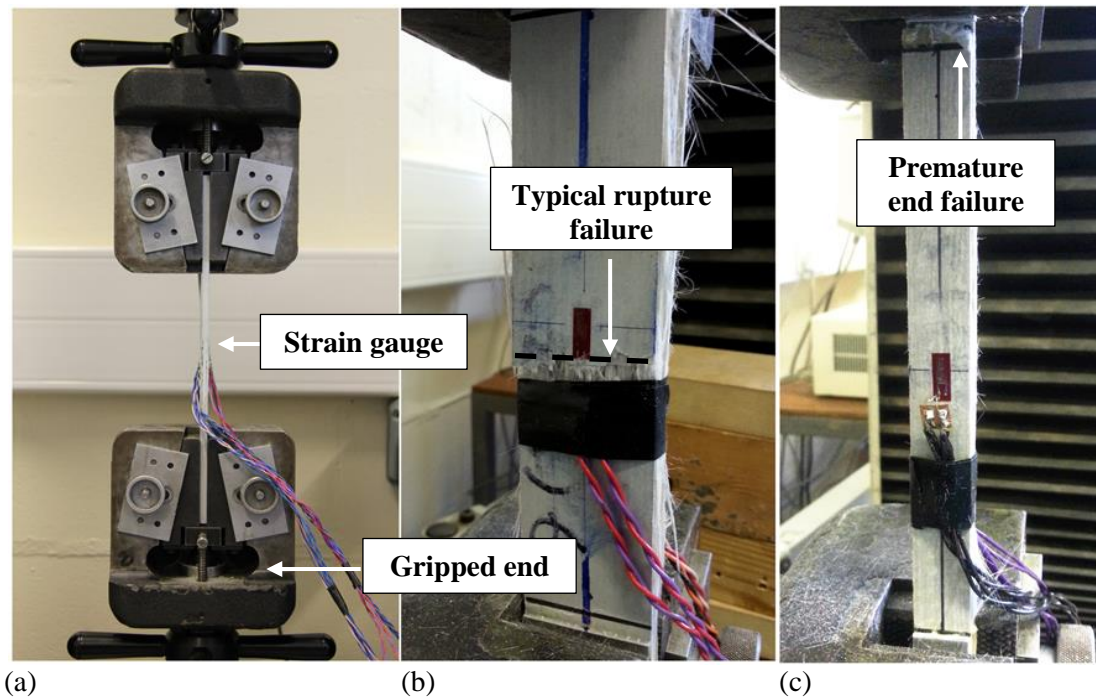
Figure 3.5 A typical tensile test: (a) during testing; (b) a rupture; (c) a premature end failure

BS EN 527-1 recommends when determining E_L to take the strain readings in the range of 0.05% to 0.25%. This can be done via either the chord modulus between the start point (i.e. $\varepsilon_L = 0.05\%$) and end point (i.e. $\varepsilon_L = 0.25\%$) or the slope of the linear least-squares (best fit) line within the strain interval. The latter was adopted. This standard is for unreinforced plastics and not for PFRP. Such a low range of strain (e.g. 0.05% to 0.25%) was chosen because a nonlinear response might occur. With PFRP material the tensile response in the longitudinal direction is known to be virtually linear up until failure (Stoddard, 1997). This study will examine if there is any significant difference when choosing different range of strains. To do so, the two ranges of strain are 0.05% to 0.25% and 0.1% to 0.5%. The latter range was chosen because it is believed to cover the maximum surface direct strain experienced in LTB testing. Evidence for this is presented in Table 3.6, where the maximum strain $\varepsilon_{LTB,max}$ (on flanges) has been estimated using:

$$\varepsilon_{\text{LTB,max}} = \frac{M_{\text{LTB,max}} \times \dfrac{h}{2}}{E_\text{L} I_\text{y}} \qquad (3.5)$$

This approximation is based on the maximum bending moment $M_{\text{LTB,max}}$ at mid-span of each section from the test results reported in Chapter 4. E_L used to estimate the maximum strain is assumed to be 28 GPa. This is a valid assumption as it will be found that the actual E_L of the sections are higher than this value. It is shown in Table 3.6 that the maximum strain in the LTB tests is 0.48%.

Table 3.6 Approximation of maximum stress and strain of beam experiences LTB failure

Section	I1	C1	C2	C3
(1)	(2)	(3)	(4)	(5)
I_y (mm^4)	2.97×10^6	2.58×10^6	1.66×10^6	1.14×10^6
Maximum bending moment $M_{\text{LTB,max}}$ (kN.mm)	4200	5800	3350	1700
Maximum strain (estimated) (%)	0.30%	0.48%	0.43%	0.3%

ASTM D3039 provides a method to determine the tensile chord (secant) modulus of elasticity with a start strain of 0.1% and an end strain of 0.3%. It stated that other methods may be defined by the user. This study will only follow the recommended method in the ASTM standard.

BS EN 527-1 recommends that Poisson's ratio should be determined at a range between 0.3% and ε_y (strain at yield). Brittle failure of PFRP means that ε_y should be taken as the ultimate failure strain which is normally >1%. It was decided to adopt the strain range from 0.3% to 0.5%. ASTM D3039 presents the chord method for obtaining Poisson's ratio with the difference between the start and end strain of 0.1%, 0.2% or 0.5%. This study adopted the range of 0.1% to 0.3% (difference is 0.2%).
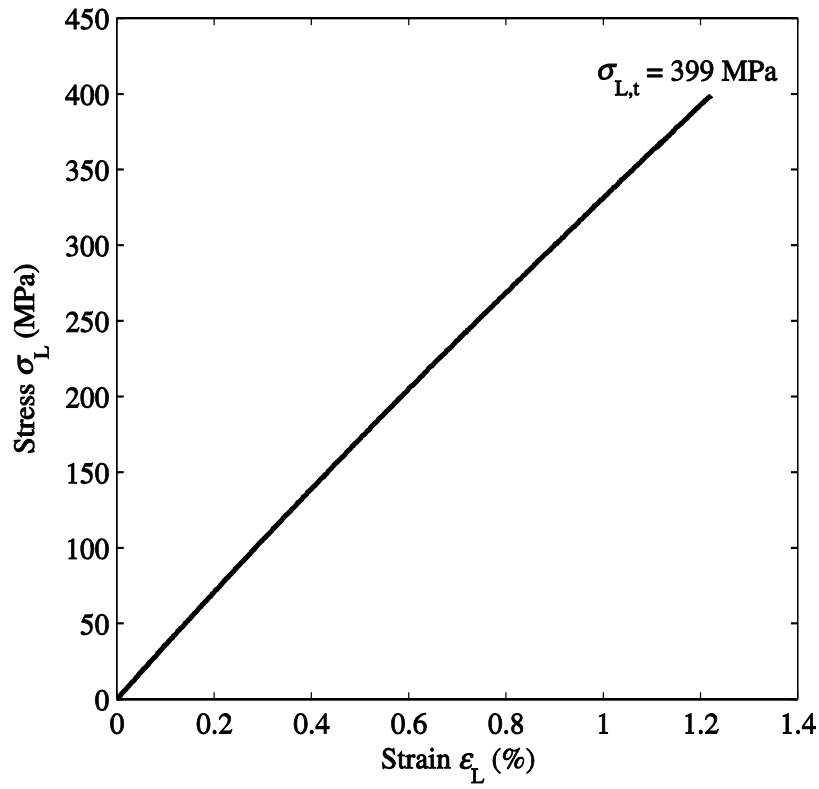
Figure 3.6 Longitudinal stress-strain curve of I-1-1 specimen
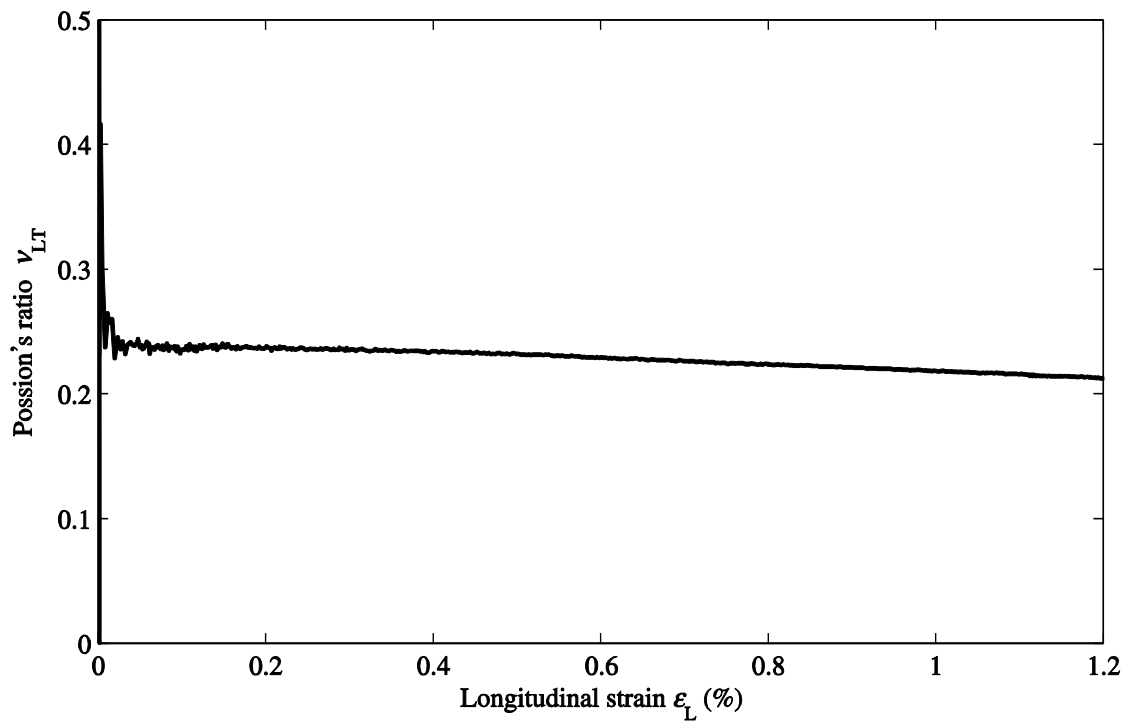
Figure 3.7 Major Poisson's ratio ν_{LT} vs. longitudinal strain ε_L of I-1-1 specimen

Figure 3.6 shows a stress-strain curve of a typical tensile test with coupon I-1-1. Figures of all 54 specimens can be found in Appendix A.1. It is as expected that the $\sigma_L - \varepsilon_L$ relationship is virtually linear up until ultimate failure. Failure occurs suddenly and there is considerable audible acoustic emission from breaking fibres. In this particular test, the specimens failed at $\varepsilon_L = 1.2\%$. Dividing the recorded maximum tension force by the measured cross-sectional area, the tensile strength is 399MPa.

Figure 3.7 shows the relationship between ε_L and ν_{LT} for the same specimen of I-1-1. The ratio decreases as ε_L increases. Mechanical properties of the PFRP material depend on the interaction of both E-glass fibres and the polyester resin matrix, and the contribution of each constituent to the material strength. The contribution of the matrix in the transverse direction is obviously more significant than that in the longitudinal direction and while the $\sigma_L - \varepsilon_L$ relationship of the fibres is linear, that of matrix is nonlinear (Stoddard, 1997). Because of this reason as the load increases, the transverse strain ε_T increases at a lower rate than the longitudinal strain ε_L so that ν_{LT} decreases. Micro cracking that could develop during the loading might also contribute to the reduction in ν_{LT} too but there is no physical observation to prove this.

Tables 3.7 - 3.10 summarize the test result in the rows. Labels for the specimens are used for the column headers. Tabulated are the mean values, Standard Deviation (SD), Coefficient of Variation (CV) for tensile E_L and ν_{LT} using methods in both standards (BS EN and ASTM). The maximum tensile stress when the coupon ruptured is reported in the last row. For determining E_L, two different ranges of strain (0.05% to 0.25% and

0.1% to 0.5%) were adopted. By comparing the results obtained using the first range, E_L is always higher, yet the difference is only 1% to 4%. This change can be considered to be insignificant. The E_L obtained using the higher strain range will be used when predicting the LTB resistance in subsequent Chapters. The modulus determined to ASTM is always higher than when using the higher BS EN strain range. The differences are again small, lying in the range of 1% to 3%. ν_{LT} was determined using the same test methods. This elastic constant is found to be between 0.21 and 0.25 to BS EN and in range of 0.21 and 0.26 to ASTM. It can also be seen that the differences are minuscule. It is noted that ν_{LT} for coupon I5-1-1 was determined with having ε_L from 0.4% to 0.6%. The reason why the approximation for this specimen couldnot follow the chosen ranges is because the strain data presented significant noise when ε_L was smaller than 0.4%. There is no explanation for this abnormal data. Given that the noise did not occur again, the comparison shows for the PFRP material that: (1) The two test standards are able to give relatively similar results; (2) the use of a higher range of strain than recommended in the standards when calculating the elastic modulus will not significantly affect the results; (3) it is acceptable if one applies the strain range in the BS EN 527-1 when determining elastic constants for any type of investigation (e.g. Euler column buckling, local buckling, etc.).

Subsequence comments are for elastic constants established from the strain range of 0.1-0.5%. It is believed that the flanges and web in the I-section have different fiber architectures. The specimens in group 1 (flange outstand I1 and I3) have an average E_L of 34.5 GPa while those in group 2 (flange outstand I2 and I4) and group 3 (web I5 and

I6) gave 30.5 GPa and 26.3 GPa, respectively. It is found that not only are the moduli of flange and web materials different, those of flanges on either side of the web are different too; the measured variation is 13%. Such a significant change in E_L has to be due to the pultrusion processing. The possibility of the differences being due to the tests themselves can be eliminated as the E_L from three tests of a flange material is relatively close, with the CV ranging from 1% to 3%. The differences, although less significant are also found between flange and web with three channel sections, despite the fact that their flanges and web of channels are believed to have the same fibre architectures. The most profound difference of 10% is with C1. For C2 and C3, they are lower at 8% and 2%, respectively. The elastic modulus of flange (34.2 GPa) is higher than in the web (31.6 GPa) in C2-section while it is smaller for the case of C1 (30.1 GPa vs. 33.1 GPa) and C3 (28.9 GPa vs. 29.5 GPa). It is worth noting that the variation in E_L will have an effect on the response of beams because the actual shear centre will not coincide with the nominal geometry location. Load acting through the nominal shear centre that is known will therefore create a load eccentric that cannot easily be accounted for in LTB testing.

Table 3.7 Elastic modulus of I-section $(120 \times 60 \times 6\ \text{mm})$

	I1			I3			I2			I4			I5			I6		
	1st test	2nd test	3rd test	1st test	2nd test	3rd test	1st test	2nd test	3rd test	1st test	2nd test	3rd test	1st test	2nd test	3rd test	1st test	2nd test	3rd test
E_L (GPa) BS EN 527-1 (0.05%-0.25%)	35.0	35.9	34.9	37.5	35.0	35.3	29.7	30.1	31.2	32.8	31.0	32.7	27.2	27.3	26.7	27.4	26.6	27.0
Mean	35.6						31.3						27.0					
SD	1.1						1.3						0.3					
CV (%)	3.1						4.1						1.2					
E_L (GPa) BS EN 527-1 (0.1%-0.5%)	34.1	35.1	34.0	35.3	33.6	34.6	29.3	29.4	30.5	31.5	30.3	31.7	26.6	26.4	26.0	26.5	25.7	26.5
Mean (GPa)	34.5						30.5						26.3					
SD (GPa)	0.7						1.0						0.4					
CV (%)	1.9						3.3						1.3					
E_L (GPa) ASTM D3039 (0.1%-0.3%)	34.6	35.7	34.7	36.7	34.6	34.8	29.9	29.9	31.3	32.4	30.9	32.2	27.0	27.3	26.5	27.1	26.3	26.8
Mean	35.2						31.1						26.8					
SD(GPa)	0.9						1.1						0.4					
CV (%)	2.4						3.5						1.4					
ν_{LT} BS EN 527-1	0.227			0.240			0.248			0.212			0.215			0.230		
ν_{LT} ASTM D3039	0.235			0.257			0.251			0.221			0.212			0.247		
Tensile strength (MPa)	399	N/A	327	339	347	N/A	326	348	371	352	312	376	331	340	339	352	321	380

Table 3.8 Elastic modulus of C1-section $(120 \times 50 \times 6\ \text{mm})$

	C1-1			C1-2			C1-3			C1-4		
	1st test	2nd test	3rd test	1st test	2nd test	3rd test	1st test	2nd test	3rd test	1st test	2nd test	3rd test
E_L (GPa) BS EN 527-1 (0.05%-0.25%)	31.0	30.9	31.0	31.2	31.5	31.8	34.5	36.2	35.3	33.0	31.7	32.7
Mean	31.2						33.9					
SD	0.4						1.7					
CV (%)	1.1						5.1					
E_L (GPa) BS EN 527-1 (0.1%-0.5%)	28.9	30.2	29.9	30.4	30.5	30.7	34.0	35.1	34.2	32.4	30.9	31.9
Mean (GPa)	30.1						33.1					
SD (GPa)	0.6						1.6					
CV (%)	2.2						4.8					
E_L (GPa) ASTM D3039 (0.1%-0.3%)	30.6	30.7	30.5	31.0	31.2	31.4	34.1	35.8	34.8	32.8	31.4	32.3
Mean	30.9						33.5					
SD(GPa)	0.4						1.7					
CV (%)	1.2						4.9					
ν_{LT} BS EN 527-1	0.210			0.224			0.247			0.233		
ν_{LT} ASTM D3039	0.231			0.234			0.253			0.240		
Tensile strength (MPa)	N/A	329	307	296	339	314	299	313	282	314	331	328

Table 3.9 Elastic modulus of C2-section $(100 \times 50 \times 6$ mm)

	C2-1			C2-2			C2-3			C2-4		
	1st test	2nd test	3rd test	1st test	2nd test	3rd test	1st test	2nd test	3rd test	1st test	2nd test	3rd test
E_L (GPa) BS EN 527-1 (0.05%-0.25%)	35.1	34.1	35.4	35.2	36.2	35.2	33.4	32.4	31.8	32.5	33.2	31.6
Mean	35.2						32.5					
SD	0.7						0.7					
CV (%)	1.9						2.2					
E_L (GPa) BS EN 527-1 (0.1%-0.5%)	34.2	33.4	34.5	34.1	35.0	34.1	32.3	31.5	31.0	31.5	32.5	30.7
Mean (GPa)	34.2						31.6					
SD (GPa)	0.5						0.7					
CV (%)	1.5						2.2					
E_L (GPa) ASTM 3039 (0.1%-0.3%)	34.7	33.8	35.1	35.1	35.7	34.7	33.0	32.0	31.6	32.2	32.9	31.3
Mean	34.9						32.2					
SD(GPa)	0.6						0.7					
CV (%)	1.8						2.1					
v_{LT} BS EN 527-1	0.221			0.232			0.225			0.220		
v_{LT} ASTM D3039	0.231			0.239			0.238			0.230		
Tensile strength (MPa)	N/A	362	427	353	410	437	368	341	425	405	391	368

Table 3.10 Elastic modulus of C3-section $(100\times30\times6$ mm)

	C3-1			C3-2			C3-3			C3-4		
	1st test	2nd test	3rd test	1st test	2nd test	3rd test	1st test	2nd test	3rd test	1st test	2nd test	3rd test
E_L (GPa) BS EN 527-1 (0.05%-0.25%)	29.6	31.7	30.3	27.0	28.6	28.6	29.6	29.0	30.0	31.0	31.0	29.9
Mean	29.3						30.1					
SD	1.6						0.8					
CV (%)	5.5						2.6					
E_L (GPa) BS EN 527-1 (0.1%-0.5%)	29.2	31.2	29.7	27.0	28.1	28.3	29.0	28.5	29.2	30.2	30.4	29.3
Mean (GPa)	28.9						29.4					
SD (GPa)	1.5						0.7					
CV (%)	5.0						2.5					
E_L (GPa) ASTM D3039 (0.1%-0.3%)	29.4	31.7	30	27.3	28.2	28.7	29.8	28.9	29.8	30.7	30.8	29.6
Mean	29.2						29.9					
SD(GPa)	1.5						0.7					
CV (%)	5.3						2.4					
ν_{LT} BS EN 527-1	0.244			0.238			0.241			0.224		
ν_{LT} ASTM D3039	0.248			0.248			0.251			0.235		
Tensile strength (MPa)	N/A	370	307	N/A	369	333	312	348	N/A	N/A	368	290

3.4. Transverse elastic modulus

3.4.1. Specimens and test procedure

Tensile coupon testing followed the requirements in BS EN 527-1 to determine the transverse elastic modulus E_T. Coupons were only cut from the web because the widths of the flanges were too short for gripping and for an adequate gauge length. There is still concern that the web coupons are of sufficient length that the clamping effect can be neglected. Gosling and Saribiyik (2003) studied the influence of geometric factors (i.e. coupon length, thickness, and tabbing length) on measuring tensile modulus by conducting finite element simulations and experiments on both short and long (standard) coupons. Their short coupons had dimensions of $50 \times 10 \times 3.1$ mm giving a slenderness ratio (length/width) of 5. They concluded from the research that the short coupon size is capable of establishing E_T but cannot be employed for E_L characterization. In this study the coupons are of 15 mm in width and 100 mm in length to give a slenderness ratio of 6.7 which is higher than that used by Gosling and Saribiyik (2003). Five coupons were prepared for each section giving a total of 20 specimens. Table 3.11 summarizes in columns (1-4) the specimen name, the length, the width and the thickness. Each has a reference code consisting of a character string. Letter 'T' is for 'Transverse', followed by the section type (i.e. I, C1, C2 or C3). The last character is for the specimen number (i.e. 1 to 5). Unidirectional 6 mm foil strain gauges were positioned on both sides of the coupons at their middle. Test machine and procedure is the same as described in sub-section 3.3.3.

Table 3.11 Measurements and tests results for transverse (web) coupons of I, C1, C2 and C3

Specimen name	Length (mm)	Width (mm)	Thickness (mm)	Transverse modulus				Transverse strength (MPa)
				E_T (GPa)	Mean (GPa)	SD (GPa)	CV (%)	
(1)	(2)	(3)	(4)	(5)	(6)	(7)	(8)	(9)
T-I-1	102.71	15.10	6.00	11.3				74.4
T-I-2	102.76	15.06	6.04	10.5				68.3
T-I-3	102.22	15.02	6.01	10.6	10.8	0.3	3.0	75.7
T-I-4	102.66	15.13	6.07	10.9				79.3
T-I-5	102.67	15.05	6.00	10.6				77.4
T-C1-1	102.12	14.91	5.84	11.2				61.9
T-C1-2	102.31	15.14	5.92	11.7				54.5
T-C1-3	102.34	15.13	5.88	12.7	11.7	0.7	5.5	56.2
T-C1-4	102.35	15.08	5.90	12.0				56.5
T-C1-5	102.14	15.06	5.87	11.1				51.7
T-C2-1	100.04	15.12	6.11	10.5				78.0
T-C2-2	99.96	14.99	6.01	12.6				87.7
T-C2-3	99.89	14.99	6.06	12.3	11.7	0.8	7.1	76.9
T-C2-4	99.98	14.93	6.05	11.7				80.2
T-C2-5	99.95	15.00	6.12	11.3				70.9
T-C3-1	99.97	15.13	5.89	9.4				63.6
T-C3-2	100.04	15.24	5.93	11.5				59.0
T-C3-3	100.03	15.18	5.92	9.0	10.5	1.2	11.6	61.1
T-C3-4	100.04	15.02	5.96	11.0				66.1
T-C3-5	100.05	15.06	5.92	11.6				67.4

3.4.2. Test results

Figure 3.8 shows a photo of a typical tensile test with the specimen loaded in the transverse direction. A strain gauged coupon was placed between the two grips and had the tensile force applied under stroke control (Figure 3.8(a)). The coupon deformed and failed with the mode transverse through-thickness cracking (Figure 3.8(b)).

Figure 3.9(a) shows the direct stress-direct strain curve for T-I-2. It is observed from the relationship that, as the strain increases above 0.4%, strain suddenly increases with a slight reduction in stress. Both stress and strain then increase with E_T seen to be virtually constant (if there is a decrease in E_T, it is insignificant). The relationship after

the first softener region is parallel to the initial behaviour. This response is observed more than one time during loading to failure.
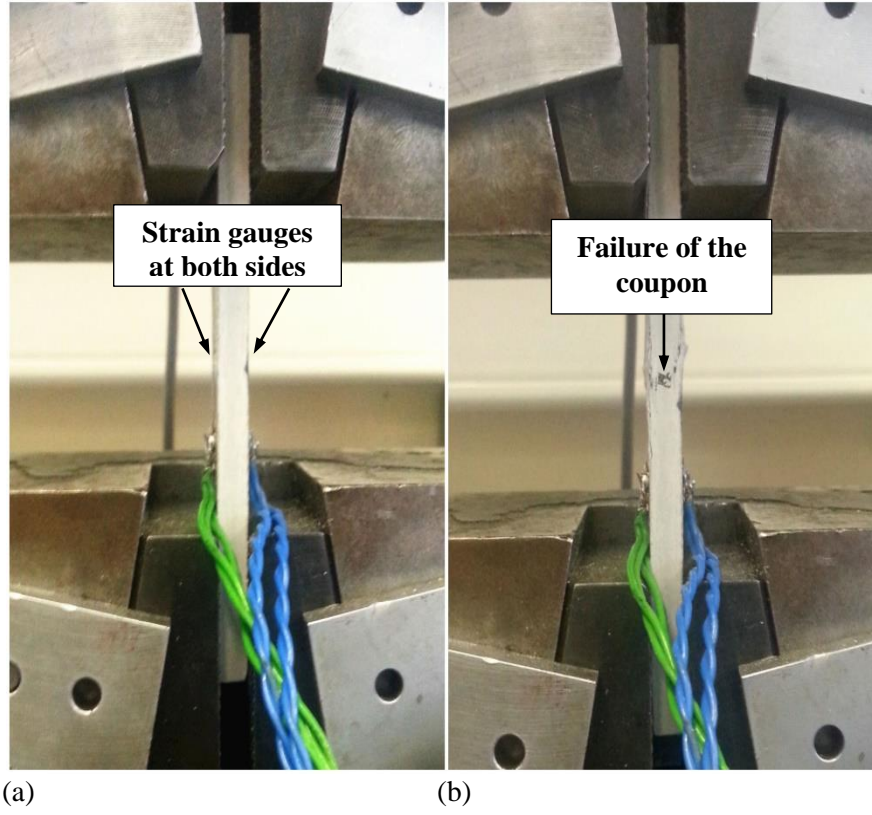
Figure 3.8 A typical transverse coupon test: (a) testing; (b) rupture
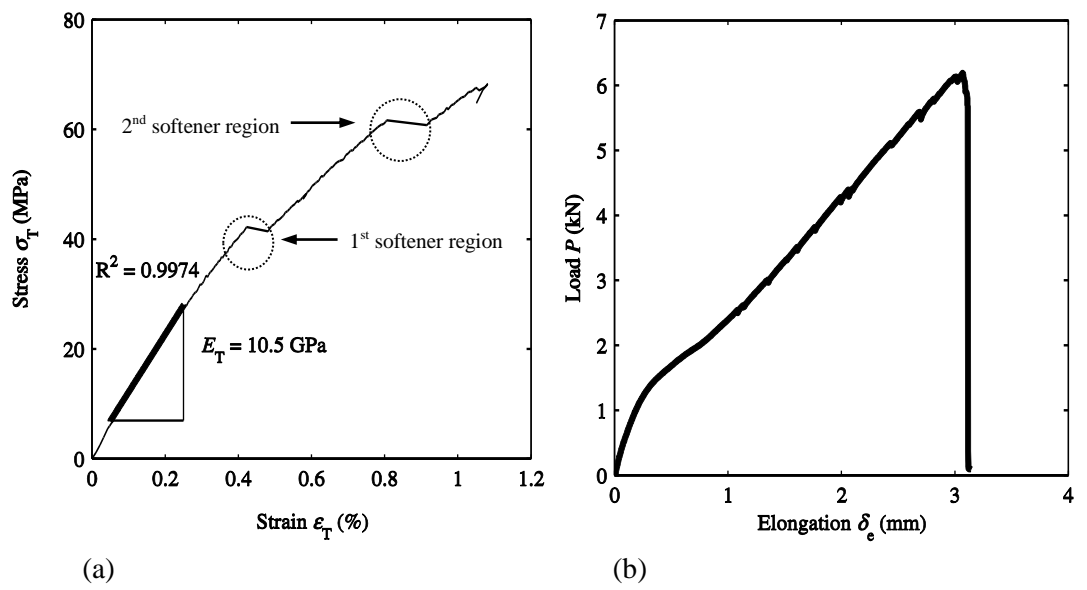
Figure 3.9 (a): σ_T vs. ε_T curve for T-I-2; (b): P vs. δ_e for T-I-2

From load vs. elongation curve in Figure 3.9(b), it is shown that the response in Figure 3.9(a) is not because the specimen has slipped in the grips. The curve of P vs. δ_e remains linear up to rupture at about 6 kN. For the transverse material, the E-glass fibres act as stress concentrators in the more flexible matrix. As a result, the transverse tensile strength of an Unidirectional (UD) fibre FRP material is lowered below that of the bulk matrix material. In other words, fibres 'aligned' with the transverse direction from the Continuous Filament Mat (CFM) reinforcement layers mainly contribute to the transverse strength. During a test internal fracture starts to progress within the thickness of UD reinforcement layers only. This cracking gradually reduces the transverse stiffness of the specimen and allows elongation to occur in the direction of extension. This explains the strain relieving regions on the stress-strain curve. It is also observed that there are two degradation stages prior to ultimate failure. Data of stress vs. strain for the all 20 tests are presented in Appendix A.2.

Previous discussion in sub-section 3.3.1 showed that the maximum ε_L in a LTB test should not exceed 0.5%. Giving that ν_{LT} is smaller than 0.25, ε_T will be < 0.13%. Based on this observation, it is reasonable to determine E_T based on the recommended strain range from 0.05% to 0.25% in BS EN 527-1. Column (5) in Table 3.11 gives E_T for the 20 specimens. Batches mean, Standard Deviation (SD) and Coefficient of Variation (CV) are given in columns (6-8), respectively. The transverse strengths are listed in column (9). Between the four sections, it is found that E_T differs slightly, with a maximum difference of 9%. The batch CVs range from 3% to 12%. Giving that the E_L of section C1 at 33.1 GPa and C2 at 31.6 GPa are higher than that of I at 26.3 GPa and C2 at 29.5 GPa, the E_T of C1 and C2 are also higher than of I and C3. Figure 3.10

gives the mean E_L and E_T in the four sections. All the numbers on the right side of the arrow pointing downwards are for E_T.
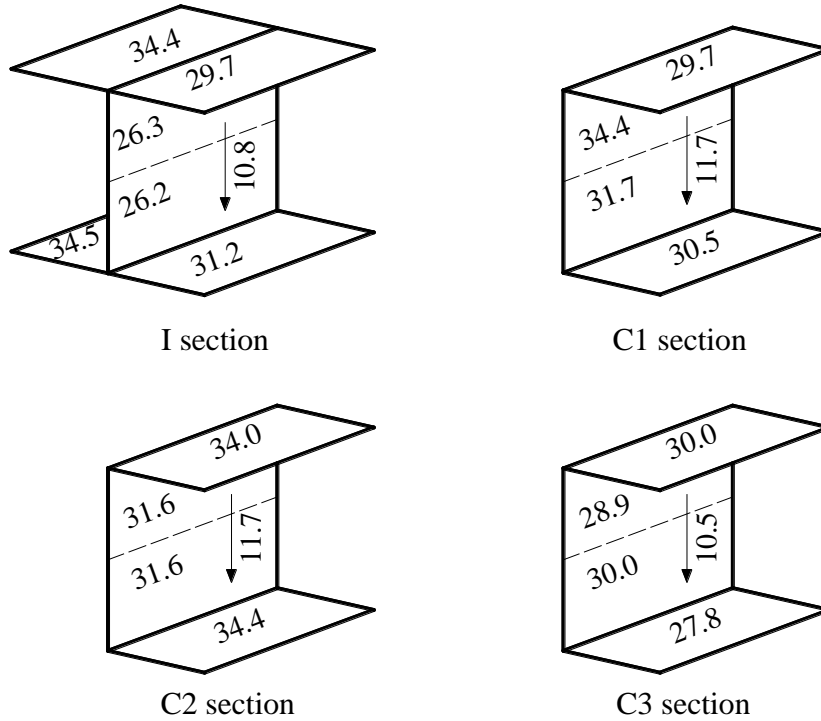
Figure 3.10 Mean E_L and E_T (GPa) of flange and web panels for four sections

3.5. In-plane shear modulus

Of the four elastic constants, the in-plane shear modulus (G_{LT}) is the most difficult to determine. To be able to measure G_{LT}, it is essential that a sufficient volume of material is subjected to pure shearing, and this is where current standard test methods are often not found to be satisfactory. Popular test methods include: Iosipescu ASTM D5379 (ASTM, 2012b); V-notched rail shear test ASTM D7078 (ASTM, 2012c); plate twist method BS EN 15310 (BSI, 2005b) and ten-degree off-axis tensile test.

The Iosopescu test method was originally developed for isotropic material by Nicholi Iosipescu and in 1993 became an ASTM standard for composite (FRP) materials

(Hodgkinson, 2000). It is one of the most commonly used tests with composite material because it allows both G_{LT} and shear strength (τ_u) to be determined. It is applicable to a wide range of materials (both isotropic and orthotropic) and the failure mechanism is that for pure shearing. Its weaknesses are as follows: (1) it requires complicated coupon shape to be accurately machined; (2) it requires a specific loading fixture with very tight dimensional tolerances; (3) load is applied by concentrated point that potentially leads to side edge-crushing (this might disturb the uniform stress state on the gauge area also); (4) the specimen size of 76 mm × 20 mm (with gauge length of 12 mm) is small, especially in terms of the volume of material subjected to pure shearing.

The V-notched rail shear test has overcome two weaknesses with the Iosipescu method. Its fixture reduces preparation time and potential stress concentrations. The gauge length of 31 mm is nearly 3 times larger than in the Iosipescu (gauge length of only 12 mm). Similar to the Iosipescu method, the V-notched rail does require a complicated coupon and a special loading fixture. An acceptable connection between test machine grips and the specimens, using either bolting or adhesive bonding is known to be difficult (Hodgkinson, 2000).

In the plate twist method BS EN 15310 (BSI, 2005b) a rectangular specimen is supported at two opposite corners and the load is applied on the two remaining corners. The G_{LT} is determined through the recorded loads and the displacement at the loading points. This test method allows a large area to be subjected to pure shearing which means the results would be more representative. It recommends a standard specimen of $150 \times 150 \, \text{mm}$ and if a non-standard specimen to be adopted, the length-to-thickness ratio should be ≥ 35. The PFRP shapes in this study have the highest length-to-thickness ratio of $120/6 = 20$ which cannot satisfy the requirement of this test method.

The ten-degree (10°) off-axis method has been employed (Chamis and Sinclair, 1977,

Hodgkinson, 2000) to obtain G_{LT} and τ_u for FRP material having continuous aligned

UD fibres. This method requires straightforward and economical specimen preparation

and only needs a standard tensile testing machine with no special loading fixture. The

weakness with this shear test is the complexity of the data reduction to determine G_{LT}.

With the help of computational software this weakness is readily resolved. Because the

test data can be sensitive to the angle between the principal axis of the UD fibres and

the tensile loading axis special care is given to the machining of the rectangular coupons.

This method is adopted next to characterize G_{LT} for the four sections because of its

simplicity and advantage in shearing a relatively much larger volume of non-

homogeneous PFRP material.

3.5.1. 10° off-axis tensile test method

With the load direction not coinciding with either the longitudinal or the transverse

direction, a biaxial stress state is induced that consist of three in-plane stresses (Figure

3.11) of longitudinal direction σ_{11}, transverse direction σ_{22} and shear stress σ_{12}. These

stresses can be expressed as a function of the three stresses σ_{xx}, σ_{yy} and σ_{xy} for the

Cartesian coordinate system that has *xx* axis aligned with the tensile load direction. The

transformation relationships are (Chamis and Sinclair, 1977):

$$
\begin{bmatrix} \sigma_{11} \\ \sigma_{22} \\ \sigma_{12} \end{bmatrix} = \begin{bmatrix} \cos^2(\theta) & \sin^2(\theta) & 2\cos(\theta)\sin(\theta) \\ \sin^2(\theta) & \cos^2(\theta) & -2\cos(\theta)\sin(\theta) \\ -\cos(\theta)\sin(\theta) & \cos(\theta)\sin(\theta) & \cos^2(\theta)-\sin^2(\theta) \end{bmatrix} \times \begin{bmatrix} \sigma_{xx} \\ \sigma_{yy} \\ \sigma_{xy} \end{bmatrix} \quad (3.6)
$$

where θ is the angle between the loading axis and the UD fibres direction.

For the tension load case (with $\theta = 10°$), it is obvious that $\sigma_{yy} = \sigma_{xy} = 0$, and so Eq. (3.6) gives:

$$\sigma_{11} = \cos^2(\theta)\sigma_{xx} = 0.97\sigma_{xx} \tag{3.7}$$

$$\sigma_{22} = \sin^2(\theta)\sigma_{xx} = 0.03\sigma_{xx} \tag{3.8}$$

$$\sigma_{12} = -\cos(\theta)\sin(\theta)\sigma_{xx} = 0.17\sigma_{xx} \tag{3.9}$$
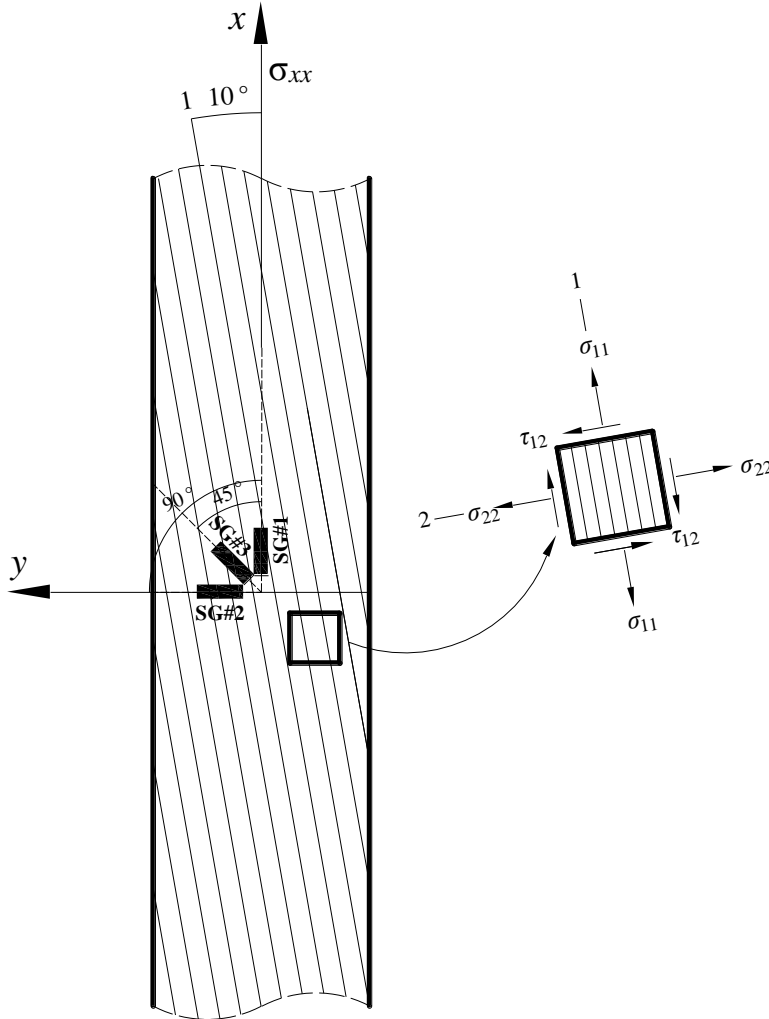
Figure 3.11 Schematic of specimen with the biaxial stress field, after Chamis and Sinclair (1977)
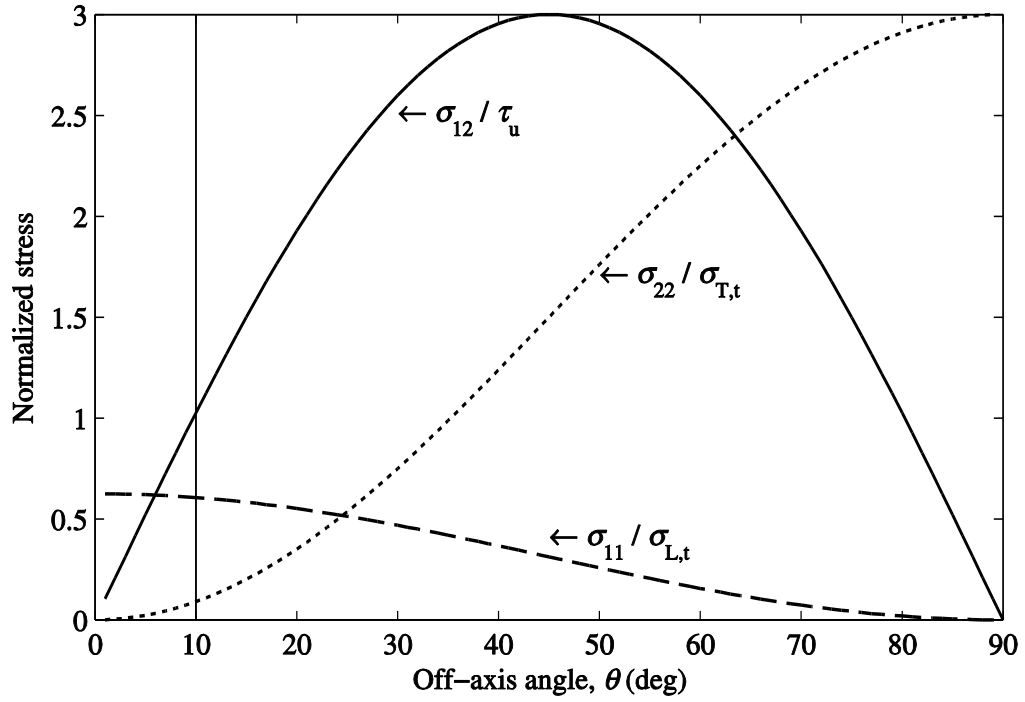
Figure 3.12 Variation of three normalized stresses with off-axis angle θ

For a specimen to fail in shear, the shear stress σ_{12} must be the principal stress that attains its strength value first. From the Fiberline Design Manual (Anon., 2014a), the shear strength is $\tau_u = 25\,\text{MPa}$, the longitudinal tensile strength is $\sigma_{L,t} = 240\,\text{MPa}$ and transverse tensile strength is $\sigma_{T,t} = 50\,\text{MPa}$. Now we define the normalized stress to be the ratio of the current principal stress and its strength (e.g. for shear it is σ_{12}/τ_u). The normalized stress will be 1.0 when that stress reaches its strength. Figure 3.12 presents a plot of the normalized stress vs. the off-axis angle θ when the applied stress is taken to be a reference value of 150 MPa. It is observed from this figure that, when θ is 10°, the normalized shear stress is 1.0 while that for longitudinal and transverse stresses are only 0.6 and 0.09. This finding implies that the specimen should fail first in shear, and partly explains why $\theta = 10^\circ$ has been chosen for the off-axis shear test method.

Converting the transformation equations for strains we have:

$$\begin{bmatrix} \varepsilon_{11} \\ \varepsilon_{22} \\ \frac{1}{2}\gamma_{12} \end{bmatrix} = \begin{bmatrix} \cos^2(\theta) & \sin^2(\theta) & 2\cos(\theta)\sin(\theta) \\ \sin^2(\theta) & \cos^2(\theta) & -2\cos(\theta)\sin(\theta) \\ -\cos(\theta)\sin(\theta) & \cos(\theta)\sin(\theta) & \cos^2(\theta)-\sin^2(\theta) \end{bmatrix} \times \begin{bmatrix} \varepsilon_{xx} \\ \varepsilon_{yy} \\ \frac{1}{2}\gamma_{xy} \end{bmatrix} \qquad (3.10)$$

Substituting for $\theta = 10^\circ$ in Eq. (3.10) gives for the principal shear strain the relationship:

$$\gamma_{12} = -0.340(\varepsilon_{xx} - \varepsilon_{yy}) + 0.940\gamma_{xy} \qquad (3.11)$$
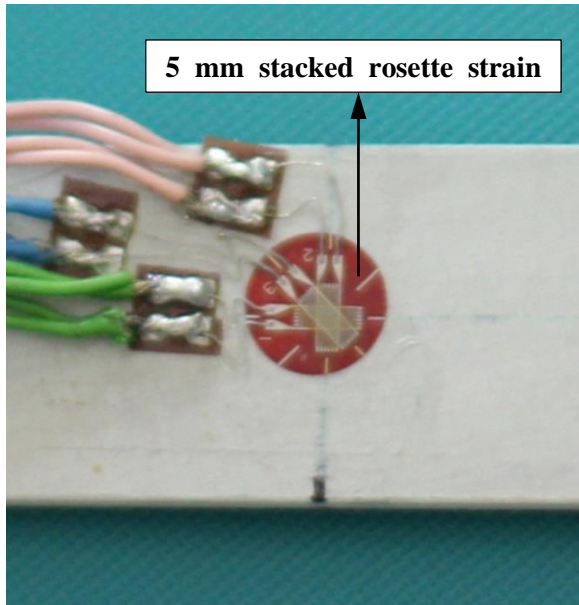
Figure 3.13 Stacked rosette strain gauge on test specimen

Stacked rectangular "rosette" strain gauge can be used to measure the three strain components of ε_{xx}, ε_{yy} and γ_{xy}. Figure 3.13 shows the rosette in testing with three gauges oriented at $0^\circ, 45^\circ$ and 90° with the tensile loading direction. The schematic set-up is illustrated in Figure 3.11 where strain gauge SG#1 (for ε_0) aligned 0° with the loading direction, gauge SG#2 placed perpendicular for ε_{90} and SG#3 located at a 45° direction to measure ε_{45}.

The strain transformations between $(\varepsilon_0, \varepsilon_{90}, \varepsilon_{45})$ and $(\varepsilon_{xx}, \varepsilon_{yy}, \frac{1}{2}\gamma_{xy})$ are:

$$
\begin{bmatrix} \varepsilon_0 \\ \varepsilon_{90} \\ \varepsilon_{45} \end{bmatrix} = \begin{bmatrix} \cos^2(\theta_1) & \sin^2(\theta_1) & 2\cos(\theta_1)\sin(\theta_1) \\ \cos^2(\theta_2) & \sin^2(\theta_2) & 2\cos(\theta_2)\sin(\theta_2) \\ \cos^2(\theta_3) & \sin^2(\theta_3) & 2\cos(\theta_3)\sin(\theta_3) \end{bmatrix} \times \begin{bmatrix} \varepsilon_{xx} \\ \varepsilon_{yy} \\ \frac{1}{2}\gamma_{xy} \end{bmatrix} \quad (3.12)
$$

Where θ_1, θ_2 and θ_3 are the angles between the loading axis x with the strain gauges measuring ε_0, ε_{90} and ε_{45}. Substituting in Eq. (3.12) for $\theta_1 = 0^\circ$, $\theta_2 = 90^\circ$ and $\theta_3 = 45^\circ$, the three rows give expressions:

$$\varepsilon_0 = \varepsilon_{xx}$$

$$\varepsilon_{90} = \varepsilon_{yy}$$

$$\varepsilon_{45} = \frac{1}{2}\varepsilon_{xx} + \frac{1}{2}\varepsilon_{yy} + \frac{1}{2}\gamma_{xy}$$

Combining the above expressions we have:

$$\gamma_{xy} = 2\varepsilon_{45} - \varepsilon_{xx} - \varepsilon_{yy} = 2\varepsilon_{45} - \varepsilon_{90} - \varepsilon_0 \quad (3.13)$$

Substituing Eq. (3.13) into Eq. (3.11) the required shear strain in terms of the measured strains is given by:

$$\gamma_{12} = 1.88\varepsilon_{45} - 1.28\varepsilon_0 - 0.60\varepsilon_{90} \quad (3.14)$$

We can now write down the expression for the in-plane shear modulus as:

$$G_{12} = \frac{\sigma_{12}}{\gamma_{12}} = \frac{\text{Eq. (3.9)}}{\text{Eq. (3.14)}} = \frac{0.17\sigma_{xx}}{1.88\varepsilon_{45} - 1.28\varepsilon_0 - 0.60\varepsilon_{90}} \quad (3.15)$$

The 10° off-axis method does not possess an ISO or ASTM standard. There is no standard information for the coupon dimensions; specimen preparation; test procedure or the strain ranges when establishing G_{LT}. One option is to follow the basic

requirements in Part 5 of the BSI (2012b) that provides the 'test conditions for the determination of tensile properties of unidirectional FRPs'. This standard requires the specimen to have dimensions of 25 mm (width) $\times$ 250 mm (length) and a thickness of 2 mm. Specimens in this study have a nominal size of 30 mm (width) $\times$ 300 mm (length) and the section thickness of 6 mm. A high aspect ratio (i.e. length/width =10) is employed to reduce, as much as possible, any end constraint effect.

Table 3.12 Approximation of maximum average shear strain found in LTB testing

(1)	Section name	I1	C1	C2	C3
(2)	Maximum load $P_{\text{LTB,max}}$ (kN)	9.2	12.7	7.32	3.72
(3)	Maximum shear force V_{max} (kN)	4.6	6.4	3.7	1.9
(4)	Shear area A_{v} (mm^2)	684	684	564	564
(5)	Maximum(average) shear stress $\tau_{\text{max}} = \dfrac{V_{\text{max}}}{A_{\text{v}}}$ (N/mm^2)	6.7	9.3	6.5	3.3
(6)	Maximum (average) shear strain (assuming G$_{\text{LT}}$=3 GPa) $\gamma_{\text{max}} = \dfrac{\tau_{\text{max}}}{G_{\text{LT}}}$ (%)	0.2	0.3	0.2	0.1
(7)	Maximum (average) shear strain (assuming G$_{\text{LT}}$=5 GPa) $\gamma_{\text{max}} = \dfrac{\tau_{\text{max}}}{G_{\text{LT}}}$ (%)	0.1	0.2	0.1	0.1

In term of strain range, Table 3.12 presents an approximation to the maximum shear strain experienced by the four sections in their LTB tests. The maximum LTB loads ($P_{\text{LTB,max}}$) presented in Chapter 4 will give the maximum shear forces from $V_{\text{max}} = P_{\text{LTB,max}}/2$. The maximum average shear stress can be approximated by $\tau_{\text{max}} = V_{\text{max}}/A_{\text{v}}$, where the shear area A_{v}, as stated in section 3.2, is assumed to be $(h - 2 \times t_{\text{f}}) \times t_{\text{w}}$. The maximum shear strain can be found from $\gamma_{\text{max}} = \tau_{\text{max}}/G_{\text{LT}}$. Mottram (2004b) has shown that G_{LT} for standard PFRP material is in range of 3-5 GPa.

Listed in rows (6) and (7) of Table 3.12 are the $\gamma_{\max}$s obtained when G_{LT} is taken to be the lower bound and upper bound respectively. It can be seen that the shear strain is going to be below 0.3% when $G_{LT} = 3$ GPa, and lowers still, at 0.2% when $G_{LT} = 5$ GPa. Using the $\gamma_{\max}$ values in Table 3.12 and considering guidance in BS EN 527-5 (BSI, 2012b), it was decided to take a strain range from 0.05% to 0.25% when determining G_{LT} for each of the four sections.

3.5.2. Test procedure and results

Five specimens were prepared from the web panel in sections I, C1, C2 and C3. The 20 coupons were given a reference code to indicate type of test, section and test number. For example, specimen labelled S-I-1 is the '1st'coupon for the 'Shear test' of 'I' section material. Specimens were machined so that the UD fibre reinforcement was oriented at 10 degree with the tensile loading direction. It can be shown using Eq.(3.9) that an increase of 1° (i.e. $\theta = 11^o$) has the potential to increase the shear stress by 10% whilst a decrease of 1° (i.e. $\theta = 9^o$) lowers this stress by 11 %. It can be expected that there will be a potential uncertainty in G_{LT} because the tolerance on θ is likely to be $\pm 0.5^o$. The 5 mm foil rosette strain gauge was placed at midpoint with the gauges oriented as shown in Figure 3.13. One 6 mm unidirectional foil strain gauge was placed on the opposite side to the rosette gauge to allow the influence of flexure to be monitored. This arrangement is shown in Figures 3.14 and 3.15. The difference will then be utilized to eliminate flexure effect in other strain gauges (Pindera and Herakovich, 1986).
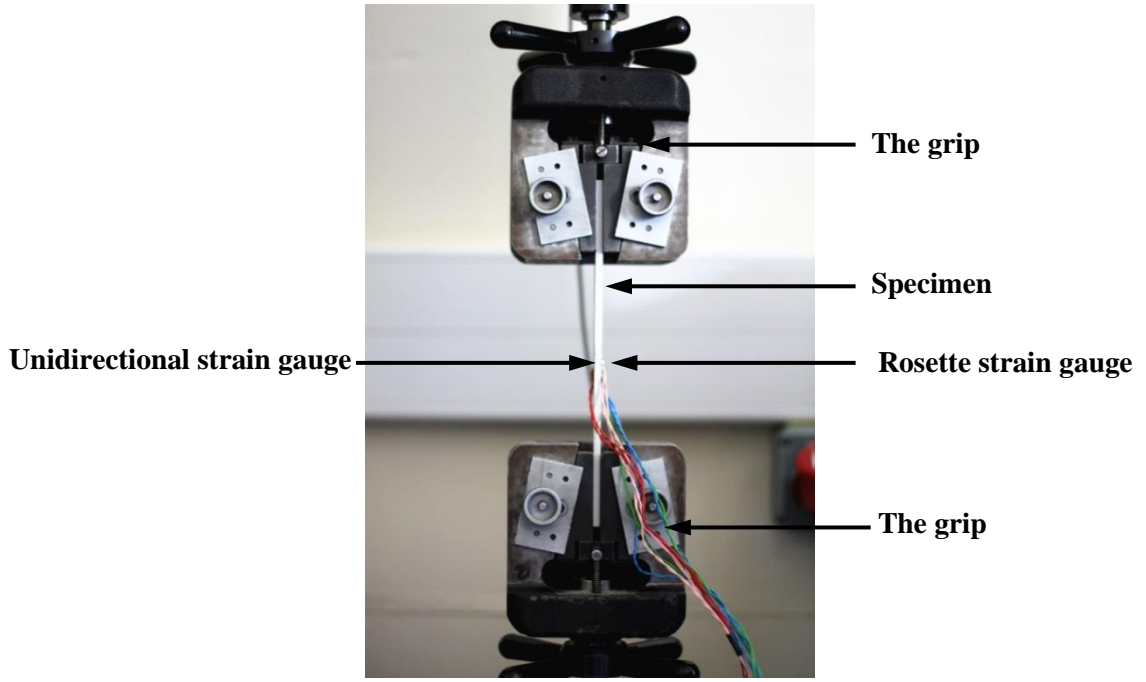
Figure 3.14 10° off-axis tensile test arrangement

Another correction that might need to be accounted for is the error owning to the transverse sensitivity of strain gauges. This is a measurement error that exists in a biaxial strain field. For the rosette gauge, the three correction equations (Measurements Group Inc, 1983) can be expressed as:

$$\varepsilon_0 = \frac{1-v_0 K_t}{1-K_t^2}\left(\varepsilon_{0,r} - K_t \varepsilon_{90,r}\right) \tag{3.16}$$

$$\varepsilon_{90} = \frac{1-v_0 K_t}{1-K_t^2}\left(\varepsilon_{90,r} - K_t \varepsilon_{0,r}\right) \tag{3.17}$$

$$\varepsilon_{45} = \frac{1-v_0 K_t}{1-K_t^2}\left(\varepsilon_{45,r} - K_t \left(\varepsilon_{0,r} + \varepsilon_{90,r} - \varepsilon_{45,r}\right)\right) \tag{3.18}$$

In Eqs. (3.16)-(3.18) strains $\varepsilon_{0,r}$, $\varepsilon_{90,r}$ and $\varepsilon_{45,r}$ are the recorded strains and other three strain gauges ε_0, ε_{90} and ε_{45} are the corrected strains. K_t is the transverse sensitivity factor of the strain gauges which is -0.1% for the rosette gauges. v_0 is the Poisson's ratio of the material on which the gauge factor was measured by the gauge manufacturer. It

57

normally takes the value of 0.285. Given that $K_t = -0.1\%$, it can be seen that the effect of transverse sensitivity on the apparent strain is very small with a correction of lesser than 0.5%. This correction will not be applied. The corrected strains were transformed to the material principal coordinate system with σ_{12} and γ_{12} to be calculated accordingly. Details of the transformation have been presented in sub-section 3.5.1.

Plane of shear failure

(a)   (b)
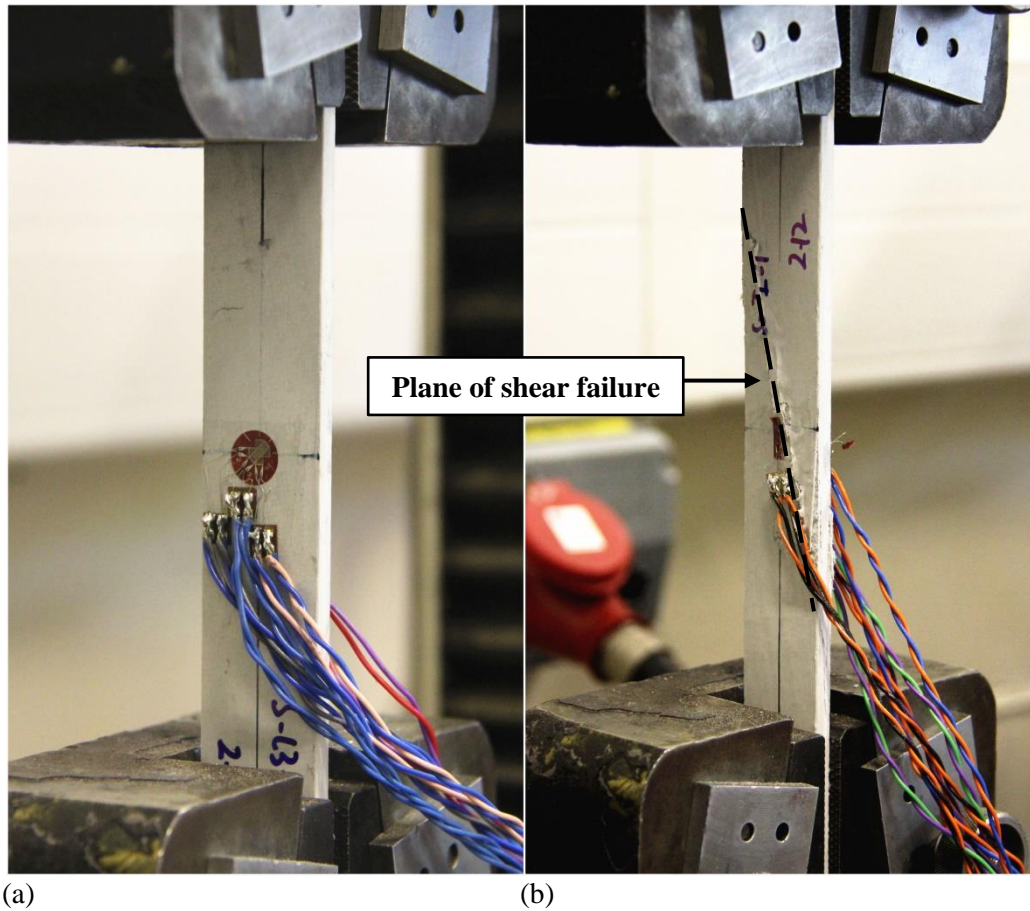
Figure 3.15 10° off-axis test: (a) during loading; (b) after failure.

Figure 3.15 presents images for, (a) before failure, and, (b) afterwards. It can be seen that, as expected, a shear failure occurred along the 10 degree plane. This demonstrates that the shear stress was the first principal stress to reach its strength (τ_u) value. When the shear failure happened, the longitudinal and transverse stresses were much lower than their strengths.
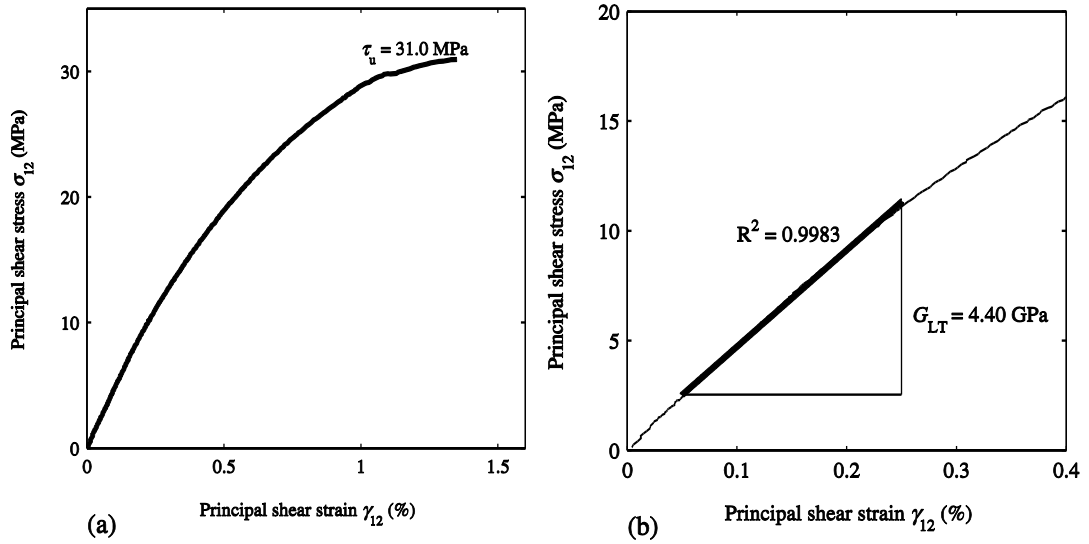
Figure 3.16 σ_{12} vs. γ_{12} for S-I-1: (a) full response; (b) γ_{12} from 0% to 0.4%

Figure 3.16(a) shows the full response of σ_{12} against γ_{12} for specimen S-I-1. The shear strength of this specimen is found at 31 MPa, which is 24% higher than the nominal value given in the Fiberline Design Manual (Anon., 2014a). This typical curve has relatively linear behaviour to about 0.2%, after which a nonlinear response grows until there is shear failure at 1.35%. Figure 3.16(b) is the plot for the same specimen with γ_{12} from 0 to 0.4% and a least-squares (best fit) straight line using the strain range of 0.05 to 0.25%. The R^2 on this line is 0.9983 and its gradient predicts G_{LT} to be 4.4 GPa. Plots for all 20 shear modulus tests are presented in Appendix A.3.

Presented in columns (1-3) of Table 3.13 are the name, width and thickness of the shear test specimens. Columns (4-7) report for the batches of five the Mean G_{LT}, the Standard Deviation (SD) and the Coefficient of Variation (CV). Similarly, columns (8-11) give τ_u, Mean τ_u, SDs and its CVs. G_{LT} seen to be in the range of 4.15 GPa to 4.8 GPa, with the CVs between 3% to 9%. The range of CVs is reasonable giving that the

measurement of G_{LT} is very sensitive to the precision of the cutting and specimen positioning to maintain during testing the 10° off-axis angle. The differences between the shear moduli of the four sections can be related to their E_L value (Mottram, 2004b). From Figure 3.10 the averages of E_L for I, C1, C2 and C3 are 27.1 GPa, 33.1 GPa, 31.6 GPa and 29.5 GPa. Sections C2 and C3 have higher E_L and also have the highest G_{LT}. For shear strength, the CVs are in range of 2% to 11% and τ_u is from 27.2 MPa to 32.5 MPa. This shear strength measurement shows that the nominal shear strength value of 25 MPa provided in Fiberline Design Manual (2014a) is appropriate.

Table 3.13 Measurements and tests results for 10° off-axis specimens of I, C1, C2 and C3

Specimen name	Width (mm)	Thickness (mm)	shear modulus G_{LT} (GPa)				Shear strength τ_u (MPa)			
			G_{LT} (GPa)	Mean (GPa)	SD (GPa)	CV (%)	τ_u (MPa)	Mean (MPa)	SD (MPa)	CV (%)
(1)	(2)	(3)	(4)	(5)	(6)	(7)	(8)	(9)	(10)	(11)
S-I-1	30.59	6.06	4.40				31.0			
S-I-2	29.81	6.10	3.82				37.6			
S-I-3	30.26	6.05	4.42	4.15	0.34	8	29.1	32.5	3.7	11
S-I-4	30.55	6.04	4.45				28.6			
S-I-5	30.15	6.10	3.66				36.0			
S-C1-1	30.14	5.86	4.74				28.2			
S-C1-2	30.28	5.85	4.52				27.1			
S-C1-3	30.15	5.90	4.69	4.74	0.14	3	28.5	27.2	1.2	5
S-C1-4	30.10	5.83	4.95				27.1			
S-C1-5	30.03	5.92	4.83				25.0			
S-C2-1	30.31	5.96	4.57				32.0			
S-C2-2	30.20	5.98	5.10				30.5			
S-C2-3	30.05	5.93	4.83	4.76	0.20	4	29.9	30.4	1.0	3
S-C2-4	30.28	5.97	4.55				29.1			
S-C2-5	30.16	5.97	4.73				30.6			
S-C3-1	30.05	5.98	4.39				31.4			
S-C3-2	30.19	5.94	4.16				29.9			
S-C3-3	30.07	5.94	3.66	4.18	0.36	9	30.3	30.4	0.6	2
S-C3-4	30.22	6.01	4.73				30.4			
S-C3-5	30.21	6.03	3.96				29.8			

3.6. Discussion

The elastic constants of E_L, E_T, ν_{LT} and G_{LT} have been characterized. These mechanical properties are necessary as input data for the Finite Element Analysis (FEA) or the closed-form equations (Eq. 2.1) that predict the LTB resistance of PFRP beams. Three tensile coupon test series have been conducted in the longitudinal direction, transverse direction and 10° off-axis to determine: (1) E_L and ν_{LT} (Tables 3.7-3.10); (2) E_T (Table 3.11); and (3) G_{LT} (Table 3.13).

Table 3.14 Elastic constants of all sections

Section	Mean longitudinal modulus E_L(GPa)	Mean in-plane shear modulus G_{LT}(GPa)	Mean transverse modulus E_T(GPa)	Mean major Poisson's ratio ν_{LT}	Minor Poisson's ratio ν_{TL}	Full-section elastic modulus E(GPa)	Full-section shear modulus G(GPa)
(1)	(2)	(3)	(4)	(5)	(6)	(7)	(8)
I	30.6	4.2	10.8	0.229	0.081	33.0	4.8
C1	31.7	4.8	11.7	0.229	0.085	32.6	4.5
C2	32.9	4.8	11.7	0.225	0.080	32.5	3.8
C3	29.2	4.2	10.5	0.237	0.085	31.9	3.5

The closed-form equation for LTB resistance requires only the two elastic constants of E and G. As illustrated in Figure 3.10 the coupon testing has given us a range of E_Ls for flange and web. Means for E_L and G_{LT} for a PFRP section will be assigned to be the required E and G in the close-form equations. For the I shape, the mean will be obtained using results from three groups (Group 1 for I1 and I3; Group 2 for I2 and I4 and Group 3 for I5 and I6). The mean for a channel will be determined using test results from flange and web. The same method is used to achieve means for the major Poisson's ratio. Listed in Table 3.14 are the mean elastic constants with column (1) giving the section type. Columns (2-5) are used to report the four average elastic

constants. Also given in columns (7) and (8) are the full-section moduli E and G determined from the graphical technique detailed in section 3.2.

In terms of the shear modulus given in columns (3) and (8) the values obtained by two methods are inconsistent. This is a foreseeable finding since the reliability of the magnitude of the intercept is a key weakness in the graphical method. The major Poisson's ratios ν_{LT} is from 0.225 to 0.237, being fairly close to 0.23 in Fiberline Design Manual (2014a). The minor Poisson's ratio ν_{TL} determined by $\nu_{TL} = \nu_{LT} E_T / E_L$ is from 0.080 to 0.085, which is close to 0.09 in Fiberline Design manual also. These values are given in column (6).

Table 3.15 collates measurements of those moduli from previous studies. Listed in columns (1-3) is the name of the authors or pultruder and section type. Columns (4), (6) and (8) list the range of values for $E (\text{or } E_L)$, E_T and $E (\text{or } G_{LT})$ taken from the sixteen sources introduced in column (1). Columns (5), (7) and (9) state the method that was used to obtain these data given in columns (4), (6) and (8). The stiffness property information presented in Table 3.15 clearly shows there to be a wide range of elastic and shear moduli. For pultruded standard structural section the modulus of elasticity is from 16.8 to 35.6 GPa. The measured data are mainly between 20 and 30 GPa. For the shear modulus the range is from 1.2 to 5.7 GPa with most measured values between 3 and 5 GPa.

Table 3.15 Elastic modulus $E, E_{\mathrm{L}}, E_{\mathrm{T}}$ and shear modulus G, G_{LT} from design manuals and previous reseaches

Author(s) or pultruder's Design Manual	Pultruder	Section shape	E or E_{L} (GPa)	E or E_{L} test method	E_{T} (GPa)	E_{T} test method	G or G_{LT} (GPa)	G or G_{LT} test method
(1)	(2)	(3)	(4)	(5)	(6)	(7)	(8)	(9)
Fiberline (Anon., 2014a)	Fiberline A/S, Denmark	All ranges	23-28	-	8.5	-	3.0	-
Creative Pultrusions Anon. (2004)	Creative Pultrusions Inc., USA.	All ranges	17.2-20.7	Tensile coupon test	5.5-6.9	Tensile coupon test	2.9	Three points bending
Strongwell (Anon., 2014b)	Strongwell, USA.	All ranges	17.2-17.9	Tensile coupon test	5.5	Tensile coupon test	2.9	Three points bending
Bank (1990)	Creative Pultrusions Inc., USA.	I	-	-	-	-	2.4-2.8	Iosipescu
Mottram (1992a)	Morrison Molded Fiber Glass Company (MMFG)	I	22.3-22.8	Three points bending	-	-	1.2-1.3	Three points bending
Brooks and Turvey (1995)	Morrison Molded Fiber Glass Company (MMFG)	I	19.8-22.4	Three points bending	-	-	1.4	Three points bending
Sonti and Barbero (1996)	Creative Pultrusions Inc., USA	I	20.2 (flange) 18.1 (flange)	Tensile coupon test	11.4 (flange) 10.9 (web)	Tensile coupon test	3.3-3.8 (flange) 3.9-4.5 (web)	Iosipescu and Torsion
Zureick and Scott (1997)	Strongwell, USA.	I	16.8-21.9	Tensile coupon test	-	-	4.1-4.8	Iosipescu
		Box	26.8-30.7		-	-	3.9-5.7	

Stephen (1998)	Strongwell, USA.	Leg angle	19.7-23.7	Compression coupon test	-	-	3.5-4.5	Modified (Iosipescu) V-notched beam
Turvey (1998)	Strongwell, USA.	GRP sheet	17.3-17.9	Tensile coupon test	-	-	3.0-3.6	Torsion
Roberts and Al-Ubaidi (2002)	Fiberforce Composites (Now Exel Composites, UK)	I	18.9-32.3	Three point bending	-	-	4.4-4.9	Torsion
Lane (2002)	Creative Pultrusions Inc, USA.	I	26 (flange) 19 (web)	Micromechanical modelling	11	Micromechanical modelling	3.2 (web) 3.7 (flange)	Micromechanical modelling
Afifi (2007)	Creative Pultrusions Inc, USA.	I	22.8(web)	Tensile coupon test	8.9 (web)	Tensile coupon test	3.4 (web)	Iosipescu
Barros da S. Santos Neto and Lebre La Rovere (2007)	CSE Composites, Brazil	I	32.9	Three points bending	-	-	2.7	Three points bending
			35.6	Tensile coupon test (D3039)	-	-	-	-
(Correia *et al.* (2011))	Topglass firm, Italy	I	32.8	Tensile coupon test	7.4	Tensile coupon test	3.6	Three points bending
Author (2013)	Fiberline A/S, Denmark	I and Channels	31.9-33.0	Three points bending	-	-	3.5-4.8	Three points bending
			29.2-32.9	Tensile coupon test	10.5-11.7	Tensile coupon test	4.2-4.8	10° off-axis tensile test

From this summary, it is appropriate to treat PFRP material as having moduli with an upper and lower bound, especially for the in-plane shear modulus. The lower bound can be of 3 GPa as given in Fiberline Design Manual and the upper bounds are those determined by the 10° off-axis testing which is 4.2 GPa for I and C3 and 4.8 GPa for C1 and C2. The moduli and Poisson ratio in the numerical work to predict LTB resistances are those given in Table 3.14 and Figure 3.10. It is to be noted that $\sigma_{1,u}$, $\sigma_{2,u}$ and τ_u were also measured, and their usefulness is not essential to the work reported in this Ph.D. thesis. The data is, of course, beneficial to those who need to have knowledge of material strengths of these sections.

3.7. Local buckling stress

This section presents the axial compression test on PFRP stub columns to determine the local buckling stress σ_{Loc} that is required for calculating the non-dimensional slenderness $\lambda_{LT} = \sqrt{W_y \sigma_{Loc} / M_{cr}}$. It can be argued that the local buckling resistance should be obtained from a flexural test because LTB failure is for beam flexure. However, it is going to be difficult to establish σ_{Loc} by subjecting a length of a PFRP section to bending. A more straightforward test approach is to apply concentric compression to a short column of the section. The main difference between the two approaches is that in the flexure beam there is a stress gradient effect in the height direction and along the length (if not pure moment) and only the compressive flange can buckle, whilst in the stub column both flanges can buckle simultaneously (Bank, 2006). The flanges may buckle before or after the web depending on the dimensions of the

thin-walled I- or C-section. In either case, the torsional restraint on the flanges of column is less than that in a beam. The local buckling stress from column testing can be expected to be lower and this suggests it will be acceptable to use when constructing a conservative design curve for beams in bending.

This section presents predictions for σ_{Loc} obtained using theoretical formulae, FEA and physical testing. The dimensions for the half-wave lengths for local flange buckling were estimated from FEA. In testing the channels were placed back-to-back to form a doubly symmetrical I-shaped to minimize any load eccentricity. A specimen height was chosen to give four half-wave lengths. There was one test for each of I, C1 and C2 sections Dimensions were measured and with the load-deformation and stress-strain test results reported in what follows.

3.7.1. Analytical and numerical predictions

The elastic critical buckling stress for instability of a panel in a section is depended on the displacement boundary conditions along the longitudinal edges. The flange outstands in I and channel shapes (Figure 3.17) have one free edge, whilst the other is restrained at the web-flange junction. The web in these shapes is restrained along both sides. In wide-flange I and channel shapes where $h = b_{\text{f}}$, local flange buckling normally occurs prior to web buckling (Bank, 2006). This might not be the case if the shape is of the narrow-flange type $(h \geq 2b_{\text{f}})$.

A closed-form expression for the prediction of the local flange stress for I shape can be given as (Kollár, 2003, Bank, 2006):

$$\sigma_{\text{Loc,flange}} = \frac{\pi^2}{t_f \left(b_f / 2\right)^2} \left[D_L \left(\frac{b_f / 2}{a}\right)^2 + \frac{12}{\pi^2} D_s \right] \tag{3.19}$$

(a) I-section   (b) Channel section
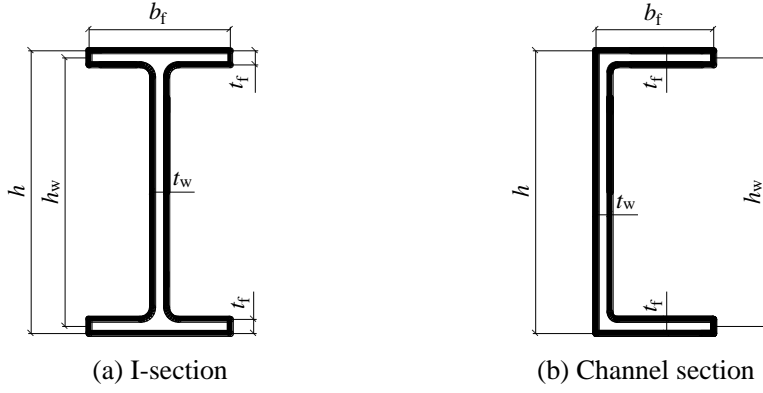
Figure 3.17 Illustration for I and channel shapes

By replacing $b_f / 2$ in Eq. (3.19) with b_f, the local flange stress for the channel shape is obtained. In Eq. (3.19) b_f is the breadth of the section and a is the buckling half-wave length.

For the web, the local buckling stress can be approximated by:

$$\sigma_{\text{Loc,web}} = \frac{2\pi^2}{t_w b_w{}^2} \left(\sqrt{D_L D_T} + D_{LT} + 2D_s \right) \tag{3.20}$$

where D_L, D_T, D_{LT} and D_s are the flexural rigidities for the orthotropic plate. From Bank (2006) they are:

$$D_L = \frac{E_L t_p^3}{12\left(1 - v_L v_T\right)} \tag{3.21}$$

$$D_T = \frac{E_T t_p^3}{12\left(1 - v_L v_T\right)} \tag{3.22}$$

$$D_{LT} = \frac{v_T E_L t_p^3}{12\left(1 - v_L v_T\right)} \tag{3.23}$$

67

$$D_s = \frac{G_{LT} t_p^3}{12} \tag{3.24}$$

In Eqs. (3.21)-(3.24) t_p is the thickness of the panel (either t_f or t_w).

If $\sigma_{Loc,flange} / (E_L)_f < \sigma_{Loc,web} / (E_L)_w$, the flange buckles first.

Research by Kollár (2003) has lead to closed-form expressions for local buckling stress that account for the torsional stiffness along the panel junctions. The buckling tress for I-flange is approximated by (Kollár, 2003, Bank, 2006):

$$\sigma_{Loc,a} = \frac{1}{(b_f / 2)^2 t_f} \left(7 \sqrt{\frac{D_L D_T}{1 + 4.12 \zeta_{I\text{-flange}}}} + 12 D_s \right) \tag{3.25}$$

where
$$\zeta_{I\text{-flange}} = \frac{(D_T)_f}{k_{I\text{-flange}} (b_f / 2)} \tag{3.26}$$

and
$$k_{I\text{-flange}} = \frac{(D_T)_w}{d_w} \left[1 - \frac{\sigma_{flange} (E_L)_w}{\sigma_{web} (E_L)_f} \right] \tag{3.27}$$

In Eqs.(3.26) and (3.27) $k_{I\text{-flange}}$ is a spring constant for the torsional restraint along the flange-web junction and $h_w (= h - t_f)$ is the depth of the web panel.

For a channel, $b_f / 2$ is replaced by b_f in Eqs. (3.25) and (3.26) and $k_{I\text{-flange}}$ is double that in Eq. (3.27) as the web is retrained by only one flange outstands and not two as in the I-section (Bank, 2006).

If $\sigma_{Loc,flange} / (E_L)_f > \sigma_{Loc,web} / (E_L)_w$, the web buckles prior to the flange. The expression for buckling stress is (Kollár, 2003, Bank, 2006):

$$\sigma_{Loc,a} = \frac{\pi^2}{h_w^2 t_w} \left[2 \sqrt{D_L D_T (1 + 4.14 \xi_{I\text{-web}})} + (D_{LT} + 2 D_s)(2 + 0.62 \xi_{I\text{-web}}^2) \right] \tag{3.28}$$

where
$$\xi_{\text{I-web}} = \frac{1}{1+10\zeta_{\text{I-web}}} = \frac{1}{1+10\left[\left(D_{\text{T}}\right)_{\text{w}} / k_{\text{I-web}}d_{\text{w}}\right]} \tag{3.29}$$

The torsional spring restraint for this case $k_{\text{I-web}}$ is given as:

$$k_{\text{I-web}} = \frac{4\left(D_{\text{T}}\right)_{\text{f}}}{b_{\text{f}}}\left[1 - \frac{\sigma_{\text{Loc,web}}\left(E_{\text{L}}\right)_{\text{f}}}{\sigma_{\text{Loc,flange}}\left(E_{\text{L}}\right)_{\text{w}}}\right] \tag{3.30}$$

Because Eq. (3.19) requires the half-wave length a, FEA was carried out by ABAQUS$^{®}$ to find an approximate value for each section. One reason why the computed value is approximated is that imperfections were ignored and the solution was an eigenvalue analysis. The local buckling load $P_{\text{Loc,FEA}}$ is also predicted. The columns analysed have heights from 600 mm to 800 mm.
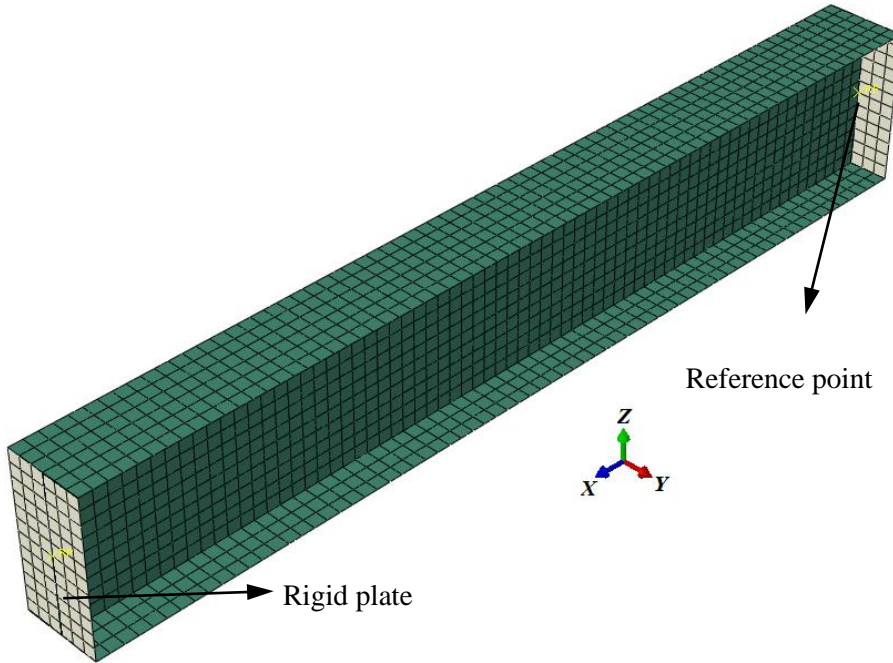
Figure 3.18 FE Cartesian coordinate and clamp-ended boundary condition

In the FEA, it is suitable to model the flange and web panels of the PFRP section as a single layer of transverse isotropic material using 8-node thick shell elements S8R (Nguyen *et al.*, 2013). The input of the material properties requires three moduli of elasticity E_L, E_T, G_{LT} and the major Poisson's ratio ν_{LT}. They are taken from Figure 3.10 for E_L, E_T, Table 3.12 for G_{LT} and Tables 3.7 to 3.10 for ν_{LT}.

To simulate a clamp-ended condition two rigid plates were fixed to both ends of the column as seen in Figure 3.18. The movement of each plate is controlled by a reference point located on that plate. By using Multi-Point Constraints (MPCs) to tie the reference node (acting as a 'master' point) and the edges of the section (acting as 'slave' points), the movement of all 'slave' points on the edges were numerically controlled by the 'master'. By imposing the six displacements degree of freedom at one reference node to be $U_y = U_z = U_{Rx} = U_{Ry} = U_{Rz} = 0$ and $U_x = U_y = U_z = U_{Rx} = U_{Ry} = U_{Rz} = 0$ at the other node, the required BCs were specified.

The compression load was applied to the reference node having $U_x \neq 0$. Linear (bifurcation) analysis was carried to obtain the eigenvalue (critical load factor) and the buckling mode shape for local buckling failure. A more detail of the modelling methodology will be presented in Chapter 5.

For the I-section ($120 \times 60 \times 6$ mm), Figure 3.19 shows the local buckling mode shapes for stub columns having lengths of 600 mm, 700 mm and 800 mm. It is observed that at the height of $H = 700$ mm there are four half-wave lengths. It has been recommended by Mottram (2004a) that to eliminate the effect of end boundary conditions on the local buckling stress the height in testing should not be shorter than four half-wave lengths.
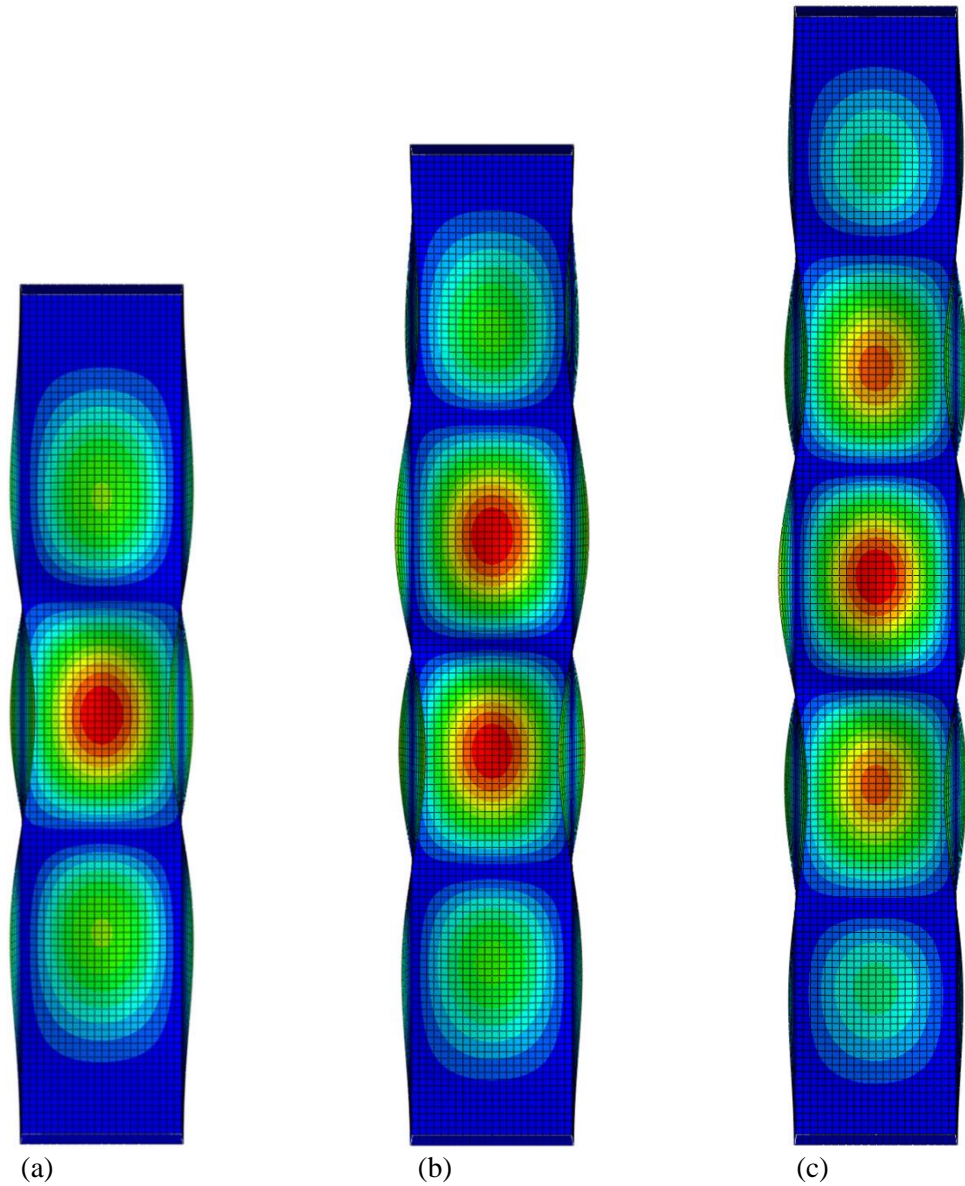
Figure 3.19 Local buckling shape of I column, heights of: (a) $H = 600$ mm; (b) $H = 700$ mm; (c) $H = 800$ mm (not to scale).

The height of the I-column was chosen to be 700 mm. FE Simulation were carried out with the C1- and C2-sections to establish that H for four half-waves is $H = 750$ mm for C1 and $H = 700$ mm for C2. The local buckling load from the eigenvalue analysis $P_{\text{Loc,FEA}}$ is 251 kN, 154 kN and 172 kN for the I-, C1- and C2-sections, respectively. The approximated half-wave length a is 160 mm for the I- and C2-sections and 180 for C1.

Table 3.16 Properties to predict $\sigma_{\text{Loc,a}}$

I shape		C1 shape		C2 shape	
Geometrical properties		Geometrical properties		Geometrical properties	
t_w	6 mm	t_w	6 mm	t_w	6 mm
t_f	6 mm	t_f	6 mm	t_f	6 mm
h_w	114 mm	h_w	114 mm	h_w	94 mm
b_f	60 mm	b_f	50 mm	b_f	50 mm
Flange elastic constants		Flange elastic constants		Flange elastic constants	
E_L	29.7 kN/mm^2	E_L	29.7 kN/mm^2	E_L	34.0 kN/mm^2
E_T	10.8 kN/mm^2	E_T	11.7 kN/mm^2	E_T	11.7 kN/mm^2
v_L	0.250	v_L	0.210	v_L	0.230
v_T	0.09	v_T	0.09	v_T	0.009
Web elastic constants		Web elastic constants		Web elastic constants	
E_L	26.6 kN/mm^2	E_L	33.1 kN/mm^2	E_L	31.6 kN/mm^2
E_T	10.8 kN/mm^2	E_T	11.7 kN/mm^2	E_T	11.7 kN/mm^2
v_L	0.23	v_L	0.24	v_L	0.23
v_T	0.09	v_T	0.009	v_T	0.009

Table 3.16 summarizes the required input data in for Eqs. (3.19)-(3.30) for sections I, C1, C2. The parameters include the nominal geometrical properties and the flange and web elastic constants. The measured material properties were taken from Figure 3.10 and Table 3.13.

Table 3.17 presents the calculations for $\sigma_{\text{Loc,a}}$ to show that for the I-section the web buckles prior to the flanges. From the Kollár (2003) equations the failure stress is 151 MPa. The buckling first happens in the flanges of the C1- and C2-sections with a uniform stress of 100 MPa and 129 MPa.

Using $P_{\text{Loc,FEA}}$s obtained from FEA, the local buckling stress for I column can be calculated as:

$$\sigma_{\text{Loc,FEA}} = \frac{P_{\text{Loc,FEA}} \times E_{\text{L,web}}}{E_{\text{L,flanges}} \times A_{\text{flanges}} + E_{\text{L,web}} \times A_{\text{web}}} = 163 \text{ MPa}$$

Those for C1 and C2 column are:

$$\sigma_{\text{Loc,FEA}} = \frac{P_{\text{Loc,FEA}} \times E_{\text{L,flange}}}{E_{\text{L,flanges}} \times A_{\text{flanges}} + E_{\text{L,web}} \times A_{\text{web}}} = 118 \text{ MPa} \text{ and } 157 \text{ MPa, respectively.}$$

It is observed that the FEA gives relatively similar local buckling stress with those by analytical prediction with difference at 8%, 18% and 22% for I, C1 and C2 respectively.

Table 3.17 Approximation of $\sigma_{\text{Loc,a}}$ for I, C1 and C2 shapes

I shape					
Flange properties		**Web properties**		**Buckling calculation**	
Symbol	Value	Symbol	Value	Symbol	Value
D_{L}	545900 N.mm	D_{L}	482370 N.mm	$k_{\text{I-web}}$	3335 N
D_{T}	216890 N.mm	D_{T}	216890 N.mm	$\xi_{\text{I-web}}$	0.1492
D_{LT}	49131 N.mm	D_{LT}	43413 N.mm	$\sigma_{\text{Loc,a}}$	151 N/mm^2
D_{s}	75600 N.mm	D_{s}	75600 N.mm		
$\sigma_{\text{flange}} = 203.1 \text{ N/mm2}$		$\sigma_{\text{web}} = 137.8 \text{ N/mm}^2$			
$\dfrac{\sigma_{\text{flange}}}{(E_{\text{L}})_{\text{f}}} = 6.84 \times 10^{-3} > \dfrac{\sigma_{\text{web}}}{(E_{\text{L}})_{\text{w}}} = 5.26 \times 10^{-3} \rightarrow$ web buckles first					
C1 shape					
Flange properties		**Web properties**		**Buckling calculation**	
Symbol	Value	Symbol	Value	Symbol	Value
D_{L}	544900 N.mm	D_{L}	608950 N.mm	$k_{\text{I-flange}}$	705 N
D_{T}	214700 N.mm	D_{T}	315250 N.mm	$\xi_{\text{I-flange}}$	6.082
D_{LT}	49040 N.mm	D_{LT}	54800 N.mm	$\sigma_{\text{Loc,a}}$	100 N/mm^2
D_{s}	86400 N.mm	D_{s}	86400 N.mm		
$\sigma_{\text{flange}} = 104.1 \text{ N/mm2}$		$\sigma_{\text{web}} = 142.7 \text{ N/mm}^2$			
$\dfrac{\sigma_{\text{flange}}}{(E_{\text{L}})_{\text{f}}} = 3.51 \times 10^{-3} > \dfrac{\sigma_{\text{web}}}{(E_{\text{L}})_{\text{w}}} = 4.31 \times 10^{-3} \rightarrow$ flange buckles first					
C2 shape					
Flange properties		**Web properties**		**Buckling calculation**	
Symbol	Value	Symbol	Value	Symbol	Value
D_{L}	624900 N.mm	D_{L}	580800 N.mm	$k_{\text{I-flange}}$	2480 N
D_{T}	215000 N.mm	D_{T}	215000 N.mm	$\xi_{\text{I-flange}}$	1.734
D_{LT}	56200 N.mm	D_{LT}	52300 N.mm	$\sigma_{\text{Loc,a}}$	129 N/mm^2
D_{s}	86400 N.mm	D_{s}	86400 N.mm		
$\sigma_{\text{flange}} = 109.3 \text{ N/mm}^2$		$\sigma_{\text{web}} = 221.8 \text{ N/mm}^2$			
$\dfrac{\sigma_{\text{flange}}}{(E_{\text{L}})_{\text{f}}} = 3.21 \times 10^{-3} > \dfrac{\sigma_{\text{web}}}{(E_{\text{L}})_{\text{w}}} = 7.02 \times 10^{-3} \rightarrow$ flange buckles first					

3.7.2. Test specimens

For the three test specimens Figure 3.20 has a line drawing and a photo showing the actual cross-sections. The nominal section dimensions are also given on the drawings. The back-to-back channels were attached by M12 bolts at three positions along the columns' height. Two bolts were located 50 mm from the ends whilst the third one was bolted at mid-height of column. After connecting the two lengths together the end surfaces were squared to ensure that the compression load can be uniformly applied over the cross-section.
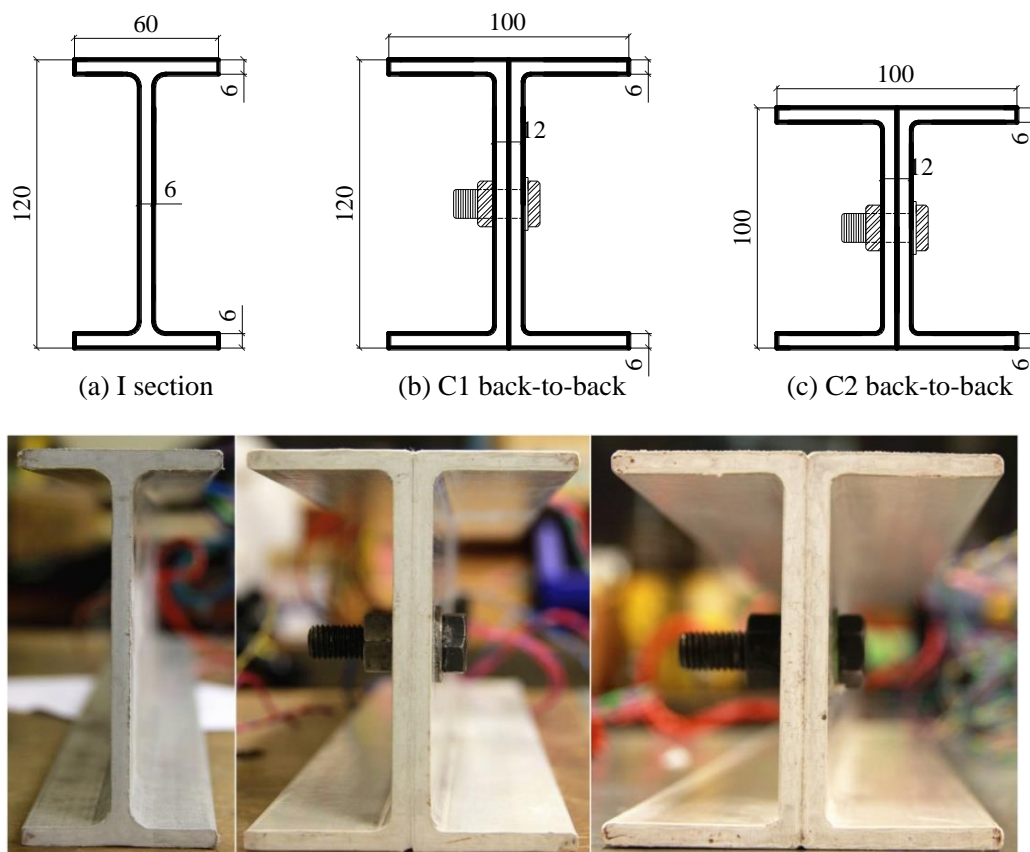
Figure 3.20 Drawing (top) and photo (bottom) for specimen: (a) I; (b) C1; (c) C2.

Table 3.18 Mean measured dimensions for I, C1 and C2

(1)	Specimen	I	C1	C2
(2)	Height (H) : mm	700	750	700
(3)	Depth (h) : mm	120.1	120.1	100.1
(4)	Breadth (b) : mm	60.05	100.9	100.8
(5)	Web thickness (t_w) : mm	6.02	12.80	12.85
(6)	Flange thickness (t_f) : mm	5.90	5.98	6.03
(7)	Cross-section area (A) : mm^2	1410	2630	2360

The section dimensions were measured with a digital calliper with repeatability to 0.01 mm. The thicknesses of the top and bottom flange (t_f) are assumed to be the same, and were determined on taking the mean average of the four outstand measurements. The web thickness (t_w) was determined as the mean thickness measurement at three heights (but not including the end of the web when the fillet radii increase thickness). Table 3.18 summarizes the geometric properties. Rows (1-2) are used to give beam identifier and column height H . Rows (3-6) list, in millimetres, the section's depth (h), breadth (b), web thickness (t_w) and flange thickness (t_f). The maximum difference between the measured values and the nominal values for h, b, t_w, and t_f is 0.9%, 0.9%, 7.1% and 1.7%.

3.7.3. Test arrangements and results

General test arrangement is depicted in Figures 3.21(a) and (b). The concentric compression force was applied by a AMSLER testing machine with a full loading capacity of 40 Tonne. The machine only operates in load control. Load was recorded by a 50 Tonne load cell placed at the bottom of a specimen. Figure 3.21 shows that the

vertical deflection was measured by having a 50 mm strain gauge displacement transducer in contact with the bottom surface the moving cross-head of the AMSLER.
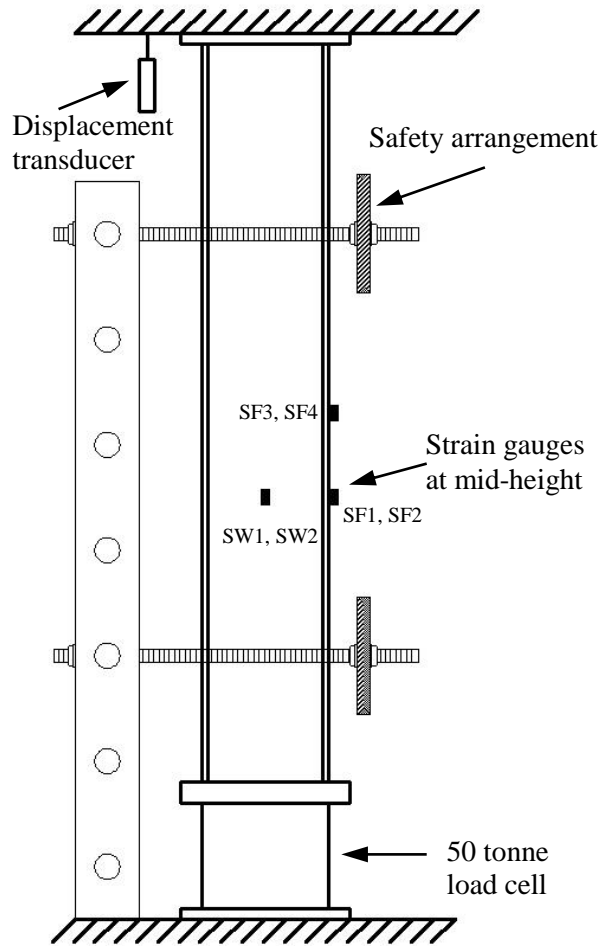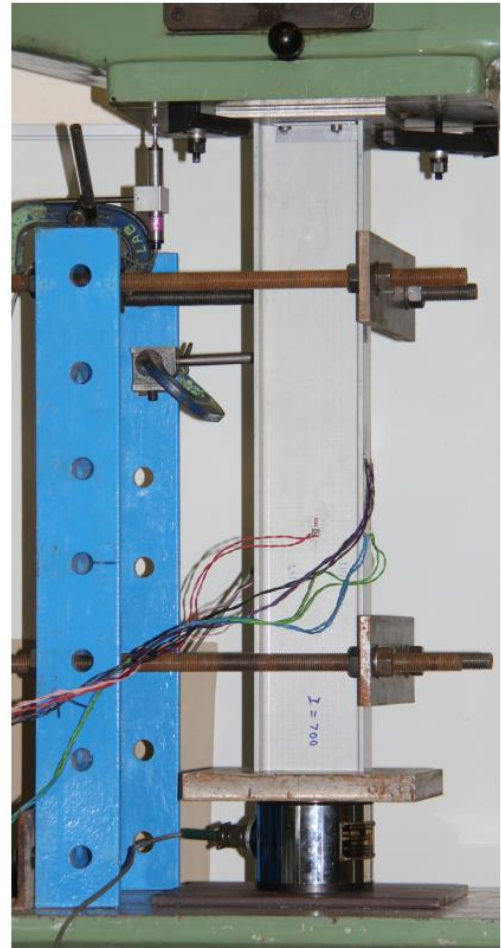
(a) Schematic set-up   (b) Experimental set-up

Figure 3.21 Colum test set-up with I-section: (a) schematics; (b) experiment

Lateral deflection in the minor axis direction was measured by having a transducer positioned at mid-depth on the web and at the mid-height of the column. Because it was placed behind the test column, it cannot be seen in Figure 3.21. Six 6 mm foil strain gauges were used to measure longitudinal strain. They were attached symmetrically about the section's minor axis (the web axis). Two strain gauges were affixed to the flanges at mid-height. Four others were placed at a distance of 80 mm (for I- and C2-

section) or 90 mm (for C1-section) from the mid-height on flanges and web. The flange strain gauges (SF1 to SF4) were placed 5 mm from the flange tip, whilst the web strain gauges (SW1 and SW2) were located at mid-depth. This arrangement of gauging was based on the FEA results with the intention of capturing the maximum strain from the amplitude of the half wave-length (a). In Figure 3.21(a) the three positions for the six strain gauges can be seen. To prevent lateral slippage at the column ends there was a steel meccano frame that, as seen in Figure 3.21, had four threaded bars to form a safety fixture enclosing the specimen.

(a)   (b)
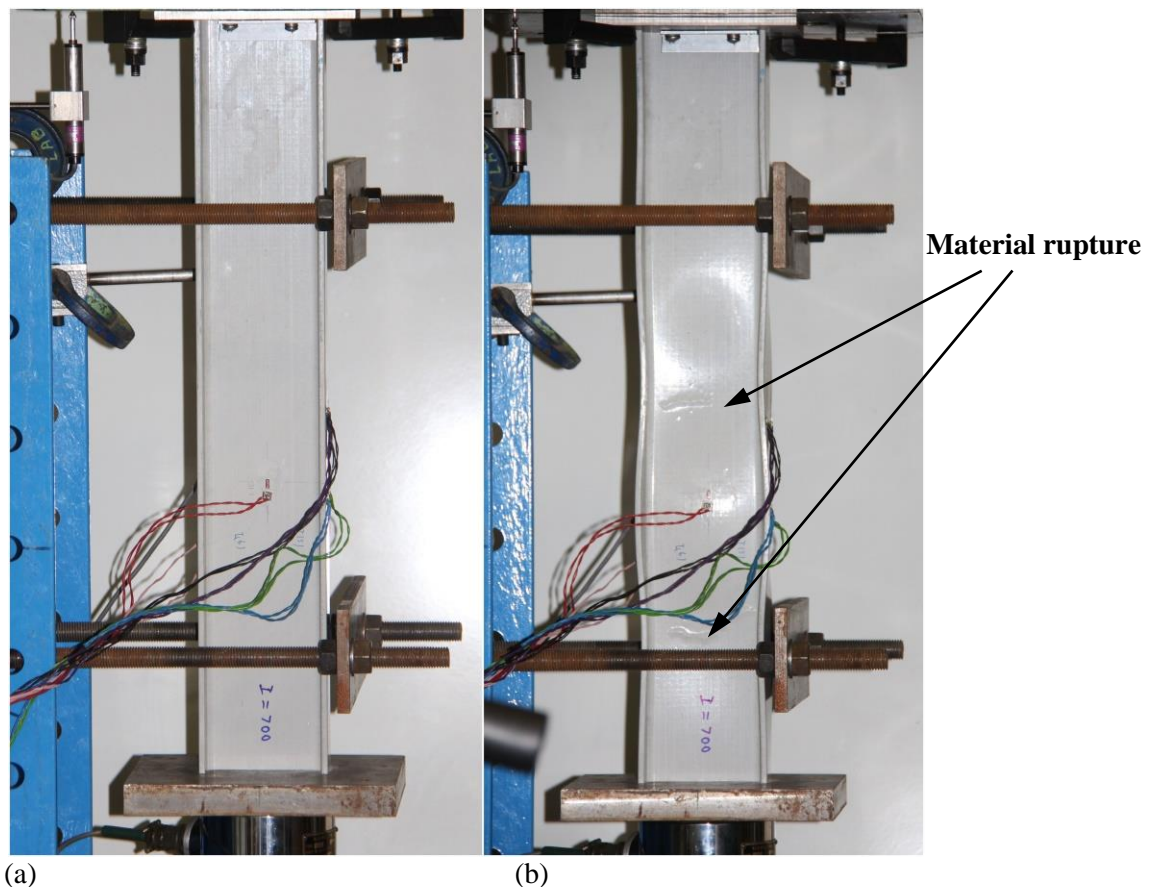
Figure 3.22 Local bucking test on I specimen: (a) under compression; (b) local buckling failure

(a)   (b)
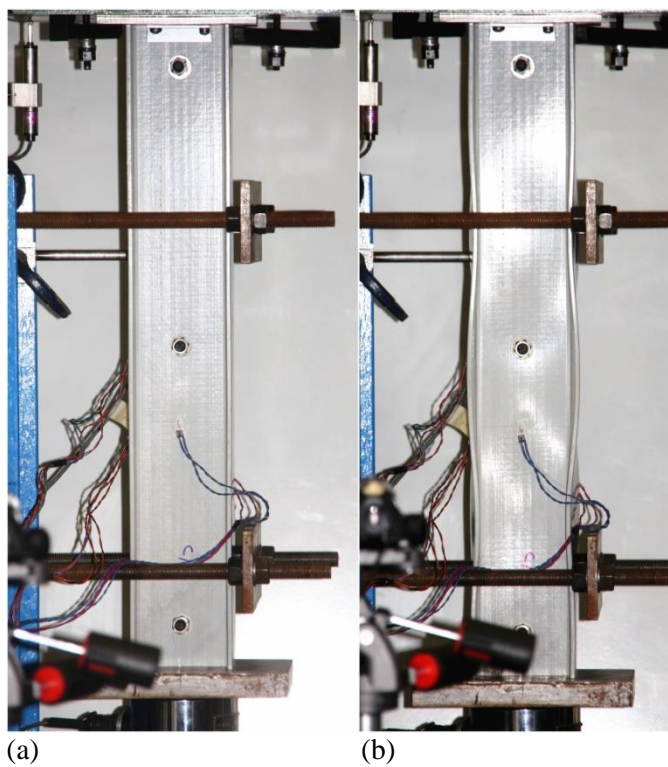
Figure 3.23 Local bucking test on C1 specimen: (a) under compression; (b) local buckling failure

"Tearing" failure at
Web - flange junction

Local "bearing" failure
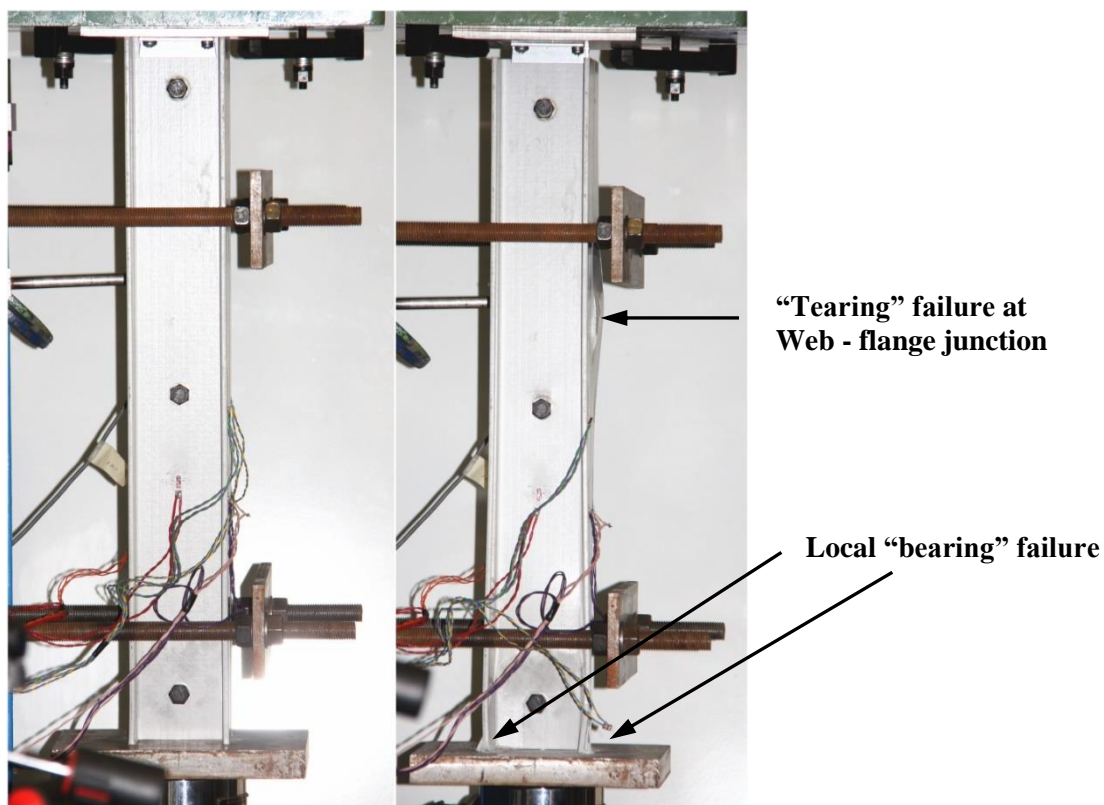
Figure 3.24 Local bucking test on C2 specimen: (a) under compression; (b) local buckling failure

Figures 3.22(a) and (b) shows the I-section before and after there has been local buckling failure. From Figure 3.22(b) three half wave-lengths and material rupture close to mid-height can be seen. A fourth half wave-length was visually observed near the top of the column (not shown in the photo). This deformation disappeared immediately as the load was released when FRP material fractured.

Figures 3.23 and 3.24 similarly show C1 and C2 back-to-back sections during testing. It is observed that whilst the first mode was compression bearing failure, the C1 specimen failed by local buckling, the C2-section did not. At the bottom and afterwards, there was "tearing" failure along part of web-flange junction. This failure of the C2 column cannot be characterized as a local buckling instability.
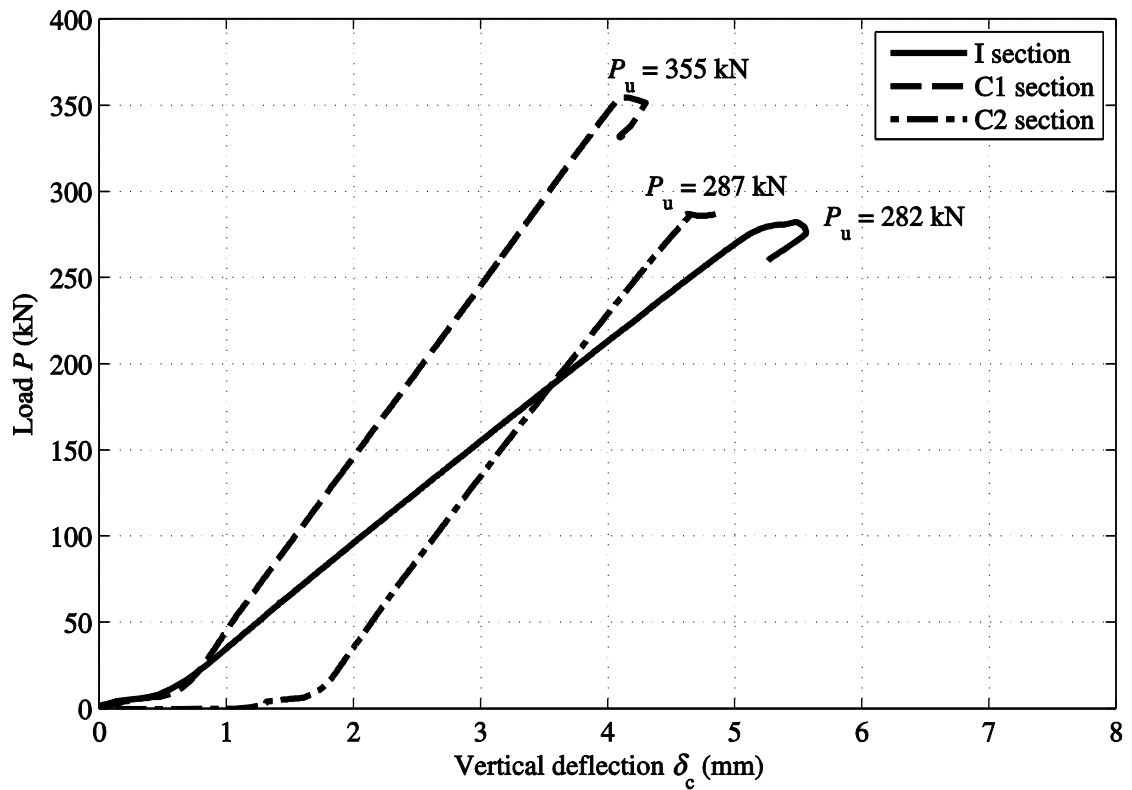
Figure 3.25 Load vs. vertical deflection curves for three tests
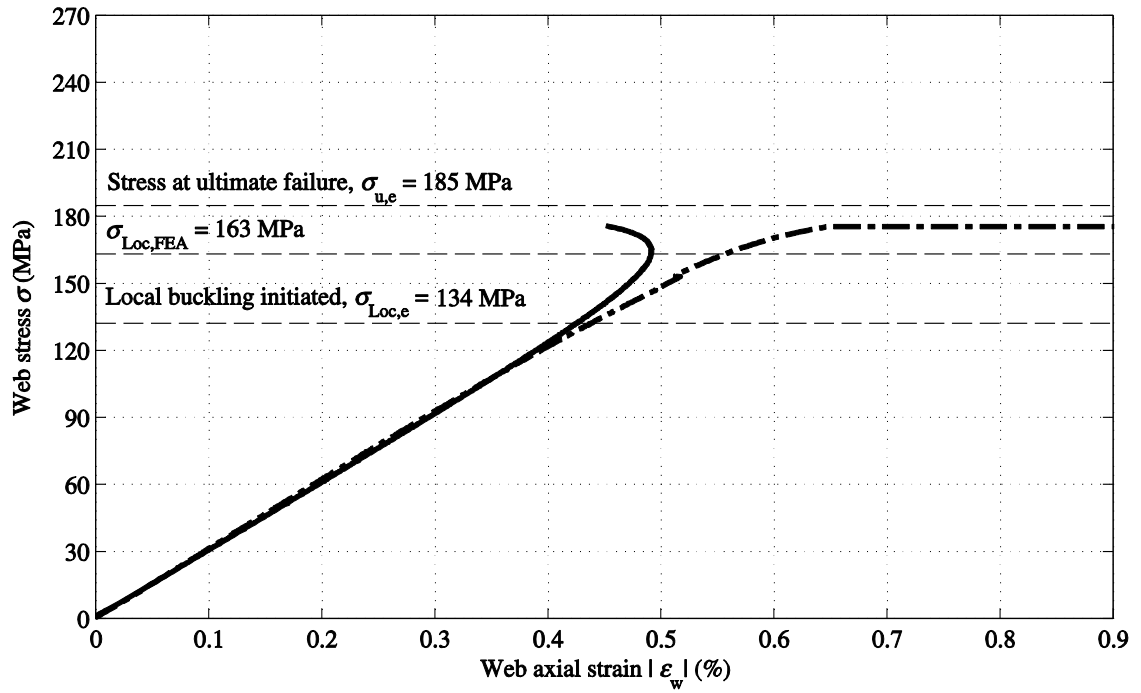
Figure 3.26 Web stress vs. web axial strain from I specimen

Figure 3.25 shows the load-vertical deflection relationships. The solid line is for the I-section, the dashed line is for the C1-section and dash-dot line is for the C2-section. The ultimate failure load (P_u) is given above the specimen's curve. P_u is for the specimen when failure had progressed into the post-buckling region. Once the specimen starts to take compression, it can be seen that P and δ_c maintain a linear relationship up to ultimate failure. It was observed at P_u that local buckling waves were visible (and obvious) with the I- and C1-sections and that there were signs of material rupture on the web or fracturing along the web-flange junctions. P_u is expected to be a higher load then when local buckling was initiated. The local buckling instability was not observed during the test with the column of section C2.

Figure 3.26 shows the two curves for web stress vs. axial strain on both sides of the web. It is observed that when $|\varepsilon_w| \geq 0.4\%$, the two strains start to diverge. The strain of one side of the web increases whilst the other decreases. This is interpreted being caused by local flexural from the onset of local (web) buckling. The three horizontal dashed-lines in Figure 3.26 are for the stress at ultimate failure at $\sigma_{u,e} = 185$ MPa , the buckling stress from FEA ($\sigma_{Loc,FEA} = 163$ MPa) and the stress at which the buckling initiated ($\sigma_{Loc,e} = 134$ MPa). It is noted that the theoretical buckling stress obtained from Eqs. (3.25) to (3.30) is $\sigma_{Loc,a} = 151$ MPa , is not given in the figure. The author believes that $\sigma_{Loc,e}$ can be assumed to represent the local buckling stress for the $120 \times 60 \times 6$ mm I-section. This strength will be used in Chapter 6 when calculating λ_{LT} for a LTB design curve corresponding to the design procedure for steel section in Eurocode 3.
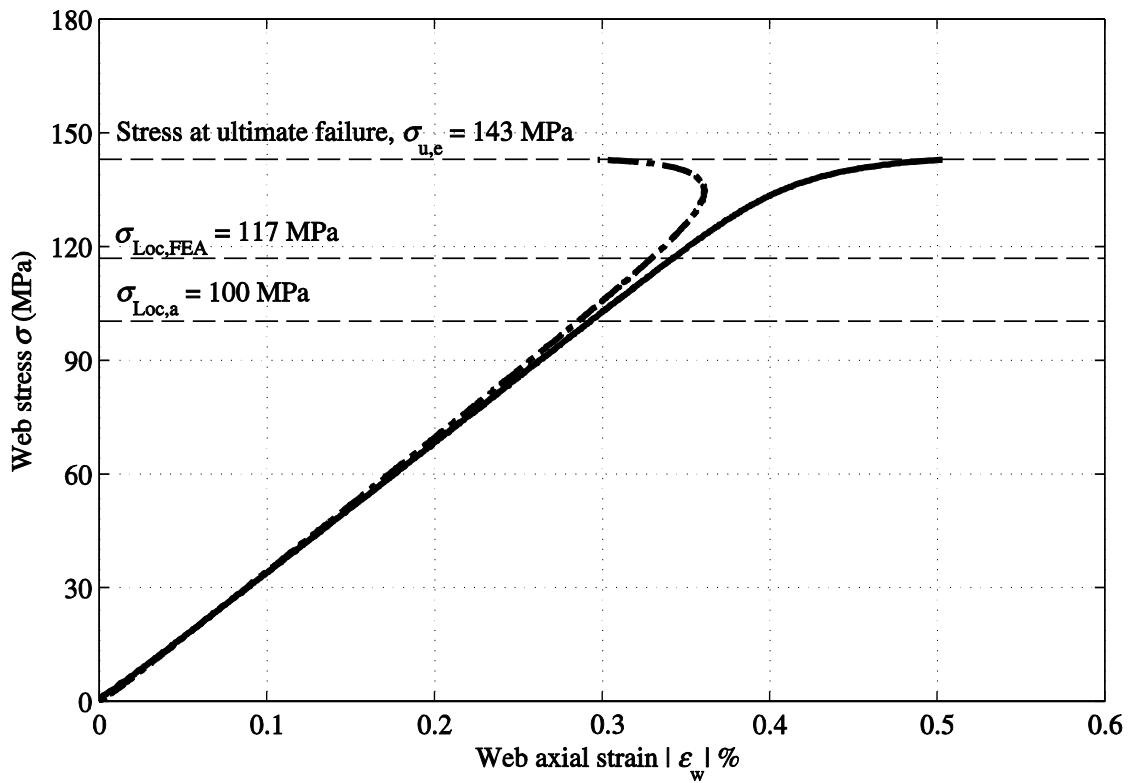
Figure 3.27 Web stress vs. web axial strain for C1 back-to-back specimen
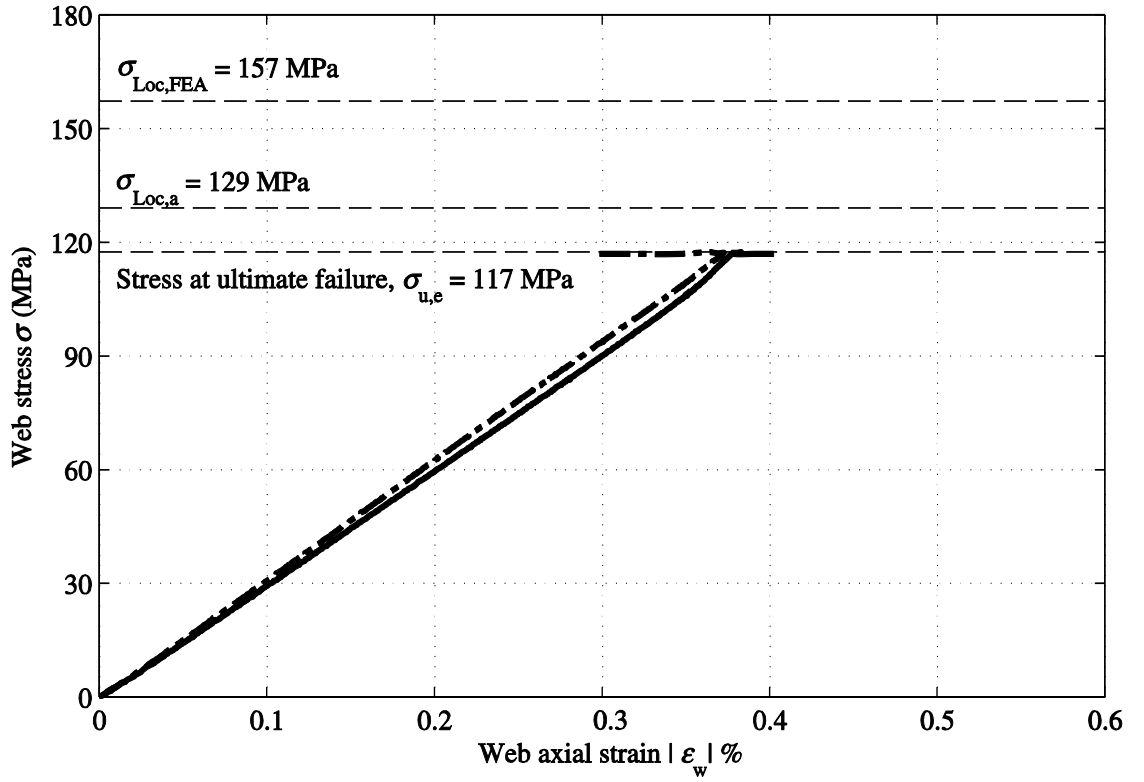
Figure 3.28 Web stress vs. web strain for C2 back-to-back specimen

Figures 3.27 and 3.28 give the equivalent plots using test results from the for C1 and C2 back-to-back specimen. It is observed that for C1-section, the analytical prediction using Eqs. (3.25) to (3.30) gives the lowest value buckling stress with $\sigma_{\mathrm{Loc,a}} = 100\,\mathrm{MPa}$. At this compression stress it is found that the strains on both sides of web have started to diverge. This change in response indicates that a local buckling mode of failure has initiated. The author believes it will be safe to adopt $\sigma_{\mathrm{Loc,a}} = 100\,\mathrm{MPa}$ as the local buckling stress for section C1.

It is from the results reported in Figure 3.28 that a local buckling instability was not captured by the measurements. It is observed that when the strain exceeded 0.1% the flexure starts to contribute to the ε_{w}. It is believe that the local buckling stress for section C2 could be higher than that at ultimate failure $\sigma_{\mathrm{u,e}} = 117\,\mathrm{MPa}$. This is shown

82

in Figure 3.28 is lower than those from analytical prediction ($\sigma_{\text{Loc,FEA}} = 157$ MPa) and FEA ($\sigma_{\text{Loc,a}} = 129$ MPa). Therefore, for the use of the local buckling stress in Chapter 6, it will be safe to adopt $\sigma_{\text{u,e}} = 117$ MPa (the lowest) as the local buckling stress for section C2.

The characterization by testing of the local buckling stress for PFRP section is difficult. The limited number of test result in this study is one difficulty. More importantly, its determination is influenced by many factors such as: geometrical properties, material properties, loading distribution, column height and the rotational stiffness along the web-flange junction. It is noted that the local buckling stress using in this Ph.D. project is just for the definition of non-dimensional slenderness in Chapters 4 and 6. It will not affect the key findings and conclusions drawn from this research.

3.8.   Concluding remarks

The study reported in this chapter has shown that:

- The actual E_{L} and G_{LT} is significantly higher (27% to 43% for E_{L}; 40% to 60% for G_{LT}) than those given in the pultruder's design manual (Anon., 2014a).

- The graphical method might be suitable to predict the elastic modulus but more consideration is needed when determining the shear modulus. The current technique could not guarantee a reliable value for this elastic constant.

- Both BS EN and ASTM standards for coupon testing give relatively similar results when determining E_{L} and the ν_{LT}. In terms of strain range for calculating the modulus, both 0.05% to 0.25% and 0.1% to 0.5% have been found to give E_{L} with minimal difference. It is appropriate to use the former range which is that

- recommended in BS EN to establish elastic constants for any type of structural engineering investigation (Euler buckling, local buckling, etc.)

- It is observed that for the I-section, E_L in opposite flange of the outstands differ significantly, with one side (mean) 13.3% higher than the other. This finding was not due to the testing itself because there were three coupons per outstand and the difference in a batch of specimens was no more than 3%. This might be commonly happening in PFRP material due to the manufacturing process as a more significant deviation of $> 20\%$ was found in Stoddard (1997) with a narrow flange I-section of size $101.6 \times 50.8 \times 6.4$ mm from the Strongwell range of pultruded sections.

- The major Poisson's ratio ν_{LT} was measured to be from 0.225 to 0.237 and the mean agrees closely with 0.23 listed in the Fiberline Design Manual (Anon., 2014a). It is worth noting that ν_{LT} from Fiberline is significantly lower than the 0.35 from Creative Pultrusion (Anon., 2004) and 0.33 from Strongwell (Anon., 2014b) for their standard pultruded materials.

- The 10° off-axis tensile coupon test has been used to determine G_{LT} and the results obtained appear to be relatively consistent. Furthermore, the specimens are easy to be produced and there is no particular technically difficult requirement in terms of testing machine and loading fixture. The author recommends this test method for characterizing the in-plane shear modulus of PFRP material.

- It is difficult to determine the local buckling stress σ_{Loc} from limited axial compression test on PFRP stub columns due to reasons discussed in sub-section 3.7.3. They are $\sigma_{Loc} = 134$ MPa, 100 MPa and 117 MPa for I-, C1- and C2-section respectively.

CHAPTER 4

LATERAL-TORSIONAL BUCKLING TESTS

4.1. Introduction

The review in Chapter 2 has shown that there is currently a lack of experimental data for PFRP members failing with Lateral-Torsional Buckling (LTB). Still to be fully investigated are their responses under various loading conditions (e.g. load applied on top flange, at shear centre, and on bottom flange) and changing displacement boundary conditions (e.g. free to rotate or fully restrained about minor axis). A comprehensive understanding of LTB failure by way of testing is essential to be able to provide structural designers with verified design guidance for members in bending. To allow design to be routine and similar to that with steel shapes the design provision has to be founded on one or more closed-form equations for resistance, which are shown to be reliable and relevant. To meet this goal the LTB tests were conducted on I and channel beams subjected to three-point bending configuration with three vertical load heights at mid-span and two displacement boundary conditions. This chapter will fully report the test methodology and experimental results. The comparison between test results and theoretical predictions will also be presented. The experimental study was carried out in the Structures Laboratory at the School of Engineering, University of Warwick. Part of this chapter has been presented in Nguyen *et al.* (2014).

4.2.   Test rig design

A good experiment is the one that can simulate either the assumptions in the fundamental theory that lead to the closed-form solution or those found in practice. The practical situation is complicated to characterize and those unknown influencing factors (e.g. displacement conditions, loading conditions, etc.) can either increase or decrease the 'apparent' buckling loads. Their level of influence is not easy to quantify also. Furthermore, the aim of this Ph.D. is to verify and calibrate a theoretical formula to predict LTB resistances such that it can be validated and/or modified for design purposes. The test rig was designed to satisfy in a 'practical sense' the theoretical assumptions for LTB failure.

The rig comprises of two fixtures for loading and end displacement support. The loading fixture is the system that simulates the vertical point load at mid-span and allow for different vertical and possible lateral load eccentricities. The end fixture is required to provide the simply support for major axis flexure. Reported next are the designs for the two fixtures.

4.2.1.   Loading fixture

The fundamental instability theory (Clark and Hill, 1960, Timoshenko and Gere, 1961, Trahair, 1993) assumes that: (1) the point of loading remains unchanged relative to the deformed cross-sections, and (2) the line of action keeps parallel with its initial position. These requirements are illustrated in Figure 4.1, in which two states are shown for an I beam subjected to a point load at shear centre progressing into LTB failure. In cases where the vertical load is acting above, or below, the shear centre the same two

assumptions remain valid. To meet these requirements the loading fixture was, with a slight modification, detailed in accordance with the design used by Flint (1948) for his Ph.D. work.

Flexural equilibrium

LTB failure

P

P

Line of action

Φ
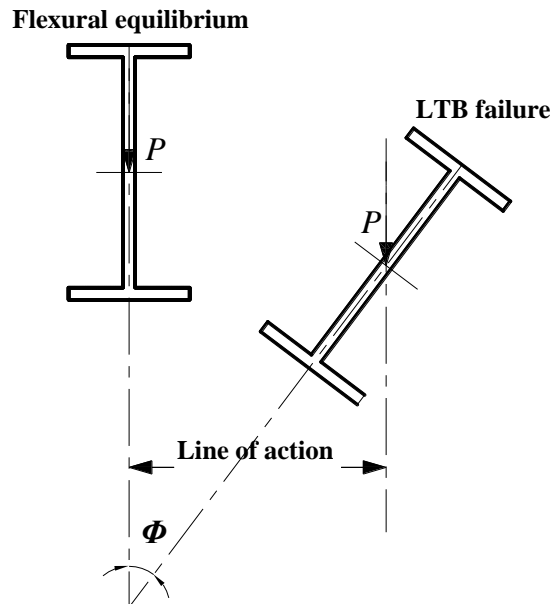
Figure 4.1 Schematic of LTB theoretical loading requirements

Flexural equilibrium

LTB failure

Clamping plate

Loading disc

Beam shear centre

Steel cable

Line of load action

Pulley

Ball bearing

Weight increments
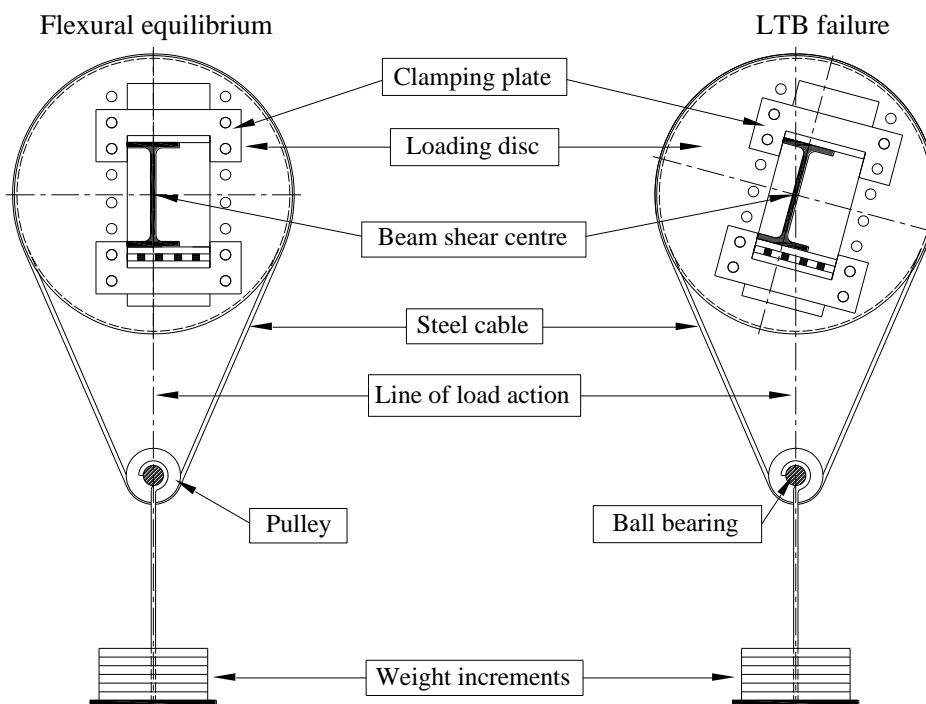
Figure 4.2 Schematic set-up of the loading fixture

Figure 4.2 shows a schematic set-up of the loading fixture during static testing and after LTB failure. It consists of a steel disc and a pulley system. The disc has a groove into which a high strength steel cable, diameter of 6 mm, is fitted so that a pulley can transfer the vertical downward load. A ball bearing is fitted inside the pulley to allow LTB deformations to coexist with the loading remaining vertical. When the beam bends laterally and twists for LTB failure, the load is free to move with its effective loading point staying at the disc's centre. By fixing the disc to the flanges of the specimen in such a way that its centre coincides with the beam's shear centre, it is practical to have the vertical point load acting through the shear centre as shown in Figure 4.2. Similarly, by aligning the disc position vertically until its horizontal centre line coincides with the top or bottom flange level, the loading at a height for top or bottom flange can be obtained. This can be done by moving the two pairs (for both sides of the disc) of clamping plates up or down. The shape of the disc fixture was not symmetric about either its horizontal or vertical axes. This is to accommodate for different beam depths (i.e. h is 120 mm or 100 mm) and to allow for the centre of the load to coincide with the shear centre of a Channel section beam.
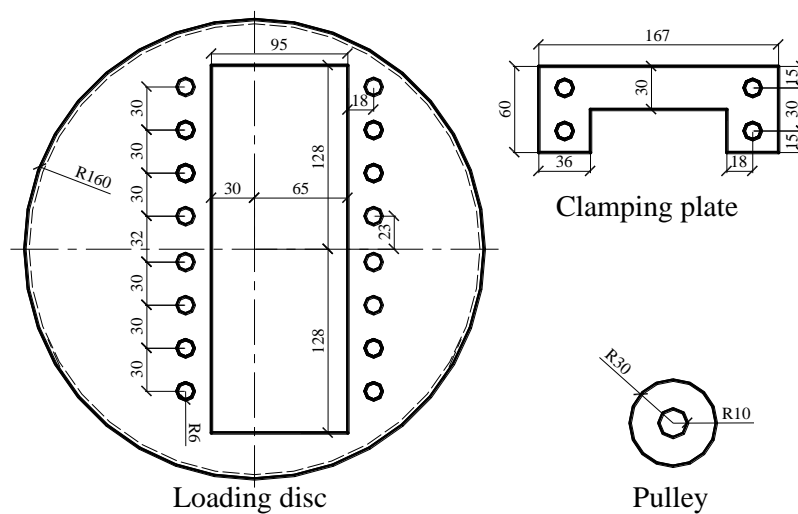
Figure 4.3 Detail dimensions in millimetres of three main parts of loading fixture: Loading disc, clamping plate and pulley

Figure 4.3 gives, in millimetres, the dimension of the disc, clamping plate and pulley. Their thicknesses, which are not shown in the figure, are 12 mm, 10 mm and 20 mm, respectively.
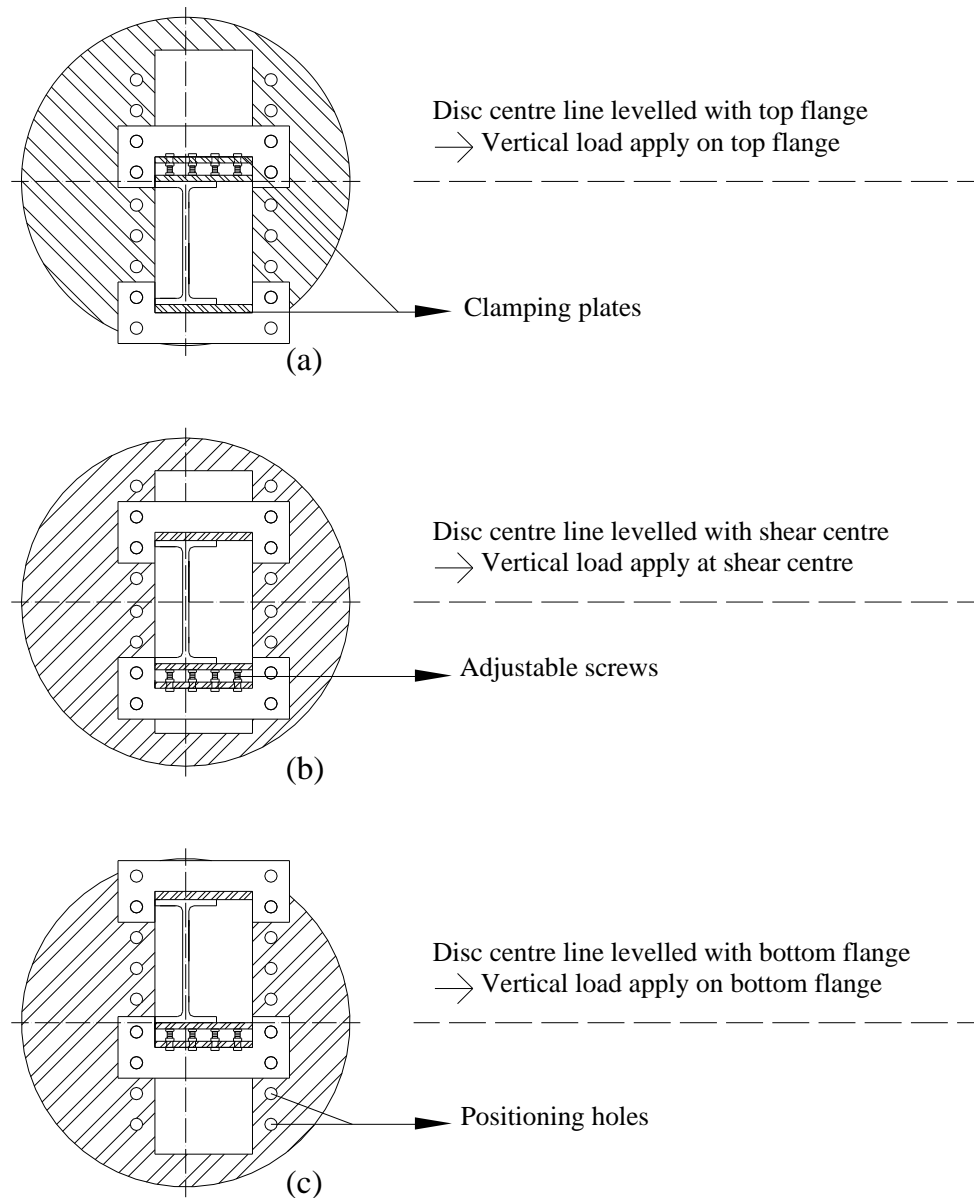
Figure 4.4 Three vertical load positions for: (a) Top flange; (b) Shear centre; (c) Bottom flange

Figures 4.4(a) to (c) show the schematics for the three vertical load positions of top flange (a), shear centre (b) and bottom flange (c) loading when the beam is I-shaped. The beam is positioned between two clamping plates (Figure 4.4(a)) that can move

vertically in the loading disc, using a series of positioning holes (Figure 4.4(c)). After adjusting the vertical centre line of the loading disc to coincide with the beam's vertical shear centre line and the required horizontal level, the beam was secured to the disc using a series of four adjustable screws (Figure 4.4(b)).

(a) I-section   (b) Channel section
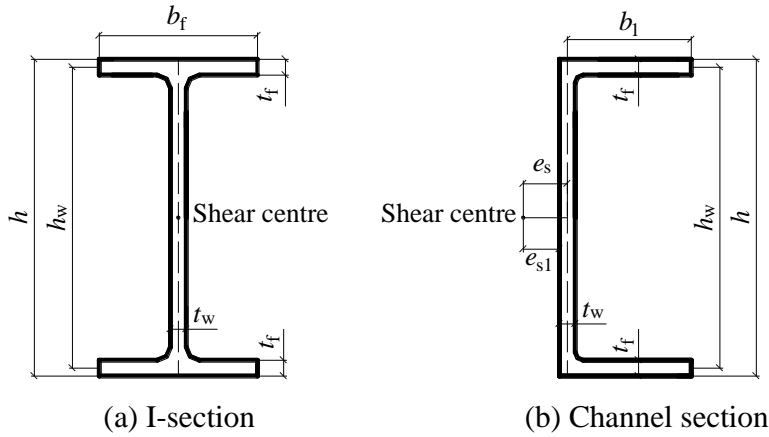
Figure 4.5 I- and channel sections

In terms of the shear centre position, the I-section is doubly symmetric and the nominal shear centre coincides with the section centroidal centre (Figure 4.5(a)). Channels C1, C2 and C3 are only symmetric about their major axis with their nominal shear centre lying outside of the sections area as shown in Figure 4.5(b). The distance from the reference point (vertical centre line of the web panel) to position of the shear centre can be approximated by (Pilkey, 2005) :

$$e_s = \frac{3t_f b_1^2}{6b_1 t_f + h_w t_w} \tag{4.1}$$

In Eq. (4.1) b_1 is the distance from the flange outstand to the middle vertical axis of the web and h_w is the distance from mid-depth of top flange to mid-depth of bottom flange.

Given that the web and flange thickness (t_w and t_f) are nominally the same, the position of shear centre, for convenience, is redefined to be the distance between shear centre and the outer surface of web. This distance is $e_\mathrm{s1} = e_\mathrm{s} - t_\mathrm{w}/2$. On substitution, Eq. (4.1) becomes:

$$e_\mathrm{s1} = \frac{3b_1^2}{6b_1^2 + h_\mathrm{w}} - \frac{t_\mathrm{w}}{2} \tag{4.2}$$

For sections C1, C2 and C3, e_s1 is 13.7 mm, 14.6 mm and 5.5 mm, respectively.

To have the point load acting through the vertical plane of shear centre, the section is positioned such that a distance of e_s1 is obtained between the centre of the disc and the outer surface of the web of the channel.

4.2.2. End fixture

For simply upported Boundary Condition (BC), the end fixture must allow for free rotation about major axis, for 'free' or fully fixed restraint to warping and minor axis rotation, and always fully restraint to twisting along the beam's length. In terms of axial restraint, one end of the beam must allow for free movement. The change in warping restraint or minor axis rotation restraint from fully free to fully restrained would give four different simply supported BCs. The two types of displacement BCs considered in this study are with 'free' warping and with or without restrained minor axis rotation. For free rotation about the minor axis, this end boundary condition is given the label EC1. When lateral rotation is fully fixed, the labelling is EC2.
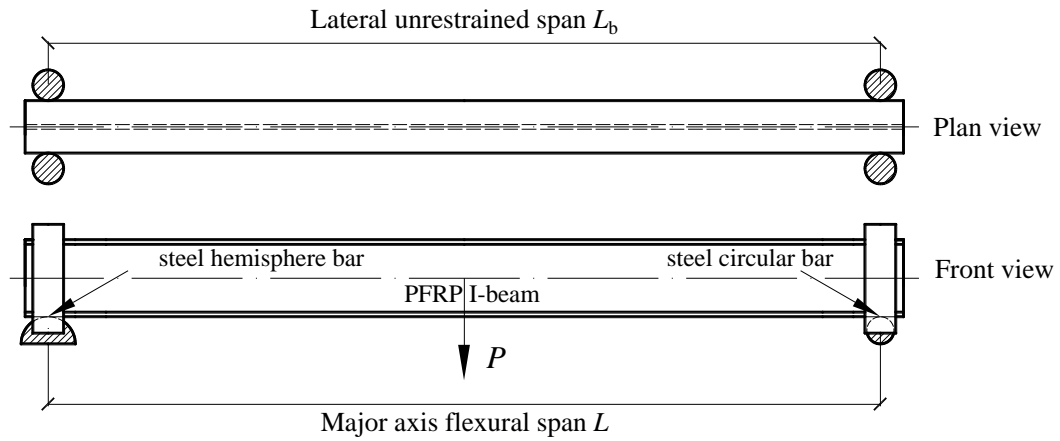
Figure 4.6 Schematic arrangement of end condition EC1
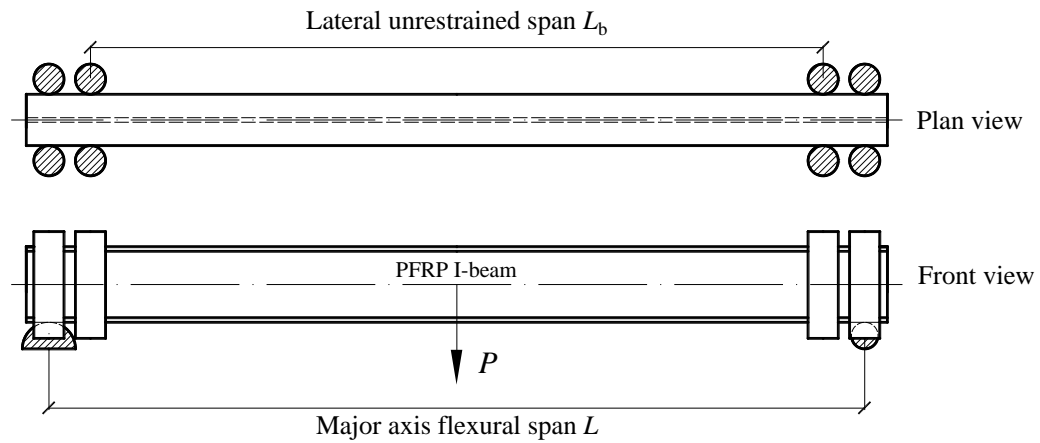
Figure 4.7 Schematic arrangement of end condition EC2

Figures 4.6 and 4.7 give schematic illustrations for EC1 and EC2. EC1 is implemented by having one pair of steel vertical rods, diameter of 20 mm, arranged in contact with the beam flanges on both side. This arrangement will allow the beam to rotate about its minor axis while restraining any twisting displacement. By adding a second pair of the steel rods, the support condition enforces 'full' fixity to lateral flexure. The longitudinal distance between the two pair of steel rods is 102 mm which is the distance between two holes in the meccano. To simulate a roller end for free horizontal movement, a 20 mm

diameter steel cylinder is placed underneath the bottom flange. A hemispherical shape of 40 mm diameter is located at the other end to restrain the axial movement. Also defined in the two figures are the major axis flexural span L and the lateral unrestrained span L_b. For EC1, these two spans are the same whilst for EC2 L_b is 204 mm shorter than L due to the arrangement of the supports at the bottom.
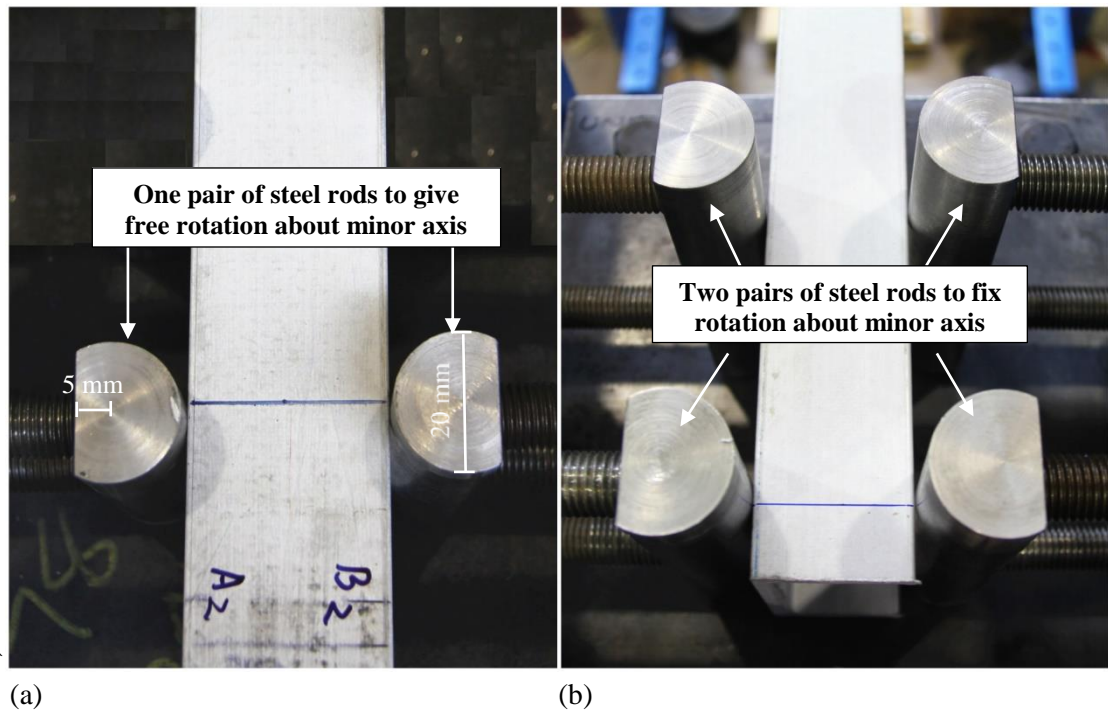
Figure 4.8 Top views of: (a) EC1 end support; (b) EC2 end support

Figures 4.8(a) and (b) are photographs showing a top view of the actual EC1 and EC2 conditions, respectively. To be able to apply the end conditions with different section widths (i.e. 60 mm for I, 50 mm for C1 and C2 and 30 mm for C3), one end of a threaded bar was screwed into the circular shaped steel rod and the other end is connected by nuts to a meccano channel. This test rig feature is shown in Figure 4.9. By adjusting the length of the threaded bars the change of section widths from 30 mm to 60 mm can be accommodated.
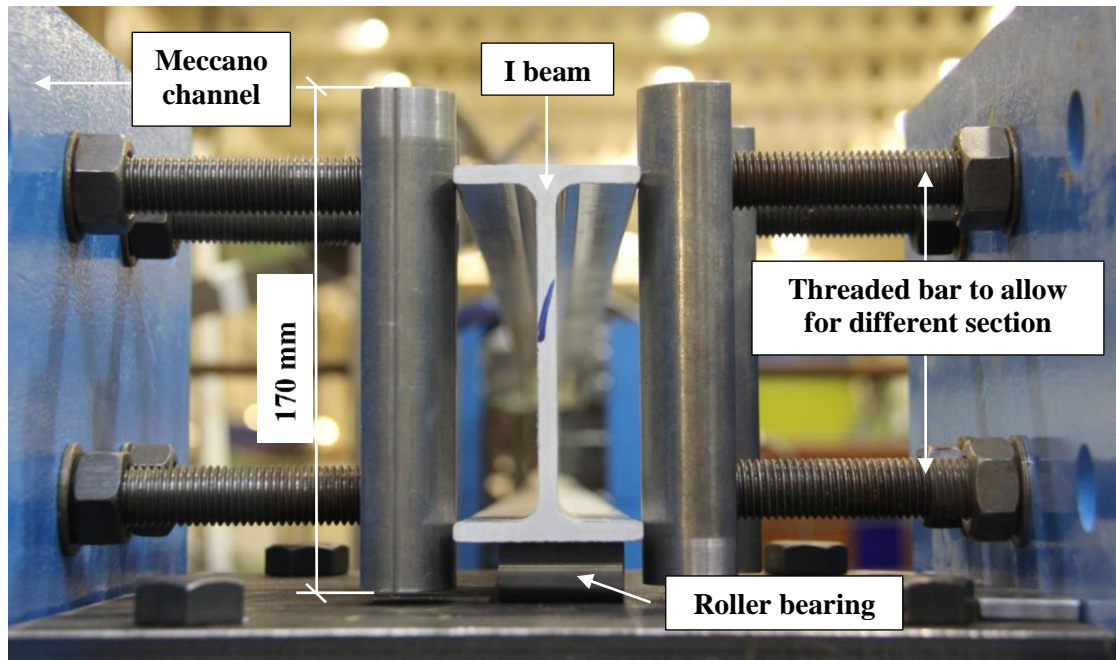
Figure 4.9 Side view of the end support

It is worth noting that the four or eight vertical steel rods and two horizontal supporting 'cylinders' will partially restrain the beam flanges from warping. To create a 'free warping', the end supports cannot be in contact with flanges. With the requirement for the beam to have unrestrained rotation about both major and minor axes the overall set of displacement boundary conditions is impractical to achieve.

4.2.3. Load application method

Two load application methods were adopted. The ideal approach that satisfy the theoretical assumptions for loading is gravity loading by dead weights (Flint, 1948). However, for reason of Health and Safety the maximum limit of dead weight was taken to be 200 kg. Beams with higher LTB resistance had to be loaded via a hydraulic

tension jack. The tension jack is mounted and can rotate around the fixing point on the strong floor when the beam twists and moves laterally progressing into LTB failure.
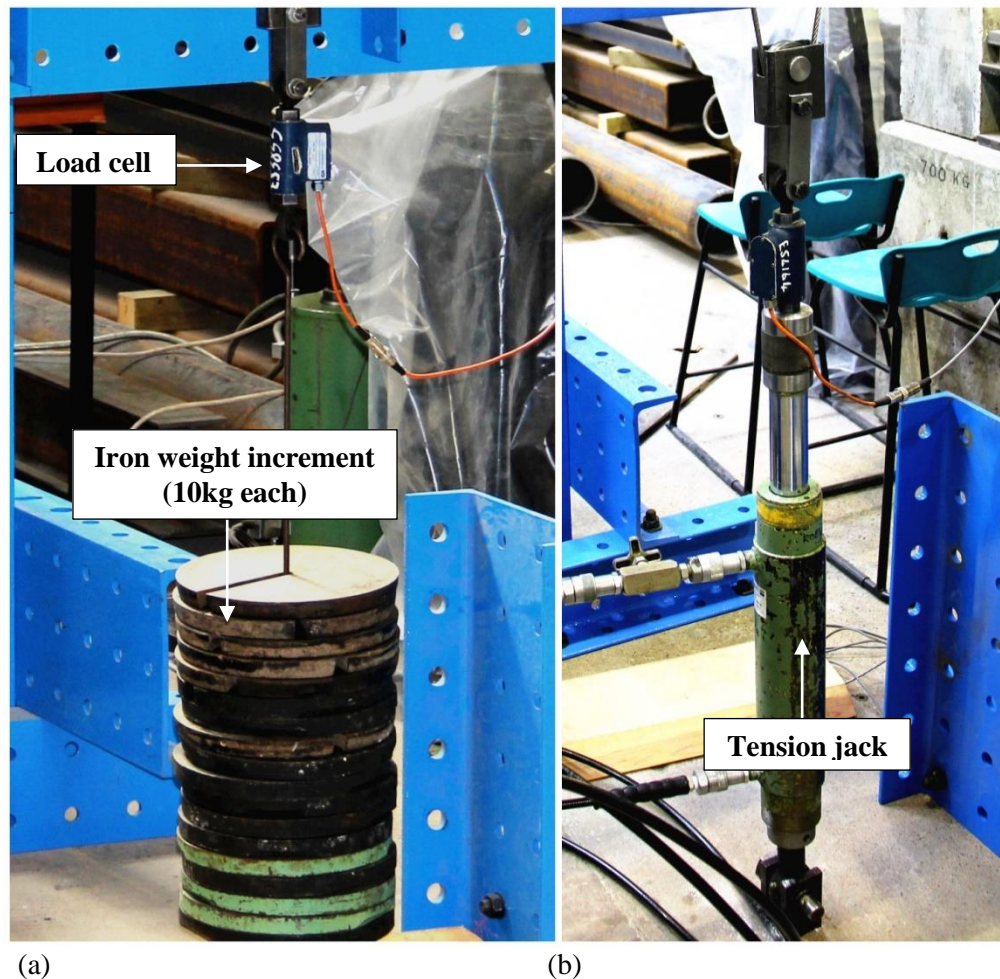
Figure 4.10 Two load application methods: (a) Dead weight; (b) Tension jack

Figures 4.10(a) and (b) show the arrangement of the two load application methods for (a) the dead weight and (b) the tension jack. In a test with hydraulic jack, the lateral and twist deformations inherently develops 'stretching' in the jacking system. An additional horizontal force, whose magnitude depends on the system's length and the amount of the lateral deflection at mid-span, will be created. With a system length > 1000 mm and a maximum mid-span twist < 10 degree (or 175 mrad) the maximum amount of 'stretching' at 0.15 mm is believed to be neglectable. The results obtained will show

that this assumption is appropriate. In this study, dead weights were used when beam span L is 3454 mm and 4064 mm with all four sections and when L is 2438 , 2844 and 3454 mm for section C3. For all other beams the tension jack loading method was employed.

4.3.   Test specimens and geometric properties

Chosen from Fiberline Composites A/S sectional range of standard pultruded shapes are the four cross-sections shown in Figure 4.11. They were chosen for the LTB tests because their buckling resistances are within the bearing capacity of the in-house testing rig and fixtures. The three sections (I, C1 and C2) in Figure 4.11 were tested at five spans (*L*) of 1828, 2438, 2844, 3454 and 4064 mm. Section C3 was not tested at the longest span of 4064 mm because the LTB load for these spans will be too low to measure.
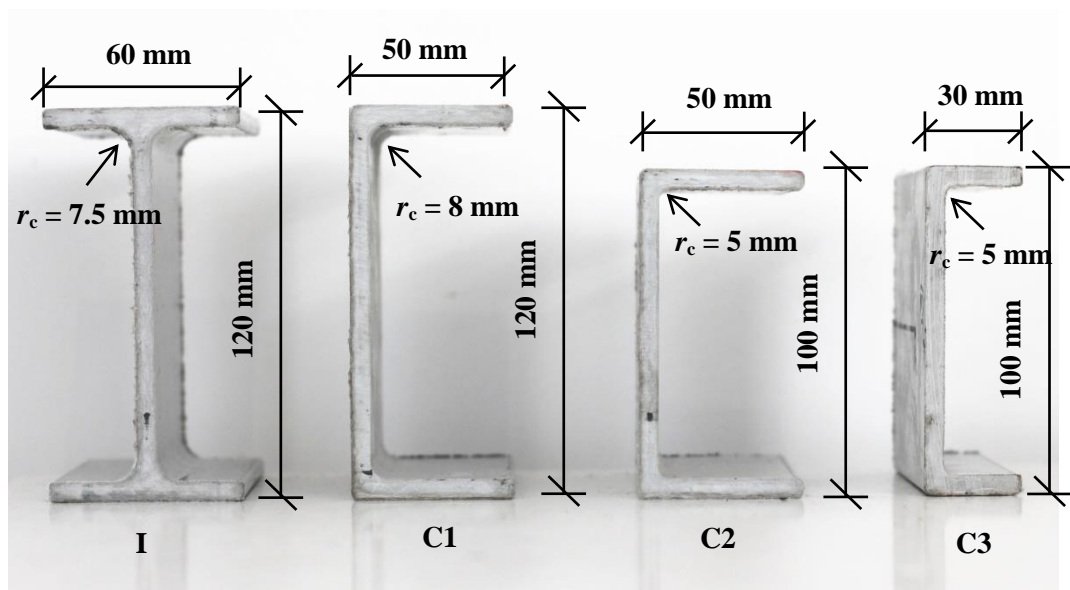
Figure 4.11 Nominal section sizes for the I- and channel sections

It is worth mentioning that the actual beam lengths are 1900, 2500, 3000, 3500 and 4100 mm, as they were cut to longer lengths than the test spans, to provide a short overhang of 18 mm to 78 mm at both ends.

Table 4.1 Measured geometric properties of the test beams

Specimen	Span L (mm)	Depth h (mm)	Breadth b_f (mm)	Web Thickness t_w (mm)	Flange thickness t_f (mm)
(1)	(2)	(3)	(4)	(5)	(6)
I-4064	4064	120.14	59.95	6.03	5.97
I-3454	3454	120.05	60.10	6.07	6.00
I-2844	2844	120.10	59.89	6.04	6.06
I-2438	2438	120.04	59.88	5.96	6.02
I-1828	1828	120.12	59.91	6.03	6.03
Mean (mm)		120.09	59.95	6.03	6.02
SD (mm)		0.04	0.07	0.03	0.03
CV (%)		0.03	0.12	0.55	0.46
C1-4064	4064	119.89	49.91	6.03	6.03
C1-3454	3454	120.03	49.99	6.03	5.94
C1-2844	2844	120.16	49.87	5.99	6.13
C1-2438	2438	120.03	49.81	6.03	5.97
C1-1828	1828	120.03	50.12	6.03	6.10
Mean (mm)		120.03	49.94	6.02	6.03
SD (mm)		0.09	0.11	0.02	0.07
CV (%)		0.07	0.21	0.27	1.21
C2-4064	4064	100.05	50.02	5.98	5.95
C2-3454	3454	99.97	49.97	5.98	5.94
C2-2844	2844	99.92	50.10	5.96	5.99
C2-2438	2438	99.97	50.06	5.98	5.97
C2-1828	1828	100.10	50.01	6.02	6.00
Mean (mm)		100.00	50.03	5.98	5.97
SD (mm)		0.06	0.04	0.02	0.02
CV (%)		0.06	0.09	0.33	0.38
C3-3454	3454	100.03	30.06	5.98	6.02
C3-2844	2844	99.97	30.05	6.03	6.02
C3-2438	2438	99.99	30.00	5.96	6.00
C3-1828	1828	100.01	30.04	6.02	5.98
Mean (mm)		100	30.04	6.00	6.01
SD (mm)		0.02	0.02	0.03	0.02
CV (%)		0.02	0.08	0.48	0.28

The depth (h), breadth (b_f) and thickness of web (t_w) and flanges (t_f) of the four PFRP sections were measured using a digital calliper with a repeatability to 0.01 mm. The thicknesses of the top and bottom flanges are assumed to be constant and its value was determined on taking the average of four t_f outstand measurements. Wall thickness (t_w) was determined as the average measurement at three web heights. Table 4.1 reports the geometric properties of the sections. Columns (1-2) are used to give beam labelling and spans L. Columns (3-6) present, in millimetres, the measured geometry parameters of h, b_f, t_w and t_f. The Mean value, Standard Deviation (SD) and Coefficient of Variation (CV) for each section are also reported. The maximum CVs for h, b_f, t_w, and t_f are found to be small at 0.07%, 0.21%, 0.55% and 1.21%, and so the average values can be used to establish geometric properties.

4.4.   Initial geometric imperfection

Structural PFRP shapes are manufactured with initial geometric imperfections such as: out-of-straightness, twist, flatness, angularity, etc. To apply nonlinear FEA to predict the buckling loads of real beams, these imperfections must be measured and characterized. An acceptable approach in FEA to account for these geometric imperfections is by considering only the dominant type of imperfections with high magnitudes (Nguyen *et al.*, 2013). Two geometric imperfections that would have a dominant influence on the LTB capacity of a beam are minor axis out-of-straightness and twist rotation because they link to the two governing deformations in LTB failure. As it is impractical to measure the initial twist imperfection of the beam, only

measurement of minor axis out-of-straightness imperfections were carried out and later introduced into the FE model.
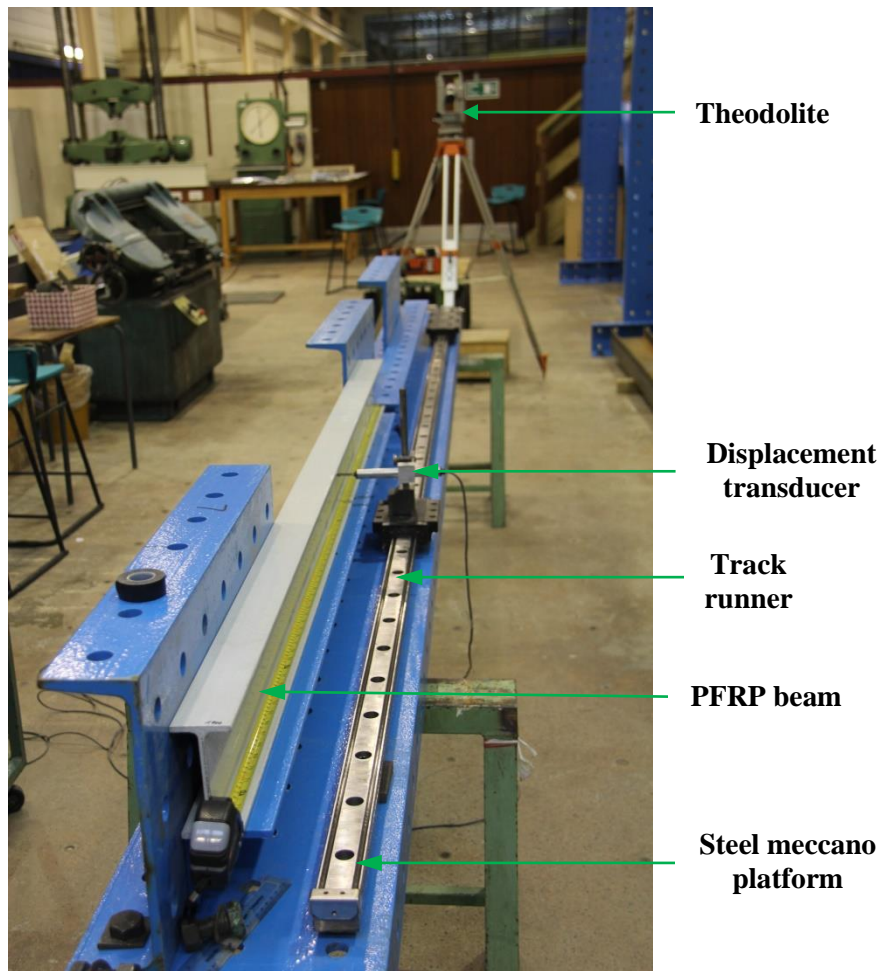
Figure 4.12 Arrangement to measure the minor axis out-of-straightness imperfection

To measure the minor axis out-of-straightness (δ), a beam was placed on a levelled platform of steel meccano. A displacement transducer was mounted on a track runner with its pointer contacting the beam at mid-depth. Two short tracks having length of 1800 mm were connected together to give a longer track of 3600 mm and were aligned by using the theodolite as seen in Figure 4.12. To ensure the transducer was perpendicular to the specimen's axis, a spirit level was placed on top of the transducer's fixture that is seen in Figure 4.13.

Web mid-depth

Spirit level

Displacement Transducer
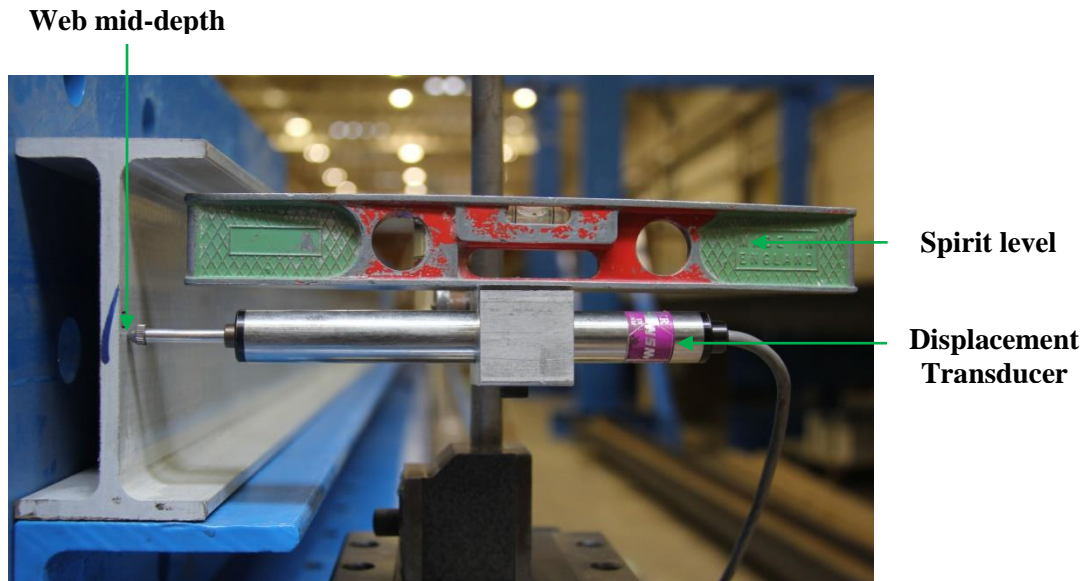
Figure 4.13 Method to level the displacement transducer to record the out-of-straightness

1st reading   *2nd reading*   *3rd reading*
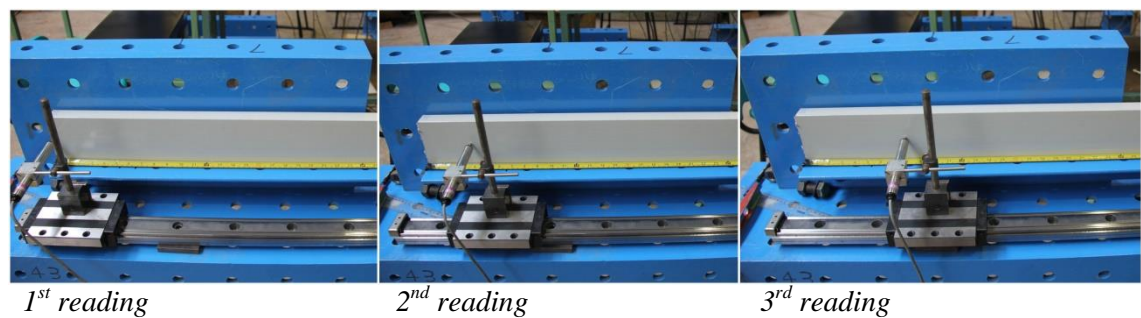
Figure 4.14 Illustration of how to measure the out-of-straightness

The displacement reading was set to zero at one end of the beam and lateral displacement measurements were taken along the track every 100 mm. Figure 4.14 illustrates how the readings were taken. After recording the first reading at one end, the transducer was moved to the next position to take the second reading. The third reading was taken at 100 mm away from the second, and so on, until the other end of the beam was reached. The measurements were then corrected by taking a straight line between the two ends as reference.

This geometric imperfection was measured on both sides of the web and because the length of the track runner was 3600 mm, the mearusements were only taken on 16 out of the 19 beams. The imperfections of specimens with span of 4064 mm were not measured.
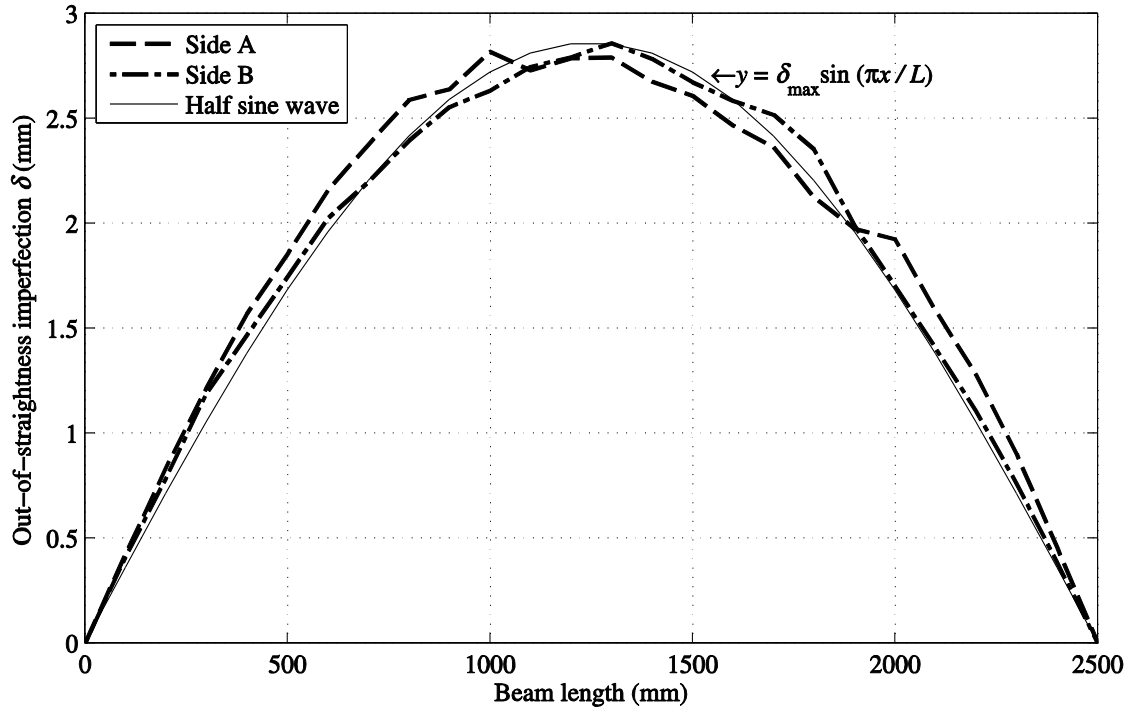
Figure 4.15 A typical plot of out-of-straightness along the length for I-2438

Figure 4.15 shows a typical plot of out-of-straightness along the length for I-2438. The horizontal axis gives the beam length with the ends at 0 mm and 2500 mm. The vertical axis gives, in millimetres, the out-of-straightness δ related to position along the beam span. The dashed curve is for one side (A) and the dot-dashed curve is for opposite side (B). The plots for all 16 beams are given in appendix B1. It was found from the plots for 16 beams that the maximum of imperfection δ_{max} is normally located at mid-span. The measurements (such as shown in Figure 4.15) would allow for the recreation of the actual minor axis imperfection, but it is not needed in the FE modelling. Instead, it

would be reasonable to assume that the out-of-straightness imperfection have a shape of a half sine wave length with amplitude δ_{max} at mid-span. As this assumed shape is considered to be the worst case for simply supported beam in bending, this adoption remains valid (Nguyen *et al.*, 2013). Figure 4.15 shows the solid curve for the half sine wave of $y = \delta_{max} \sin(\pi x / L)$. It is observed that this curve has a similar shape with those measured on either side A and B.

Table 4.2 Initial out-of-straightness imperfections of test beams

Beam specimen	Maximum minor axis imperfection δ_{max} (mm)	Maximum allowance of out-of-straightness imperfection D (mm) - BS-EN 13706-2	Maximum allowance of out-of-straightness imperfection D (mm) - ASTM D3917
(1)	(2)	(3)	(4)
I-4064	-	8.26	16.93
I-3454	2.72	5.97	14.39
I-2844	1.95	4.04	11.85
I-2438	2.86	2.97	10.16
I-1828	0.78	1.67	7.62
C1-4064	-	8.26	16.93
C1-3454	1.72	5.97	14.39
C1-2844	1.55	4.04	11.85
C1-2438	0.80	2.97	10.16
C1-1828	0.27	1.67	7.62
C2-4064	-	8.26	16.93
C2-3454	0.62	5.97	14.39
C2-2844	1.78	4.04	11.85
C2-2438	0.90	2.97	10.16
C2-1828	0.21	1.67	7.62
C3-3454	8.31	5.97	14.39
C3-2844	4.78	4.04	11.85
C3-2438	5.79	2.97	10.16
C3-1828	2.26	1.67	7.62

Table 4.2 summarizes in columns (1-2) the specimen name and the measured maximum minor axis out-of-straightness δ_{max}. It is shown that the specimens of C3 possess δ_{max} of 2.26 mm to 8.31 mm which are relatively larger compared to those of other three sections. The maximum imperfections are 0.78 mm to 2.86 mm, 0.27 mm to 1.72 mm

and 0.21 mm to 1.78 mm for I, C1 and C2 sections, respectively. Column (3) is the maximum allowable (e.g. manufacturing tolerance) for the out-of-straightness imperfection (D), taken from the BS EN 13706-2 (BSI, 2002b). This European standard specifies out-of-straightnes tolerances for reinforced plastic pultruded sections with $D \leq 0.0005L^2$ (D and span length L in metres). Column (4) provides the allowable of out-of-straightness taken from American standard for dimensional tolerances ASTM 3917 (ASTM, 2012a). It requires that the deviation from straightness $D \leq L/240$ (with both D and L in millimetres). IT is obvious that the allowables of the two standards are different with a same beam span. By comparing the maximum allowables from the two standards in columns (3) and (4), it is seen that those given by BS EN standard are significantly higher than those allowed by the ASTM standard.

Comparing data in Columns (2) and (3), it is found that all specimens of C3 possess δ_{max} that are higher than D permitted by the BS EN 13706-2. Specimens of I, C1 and C2 sections have δ_{max} that are lower than the limit. Comparing results in Columns (2) and (4) it is found that all 16 beams satisfy the manufacturing requirement for the out-of-straightness limit in accordance with ASTM 3917.

4.5. Test instruments and procedure

Instruments were calibrated and connected to an Orion data logger. The load P was measured using a load cell having one end connected to the pulley system and other end attached to the load hanger or the tension jack. Two load cells with measurement capacities of 2000 lbs (or 9 kN) and 2250 kg (or 22 kN) were used. They both have a

resolution to ±0.001 kN. Two 50 mm strain gauge displacement transducers were placed at mid-span to measure the lateral and vertical deflections of the shear centre. The lateral displacement transducer was located at mid-depth of the section while the vertical displacement transducer has its pointer touches the top flange. The mid-span rotation in the vertical plane (ϕ) was measured using an Accustar® inclinometer mounted at mid-depth of the web. Rotation was recorded to a resolution of 0.02 mrad (linear to ±1% over a 10° range). It is to be noted that when a beam moves laterally and twists, as the two displacement transducers cannot go with the deformed section, their readings cannot give the exact movement of the shear centre.

There are techniques (Brooks and Turvey, 1995, Davalos *et al.*, 1997) that could help to give the actual deflections which were deemed to be too complicated for this test programme. More importantly, the readings of ϕ and the applied load P together are able to signal the onset of LTB failure. The readings recorded by the data logger were transferred to the computer into a text file. The text files were given a name for the section (i.e. I, C1, C2 or C3), span length (i.e. 1828, 2438 2844, 3454 or 4064 mm), type of end boundary conditions (i.e. EC1 or EC2) and type of vertical load height (i.e. TF for top flange, SC for shear centre and BF for bottom flange loading). As an example, the file named I-4064_EC1_TF has the test measurements for the 120×60×60 mm I-shape of length (L) 4064 mm with 'free' end lateral flexure (EC1) and Top Flange (TF) loading. The test results to be reported in this chapter also followed this labelling scheme.
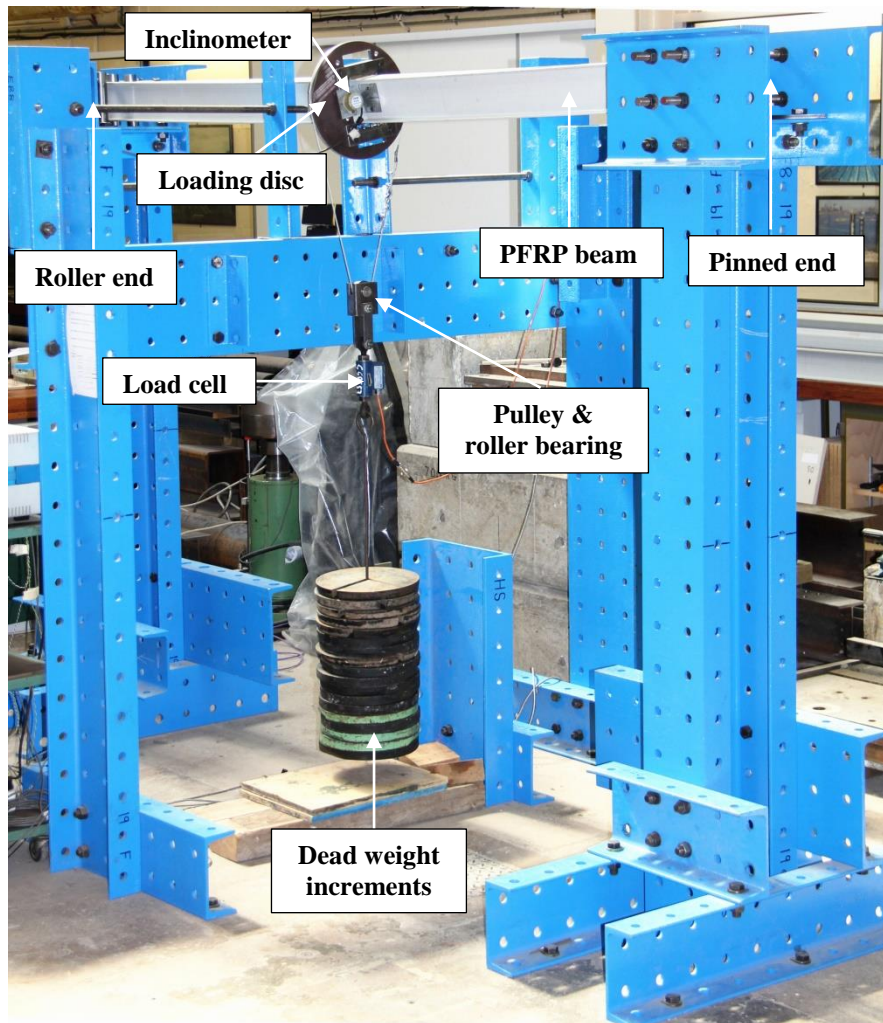
Figure 4.16 General arrangement of LTB test with dead weight system

A specimen can be expected to fail elastically (Mottram, 1992a, Correia *et al.*, 2011) and so it will recover to its original cross-sectional shape when unloaded. It has been shown in Chapter 3 that when a beam fails with LTB, the maximum longitudinal strain will be ≤ 0.5%. It is known that the PFRP material will fail at strains higher than 1% and that material response is virtually linear elastic up until failure. This means that a beam can be reutilized many times without the previous test influencing the test results from the next one. Each beam was tested six times for three different vertical load heights and at two different end boundary conditions. There was no test repetition in the programme. For those LTB tests that were carried out using dead weights one increment

was a 10 kg (or 98 kN) of slotted iron plate. Lighter plates of 5 kg (or 49 kN) or 2.5 kg (or 24.5 kN) were employed when the applied load were tending towards the critical buckling value. The set-up of the LTB test with dead weight system is shown in Figure 4.16. During the test there was a ten seconds delay time between two load increments to keep the load rate constant and for any transient disturbance in the loading system (e.g. when placing the mass on the hanger) to disappear.

(a)   (b)
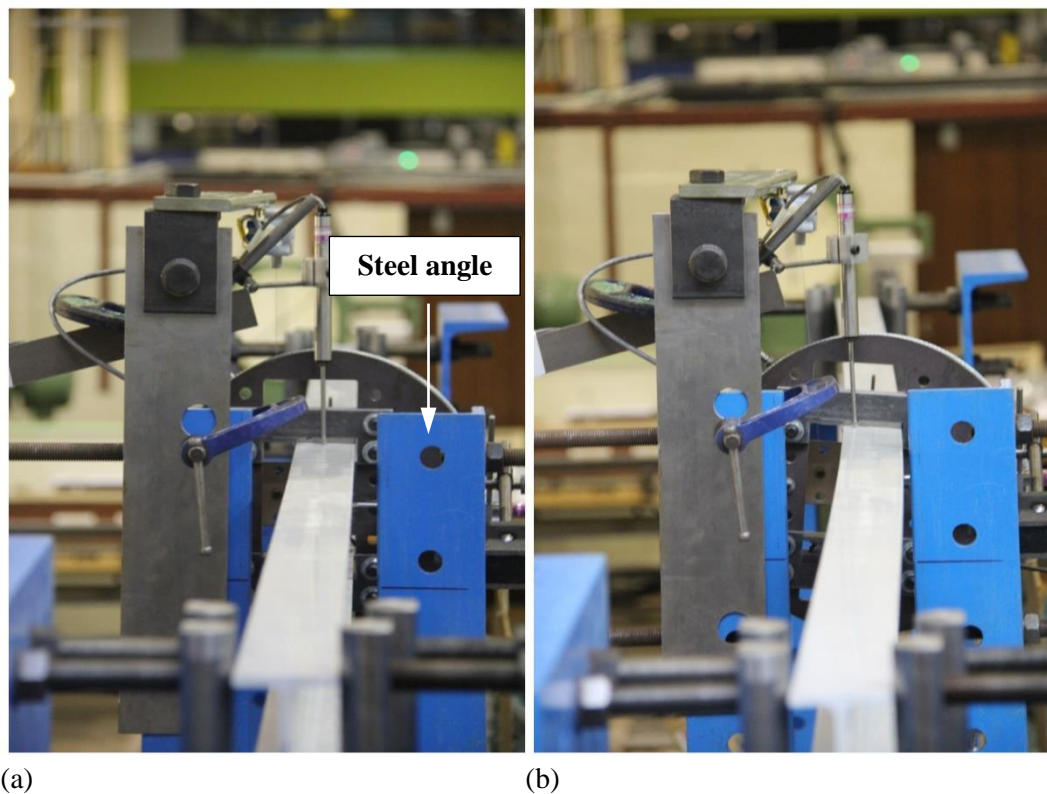
Figure 4.17 Deformation during testing: (a) in flexure; (b) after LTB failure

To stop the specimen from movement after LTB instability has occurred, two leg-angle meccano sections of steel were placed on either side of the beam. Testing was terminated when one of the two top flange outstands made contact with its limiter. This feature can be seen in Figure 4.17. This figure also shows two states from testing in Figure 4.17(a) to after failure in Figure 4.17(b).
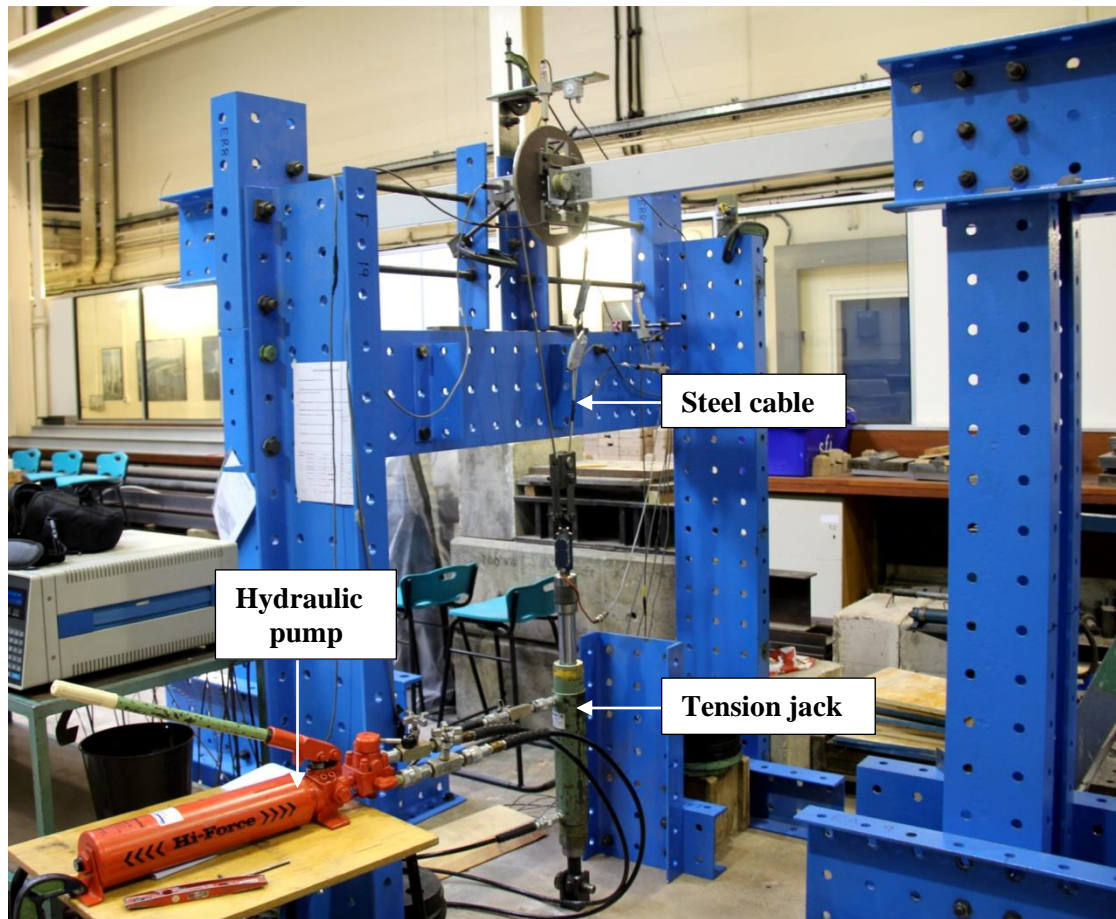
Figure 4.18 General arrangement of LTB test with tension jack system

The tension jack system controlled the stroke and not the magnitude of load at each increment. The jack could accommodate a downward stroke of 150 mm. There is a five seconds delay between two consecutive stroke applications. Figure 4.18 shows the testing arrangement with the tension jack system.

There were five of the 114 tests for: I-1828_EC2_TF, I-1828_EC2_BF, C1-3454_EC2_BF, C2-1828_EC2_SC and C2-1828_EC2_BF when the PFRP beam continued to undergo in-plane deformation without any sign of LTB failure (e.g. lateral deflection and twisting). These tests had to be terminated when the vertical load attained 10 kN for the tension jack and 2 kN for the dead weights. Test results for these tests will not be reported in the thesis.

4.6.   Onset of buckling and data reduction method

Theoretically, the beam fails instantaneously when the vertical load reaches a critical value. There would be no lateral movement or twist rotation prior to the failure. This type of failure is characterized as 'bifurcation buckling' (Timoshenko and Gere, 1961, Trahair, 1993) which only occurs under three specific conditions of: (1) beam is perfectly straight, (2) beam material is homogeneous and (3) load acting exactly through the shear centre. In reality or even under controlled laboratory setting this type of failure is rarely observed.

It is obvious that as initial geometric imperfections always exist, a beam cannot be absolutely straight. The PFRP material is not homogeneous. Applying the load accurately through the section's shear centre is impractical due to the degree of uncertainty on whether the nominal shear centre coincides with the actual one. The more commonly observed in testing is that of 'progressive failure', where a beam starts to twist and move laterally from the beginning of the load increments. As the beam fails 'progressively', this type of LTB failure gives no critical buckling point.

In the author's series of tests both types of LTB failure were observed. These two different behaviours are demonstrated by the load vs. mid-span rotation curves in Figure 4.19. The solid-lined curve for C2-3454_EC1_SC shows a 'bifurcation-like' type of failure with the beam having virtually no rotation up to 1.22 kN and suddenly became unstable afterwards. For those tests experiencing this 'bifurcation-like' failure, the LTB load ($P_{cr,e}$) is the peak load. The subscript 'e' is for experimental obtained.
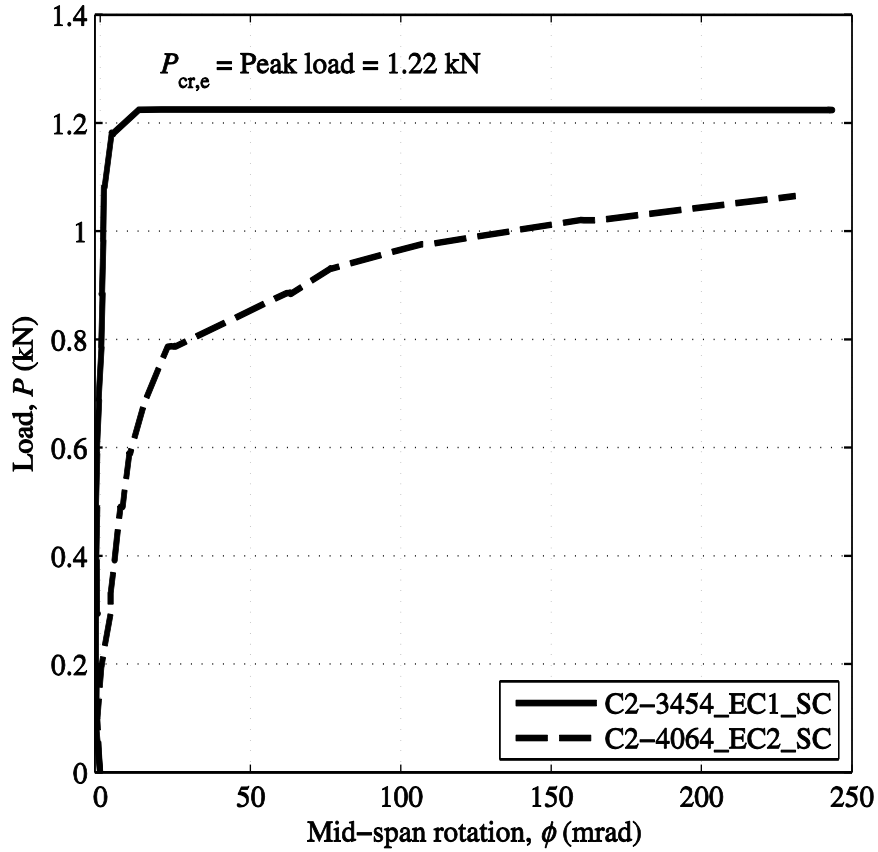
Figure 4.19 Two typical LTB failures

In contrast, the dashed-lined curve for C2-4064_EC2_SC shows the progressive failure where the specimen starts twisting from beginning of the loading. Because its $P - \phi$ curve does not give a distinct buckling load, $P_{cr,e}$ was established using the Southwell plots method. This plotting technique was originally proposed by Southwell (1932) to predict the critical buckling load of column by plotting v/P against lateral deflection v. The inverse slope of the straight line given by this plot is the critical load, while the intercept on abscissa axis is for the initial lateral geometric imperfection. One may argue that the situation is more complicated as LTB failure involves twist rotation and lateral deflection at the same time whilst an axially loaded column only undergoes lateral deflection.

It is generally accepted (Dumont and Hill, 1940, Cheng and Yura, 1988, Attard, 1983, Mandal and Calladine, 2002) that a simple plot of either v/P vs. v or ϕ/P vs. ϕ can accurately predict the critical load for LTB failure. For this investigation, the determination approach with ϕ/P vs. ϕ is adopted.
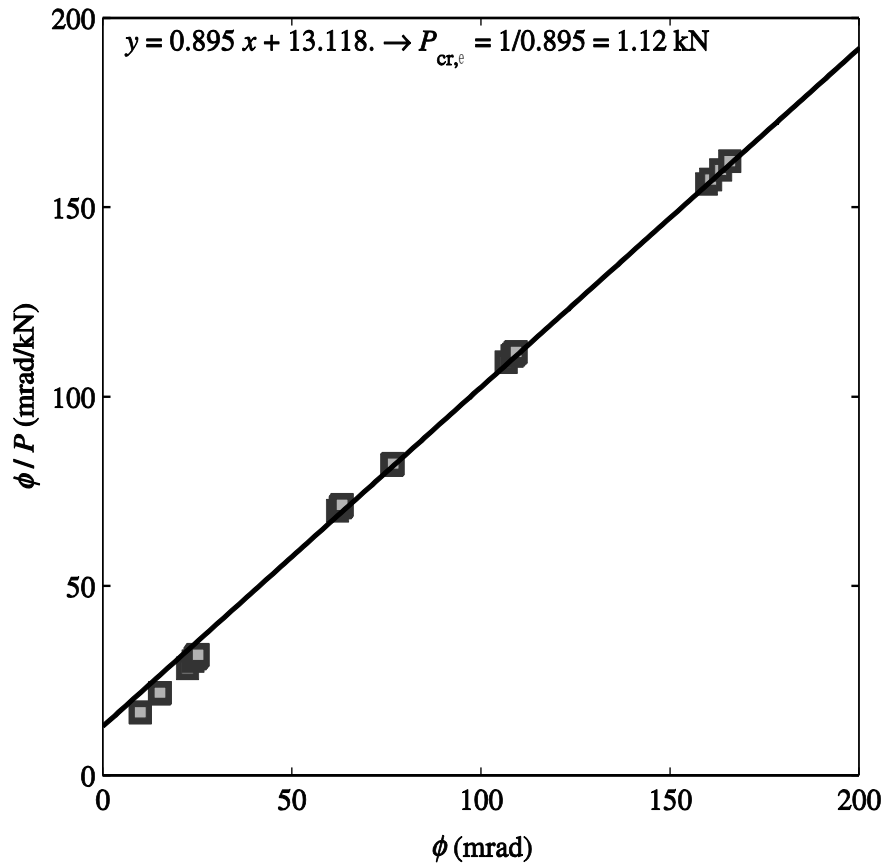
Figure 4.20 Southwell plot with test data from C2_4064_EC2_SC

Figure 4.20 shows the Southwell plot generated in Matlab® (Mathworks Inc, 2013) using the test results from C2-4064_EC2_SC. The data points give a virtually straight line fit with R^2 equal to 0.998. An estimation for the elastic critical buckling load at 1.12 kN is given by the gradient to the straight line fit. It is worth mentioning $P_{cr,e}$ on Figure 4.20 is on the lower side because it does not include, at 0.12 kN, the self-weight of the loading disc system. Load cell only measures the applied load P discounting the

self-weight of the loading system which is already applied on the specimens. Plots for all LTB tests are presented in Appendix B2.

4.7. Theoretical predictions

From the literature review in Chapter 2 a closed-form equation (Eq. (2.1)) is found to has been widely adopted in structural steel design for the LTB mode of failure. The review was further used to show that such an isotropic expression can, with suitable choice substitute choice of moduli of elasticity, be used with orthotropic PFRP beams. A comparison between the test $P_{cr,e}$ and Eq. (2.1) is presented in Nguyen *et al.* (2014). The input moduli of elasticity of $E_L = 23\,\text{GPa}$ and $G_{LT} = 3\,\text{GPa}$ are the design values in the Fiberline Design Manual (Anon., 2014a). It is found from Figures 14 and 15 in Nguyen *et al.* (2014) that the test results are all significantly higher. This is important to know as it strongly suggests that by choosing the pultruder's tabulated values for E_L and G_{LT} a closed-form formula is likely to give a LTB design resistance that is on the safe side. Presented herein is the same comparison with actual moduli of elasticity reported in Chapter 3.

To adopt Eq. (2.1) to determine LTB resistances the two factors C_1 and C_2, whose value depends on the displacement boundary conditions, are needed. For the study in this chapter the two displacement boundary conditions are defined by $k = k_w = 1.0$ for EC1, and $k = 0.5$ and $k_w = 1.0$ for EC2. It is found that three references (Clark and Hill, 1960, BSI, 1992, Bureau, 2006) give slightly different C_1 and C_2 values for steel. For isotropic beam with EC1 they are 1.365 and 0.553 from Clark and Hill (1960) and DD ENV 1993-1-1 (BSI, 1992). In a Non-Contradictary Complementary Information

(NCCI) sheet from Access Steel (Bureau, 2006) they are 1.348 and 0.630. These differences are due to developments in computational analysis that generated these numerical factors in the 1960s and later in the 1990s. The factors obtained most recently ($C_1 = 1.348$ and $C_2 = 0.630$) will be used for EC1 as they are expected to be more reliable. For the EC2 case only the older factors are found in the public domain (BSI, 1992) and they are $C_1 = 1.07$ and $C_2 = 0.432$. Both sources Clark and Hill (1960) and Bureau (2006) do not provide the C factors for the EC2.

For EC1, the critical elastic LTB load (P_{cr}) is to be given by:

$$P_{cr} = \frac{5.39\pi^2 E_L I_z}{L^3} \left(\sqrt{\frac{I_w}{I_z} + \frac{L^2 G_{LT} I_t}{\pi^2 E_L I_z} + 0.40 z_g^2} - 0.63 z_g \right) \tag{4.3}$$

For EC2 , P_{cr} can be determined as:

$$P_{cr} = \frac{8.56\pi^2 E_L I_z}{L^3} \left(\sqrt{\frac{I_w}{I_z} + \frac{L^2 G_{LT} I_t}{\pi^2 E_L I_z} + 0.75 z_g^2} - 0.86 z_g \right) \tag{4.4}$$

Because the measured dimensions of test specimens presented in Table 4.1 of Section 4.3 do not differ significant from the nominal values the latter were used to calculate the geometric properties of I_z, I_t, I_w and z_g in Eqs. (4.3) and (4.4).

Given that the web and flange thickness is the same $(t_f = t_w = t)$, I_z can be calculated from:

$$I_z = \frac{1}{6} t b_f^3 + \frac{1}{12}(h - 2t) t^3 \tag{4.5}$$

To calculate I_z for a C-section, the horizontal position of the section centroid needs to be determined. The horizontal distance to the centroid from the outer surface on the web is determined from:

$$X_0 = \frac{b_f^2 t + (h - 2t)t^2 / 2}{2b_f t + (h - 2t)t} \tag{4.6}$$

I_z can be expressed as:

$$I_z = \frac{1}{6}tb_f^2 + 2tb_f\left(\frac{b_f}{2} - X_0\right)^2 + \frac{1}{12}(h - 2t)t^3 + (h - 2t)t\left(\frac{t}{2} - X_0\right)^2 \tag{4.7}$$

I_w for an I-section is given by (Young and Budynas, 2002, Pilkey, 2005):

$$I_w = \frac{1}{24}b_f^3 h_w^2 t \tag{4.8}$$

For C-section it is (Young and Budynas, 2002, Pilkey, 2005):

$$I_w = \left(\frac{b_1^3 h_w^2 t}{12}\right)\left(\frac{2h_w + 3b_1}{h_w + 6b_1}\right) \tag{4.9}$$

where $h_w = h - t$ and $b_1 = b_f - \dfrac{t}{2}$ as shown in Figure 4.5 for both I- and channel sections.

I_t for I-section can be simply approximated without accounting for the fillet radius areas between web-flange junction by (Young and Budynas, 2002, Pilkey, 2005):

$$I_t = \frac{t^3}{3}(2b_f + h_w) = \frac{t^3}{3}(2b_f + h - t) \tag{4.10}$$

For C-section (Young and Budynas, 2002, Pilkey, 2005) it is:

$$I_t = \frac{t^3}{3}(2b_1 + h_w) = \frac{t^3}{3}(2b_f + h - 2t) \tag{4.11}$$

113

Eqs. (4.5)-(4.11) are broadly employed in structural design because of their simplicity and the lower values (compared to those account for fillet radius areas) obtained provide design that is on the safe side. Table 4.3 presents in columns (2-4) I_z, I_t and I_w calculated by these simplified expressions. Values are given to three significant figures.

Table 4.3 Section properties for I- and C-sections, ignored the fillet radius areas

Section name	I_z (mm^4)	I_t (mm^4)	I_w (mm^6)
(1)	(2)	(3)	(4)
I	2.18×10^5	1.68×10^4	7.02×10^8
C1	2.78×10^5	1.50×10^4	6.29×10^8
C2	2.63×10^5	1.35×10^4	4.01×10^8
C3	5.94×10^4	1.07×10^4	9.14×10^7

When the fillet radius areas are taken into account when calculating the section propreties, only I_t will change significantly. Young and Budynas (2002) and Pilkey (2005) provide different expressions to determine the new I_t. For I-section, Young and Budynas (2002) suggests that:

$$I_t = \frac{t^3}{3}\left(2b_f + h - 2t\right) - 0.420t^4\left(1 - \frac{t^4}{12b_f^4}\right) + 2\alpha D^4 \tag{4.12}$$

where:
$$\alpha_c = 0.15 + 0.1\frac{r_c}{t} \tag{4.13}$$

$$D_c = \frac{\left(t + r_c\right)^2 + r_c t + t^2/4}{\left(2r_c + t\right)} \tag{4.14}$$

D_c is the diameter of the largest inscribed circle and r_c is the fillet radius.

For a C-section I_t is (Young and Budynas, 2002):

114

$$I_t = \frac{t^3}{3}\left(2b_f + h - 2t\right) - 0.630t^4\left(2 - \frac{t^4}{12b_f^4} - \frac{t^4}{12(h-2t)^4}\right) + 2\alpha_c D^4 \qquad (4.15)$$

where:
$$\alpha_c = 0.07 + 0.076\frac{r_c}{t} \qquad (4.16)$$

$$D_c = 2\left[2t + 3r_c - \sqrt{2}\left(2r_c + t\right)\right] \qquad (4.17)$$

Pilkey (2005) gives the same expression for both I- and C-section. It is:

$$I_t = \frac{t^3}{3}\left(2b + h - 2t\right) - 0.420t^4 + 2\alpha_c D^4 \qquad (4.18)$$

where D_c is calculated as in Eq. (4.14) for I-section and as in Eq. (4.17) for C-section.

The correction factor α_c in Eq. (4.18) for I-section is (Pilkey, 2005) :

$$\alpha_c = 0.1180 - 0.0087\left(\frac{r_c}{t}\right) + 0.1029\left(\frac{r_c}{t}\right)^2 - 0.0533\left(\frac{r_c}{t}\right)^3 \qquad (4.19)$$

For C-section α_c is calculated by:

$$\alpha_c = 0.0789 + 0.0510\left(\frac{r_c}{t}\right) - 0.0263\left(\frac{r_c}{t}\right)^2 + 0.0191\left(\frac{r_c}{t}\right)^3 \qquad (4.20)$$

The difference on how α_c is approximated in Young and Budynas (2002) and Pilkey (2005) give I_t that differs significantly for the I-section. To show the effectiveness of those expressions, advanced section calculator software ShapeDesigner was employed (MechaTools Technologies Inc, 2013). This software allows a section's I_z, I_w and I_t to be calculated using advanced FE approach without any assumptions or restrictions. The software can be found at http://www.mechatools.com/en/shapedesigner.html.

Table 4.4 Section properties for I- and C-sections, accounted for the fillet radius areas

Section name	I_z (mm^4)	I_w (mm^6)	I_t (mm^4)		
			ShapeDesigner (2013)	Young and Budynas (2002)	Pilkey (2005)
(1)	(2)	(3)	(4)	(5)	(6)
I	2.19×10^5	6.83×10^8	2.15×10^4	2.47×10^4	2.10×10^4
C1	2.79×10^5	6.35×10^8	1.72×10^4	1.73×10^4	1.71×10^4
C2	2.63×10^5	4.08×10^8	1.45×10^4	1.43×10^4	1.43×10^4
C3	5.94×10^4	9.27×10^7	1.16×10^4	1.14×10^4	1.14×10^4

Table 4.4 summarizes in columns (2-4) I_z, I_w and I_t obtained by ShapeDesigner software. Columns (5) and (6) give the calculation of I_t using expressions by Young and Budynas (2002) and formulae by Pilkey (2005), respectively. It is found that the calculations from ShapeDesigner (MechaTools Technologies Inc, 2013) and Pilkey (2005) gave relatively similar I_t for all four sections. For the I-section, I_t using the Young and Budynas (2002) expression is 15% higher. By comparing data in columns (2-4) of Table 4.3 with equivalents in Table 4.4 it can be seen that the contribution of the fillet radius areas to I_z and I_w are insignificant. It is only <0.2% for I_z and < 2.7% for I_w. For I_t this contribution is significant at 7.4% to 28.0%.

By substituting the values from columns (2-4) in Tables 4.3 and 4.4 into Eqs. (4.3) and (4.4), the LTB resistances for both sets of geometric properties can be determined. Those predictions obtained using data in Table 4.3 are denoted as $P_{cr,1}$ and those with Table 4.4 data are $P_{cr,2}$. The plots for $P_{cr,2} / P_{cr,1}$ vs. beam span L presented in Figures 4.21(a) to (d) show the sensitivity of changing in geometric parameters. In the figures, the predictions for EC1 are presented by circular symbol whilst those for EC2 are illustrated by rectangular shape.
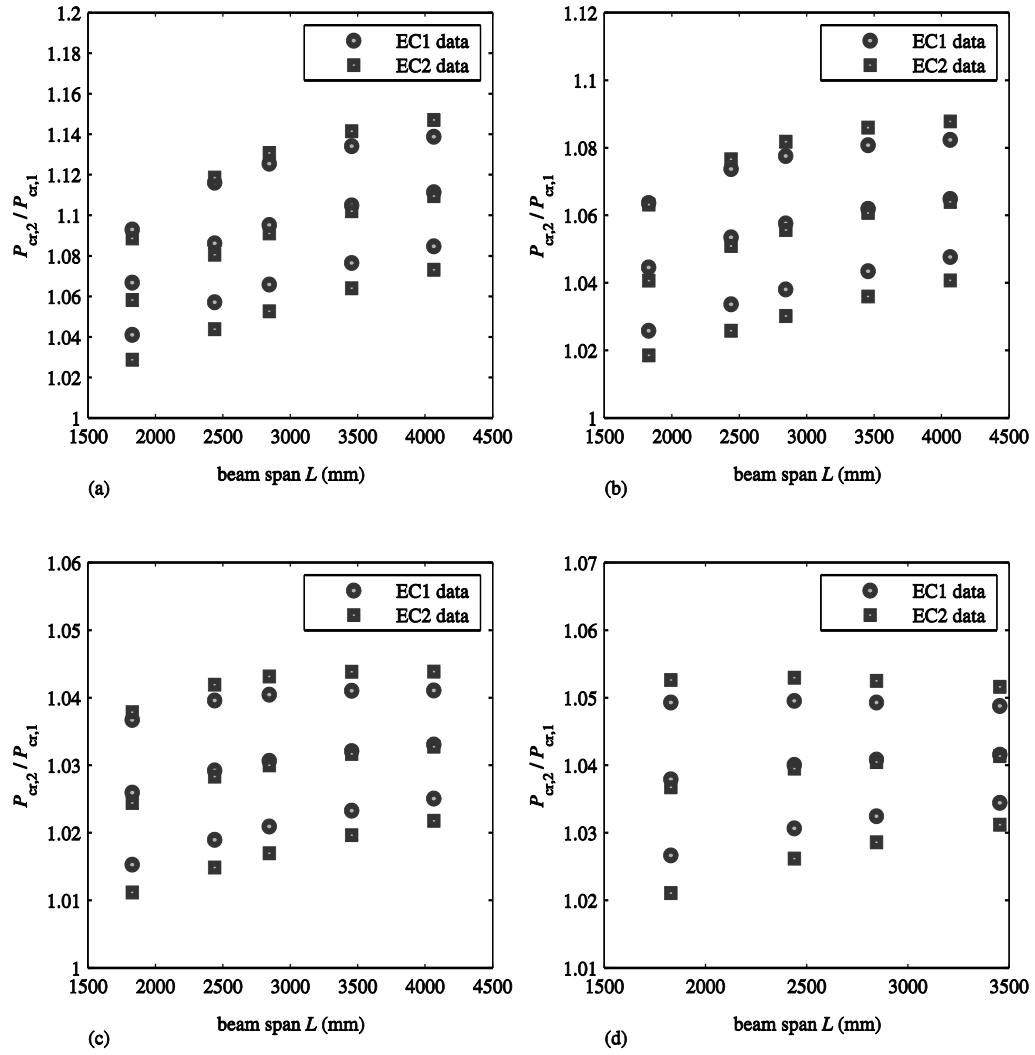
Figure 4.21 Sensitivity of P_{cr} with I_t for: (a) I; (b) C1; (c) C2; (d) C3

It is found that the predicted resistances increase significantly for I and C1 when the fillet radius areas are accounted for. The increase with I-section is 4-14% for EC1 and 3-15% for EC2. For C1, they are 3-8% and 2-9%. With C2 and C3, the differences are lower, at 2-4% and 1-4% for C2 and 1-5% and 1-5% for C3. In the following sections I_z, I_t and I_w given in columns (2-4) of Table 4.4, obtained by ShapdeDesigner software, is adopted when determine the LTB resistance by closed-form equations.

4.8. Test results and discussion

Presented in Table 4.5 are the results from 57 specimens with displacement boundary conditions EC1, whilst Table 4.6 collated those 57 tested with EC2. Each buckling resistance $(P_{cr,e})$ was determined either from the 'peak' load or Southwell plot method. A peak load result is acknowledged by adding the identifier '(B)' (for Bifurcation) on the right-side of the test result. Column (1) gives the labels for the 19 beam configurations whose geometries are given in Table 4.1. The results for this group of 19 specimens having the same end and load height conditions are reported in the same columns. It is column (2) for TF loading and columns (5) and (8) for SC and BF loadings.

The theoretical LTB resistances (P_{cr}) are predicted using Eqs. (4.3) and (4.4) with input geometric properties, that accounted for the fillet radius areas, taken from columns (2-4) of Table 4.4. The measured elastic constants E_L and G_{LT} used in the predictions are taken from Table 3.14. For the group with load applied on TF they are presented in columns (2-4), for SC loading they are in columns (5-7) and for BF loading, columns (8-10) are used. Columns (3), (6) and (9) present the theoretical P_{cr}. The ratio of $P_{cr,e} / P_{cr}$ are reported in columns (4), (7) and (10), respectively.

4.8.1. I beam test results

From the buckling loads for the I-section with EC1 reported in rows (1-5) of Table 4.5, it is found that $P_{cr,e}$s are all higher than P_{cr}s, with $P_{cr,e} / P_{cr}$ from 1.07 to 1.21 for TF, 1.06 to 1.19 for SC and 1.02 to 1.17 for BF. The equivalent results presented in Table 4.6 for EC2 the ranges are 1.00 to 1.18, 0.94 to 1.01 and 0.79 to 0.89 for TF, SC and BF loading, respectively.

Table 4.5 Buckling results for beams with EC1 and vertical load applied at Top Flange (TF), Shear Centre (SC) and Bottom Flange (BF)

Beam specimen	Load applied on top flange (EC1_TF)			Load applied at shear centre (EC1_SC)			Load applied on bottom flange (EC1_BF)		
	Experimental buckling load $P_{cr,e}$ (kN)	Theoretical buckling load P_{cr} (kN) (Eq. (4.3))	$\dfrac{P_{cr,e}}{P_{cr}}$	Experimental buckling load $P_{cr,e}$ (kN)	Theoretical buckling load P_{cr} (kN) (Eq. (4.3))	$\dfrac{P_{cr,e}}{P_{cr}}$	Experimental buckling load $P_{cr,e}$ (kN)	Theoretical buckling load P_{cr} (kN) (Eq. (4.3))	$\dfrac{P_{cr,e}}{P_{cr}}$
(1)	(2)	(3)	(4)	(5)	(6)	(7)	(8)	(9)	(10)
I-4064	0.72	0.67	1.07	0.90	0.85	1.06	1.11	1.08	1.03
I-3454	1.08	0.92	1.17	1.29	1.21	1.07	1.61	1.58	1.02
I-2844	1.64	1.35	1.21	2.09	1.85	1.13	2.59	2.53	1.02
I-2438	2.07	1.84	1.13	2.90	2.61	1.11	3.94	3.71	1.06
I-1828	3.79 (B)	3.37	1.12	6.12 (B)	5.13	1.19	9.12 (B)	7.80	1.17
C1-4064	0.65 (B)	0.71	0.92	0.8 (B)	0.94	0.85	1.11	1.24	0.90
C1-3454	1.12	0.97	1.15	1.49 (B)	1.33	1.12	1.76 (B)	1.83	0.96
C1-2844	1.45	1.40	1.04	1.96	2.03	0.97	2.65	2.95	0.90
C1-2438	1.82	1.91	0.95	3.03	2.88	1.05	4.23	4.35	0.97
C1-1828	3.31	3.47	0.95	5.54	5.67	0.98	7.57	9.27	0.82
C2-4064	0.64	0.65	0.98	0.81 (B)	0.84	0.96	1.1	1.08	1.02
C2-3454	0.97	0.89	1.09	1.34 (B)	1.19	1.13	1.59 (B)	1.59	1.00
C2-2844	1.29	1.28	1.01	1.6	1.81	0.88	2.67	2.54	1.05
C2-2438	1.87	1.73	1.08	2.66	2.54	1.05	4.12	3.73	1.10
C2-1828	4.03	3.10	1.30	5.85 (B)	4.93	1.19	7.32	7.85	0.93
C3-3454	0.38	0.36	1.06	0.44	0.42	1.05	0.47	0.50	0.94
C3-2844	0.60 (B)	0.52	1.15	0.62	0.63	0.98	0.94 (B)	0.77	1.22
C3-2438	0.78	0.69	1.13	0.88	0.87	1.01	1.07	1.09	0.98
C3-1828	1.12	1.18	0.95	1.47	1.59	0.92	1.92	2.14	0.90

Table 4.6 Buckling results for beams with EC2 and vertical load applied at Top Flange (TF), Shear Centre (SC) and Bottom Flange (BF)

Beam specimen	Load applied on Top flange (EC2_TF)			Load applied at shear centre ((EC2_SC)			Load applied on bottom flange (EC2_BF)		
	Experimental buckling load $P_{cr,e}$ (kN)	Theoretical buckling load P_{cr} (kN) (Eq. (4.4))	$\dfrac{P_{cr,e}}{P_{cr}}$	Experimental buckling load $P_{cr,e}$ (kN)	Theoretical buckling load P_{cr} (kN) (Eq. (4.4))	$\dfrac{P_{cr,e}}{P_{cr}}$	Experimental buckling load $P_{cr,e}$ (kN)	Theoretical buckling load P_{cr} (kN) (Eq. (4.4))	$\dfrac{P_{cr,e}}{P_{cr}}$
(1)	(2)	(3)	(4)	(5)	(6)	(7)	(8)	(9)	(10)
I-4064	1.03	1.03	1.00	1.34	1.43	0.94	1.68	2.00	0.84
I-3454	1.47	1.40	1.05	2.01	2.06	0.98	2.63	3.02	0.87
I-2844	2.1	2.06	1.02	3.24	3.22	1.01	4.48	5.03	0.89
I-2438	3.33	2.82	1.18	4.53	4.65	0.97	6.04	7.66	0.79
I-1828	6.29 (B)	5.31	1.18	NO LTB	9.65	-	NO LTB	17.5	-
C1-4064	1.01 (B)	1.06	0.95	1.26	1.58	0.80	1.59 (B)	2.34	0.68
C1-3454	1.46 (B)	1.44	1.01	2.01 (B)	2.26	0.89	NO LTB	3.56	-
C1-2844	1.87	2.10	0.89	3.49 (B)	3.54	0.99	4.29	5.99	0.72
C1-2438	3.28 (B)	2.86	1.15	4.92	5.13	0.96	7.32	9.20	0.80
C1-1828	5.02	5.34	0.94	8.44	10.7	0.79	12.7	21.4	0.59
C2-4064	0.8 (B)	0.94	0.85	1.24	1.37	0.91	1.68	1.98	0.85
C2-3454	1.22	1.28	0.95	1.91 (B)	1.96	0.97	2.37 (B)	3.00	0.79
C2-2844	1.81	1.84	0.98	2.37	3.04	0.78	3.71	5.03	0.74
C2-2438	2.62	2.50	1.05	3.83	4.38	0.87	4.95(B)	7.68	0.64
C2-1828	5.47	4.59	1.19	NO LTB	9.00	-	NO LTB	17.7	-
C3-3454	0.52	0.56	0.93	0.66	0.71	0.93	0.8	0.91	0.88
C3-2844	0.8 (B)	0.81	0.99	1.02	1.08	0.94	1.35 (B)	1.45	0.93
C3-2438	1.12	1.08	1.04	1.38 (B)	1.51	0.91	2.22 (B)	2.12	1.05
C3-1828	1.9	1.87	1.02	2.66	2.89	0.92	3.72	4.49	0.83

Test results and closed-form predictions were plotted with the abscissa axis takes the non-dimensional buckling load $y = P_{cr}L_b L / \sqrt{E_L I_z G_{LT} I_t}$ and the ordinate axis uses the non-dimensional beam parameter $x = \sqrt{\pi^2 E_L I_w / (G_{LT} I_t L_b^2)}$. Variables y and x will be used for a curve fitting evaluation. It is noted that the non-dimensional form in the plotting (i.e. y vs. x) for a theoretical prediction by Eqs. (4.3) and (4.4) is independent of the beam's E_L and G_{LT}.

The analytical predictions are plotted as continuous curves. The solid line curve is for TF loading, whilst the dashed line and dash-dot line curves are for SC and BF loading, respectively. The measured $P_{cr,e}$s are plotted with an open circle; open rectangular; open triangle symbols for TF, SC and BF loading cases.
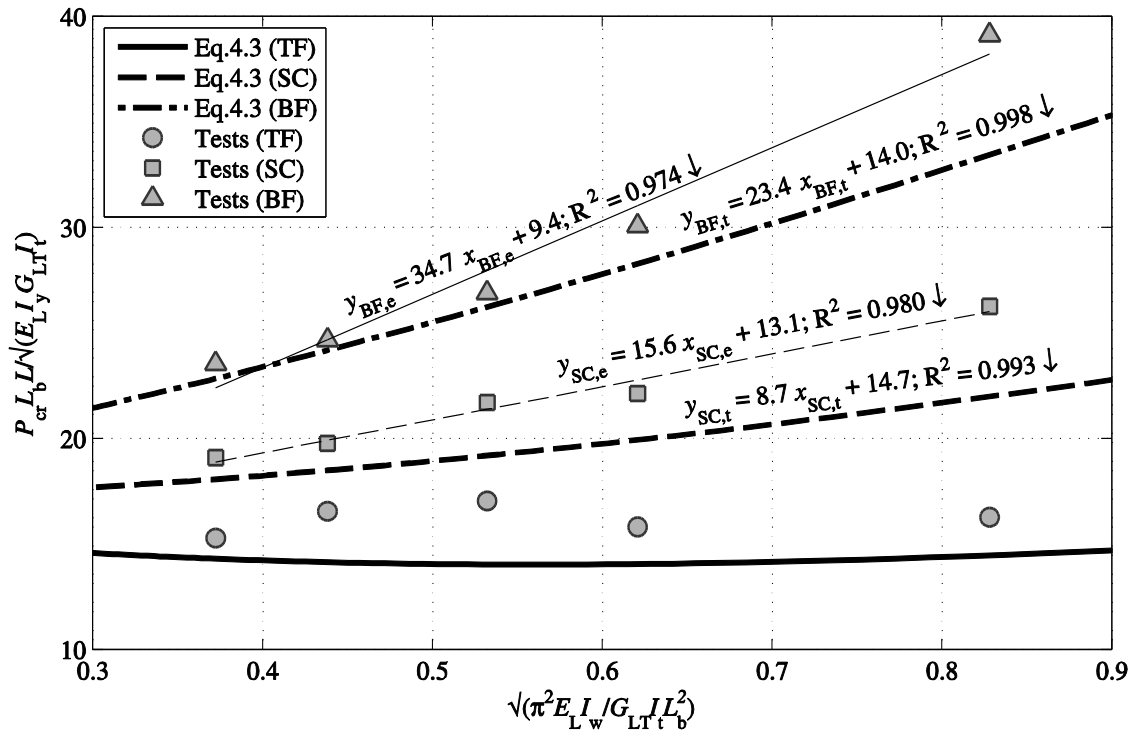
Figure 4.22 Plots for I-section with EC1 at three load heights for TF, SC and BF
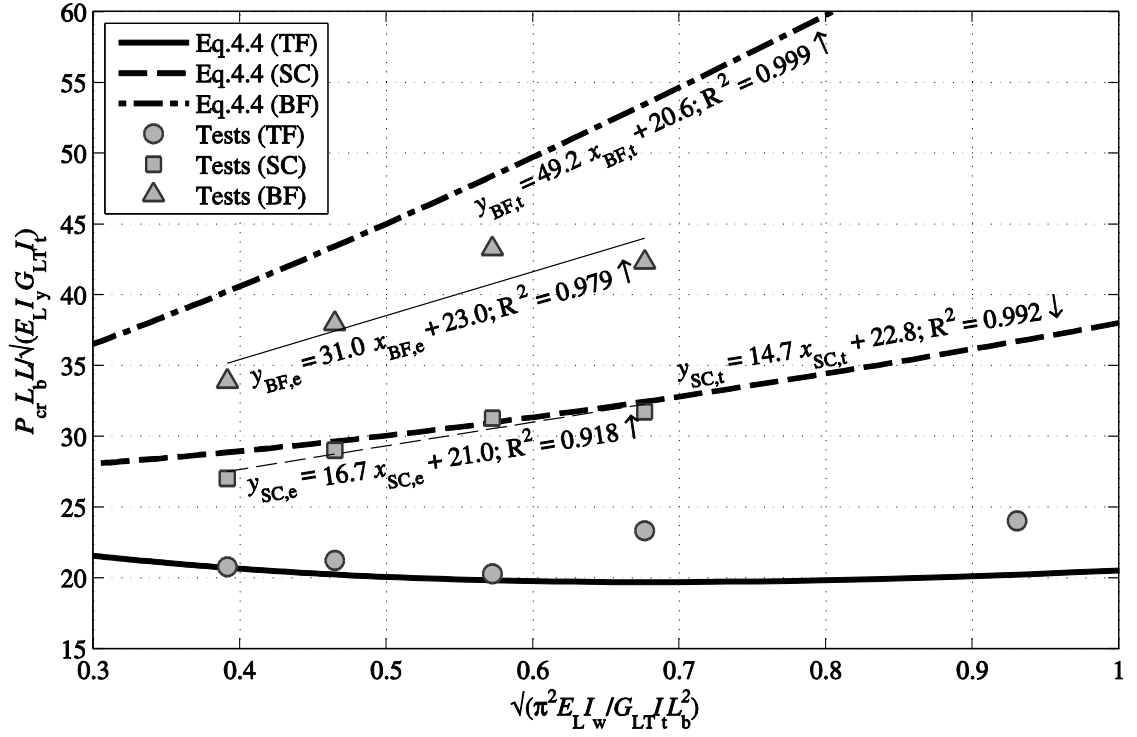
Figure 4.23 Plots for I-section with EC2 at three load heights for TF, SC and BF

Figures 4.22 and 4.23 present the curves for EC1 and EC2, respectively. Linear fitting was implemented on theoretical and experimental results for BF and SC loading and with EC1 and EC2. The linear expressions and best-fit lines are presented in the figures. In the expressions, the subscript 'e' is for 'experimental' and 't' is for 'theoretical'.

It is found R^2 is >0.99 for all theoretical cases to indicate that the theoretical trends over the tested span range offer a linear relationship. Because R^2 for the test results lie in the range of 0.92 to 0.98 they also show the linear trend. This finding strongly advocates that the I beams testing was properly conducted, and that the form of the closed-form expressions Eqs. (4.3) and (4.4) is suitable for PFRP material.

It is well-known (Allen and Bulson, 1980) that for a simply supported ($k = k_w = 1$) thin-walled member whose warping rigidity (I_w) is negligible, such as in narrow

rectangular sections, the LTB resistance can be approximated by $P_{cr} = \dfrac{16.9}{L^2}\sqrt{E_L I_z G_{LT} I_t}$.

This form of expression can be obtained directly from Eqs. (4.3) or (4.4) by ignoring the term for I_w (i.e. assuming that $I_w = 0$) and load height z_g (i.e. $z_g = 0$). By neglecting I_w, the predicted curve for EC1 in Figure 4.22 would become a constant line for $y = 16.9$ and the curve for EC2 in Figure 4.23 becomes $y = 26.7$. This implies that the gradient m is mainly capturing the resistance contribution from warping rigidity. It can be seen that the gradients m of 8.7 and 15.6 for SC_EC1; 23.4 and 34.7 for BF_EC1; 14.7 and 16.7 for SC_EC2; 31.0 and 49.2 for BF_EC2 are different. This indicates that the warping contribution to the LTB resistance is different in how the beams were tested and in how the analytical predictions have been obtained.

Trumpf (2006) discovered that warping in his test series were either fully ($k_w = 1$) or partly restrained ($0.5 < k_w < 1$) and could not be 'free' ($k_w = 1$), as assumed in theoretical treatment. Lindner (1996) found that 'free' warping with steel could not be achieved in practice since it is partly restrained by the end plates in a beam-column connection. The level of restraint depends mainly on the thickness of the end plate. He took into account this influence by modifying the warping restraint factor k_w to be a function of span length L and a warping spring c_w. The expression is:

$$k_w = \sqrt{1 - \frac{0.5}{1 + \dfrac{2EI_w}{c_w L}}} \tag{4.21}$$

In Eq. (4.21) $c_w = Gt^3 b(h-t)/3$ with b and h is the width and depth of the end plate.

Eq. (4.21) shows that the influence of warping restraint will be more significant at shorter span. This is observed in Figure 4.22 where the differences between test results and predicted values are higher for x tending towards 0.8.
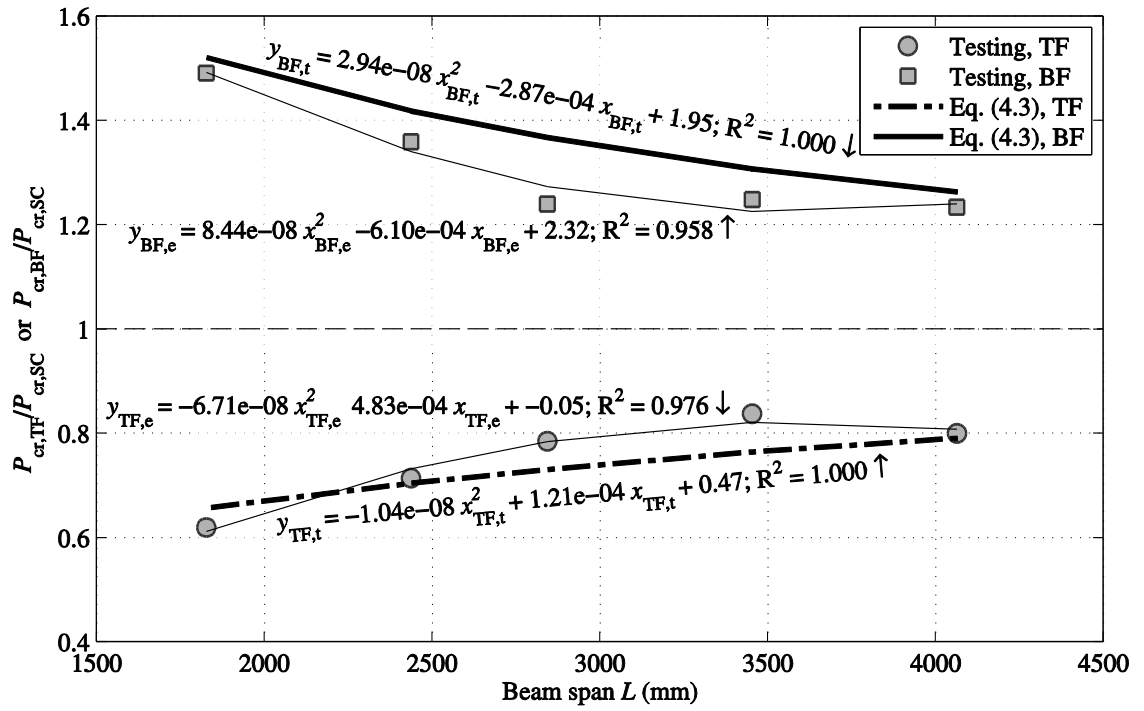
Figure 4.24 Effect of vertical load height for I beams with EC1

$y_{BF,t} = 2.94\text{e--}08\ x^2_{BF,t} - 2.87\text{e--}04\ x_{BF,t} + 1.95;\ R^2 = 1.000 \downarrow$

$y_{BF,e} = 8.44\text{e--}08\ x^2_{BF,e} - 6.10\text{e--}04\ x_{BF,e} + 2.32;\ R^2 = 0.958 \uparrow$

$y_{TF,e} = -6.71\text{e--}08\ x^2_{TF,e}\ 4.83\text{e--}04\ x_{TF,e} + -0.05;\ R^2 = 0.976 \downarrow$

$y_{TF,t} = -1.04\text{e--}08\ x^2_{TF,t} + 1.21\text{e--}04\ x_{TF,t} + 0.47;\ R^2 = 1.000 \uparrow$
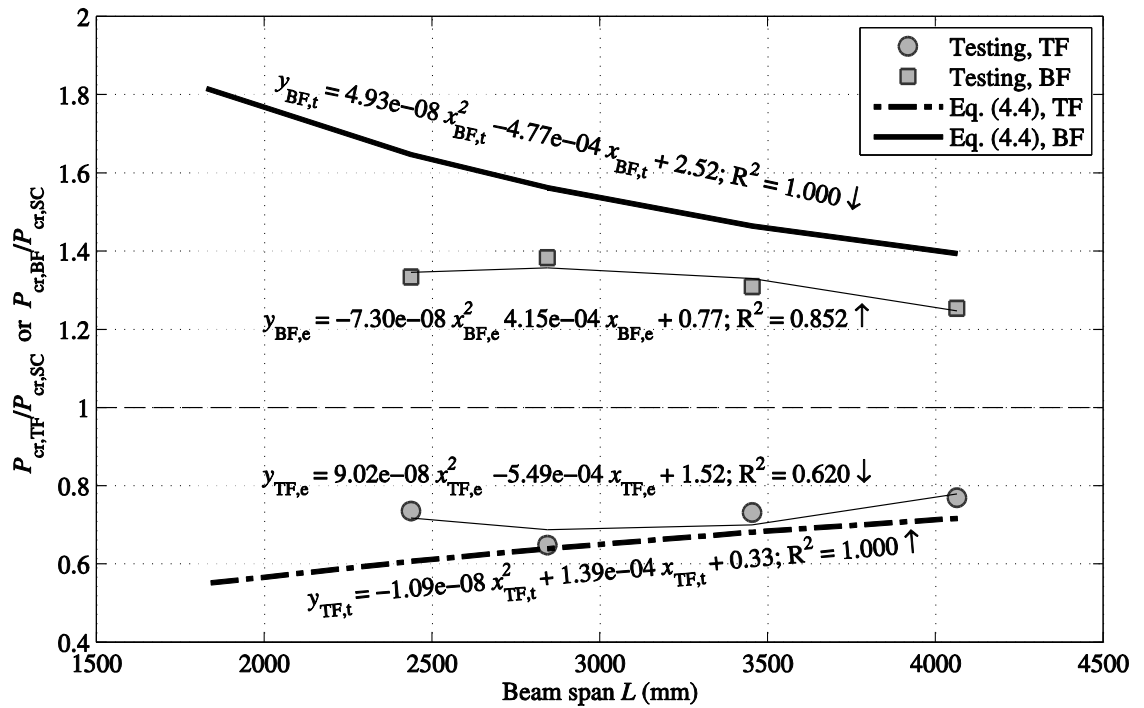
Figure 4.25 Effect of vertical load height for I beams with EC2

$y_{BF,t} = 4.93\text{e--}08\ x^2_{BF,t} - 4.77\text{e--}04\ x_{BF,t} + 2.52;\ R^2 = 1.000 \downarrow$

$y_{BF,e} = -7.30\text{e--}08\ x^2_{BF,e}\ 4.15\text{e--}04\ x_{BF,e} + 0.77;\ R^2 = 0.852 \uparrow$

$y_{TF,e} = 9.02\text{e--}08\ x^2_{TF,e} - 5.49\text{e--}04\ x_{TF,e} + 1.52;\ R^2 = 0.620 \downarrow$

$y_{TF,t} = -1.09\text{e--}08\ x^2_{TF,t} + 1.39\text{e--}04\ x_{TF,t} + 0.33;\ R^2 = 1.000 \uparrow$

By examining $P_{cr,e}$ in columns (2, 5 and 8) of in Tables 4.5 and 4.6, the influence of changing vertical load height (z_g) is observed. For an example, beam I-4064 from Table 4.5 (for EC1) has $P_{cr,e}$s of 0.72 kN, 0.90 kN and 1.11 kN for TF, SC and BF loading, respectively. As known from theory (Clark and Hill, 1960, Trahair, 1993), LTB resistance increases when load position moves downwards from top to bottom flange.

To further show the performance of test rig with the change in z_g, the ratio of $P_{cr,TF} / P_{cr,SC}$ and $P_{cr,BF} / P_{cr,SC}$ was plotted against the beam span L in Figure 4.24 for EC1 and Figure 4.25 for EC2. The notation $P_{cr,TF}$, $P_{cr,SC}$ and $P_{cr,BF}$ is for LTB load (obtained from either Eqs. (4.3) and (4.4) or testing) for TF, SC and BE loading, respectively. In the figures, the test results for TF use the circular symbol whilst those for BF adopt the rectangular symbol. The TF curve generated from Eq. (4.3) or Eq. (4.4) is presented with dash-dot line and BF curve is shown by solid line. Each group of five (or four) data points was fitted to a second degree polynomial curve.

It is found from Figure 4.24 that R^2 for TF curves is 1.000 for Eq. (4.3) and 0.958 from test results. For BF the curves they are 1.000 and 0.976. This indicates that the quadratic function can be employed to fit either theoretical or experimental data results. For EC2 in Figure 4.25, the 2nd degree polynomial equation is found not fit to the test results as $R^2 = 0.620$ and 0.852 for TF and BF, respectively. It is discovered that the test data points (especially with BF loading) are now closer to the straight line $y = 1$ than by the predicted curves. This means the effect of load height, with BF_EC2 in testing, is less significant. This may be due to the effectiveness of EC2 to prevent minor axis rotation (i.e. $k = 0.5$) that is believed to be reducing as the load height changes from top to bottom flange. A plausible explanation for this observation is that, as more load is

applied, the four steel rods become increasingly less effective in preventing the development of minor axis rotation.

As illustrated in Figures 4.6 and 4.8 of sub-section 4.2.2, two vertical steel rods at the beam's ends allow free lateral deflection. The positions of these rods were adjusted such that the beam fitted precisely between them. During this set-up process, it was likely that there were horizontal forces, pushing on both sides, of the beam. Such contact will create frictional forces that might have provided a degree of restraint against 'free' minor axis rotation. If rotation were, indeed, partly restrained, the 'apparent' buckling load $P_{cr,e}$ would have increased. This is one possible explanation why the two TF test results of I-2844 and I-3454 (and others) are significantly higher than the predicted values.

The comparison does show that tests with the I-section were properly conducted and the form of Eq. (2.1) is also suitable to predict the LTB resistance for PFRP beam. The loading fixture was able to execute different vertical loading positions. The testing has been found to represent the two displacement boundary conditions EC1 and EC2. However, the level of end restraint is found to be somewhere between fully 'free' and fully restrained. The warping effect at both ends is also found to have a significant effect. The form of end fixture employed could not provide the desired fully-free warping condition. There is always a degree of warping restraint that comes to light when comparing the linear trends using the predicted and test buckling loads.

4.8.2. Channel beam test results
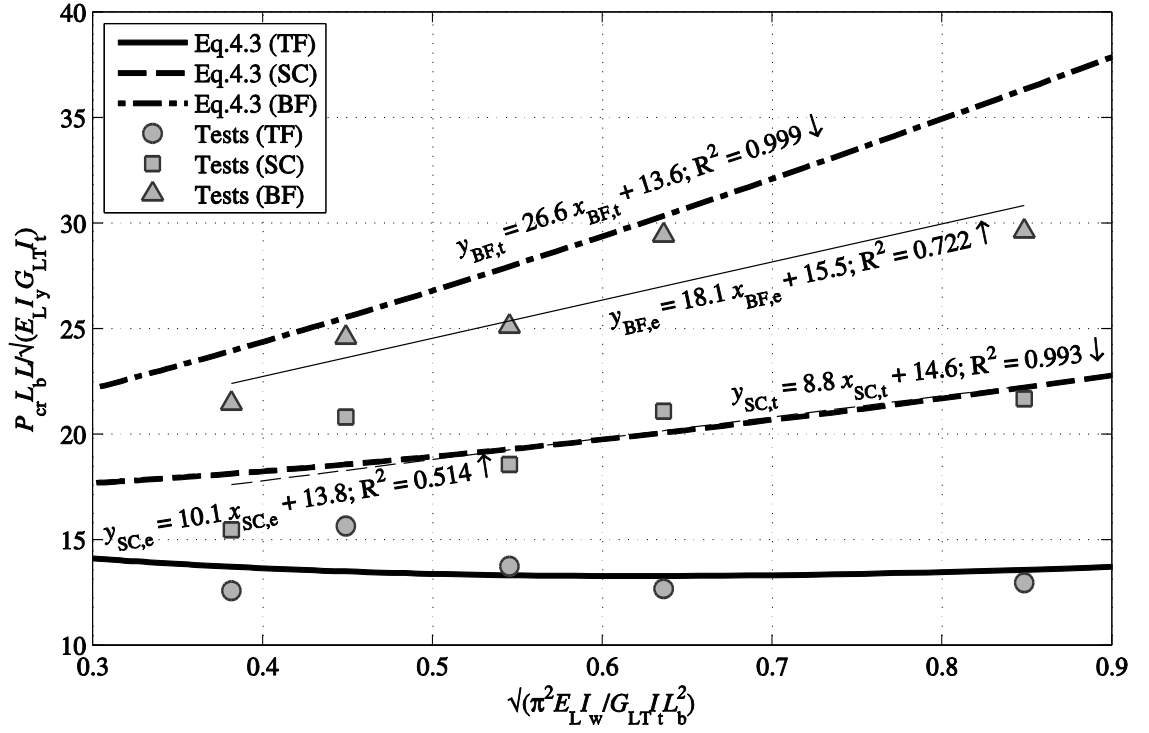
Figure 4.26 Plots for C1-section with EC1 at three load heights for TF, SC and BF
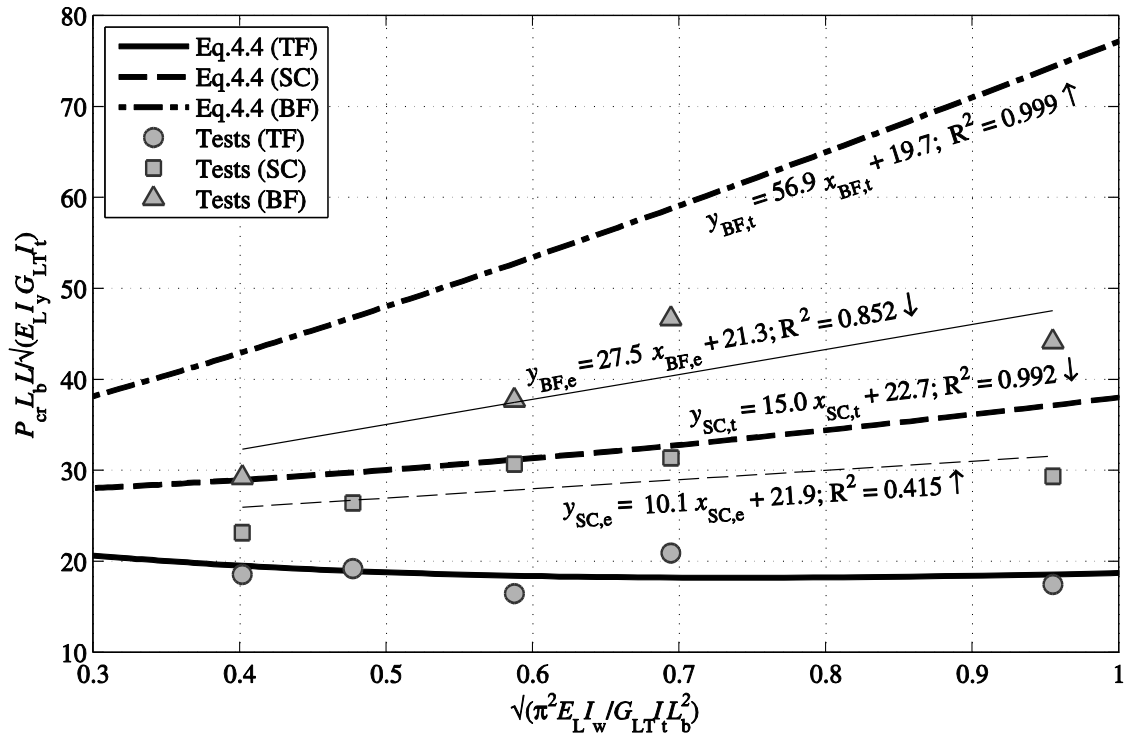
Figure 4.27 Plots for C1-section with EC2 at three load heights for TF, SC and BF
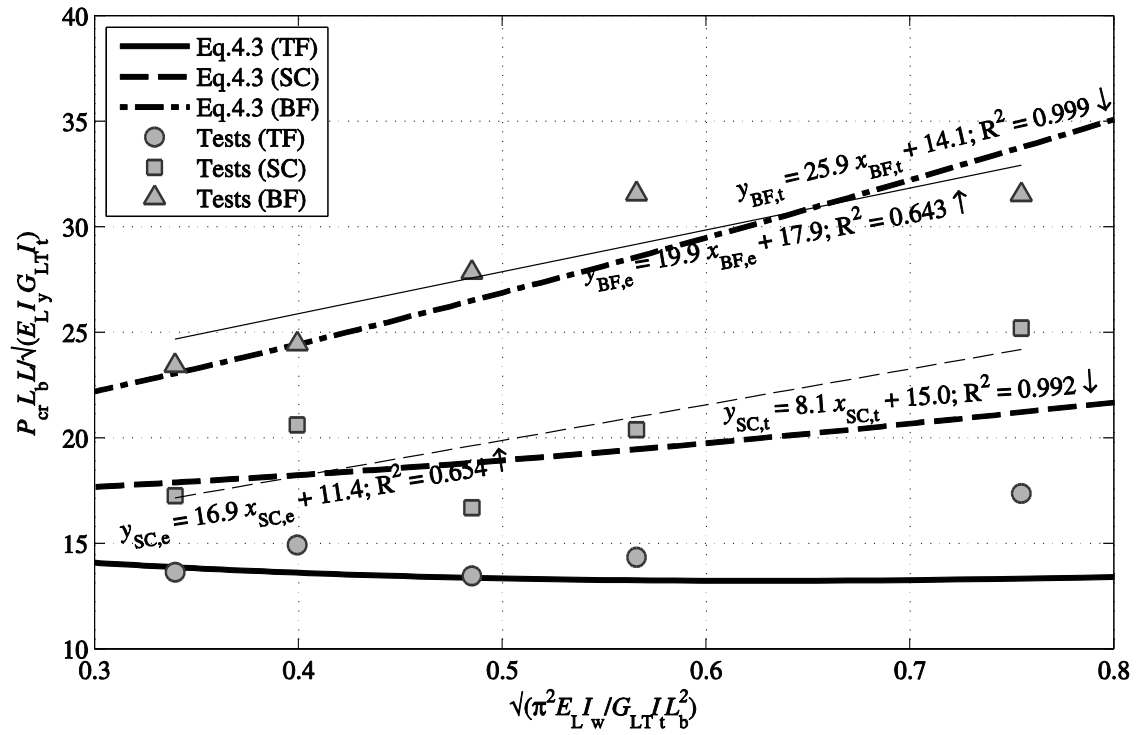
Figure 4.28 Plots for C2-section with EC1 at three load heights for TF, SC and BF
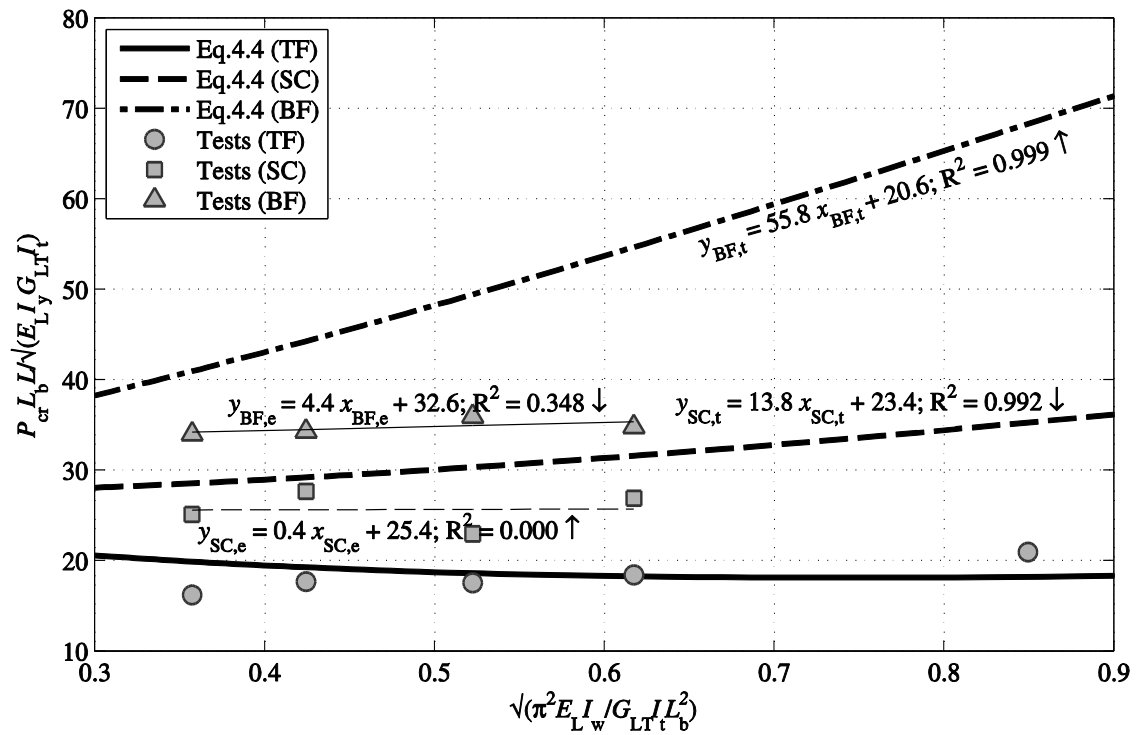
Figure 4.29 Plots for C2-section with EC2 at three load heights for TF, SC and BF

128
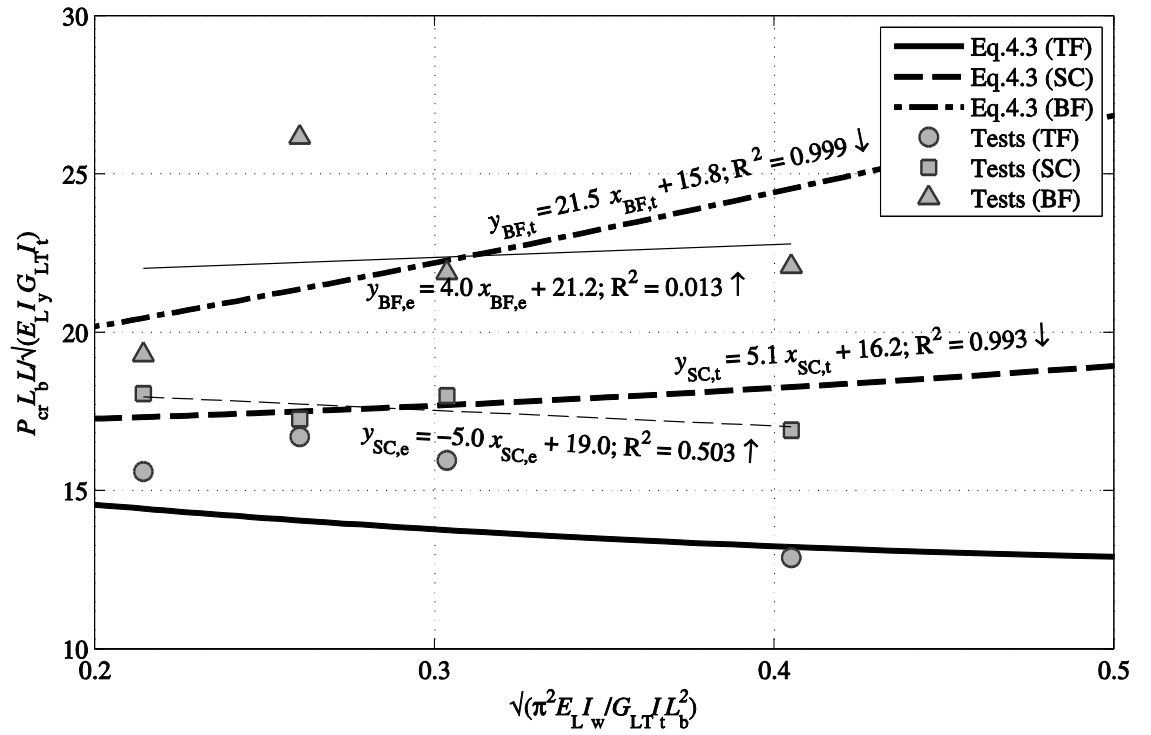
Figure 4.30 Plots for C3-section with EC1 at three load heights for TF, SC and BF
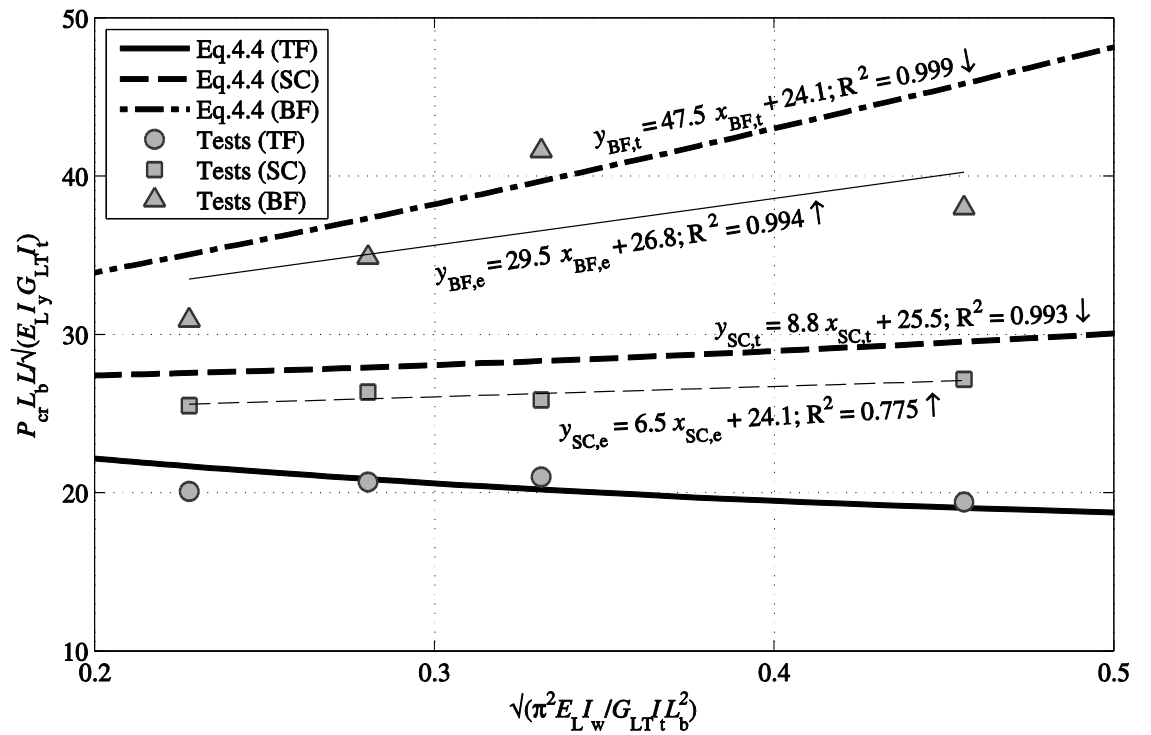
Figure 4.31 Plots for C3-section with EC2 at three load heights for TF, SC and BF

Presented in Figures 4.26 to 4.31 are six plots for C1, C2 and C3 for end conditions EC1 and EC2. These plots are constructed in the same way as are the plots in Figures 4.22 and 4.23 for the I-section. It is found that the channel beam test results show a more significant degree of inconsistency. It is believe that the lower variation with the I-beam is because its shear centre nearly coincident with the geometrical centre of the symmetric cross-section. This desirable geometric feature makes setting-up of the loading disc (Figure 4.4) more straightforward, with less likelihood for introducing a load eccentricity, which adversely influences flexural response.

Addition to the reasons that have been presented in sub-section 4.8.1 for why there are factors that could contribute to differences between theory and practice, the shear centre of a C-section is seen in Figure 4.32 to lie outside the centre of the end supports. This extra test variable can be considered as a form of load eccentricity. When combined with the inherent lateral load eccentricity and beam's initial geometric imperfections there is to be a downward or upward change in the buckling resistance that cannot be easily quatified.
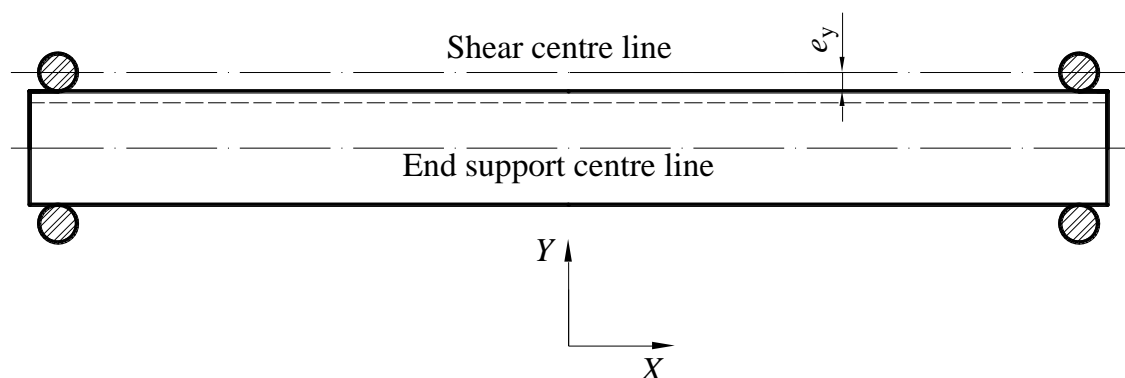
Figure 4.32 Top view of channel test beam
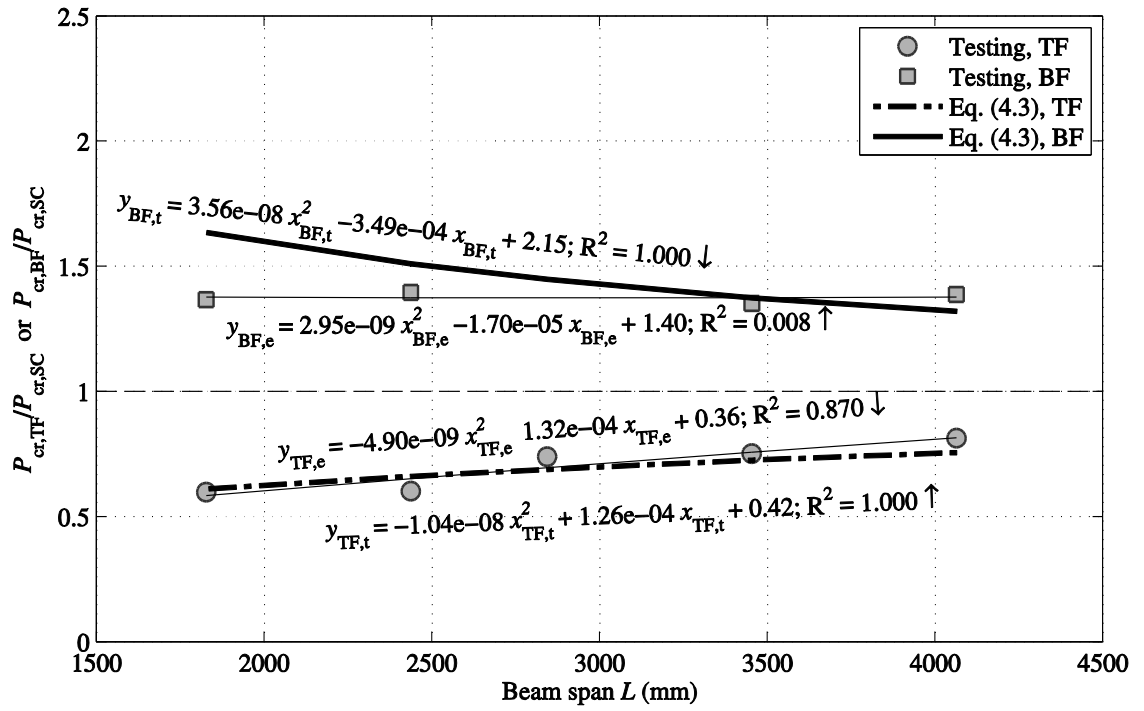
Figure 4.33 Effect of load height for C1 beams with EC1
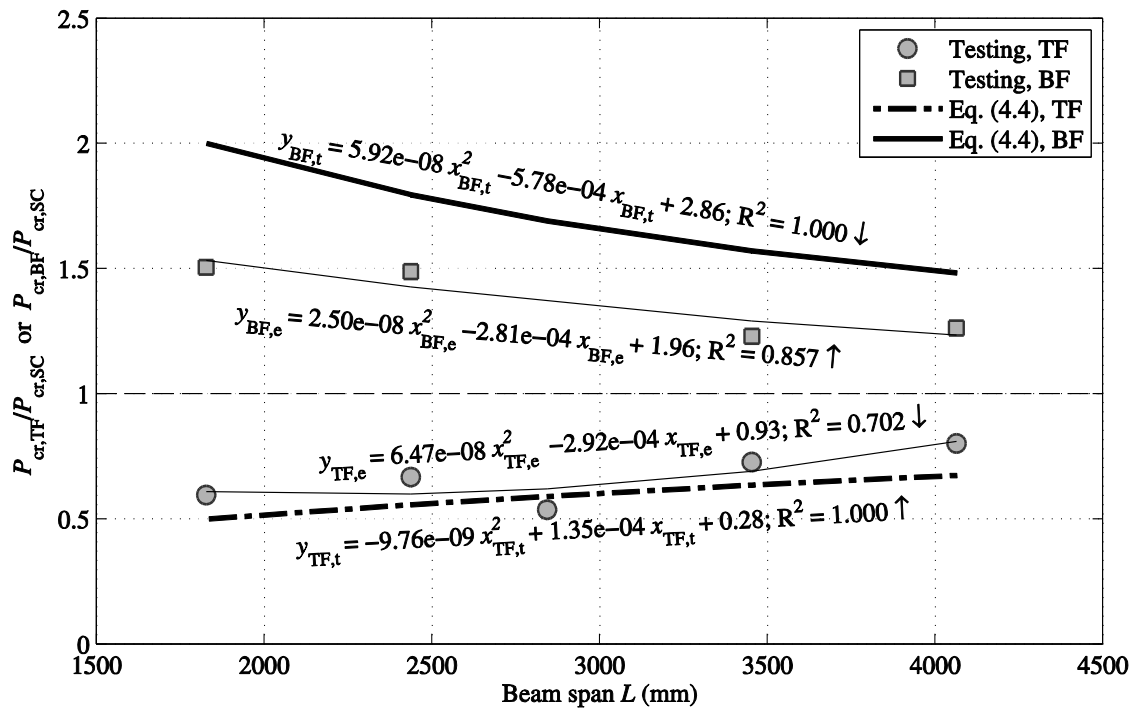
Figure 4.34 Effect of load height for C1 beams with EC2
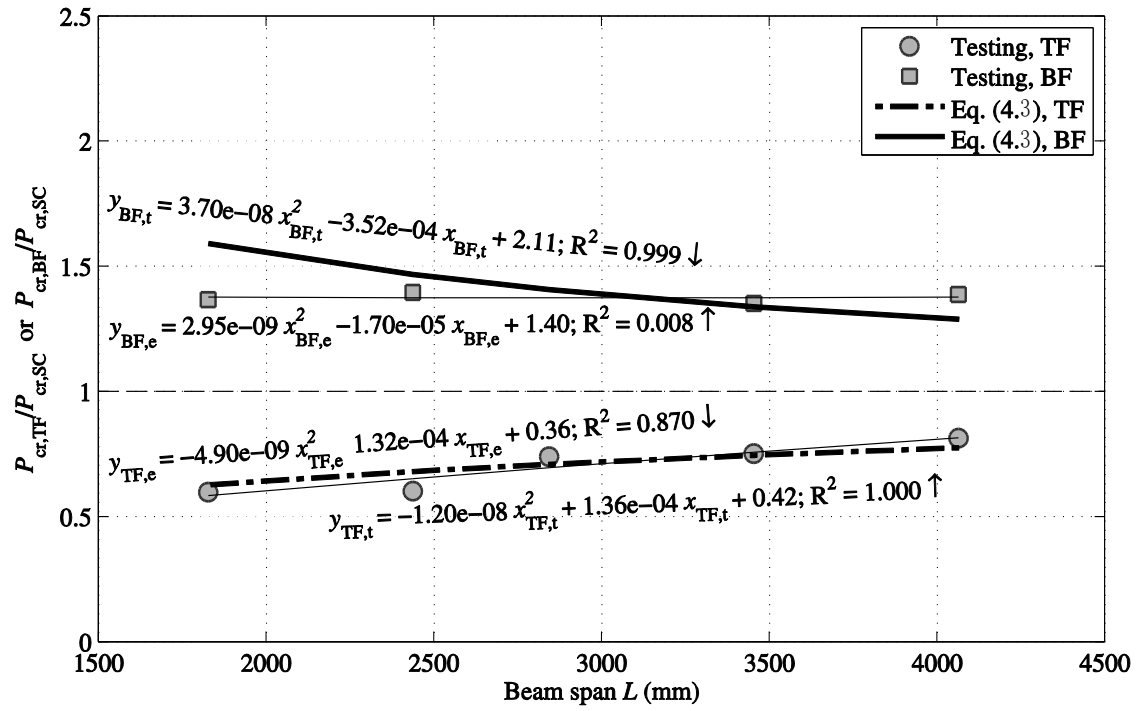
Figure 4.35 Effect of load height for C2 beams with EC1
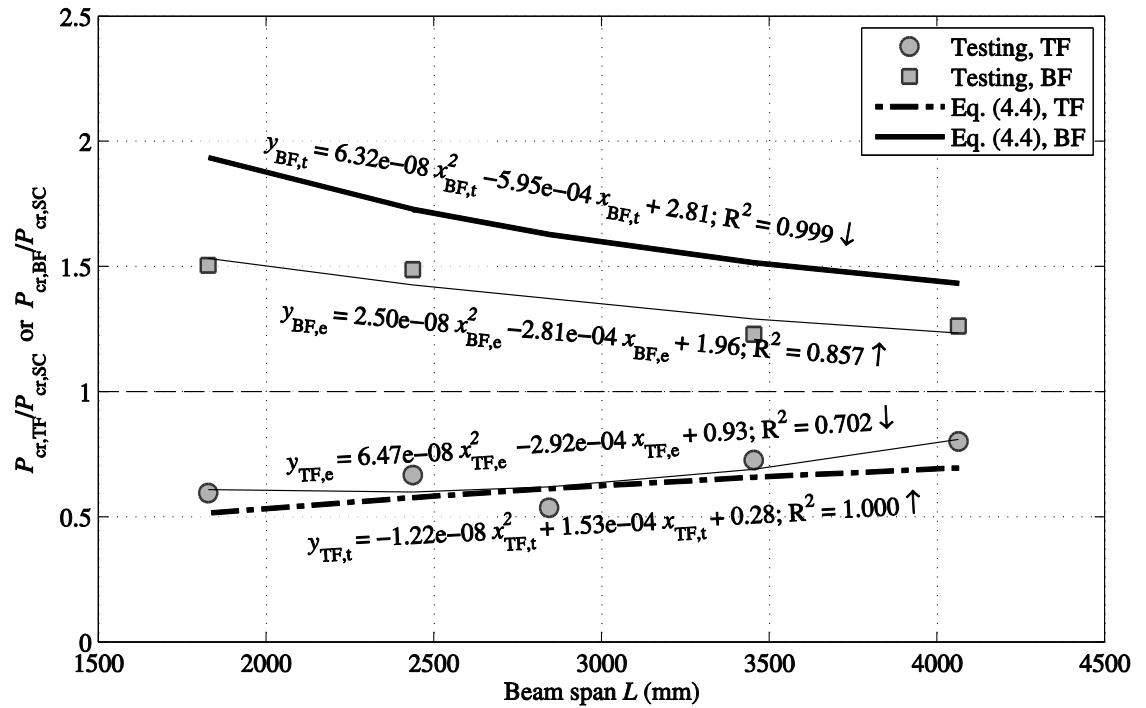
Figure 4.36 Effect of load height for C2 beams with EC2
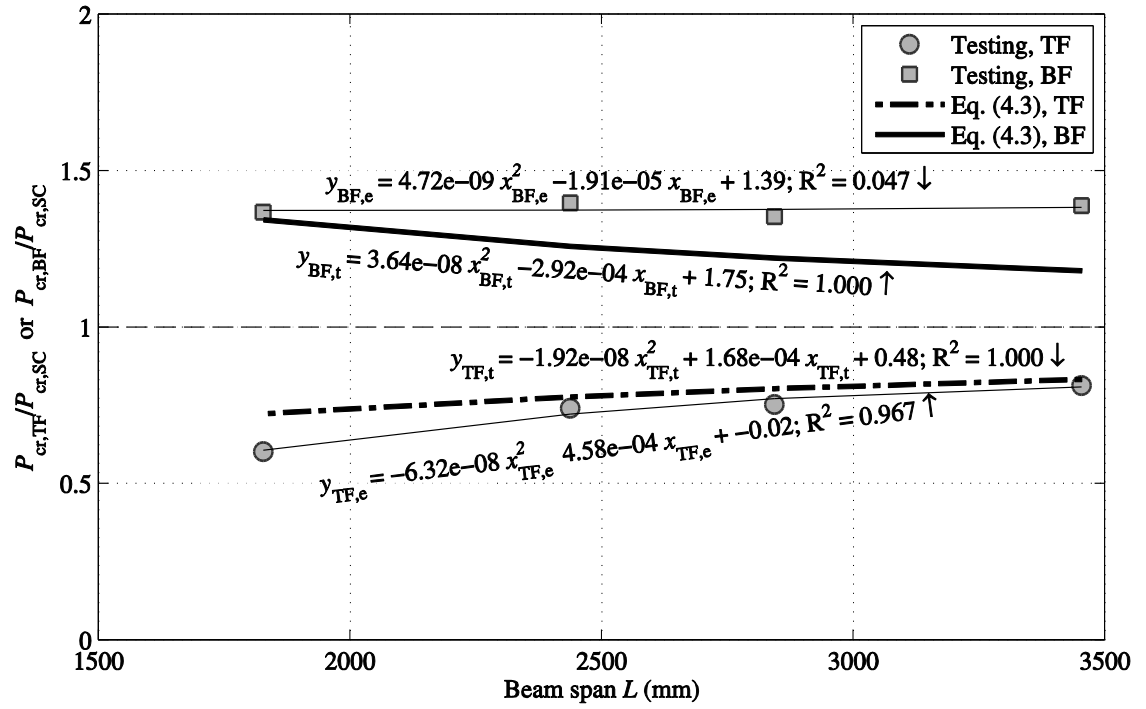
Figure 4.37 Effect of load height for C3 beams with EC1
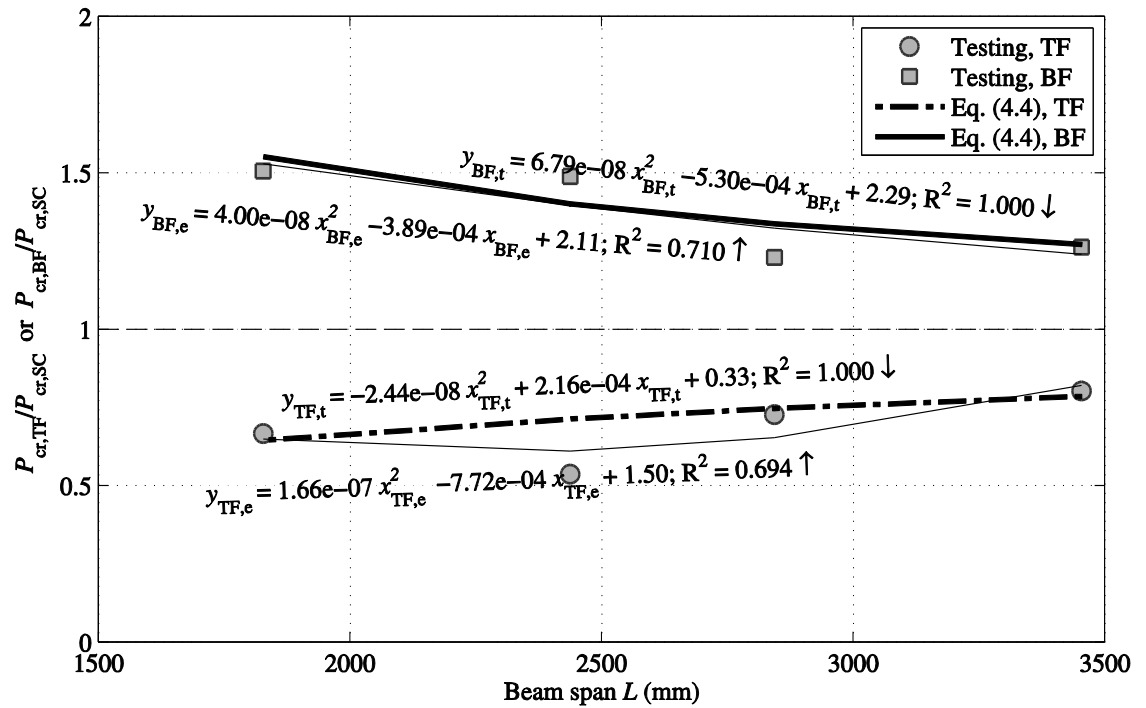
Figure 4.38 Effect of load height for C3 beams with EC2

Figures 4.33 to 4.38 give the plots to show the effect of load height for C1, C2 and C3 sections with EC1 and EC2. It is found that for C1and C2 with EC2, the effect of load height for bottom flange loading a significantly lower than predicted by theory. This is not the case for EC1. This observation supports the point making in sub-section 4.8.1 about the effectiveness in the EC2 end condition of the four steel rods in restraining the minor axis rotation as load increases. This behaviour was not found for C3 beam because they were failed at much lower loads compared to those of other section and at a lower load, the 'four steel rods' system was able to give a better (higher) restraint about the minor axis rotation.

4.9.   Concluding remarks

Presented in this chapter is a test methodology to determine LTB resistance of simply supported PFRP beams under to three-point bending. The test rig and fixtures were designed to provide loading and displacement boundary conditions that are assumed in theoretical treatment for LTB problem. 114 individual tests were conducted on 19 beams with two displacement end conditions for EC1 and EC2 and at three load heights for TF, SC and BF. The experimental buckling load $P_{cr,e}$ was established with 'peak' load or Southwell plot methods, depending on the load vs. mid-span rotation response. It is shown that the test configuration is adequately, but not exactly, satisfying the theoretical boundary conditions for buckling failure in the LTB mode.

By taking the two moduli of elasticity in a closed-form equation to be the design values reported in the pultruder's design manual it is found (Nguyen *et al.*, 2014) that the test

results are all significantly higher than predicted. One of the main reasons for this finding is that the elastic constants for design are lower than actual. This is important to know because it shows that by choosing the pultruder's tabulated values for the moduli of elasticity the closed-formed equations will give a LTB design resistance that is safe.

By making a comparison between test results and predictions for the I-section using measured moduli of elasticity, it is shown that the test rig is performing properly and is able to give resistance measurement at different load height positions. Furthermore, the comparison is used to show that the relevant closed-form equation for the elastic critical buckling load is applicable. The differences between testing and theory are due to the displacement boundary conditions in the testing not fully satisfying those assumed in the theoretical treatment. The level of influence of experimental restraint above the desired 'free' warping restraint remains unknown. The combination of material, geometric and loading imperfection might have a significant effect on the LTB resistance. This feature will be investigated numerically in Chapter 5. For the three C-sections, the comparisons reported in Tables 4.5 and 4.6 and Figures 4.26 and 4.31 have shown a significant scatter for reasons discussed.

Figure 4.39 presents all the data points in a form of non-dimensional moments M_e / M_{Loc} vs. generalised slenderness $\lambda_{LT} = \sqrt{M_{Loc} / M_{cr}}$. The testing buckling moment (M_e) is calculation for a simply supported condition by $M_e = P_{cr,e}L/4$. The local buckling moment (M_{Loc}) is calculated as $M_{Loc} = \sigma_{Loc,e}I_y / (h/2)$. The local buckling stress for the I-section $(\sigma_{Loc,e} = 134 \, \text{MPa})$ is taken from Section 3.7 of Chapter 3. The equivalent plotting in Figure 4.40 for steel section is taken from Trahair *et al.* (2007). The two figures show that a one-to-one correlation cannot be expected between the closed-form predictions and experimental results for either PFRP or steel

and thus a calibration is crucial to provide designers with a procedure suitable for a code of practice that is safe and relevant. The calibration process to be presented in Chapter 5 will followed the Eurocode 0 approach to establish the material partial factor for the LTB (ultimate) mode of failure.
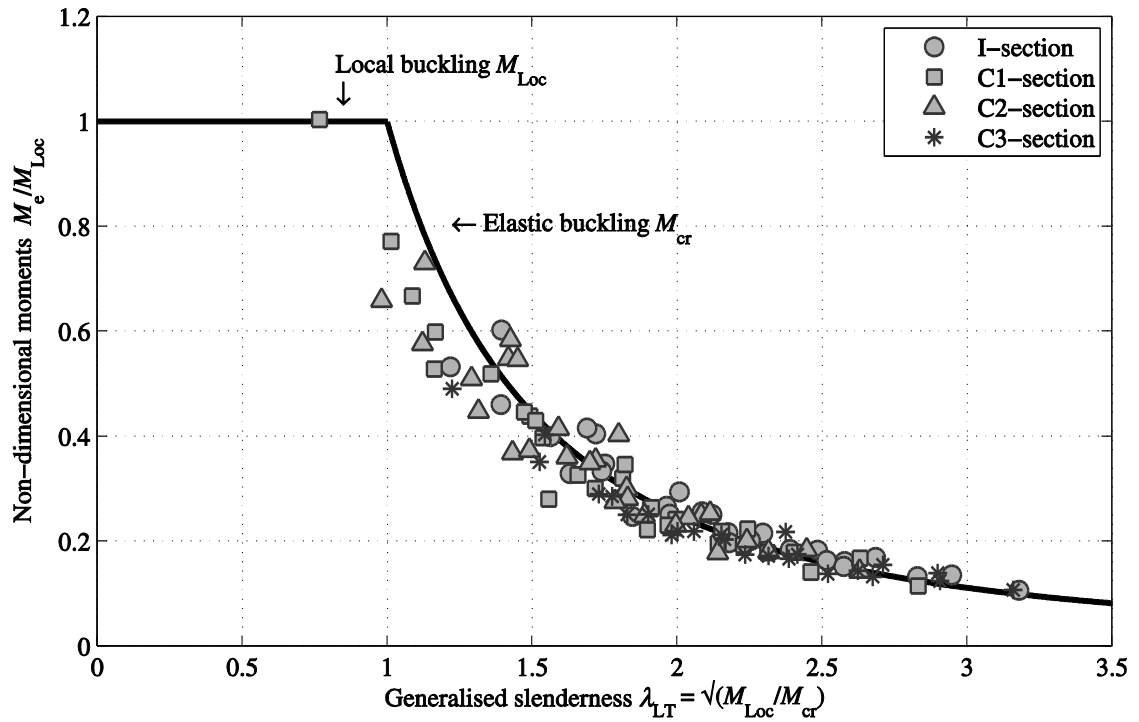
Figure 4.39 Moment resistance of beams from author's test results
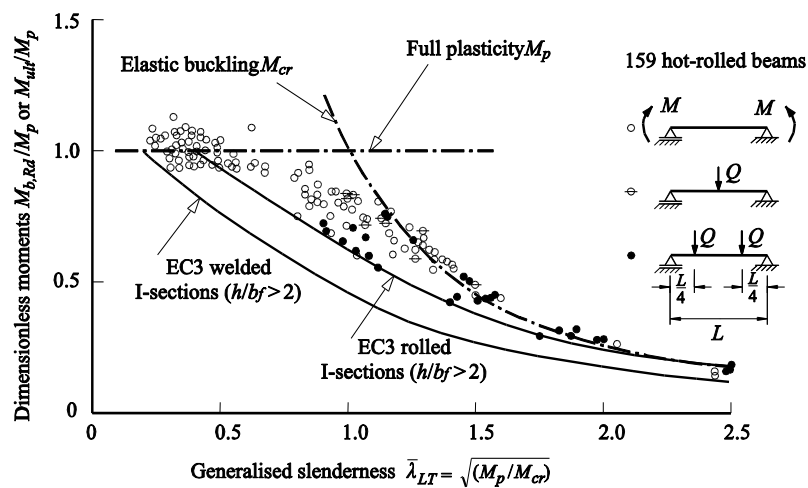
Figure 4.40 Moment resistance of beams in near-uniform bending, from Trahair *et al.* (2007)

CHAPTER 5

NUMERICAL INVESTIGATION

5.1. Introduction

This chapter presents the Finite Element Analysis (FEA) investigation by ABAQUS$^{\circledR}$ to simulate the LTB response of the PFRP beams in testing. The end displacement Boundary Conditions (BCs) were either EC1 or EC2 as defined in Chapter 4. Three vertical load positions for Top Flange (TF), Shear Centre (SC), and Bottom Flange (BF) loading were investigated. Numerical simulations were implemented for linear eigenvalue and geometric nonlinear analyses. For nonlinear analyses, measured initial out-of-straightness geometric imperfections were introduced into the beam's FE mesh as a form of a half sine wave shape with the maximum value $\delta_{\max}$ located at mid-span. The modelling technique and results for I- and C1-sections will be presented. The material properties for inputting into the Finite Element (FE) models were the mean values experimentally determined in Chapter 3. Sensitivity analyses were carried out on the influence of torsional constant, changes in modulus of elasticity, lateral load position, geometric imperfection and overhang length to evaluate their influences on the LTB resistances. The purpose of this chapter is to simulate the actual response of the tested beams under the laboratory set-up. Part of this chapter has been reported in Nguyen *et al.* (2013).

5.2. Modelling methodology

The degree of accuracy of the FEA is affected by the decision made on the choice of modelling technique, element type and meshing density. Plate materials of PFRP shape are made of 'matrix' and 'fibre reinforcement'. Reinforcement materials are layers of unidirectional E-glass fibres and continuous mats. ABAQUS® (Dassault Systèmes Simulia Corp, 2013b) offers three approaches to model the plate materials: (1) 'microscopic' approach, where matrix and reinforcement materials are modelled separately; (2) 'macroscopic' approach where plate materials are modelled as a single layer of orthotropic material. This technique is suitable for the modelling of overall structural behaviour of composite member. It requires the knowledge of E_L, E_T, G_{LT} and ν_{LT} which have been experimentally characterized in Chapter 3; (3) 'mixed' approach where the panels are modelled to have a number of discrete 'macroscopic' orthotropic layers. Of the three techniques, the second one is appropriate for this Ph.D. work. The two others require further knowledge of fibre architectures and mechanical properties of matrix and reinforcement which were not evaluated for this study. In terms of modelling and computational efficiency, the chosen method is the most reliable.

Element type, meshing density is chosen based upon the performances of several popular elements that are evaluated by conducting an eigenvalue analysis on orthotropic beam buckling problem and compare the results for each elements type against the closed-form solution. Geometrical modelling to take into account the influence of the fillet areas, the modelling of EC1 and EC2 and method of simulating the point load for C-sections are also presented.

5.2.1. Input of material properties

As shown in Chapter 3, LTB failure of a PFRP beam will normally happen when the longitudinal strains are within the elastic range. Experimental studies have also confirmed this observation (Correia *et al.*, 2011, Nguyen *et al.*, 2014). Linear elastic material model is chosen for the FE modelling.
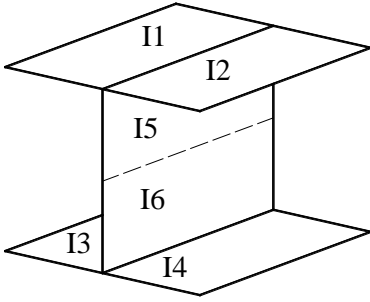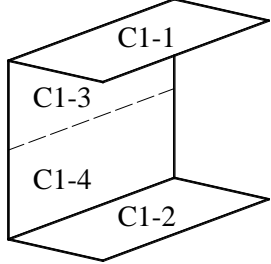
FRP materials can be considered as either orthotropic or transversely isotropic (Hyer and White, 1998, Tuttle, 2012). Orthotropic material has three mutually orthogonal axes on which the mechanical properties are different. Transversely isotropic material is a special case of orthotropic. It has a transverse plane with material properties the same (isotropic) in all directions. By denoting '1' for the unidirectional (longitudinal) fibres direction; '2' for the transverse (perpendicular to the fibres) direction; and '3' for the through-thickness direction, the definition of orthotropic material involves nine independent elastic constants namely: three moduli (E_1, E_2, E_3), three shear moduli (G_{12}, G_{13}, G_{23}) and three Poisson's ratios $(\nu_{12}, \nu_{13}, \nu_{23})$. If the distribution of fibres in the 2- and 3- directions is the same, the material can be assumed to be transversely isotropic (Tuttle, 2012). PFRP materials comprise of layers of unidirectional fibres and layers of fibres that can be assumed to be randomly and uniformly distributed. It is acceptable to assume these materials as transversely isotropic. The input for transversely isotropic material requires five independent properties for $E_1, E_2, \nu_{12}, \nu_{23}$ and G_{12}. It is to be noted that $E_1, E_2, G_{12}, \nu_{12}$ are for $E_L, E_T, G_{LT}, \nu_{LT}$, respectively. The simplest way to define a transversely isotropic material in ABQUS$^{\circledR}$ is by specifying the nine engineering constants. They are $E_1, E_2 = E_3$, $\nu_{12} = \nu_{13}, \nu_{23}$, $G_{12} = G_{13}, G_{23}$

with
$$G_{23} = \frac{E_2}{2(1+\nu_{23})}.$$
(5.1)

It is worth noting that under plane stress conditions, as in shell finite elements, only material properties on the 1-2 plane for E_1, E_2, G_{12} and ν_{12} are needed (Tuttle, 2012). G_{13} and G_{23} are only important for the modelling of transverse shear deformation (Dassault Systèmes Simulia Corp, 2013c). For PFRP material, ν_{23} is a matrix dominant elastic constant and is known to be higher than 0.35 (Tuttle, 2012). By letting $\nu_{23} = 0.35$ for all panels in a PFRP shape G_{23} can be obtained using Eq. (5.1). The modelling values of I and C1 shapes are given in Table 5.1.

Table 5.1 Material properties for flange and web panels of I- and C1-sections

Shape	Flange I1	Flange I2	Flange I3	Flange I4	Web I5	Web I6
I section	(1)	(2)	(3)	(4)	(5)	(6)
E_1 (GPa)	34.4	29.7	34.5	31.2	26.3	26.2
E_2 (GPa)	10.8	10.8	10.8	10.8	10.8	10.8
G_{12} (GPa)	4.2	4.2	4.2	4.2	4.2	4.2
G_{23} (GPa)	4.0	4.0	4.0	4.0	4.0	4.0
ν_{12}	0.23	0.25	0.24	0.21	0.22	0.23
C1 section	Flange C1-1		Flange C1-2		Web C1-3	Web C1-4
E_1 (GPa)	29.7		30.5		34.4	31.7
E_2 (GPa)	11.7		11.7		11.7	11.7
G_{12} (GPa)	4.8		4.8		4.8	4.8
G_{23} (GPa)	4.3		4.3		4.3	4.3
ν_{12}	0.21		0.22		0.25	0.22

It has been shown in Chapter 3 that the four flanges and web in the I-section possess different values of the longitudinal modulus of elasticity E_L. The transverse modulus of elasticity E_T was only determined for the web material and this is not important because the influence of changing E_T on the LTB resistance is insignificant. A change in 30% of E_T reduces or increases the LTB resistance only by $< 1\%$ (Stoddard, 1997). The major Poisson's ratio v_{LT} was determined for all flanges and web materials. The in-plane shear modulus was determined for the web only. It is acceptable to assume that the flanges have the same E_T and G_{LT} as does the web. These values are collected from Figure 3.10 and Table 3.14 and summarized in Table 5.1 for I and C1.

5.2.2. Element types and mesh sizes

The choice of element is between solid and shell. Shell elements are popular for thin-walled structure problems in which the change of analysed character in the direction of thickness (i.e. through-thickness shear stress) can be neglected. Compared with solid elements, modelling with shell elements is generally simpler and the mesh specification is more straightforward to achieve. In terms of computational proficiency, shell elements can be time saving too, since they allow the modelling of thin properties with much fewer elements than that of solid elements. The shell element is adopted for this FE work. The three shell elements of S4R, S4R5 and S8R are commonly adopted for buckling analyses of PFRP structural members (Brooks and Turvey, 1995, Turvey, 1996, Qiao *et al.*, 2003, Shan and Qiao, 2005, Trumpf, 2006). Four-node general purpose linear shell elements S4R and S4R5 apply linear shape functions to interpolate deformation between nodes and are suitable for modelling both thin and thick shell

elements (Dassault Systèmes Simulia Corp, 2013c). The '5' in S4R5 means that each node has 5 degrees of freedom. The removed degree of freedom is for rotation about the axis normal to the element mid-surface. This element formulation improves the computational efficiency. Thick shell element S8R employs quadratic shape functions by having eight nodes per element. The formulation for the element stiffness matrix adopts the Mindlin plate theory for first-order shear deformation. This element has displacement compatibility that avoids there being any discontinuities between element sides. This modelling attribute is known to give a more accurate shell element in a coarser mesh (Mottram and Shaw, 1996). The 'R' in S4R and S8R denotes that the number of Gaussian integration points is reduced to improve computational efficiency and to avoid shear locking (Dassault Systèmes Simulia Corp, 2013c).

Eigenvalue analyses were carried out on a transversely isotropic simply supported ($k = k_w = 1$) I beam, dimension of $120 \times 60 \times 6$ mm with span of 1500 mm, subjected to a point load at mid-span, at the shear centre, to compare the performances of the three shell elements S4R, S4R5 and S8R against a closed-form solution for LTB given by Kollár and Springer (2003). This solution which has been mentioned in Section 2.2 of Chapter 2, is for the LTB for othotropic material. It is given by exchanging the force-strain relationships for isotropic by orthotropic material. It accounts for the reduction of LTB resistance due to influence of shear deformation. This reduction is higher for wide-flange beam (e.g. breadth equal to depth) and/or for materials that have ratio for E_L / G_{LT} relatively high (i.e. this ratio can be in range from 20 to 30 when fibres are of carbon). For narrow-flange beam, the reduction is within 5%. The difference between this solution and Eq. (2.1) is also insignificant. Details of the solution can be found in Sapkás and Kollár (2002).

Taking the moduli of elasticity as $E_L = 30.7$ GPa and $G_{LT} = 4.2$ GPa, the closed-form equation by Kollár and Springer (2003) gives the buckling load to be 7.6 kN. The input elastic constants for the elastic eigenvalue FEA are $E_1 (\text{or } E_L) = 30.7$ GPa ,

$E_2 (\text{or } E_T) = 10.8$ GPa , $G_{12} (\text{or } G_{LT}) = G_{13} = 4.2$ GPa , $\nu_{12} (\text{or } \nu_{LT}) = 0.23$, $G_{23} = 4$ GPa.

Mesh specification has the shell elements with an aspect ratio close to one to eliminate any loss in numerical reliability due to computation for the inclusion of shear flexibility. To create the beam mesh the shell elements are placed at the mid-planes of the two flanges and web panels. The performance of each shell element was evaluated by changing the aspect ratios of the mesh. For the flanges, the sizes are 5×5 mm, 10×10 mm, 15×15 mm and 30×30 mm. In the web, the sizes chosen are 5.2×5 mm, 9.5×10 mm, 14.25×15 mm and 28.5×30 mm.

Table 5.2 Elastic LTB loads for different shell elements with mesh refinements

Shell element side lengths (mm)	Number of elements per metre	$P_{cr,FEA}$ (kN) S4R5 element	$P_{cr,FEA}$ (kN) S4R element	$P_{cr,FEA}$ (kN) S8R element
(1)	(2)	(3)	(4)	(5)
30	267	6.15	6.15	7.48
15	1067	7.16	7.15	7.45
10	2400	7.34	7.32	7.45
5	9200	7.42	7.41	7.44

Table 5.2 reports in columns (3-5) the elastic buckling load $P_{cr,FEA}$ for three shell elements as the mesh size is refined. Number of elements per metre is given in column (2) with the length of an element along the beam given in column (1). It can be seen that there is insignificant ($< 3\%$) change in $P_{cr,FEA}$ when the element side length for S4R5 and S4R is < 15 mm (in bottom two rows of table). On doubling the side length to 30 mm the calculated bifurcation load is reduced by 16%. S8R gives more reliable results

with differences less than 1% for all mesh sizes. Because of its superior numerical performance, this double-curved thick shell element, with side lengths of 15 mm or less, is adopted in the mesh specification for the FE modelling presented next.

5.2.3. Geometrical modelling

Flange and web panels in a PFRP section are modelled as shell plates where the fillet areas between flange and web junction will be ignored. The typical shape for an I-section is shown in Figure 5.1(a). This geometrical modelling can be acceptable if the fillet areas are relatively small and/or when the torsional constant I_t is not important for the problem to be analysed. For a LTB analysis I_t plays a significant role as it represents the torsion term in the lateral-torsional deformation. The calculation of I_T for the I-section in Chapter 4 has shown that the fillet radius regions cannot be ignored in LTB analysis. The inclusion of these areas increase I_t by 28%, results in an increasing of up to 15% in the buckling resistance calculated by the closed-form equation (2.1). For C1, the increase in I_t is 15% and this gives an increase in LTB resistance of 9%. Therefore, to model the I- and C-sections in the series of test, the presence of the filler radius areas must be allowed for. A feasible way (Schleich *et al.*, 1998, Trumpf, 2006) to compensate for the 'loss' of these areas in the shell model is to assign the shell plates with difference thicknesses along the width. This change to the mesh specification is shown in Figure 5.1(b).
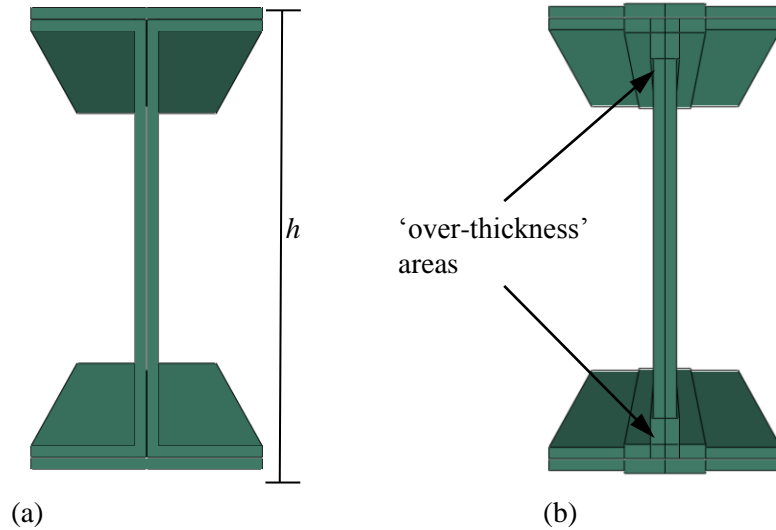
Figure 5.1 Modelling of an I-section: (a) ignoring fillet areas; (b) accounting for fillet areas
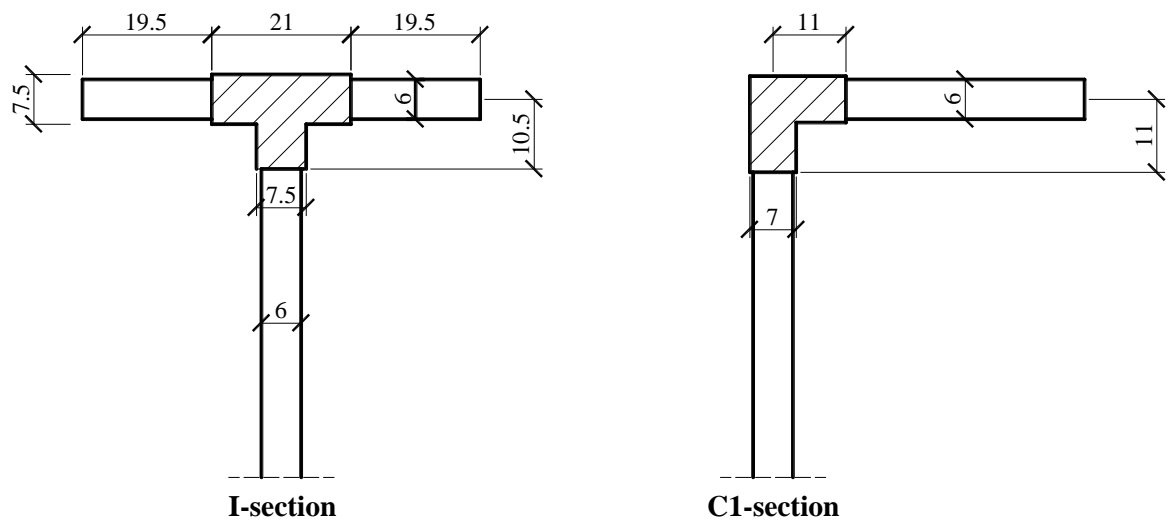
Figure 5.2 Change in thicknesses at web-flange junction for I and C1 to account for fillet radius areas

Figure 5.2 shows the modification to flange and web thicknesses to develop junction areas in I- and C1-sections.The original thickness of 6 mm is increased to 7.5 mm along a length of 21 mm for flanges and for a length of 10.5 mm for the web in the I-section. The new geometrical model gives the same I_t of 2.15×10^4 mm^4 with reported in Table

4.4. This model, however, increases the warping constant (I_w) by 3% and second moment of area about the minor axis (I_z) by 0.4%. These changes to geometrical properties do not have a significant effect on changing the LTB resistance. For the C1-section, the new thickness for the junction areas is 7 mm and the length in both panels is 11 mm. This modelling gives the same $I_t = 1.72 \times 10^4 \, \text{mm}^4$ as reported in Table 4.4 and increases I_w by 2.7% and I_z by 0.7%.

The investigation of the effect of vertical load height requires the load to be applied on Top Flange (TF), at Shear Centre (SC) or on Bottom Flange (BF). The structural members modelled by shell elements will, by default, use the shells middle surface as the reference surface where the element's nodes exist. The top or bottom flange load, in FE analyses, will be located at a distance of $t_f / 2$ below or above the top or bottom flange surfaces. ABAQUS$^®$ (Dassault Systèmes Simulia Corp, 2013b) has an option to define a distance from a reference surface, where the nodes are located, to the shell middle surface. In the FE modelling, the reference surface for top flange will be set on top of the shell plane and that for the bottom flange will be below the shell plane. This technique enables the vertical load to be applied at $z_g = +h/2$ and $z_g = -h/2$, respectively.

5.2.4. Simulation of displacement boundary conditions

FE analyses are carried out with end conditions EC1 and EC2. These are BCs that have been implemented in the physical test programme of Chapter 4. EC1 allows for 'free' warping and 'free' minor axis rotation at both ends. This is the Simply Supported (SS)

condition with buckling resistance expected to have a lowest value compared to any other SS boundary condition and thus is most conservative for design purpose. EC2 allows for 'free' warping but 'fixed' against minor axis rotation (i.e. clamped ends for lateral flexure of the beam). Figure 5.3 shows the Cartesian coordinate system for the FE modelling and defines the three translational (U_x, U_y, U_z) and three rotational displacements (UR_x, UR_y, UR_z) .
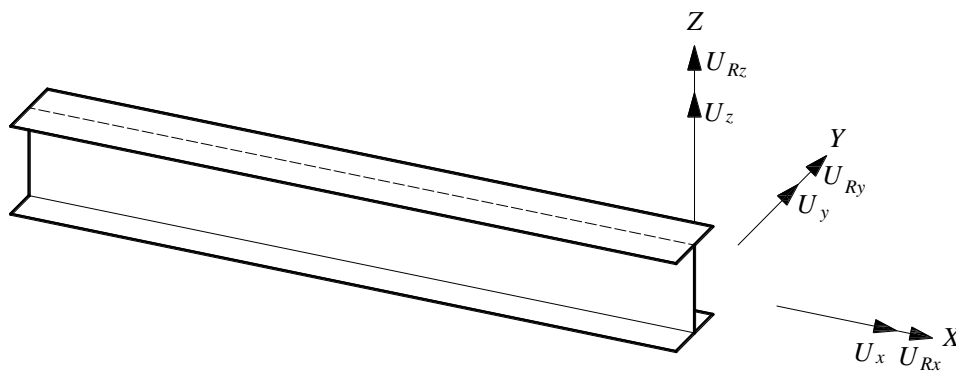
Figure 5.3 FE Cartesian coordinate system
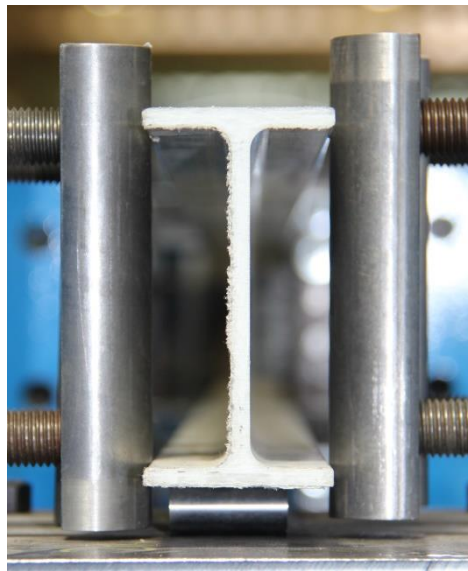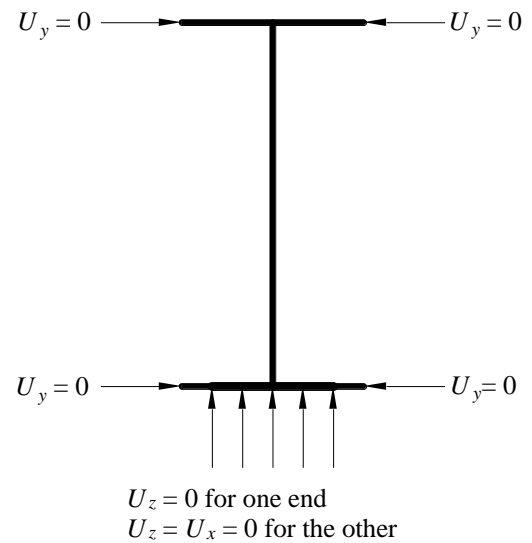
(a)   (b)

Figure 5.4 Arrangement of EC1 for I-section: (a) in testing; (b) in FEA

EC1 as shown in Figure 5.4(a) was realised by having one pair of vertical steel rods arranged in contact with both side of the section at the beam's ends. For the I-section this arrangement is simulated by restraining four nodes, one on each outstanding flange from horizontal movement as given in Figure 5.4(b). These are the contacting points between the section and the steel rods. The roller end is modelled by imposing the restraint for vertical movement U_z over the contacting areaq. For both I and C1, this area has a length of 40 mm. At the other end where the beam is stopped from moving along it axis, both U_z and U_x are restrained.
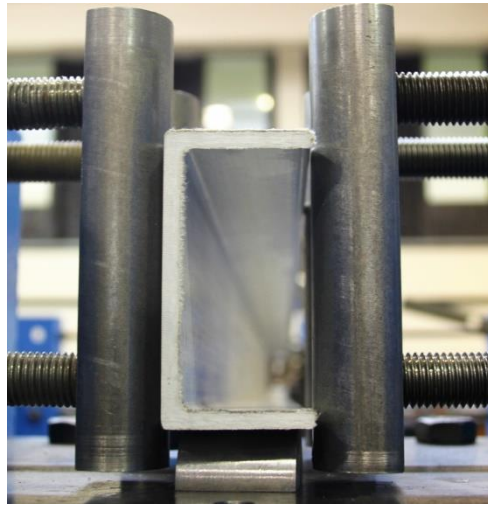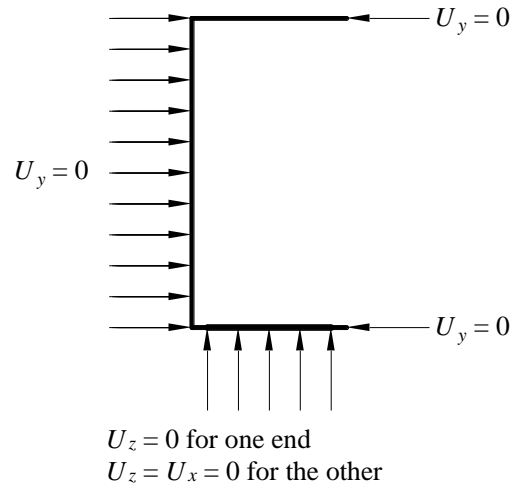
(a)   (b)

Figure 5.5 Arrangement of EC1 for C-section: (a) in tests; (b) in FEA

The modelling of EC1 for C1-section is slightly different. One of the steel rods is in contact with the whole depth of the section. This area is fully restrained from having a deflection $U_y = 0$. Figure 5.5(a) is a photo for the end boundary set-up. Figure 5.5(b) illustrates how EC1 is modelled in FEA.

The only difference between EC2 and EC1 is that two pairs of steel rods are required with the former. For the I-section, it can be modelled by having eight nodes (two on

148

each side of the outstand flanges), where the steel rods make contact with the beam end, with $U_y = 0$. In the C-section, the restraint $U_y = 0$ is imposed at four nodes, two on each outstand flange. The web areas in contact are also restrained by specifying $U_y = 0$ there. The modelling for vertical support restraints on bottom flanges are the same as in EC1. The modelling of EC2 for C-section is illustrated in Figure 5.6.
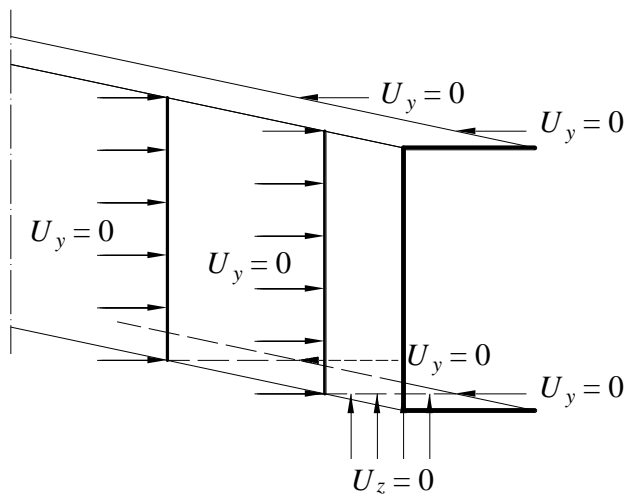
Figure 5.6 FE modelling for steel rods in EC2

5.2.5. Modelling of vertical load for channel section

Because the I-section is doubly symmetric, its shear centre can be assumed to coincide with the section's centroid (at mid-depth of the web). The vertical load for I-section is modelled simply by applying the concentrated point load on the middle surface of web panel. To introduce another modelling feature, a channel section has the shear centre located outside of the section area and this is illustrated in Figure 5.7.
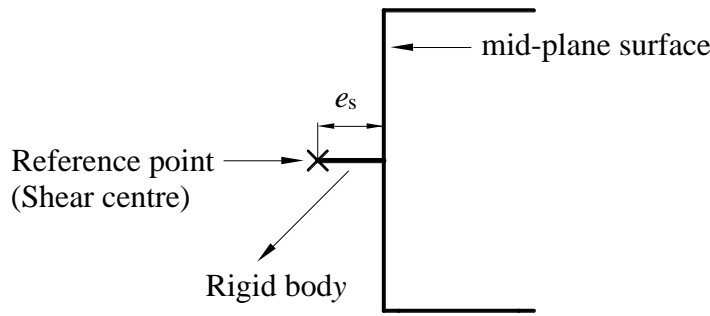
Figure 5.7 Load at shear centre of C-section in FEA

A feasible way to model the vertical load is by defining a reference point located at the shear centre as shown in Figure 5.7. This point is connected to the node at the mid-point of the web panel using 'RIGID BODY' type of constraint with 'TIE NODES'. The two points are linked together by a rigid bar (massless) that allows for both translational and rotational degree of freedom. By applying the load at this reference point, the shear centre loading for a C-section is modelled.

5.2.6. Analysis methods

Both linear eigenvalue and nonlinear analyses are carried out on I and C1 beams for LTB failure. Linear eigenvalue buckling analysis predicts the elastic critical buckling load ($P_{cr,FEA}$) of a linear elastic beam where the change in beam geometry is neglected on increasing loading, up to the bifurcation failure. By applying perturbations to the mesh geometry of the unloaded beam, and looking for local and global deflections that could promote the onset of instability due to second-order effects, the FEA gives load factors (the eigenvalues) for buckling failures. The inputted load in the FE model is multiplied by the outputted load factor to obtain the elastic critical buckling load. The associated eigenvector to each eigenvalue establishes the corresponding mode shape.

The buckling mode shape is defined by a normalized vector for nodal displacements with maximum displacement component set to 1.0 (Dassault Systèmes Simulia Corp, 2013a). The mode shape can only show how the structure buckles, but gives no information to the actual load-deflection response. ABAQUS® provides the two approaches of Lanczos and Subspace iteration to extract eigenvalue. The latter method is the default solver (Dassault Systèmes Simulia Corp, 2013b). Subspace iteration is effective for calculating a small number of eigenmodes, whilst the Lanczos method is expected to be more computational efficiency when a larger number of eigenmodes are required for a structural system that has many degrees of freedom (Dassault Systèmes Simulia Corp, 2013a). The Subspace iteration method is chosen for this FE work.

Nonlinear analysis predicts the actual load-deflection response by applying the load in small increments and calculating the current (static equilibrium) deformation state at each increment. The load follows the deformation of the linear elastic beam until instability occurs, and this corresponds to what will happen in practice. There is no material nonlinearity to be modelled as it is correct to assume that the PFRP material behaves perfectly linear elastic. This modelling assumption remains acceptable, providing loading (to failure) is short-term and deformations from material viscoelasticity remain small. ABAQUS solves the problem of a geometric nonlinear structural by employing a modified Riks method. This commonly used nonlinear numerical method, also known as the arc-length method, was originally derived by Riks (1979) and was improved for computational efficiency by Crisfield (1981). As the post-buckling response is not the main topic under consideration, the nonlinear analysis will be terminated a few increments after the beam has become unstable and its deformation is found to be progressing into the post-buckling region.

The initial minor axis out-of-straightness imperfection is introduced into the FE model to investigate the influence of this imperfection on the response of PFRP beams. The initial minor axis out-of-straightness imperfection (δ_x) along a beam of span length L is assumed to follow the sinusoidal wave with the maximum imperfection (δ_{max}) at mid-span. The imperfection is expressed by:

$$\delta_x = \delta_{max} \sin \frac{\pi x}{L}. \tag{5.2}$$

In Eq. (5.2) x is the distance along the beam from one end to the other.

Figure 5.8 Minor axis out-of-straightness imperfect shape in FEA (exaggerated)

This imperfection is introduced into the beam's mesh by modifying the nodal coordinates through the adoption of a vector field. The modified shapes are obtained by scaling the first eigenvalue buckling mode shape for Euler buckling of a perfectly straight concentrically loaded column. The deformed shape (exaggerated) from the Eigenvalue analysis is shown in Figure 5.8.

Table 5.3 Maximum out-of-straightness imperfection for I and C1 beams

Overall Span (mm)	I-section		C1-section	
	δ_{max} (mm)	L/δ_{max}	δ_{max} (mm)	L/δ_{max}
1900	0.78	2440	0.27	7040
2500	2.86	870	0.80	3130
3000	1.95	1540	1.55	1930
3500	2.72	1290	1.72	2030
Average		1540	Average	3530
4100	$2.66 = 4100/1540$	1540	$1.16 = 4100/3530$	3530

As the imperfection for the longest beam span of 4100 mm would not be measured, it was assumed to have an average value based on the measured δ_{max} at four spans between 1900 mm and 3500 mm. This average value is approximated by expressing the measured δ_{max} as a function of L (e.g. for I-1900 it is $0.78 \cong L/2440$). For the I-section the average δ_{max} is $L/1540$ and for C1-section it is $L/3530$ when the span is 4100 mm. Reported in Table 5.3 are results for δ_{max}.

Imperfect shape 1

δ_{max}

Original perfect shape

$-\delta_{max}$
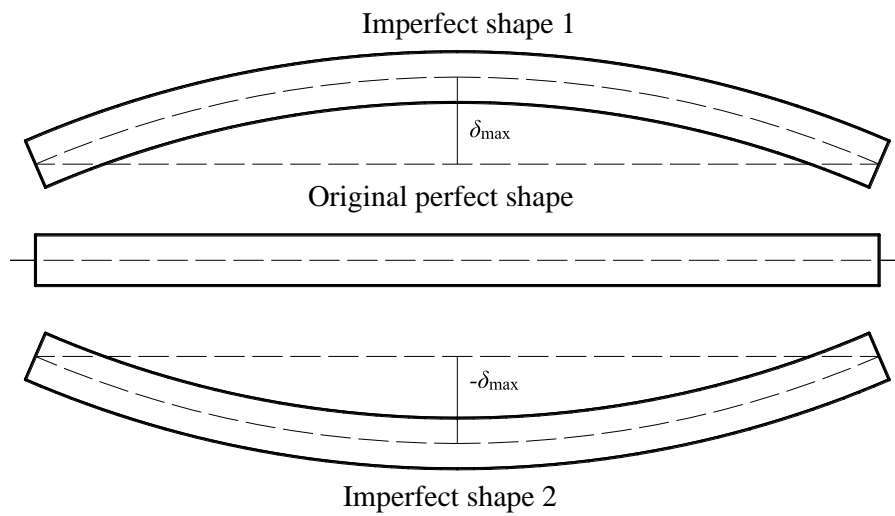
Imperfect shape 2

Figure 5.9 Two ways of introducing imperfect shapes

Figure 5.9 shows two possible directions for the imperfection. If the section has material properties that are symmetrical about both major and minor axes, the presence of either imperfect shape will give the same LTB response. However, as the sections have shown in Chapter 3 to have non-symmetrical elastic constant, their response will be different. As result of this finding both imperfect shapes will be numerically investigated. Nonlinear FEA will also be conducted on beams without this geometric imperfection ($\delta_{max} = 0$), since LTB failure will occur because of the changes in elastic constants.

5.3. Test results vs. eigenvalue analyses

Followed the FE modelling methodology, presented simulation was carried out for tested beam configurations (i.e. span lengths, material properties, vertical load positions). Configurations involved the five spans (L) of 1828, 2438, 2844, 3454 and 4064 mm. The overall section length, with overhangs, are 1900, 2500, 3000, 3500 and 4100 mm, giving an overhang length of 36, 31, 78, 23 and 18 mm at both ends. This test feature was also modelled. It will be shown in a sensitivity analysis in sub-section 5.5.6 that the overhang length does change the LTB resistance.

Each beam was tested with Shear Centre (SC) loading, followed by Top Flange (TF) loading after adjusting the loading disc to the required loading position. Bottom Flange (BF) loading was carried out, for convenience, by inverting the section, without changing the loading disc set-up, and in so doing the vertical load is applied to the bottom flange. The FE modelling follows this test procedure to simulate the different vertical load heights.

Let's now consider the I-section because the elastic constants were not the same in the four outstand flanges, the resistance for the load applied into the I1-I2 flanges (e.g. for TF loading) might be different to the case of TF loading into the I3-I4 flanges. Figure 5.10(a) shows the first loading case and Figure 5.10(b) presents the other when the section inverted. The FE results will be reported as case 1 for load positions $\big((1),(2),(6)\big)$ in Figure 5.10 and as case 2 for load positions $\big((4),(5),(3)\big)$. This represents the test procedure for the three vertical load positions of TF, SC and BF.
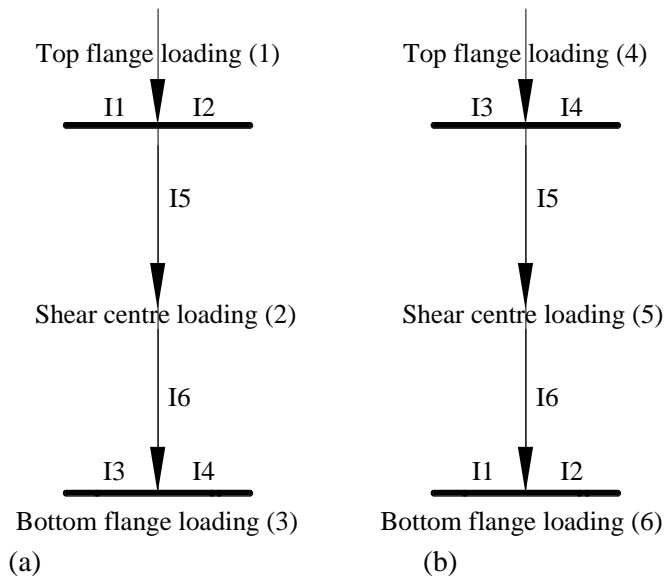
Figure 5.10 Two cases for beam in testing: (a) beam 'upright'; (b) beam 'inverted'

Table 5.4 FE results for I-section with EC1

Span L (mm)	$P_{cr,FEA,1}$ (kN) for load positions: (1), (2), (6) in Figure 5.10			$P_{cr,FEA,2}$ (kN) for load positions: (4), (5), (3) in Figure 5.10			$\dfrac{P_{cr,FEA,1}}{P_{cr,FEA,2}}$		
	TF	SC	BF	TF	SC	BF	TF	SC	BF
(1)	(2)	(3)	(4)	(5)	(6)	(7)	(8)	(9)	(10)
1828	3.86	5.38	8.24	3.92	5.46	8.14	1.02	1.01	0.99
2438	2.06	2.8	4.03	2.08	2.84	3.98	1.01	1.01	0.99
2844	1.54	2.05	2.84	1.56	2.07	2.82	1.01	1.01	0.99
3454	1.02	1.32	1.77	1.03	1.34	1.75	1.01	1.02	0.99
4064	0.75	0.95	1.22	0.75	0.95	1.21	1.00	1.00	0.99

Table 5.4 summarizes the eigenvalue buckling loads for case 1 in columns (2-4) for TF, SC and BF loading having spans given in column (1). Results for case 2 are given in columns (5-7). Comparing the buckling loads for a load position for case 1 with that equivalent for case 2 (e.g. column (2) vs. column (5)), it is found that the differences are 0% to 2% for TF, 0% to 2% for SC and are 1% for BF. It is concluded from the eigenvalue analysis that the change is insignificant. From this point forward, only numerical results for case 1 will be used when comparing FE results with the physical test results in Chapter 4.

Table 5.5 FE and test results for EC1 and EC2 with I- and C1-sections

I beam span (mm)	EC1						EC2					
	$P_{cr,FEA}$ (kN)			$P_{cr,e}$ (kN)			$P_{cr,FEA}$ (kN)			$P_{cr,e}$ (kN)		
	TF	SC	BF	TF	SC	BF	TF	SC	BF	TF	SC	BF
(1)	(2)	(3)	(4)	(5)	(6)	(7)	(8)	(9)	(10)	(11)	(12)	(13)
1828	3.86	5.38	8.24	3.79	6.12	9.12	9.49	12.6	18.8	6.29	NO LTB	NO LTB
2438	2.06	2.8	4.03	2.07	2.9	3.94	4.46	6.00	8.52	3.33	4.53	6.04
2844	1.54	2.05	2.84	1.64	2.09	2.59	3.03	4.06	5.61	2.10	3.24	4.48
3454	1.02	1.32	1.77	1.08	1.29	1.61	1.89	2.49	3.35	1.47	2.01	2.63
4064	0.75	0.95	1.22	0.72	0.9	1.11	1.3	1.68	2.19	1.03	1.34	1.68

C1 beam span (mm)	EC1						EC2					
	$P_{cr,FEA}$ (kN)			$P_{cr,e}$ (kN)			$P_{cr,FEA}$ (kN)			$P_{cr,e}$ (kN)		
	TF	SC	BF	TF	SC	BF	TF	SC	BF	TF	SC	BF
(1)	(2)	(3)	(4)	(5)	(6)	(7)	(8)	(9)	(10)	(11)	(12)	(13)
1828	4.01	5.95	9.56	3.31	5.54	7.57	9.88	14.1	22.1	5.02	8.44	12.7
2438	2.17	3.11	4.68	1.82	3.03	4.23	4.76	6.81	10.3	3.28	4.92	7.32
2844	1.61	2.26	3.28	1.45	1.96	2.65	3.14	4.52	6.66	1.87	3.49	4.29
3454	1.0	1.46	2.03	1.00	1.49	1.76	2.02	2.83	4.03	1.46	2.01	NO LTB
4064	0.77	1.02	1.38	0.65	0.80	1.11	1.37	1.81	2.61	1.01	1.26	1.59
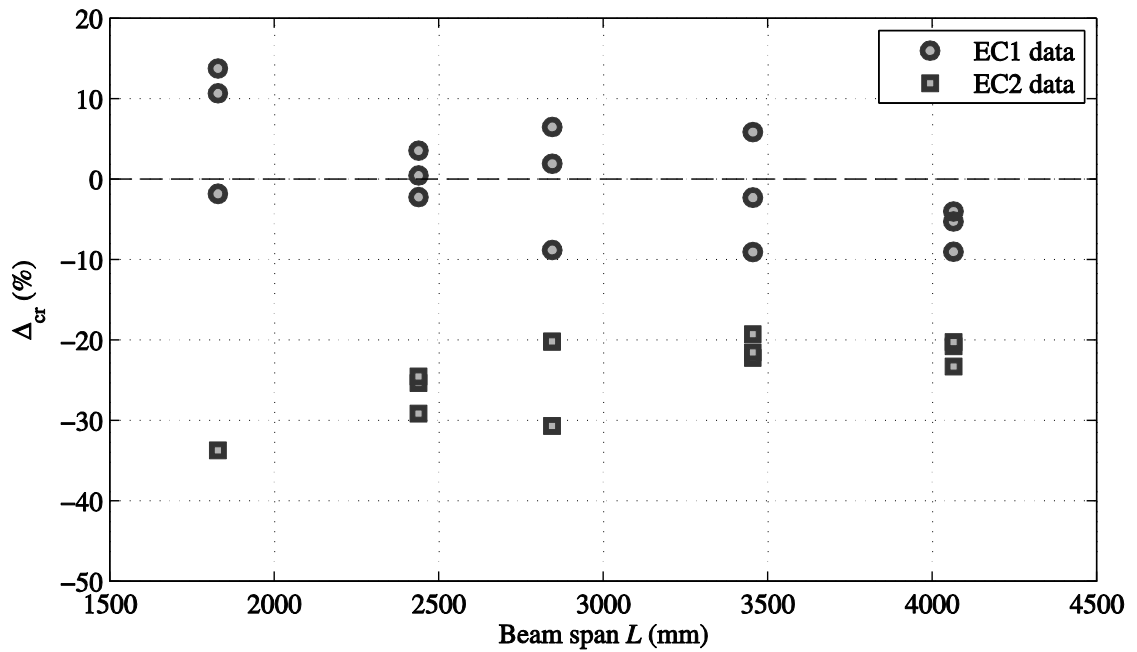
Figure 5.11 Plots for Δ_{cr} vs. span L for I beams with EC1 $(\bigcirc)$ and EC2 $(\square)$
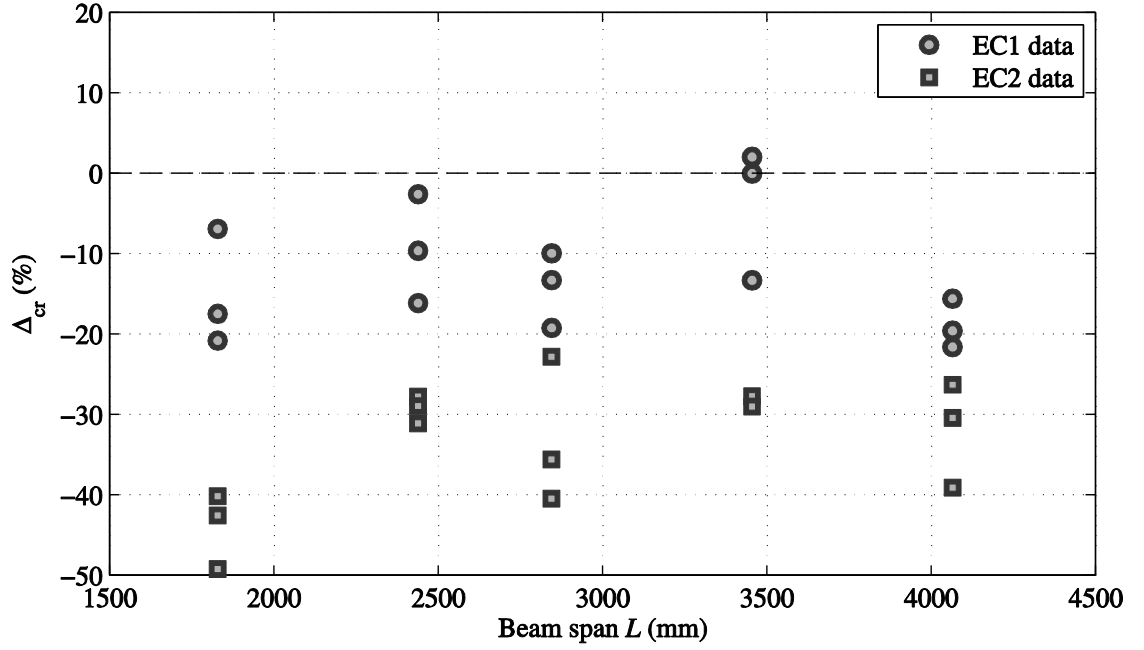
Figure 5.12 Plots for Δ_{cr} vs. span L for C1 beams with EC1 $(\bigcirc)$ and EC2 $(\square)$

Table 5.5 summarizes the FE and test results for EC1 and EC2 for I- and C1-sections. Column (1) is used to give span L. FE predictions are given in columns (2-4) for EC1 and (8-10) for EC2. Test results from Tables 4.5 and 4.6 in Chapter 4 are listed in columns (5-7) for EC1 and (11-13) for EC2. The differences between FE and test results are given by $\Delta_{cr} = (P_{cr,e} / P_{cr,FEA} - 1) \times 100\%$. This percentage ratio is plotted against span L in Figure 5.11 for the I beams and in Figure 5.12 for the C1 beams. It is seen from Figure 5.11 that for EC1 the FEA was able to give relatively good agreement with the test results; the difference is in range of -9% to 14%. Numerical results with EC2 are in the Δ_{cr} range of -34% to 19%. Figure 5.12 shows Δ_{cr} for the C1 beams are in range of -22% to 2% for EC1 and -49% to -26% for EC2.

One reason for the differences is due to the uncertainty of the inputting data in the FE model. G_{LT} has been assumed to be constant at 4.2 GPa. The summary of previous

157

studies in Table 3.15 has shown that this modulus of elasticity can be in the range of 3-5 GPa. From five coupon tests with material cut from the I-section, G_{LT} was determined to be from 3.66 GPa to 4.45 GPa in five material tests. The difference between the highest and the lowest measurement is 21.6%. It will be shown in sub-section 5.5.2 that a change of 20% in G_{LT} can increase or decrease the buckling resistance by over 10%. For C1-section, G_{LT} was measured to be between 4.52 GPa and 4.95 GPa for a 9.5% difference. It is worth mentioning here that Trumpf (2006) reported and used the lower G_{LT} of 3.1 GPa for his study with the same I-section. Other differences between FE simulation and test results are, of course, due to the inherent imperfections in the test set-up and test procedure that cannot readily be quantified.

5.4. Test results vs. nonlinear analyses for I-section

Only initial minor axis out-of-straightness imperfection was introduced into the FE model for the nonlinear analysis. Three nonlinear analyses were carried out for each of the three loading cases to involve the two imperfect shapes shown in Figure 5.9. The third analysis is without the geometric imperfection (i.e. $\delta_{max} = 0$).

The influence of imperfection can be found by examining Figure 5.13 for the load P vs. vertical deflection w. It can be shown for a specific beam configuration that the higher the imperfection is, the lower will be P at a same w. It is, however, not straightforward to quantify the level of influence of the imperfection on the LTB resistance.
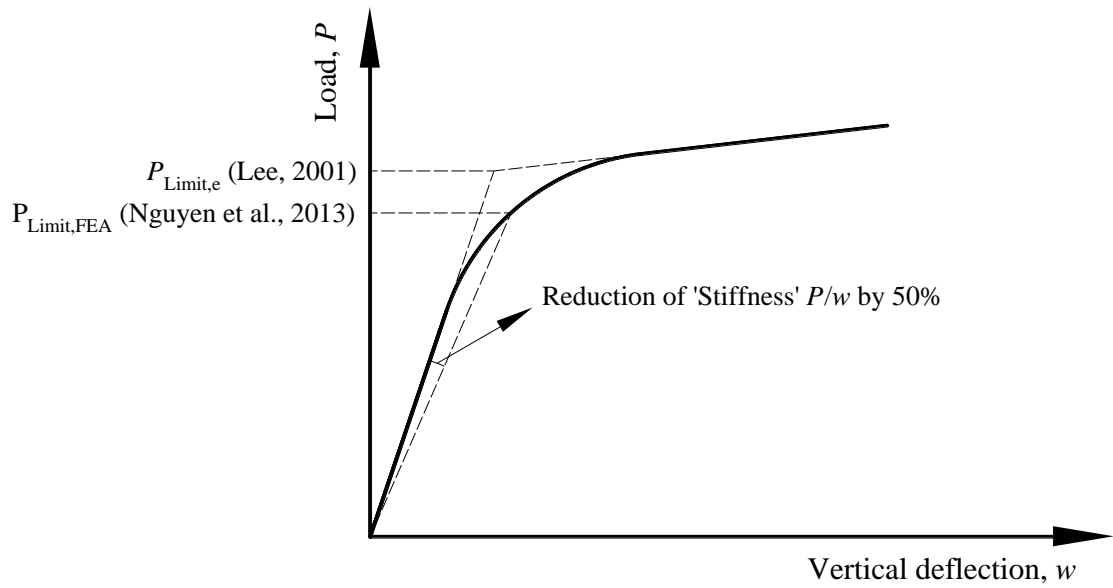
Figure 5.13 Definitions of limiting buckling load in Lee (2001) and Nguyen *et al.* (2013)

Because the FE model includes the main geometrical imperfection, there is a progresive loss of stiffness when the beam starts to twist and bend laterally from the beginning of loading. As seen in Figure 5.13 the FE buckling load is now not a critical load ($P_{cr,FEA}$) but a limiting value ($P_{Limit,FEA}$).

It is necessary to define what $P_{Limit,FEA}$ is. Singer *et al.* (1999) explain that there are a number of data reduction methods that can be employed to obtain an estimation. Lee (2001), in his Ph.D. work on the flexural-torsional buckling of T-sections, suggested that buckling load for his testing $P_{Limit,e}$ (Figure 5.13) can be estimated by the intersection point of extrapolating the two 'linear' lines for the 'pre-' and 'post-buckling' parts to the $P-w$ response. In his LTB experiments with I-beams, Stoddard (1997) choose to define the limiting buckling load to be the load when the mid-span rotation (twist) of the top flange attained 5 degrees.

To determine the LTB resistance of an end-loaded cantilever beam. Brooks and Turvey (1995) recorded their buckling load as the load at which the end-rotation started to grow rapidly. They, however, did not quantify what the rate of growth need to be. Mottram *et al.* (2003) and Afifi (2007) obtained critical buckling loads for their tested columns by applying the Southwell plot method (Southwell, 1932). Afifi also applied this method in her nonlinear FEA by commercial FEA software package ANSYS$^{®}$. It is well-known that Southwell plot method cannot be adopted to evaluate the influence of initial geometric imperfection as it is only able to predict the critical buckling load P_{cr}.

To define $P_{Limit,FEA}$, Nguyen *et al.* (2013) have proposed a 'stiffness reduction method' which is illustrated in Figure 5.13. The definition comes from the observation that, in nonlinear analyses, the beam stiffness by P/w is similar during pre-buckling for different sizes of imperfection. The limiting buckling load is defined as the P at which the secant stiffness has been reduced by 50%. To apply this method with testing requires readings for vertical deflection. This condition was not satisfied because, as mentioned in Section 4.5 of Chapter 4, when a beam fails the readings from the two displacement transducers attached at mid-span cannot give the exact movement of the shear centre. To also have limiting buckling loads from testing, the method adopted in this thesis was similar to that of Stoddard (1997) who used load-rotation measurement and a limiting angular of rotation.
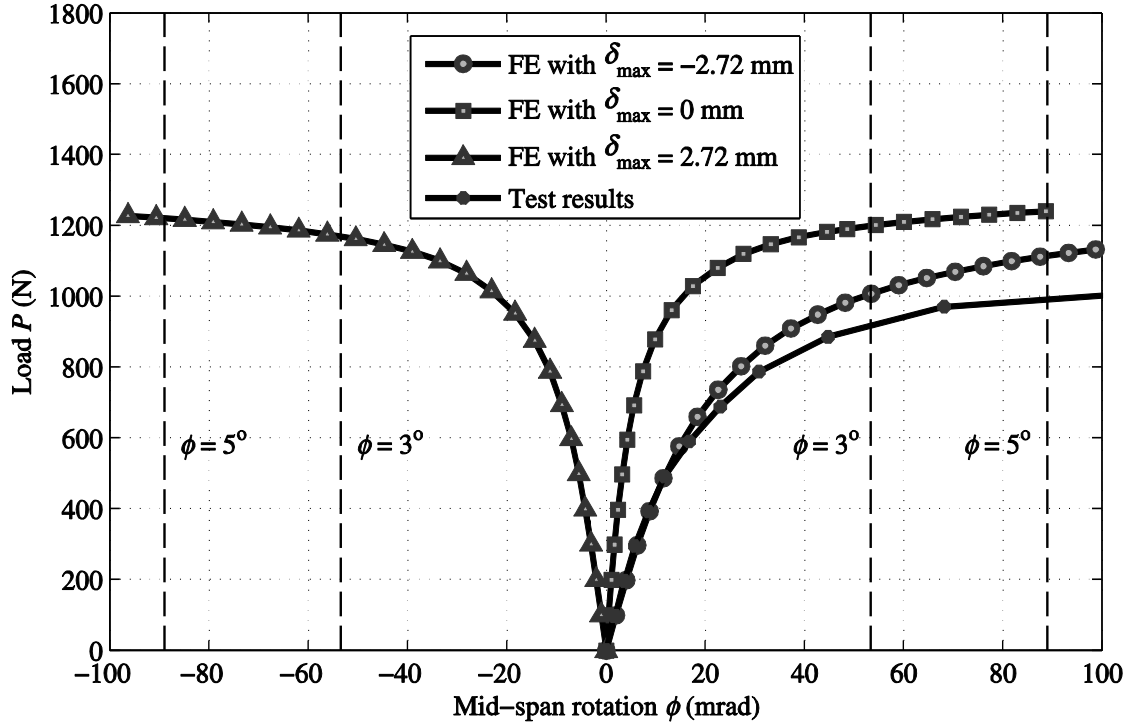
Figure 5.14 P vs. ϕ of beam EC1_3500_SC for FEA (with different δ_{max}) and test result

Figure 5.14 shows typical plots of load P vs. mid-span rotation ϕ for beam EC1_3500_SC. The plots with circular, square and rectangular symbols are from FEA having different δ_{max}. Plotting for test data is given by the asterisk markers. It is observed for testing that at a rotation of $\phi = 5^o$ as by Stoddard (1997), the beam has been deformed significantly into the post-buckling region. At this ϕ the FE curves are seen to have converged together. It is decided, for this evaluation method, to use a $P_{\text{Limit,FEA}}$ at $\phi = 3^o$.

It can be seen from Figure 5.14 that with $\delta_{max} = 0$ the beam has the same 'progressive failure' as predicted when $\delta_{max} = \pm 2.72$. Furthermore, with the same imperfection magnitude but in the opposite direction (e.g. $\delta_{max} = -2.72$ and $\delta_{max} = 2.72$) the $P-\phi$

responses are different because the I beam has varying elastic constants in the five panels. The two beam models twist in different direction.
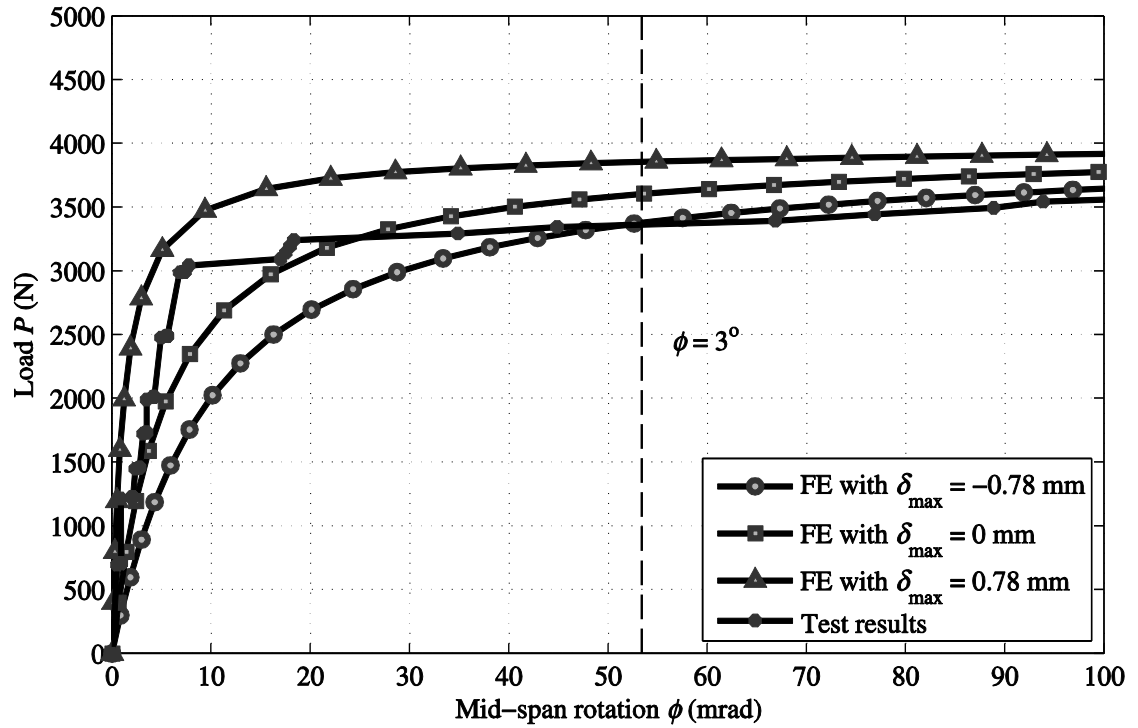
Figure 5.15 P vs. ϕ of beam EC1_1900_TF for FEA (with different δ_{max}) and test result

Figure 5.15 presents the same plots as in Figure 5.14 for beam EC1_1900_TF. It is observed that beam model with $\delta_{max} = 0.78$ mm had the highest resistance compared to other two models. This indicates that combined imperfections of geometry and material could create a condition where beam has a better response under loading than when there is no geometrical imperfection (i.e. $\delta_{max} = 0$).

It is found from Figure 5.15 that the two beam models with $\delta_{max} = -0.78$ mm and $\delta_{max} = 0.78$ mm failed to the same direction. This behaviour is different with that of beam EC1_3500_SC presented in Figure 5.14.

Table 5.6 Limiting buckling loads for FEA (with different $\delta_{\max}$) and tests for EC1

Span (mm)	TF				SC				BF			
	$P_{\text{Limit,FEA}}$ (kN)			$P_{\text{Limit,e}}$ (kN)	$P_{\text{Limit,FEA}}$ (kN)			$P_{\text{Limit,e}}$ (kN)	$P_{\text{Limit,FEA}}$ (kN)			$P_{\text{Limit,e}}$ (kN)
	$-\delta_{\max}$	0	$\delta_{\max}$		$-\delta_{\max}$	0	$\delta_{\max}$		$-\delta_{\max}$	0	$\delta_{\max}$	
(1)	(2)	(3)	(4)	(5)	(6)	(7)	(8)	(9)	(10)	(11)	(12)	(13)
1828	3.38	3.61	3.86	3.48	4.62	4.97	5.36	5.96	6.91	7.50	8.10	8.64
2438	1.56	1.93	1.81	2.10	2.05	2.58	2.44	2.50	2.80	3.52	3.39	3.83
2844	1.27	1.45	1.48	1.55	1.66	1.92	1.97	2.00	2.25	2.62	2.74	2.60
3454	0.81	0.95	0.92	0.96	1.00	1.20	1.17	1.04	1.28	1.53	1.51	1.33
4064	0.62	0.72	0.70	0.57	0.76	0.90	0.88	0.72	0.96	1.15	1.13	0.83

Table 5.7 Limiting buckling loads for FEA (with different $\delta_{\max}$) and tests for EC2

Span (mm)	TF				SC				BF			
	$P_{\text{Limit,FEA}}$ (kN)			PL (kN)	$P_{\text{Limit,FEA}}$ (kN)			$P_{\text{Limit,e}}$ (kN)	$P_{\text{Limit,FEA}}$ (kN)			$P_{\text{Limit,e}}$ (kN)
	$-\delta_{\max}$	0	$\delta_{\max}$		$-\delta_{\max}$	0	$\delta_{\max}$		$-\delta_{\max}$	0	$\delta_{\max}$	
(1)	(2)	(3)	(4)	(5)	(6)	(7)	(8)	(9)	(10)	(11)	(12)	(13)
1828	8.20	8.69	9.22	6.28	10.7	11.4	12.1	-	15.9	16.8	17.9	-
2438	3.34	4.10	3.89	3.28	4.40	5.44	5.22	3.53	6.17	7.67	7.47	5.71
2844	2.46	2.79	2.87	2.13	3.23	3.69	3.83	2.68	4.44	5.08	5.53	3.97
3454	1.47	1.75	1.70	1.32	1.89	2.28	2.22	1.49	2.52	3.04	3.00	2.06
4064	1.04	1.23	1.19	0.81	1.31	1.56	1.52	1.06	1.69	2.02	2.00	1.14

The limiting buckling loads from FEA ($P_{\text{Limit,FEA}}$) and experiment ($P_{\text{Limit,e}}$) for I beams with end boundary conditions EC1 and EC2 are presented in Tables 5.6 and 5.7. In the two tables, column (1) is used to give span L whilst FEA and test results are given in columns (2-5) for TF loading, (6-9) for SC loading and (10-13) for BF loading. For each group of loading case, the first three columns present $P_{\text{Limit,FEA}}$ for beams with three

different out-of-straightness imperfections expressed by the maximum imperfection $(-\delta_{max}, 0$ or $\delta_{max})$. The fourth column in each group gives $P_{Limit,e}$.

By comparing $P_{Limit,FEA}$ for a loading case, it can be seen that the size of δ_{max} has a significant influence. Difference between the highest and lowest (in terms of lowest) $P_{Limit,FEA}$ for TF_EC1 is between 7-24%. It is 8-26% and 8-22% for SC_EC1 and BF_EC1 respectively. It is also found that beams with $\delta_{max} = 0$ do not always give the highest $P_{Limit,FEA}$. This is illustrated in Figure 5.15 for the P vs. ϕ for EC1_1900_TF. This response reflects the outcome from combination of geometric and material imperfections on a beam. The differences when the end displacement boundary conditions are EC2 are seem to give a similar range from the three loading cases. They are 6-23%, 6-24% and 6-25% for TF, SC and BF, respectively.
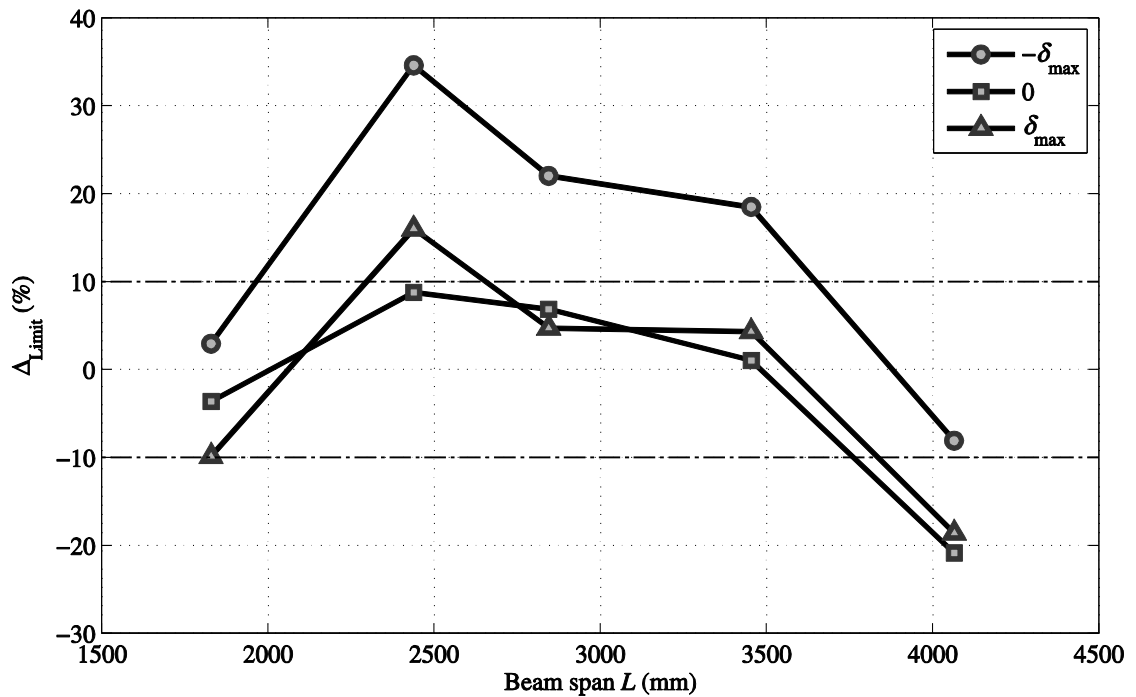
Figure 5.16 Plots of Δ_{Limit} vs. span L for TF_EC1
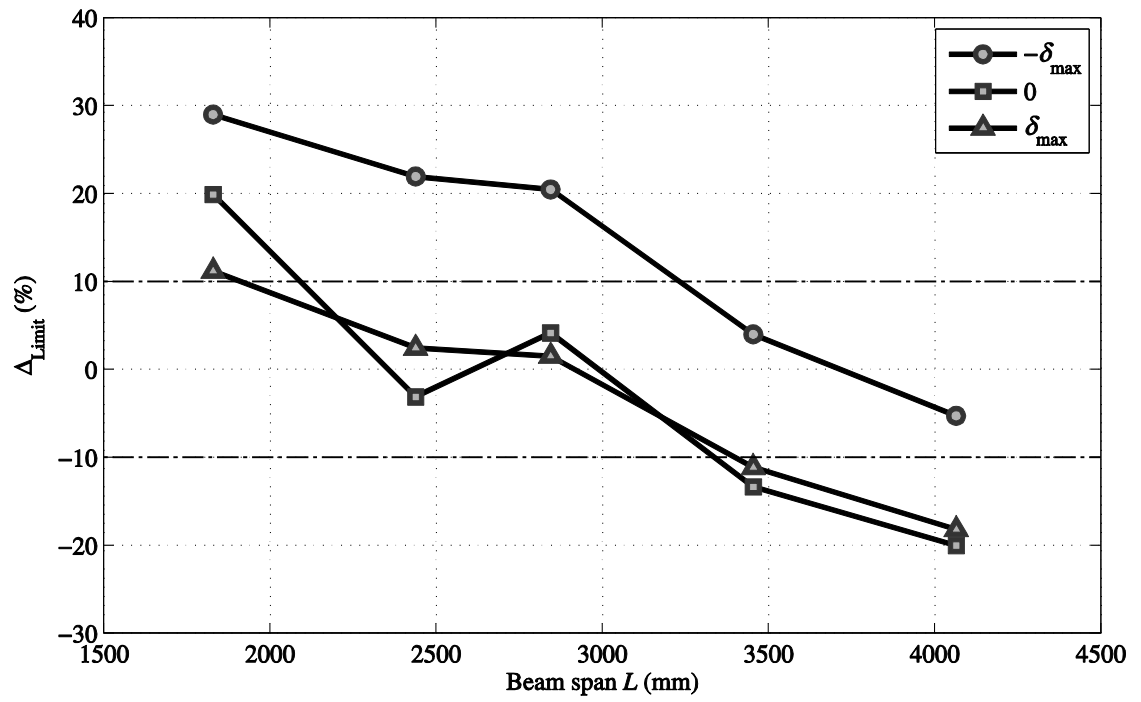
Figure 5.17 Plots of Δ_{Limit} vs. span L for SC_EC1
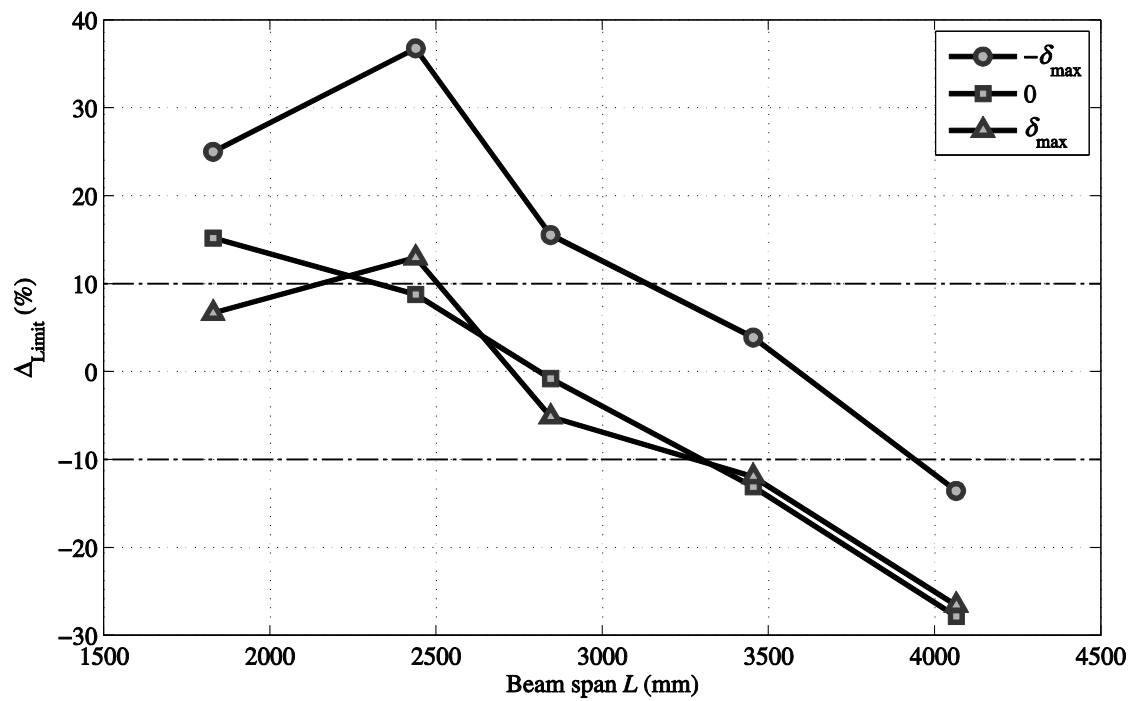
Figure 5.18 Plots of Δ_{Limit} vs. span L for BF_EC1
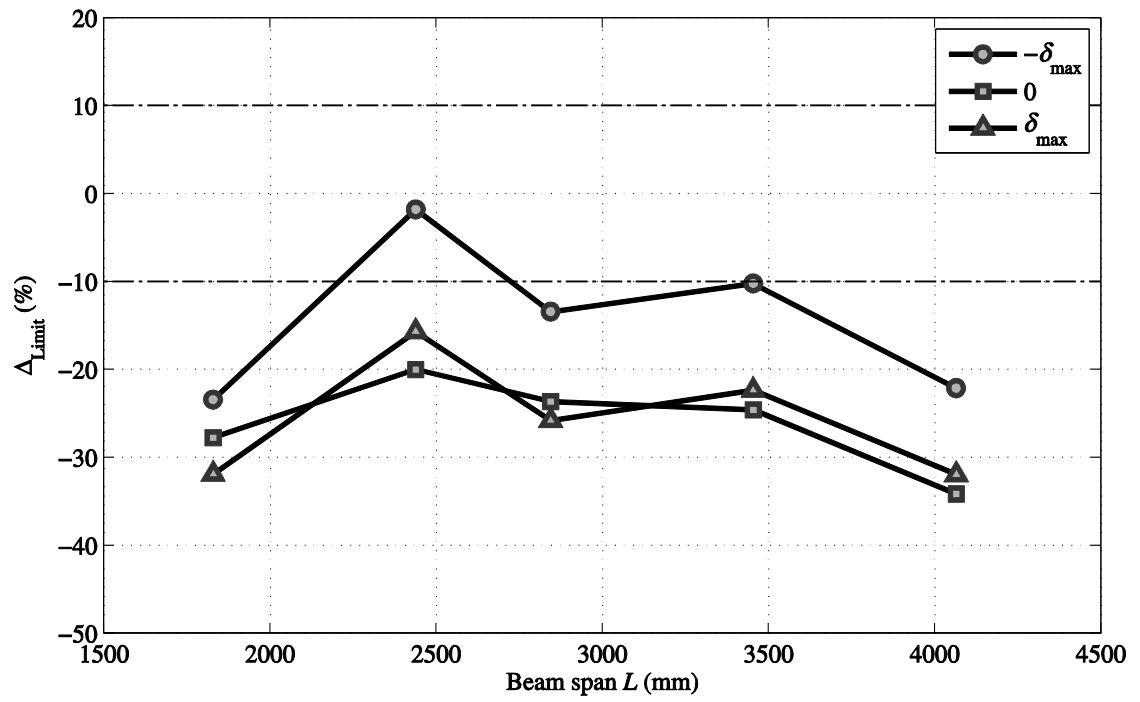
Figure 5.19 Plots of Δ_{Limit} vs. span L for TF_EC2
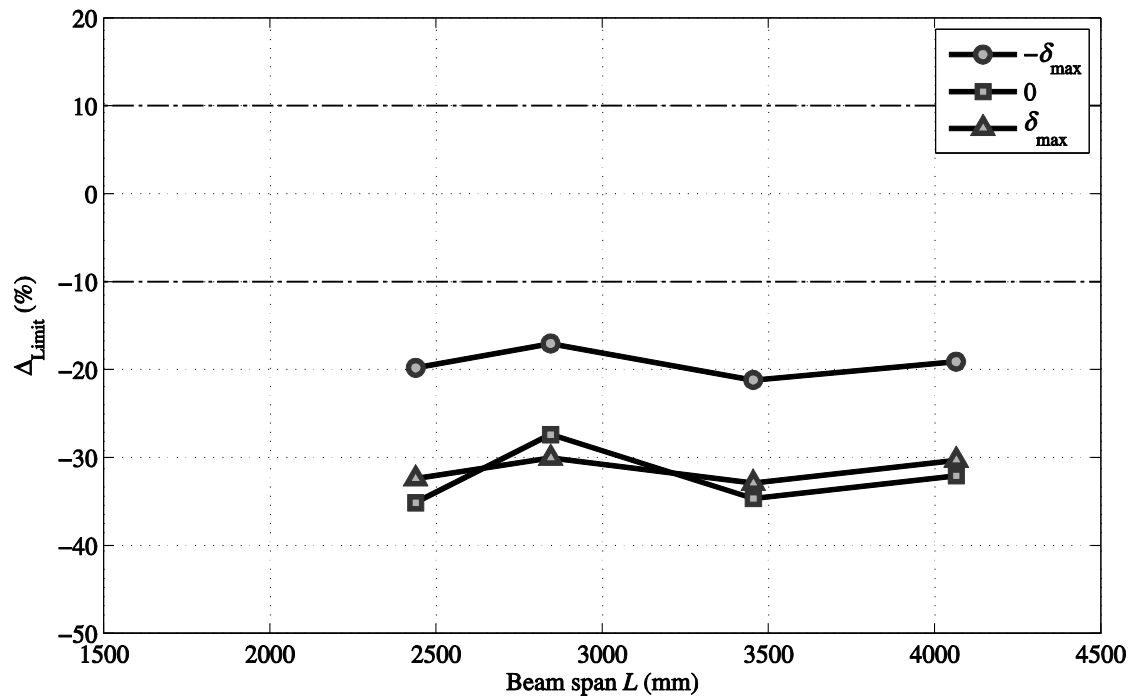
Figure 5.20 Plots of Δ_{Limit} vs. span L for SC_EC2
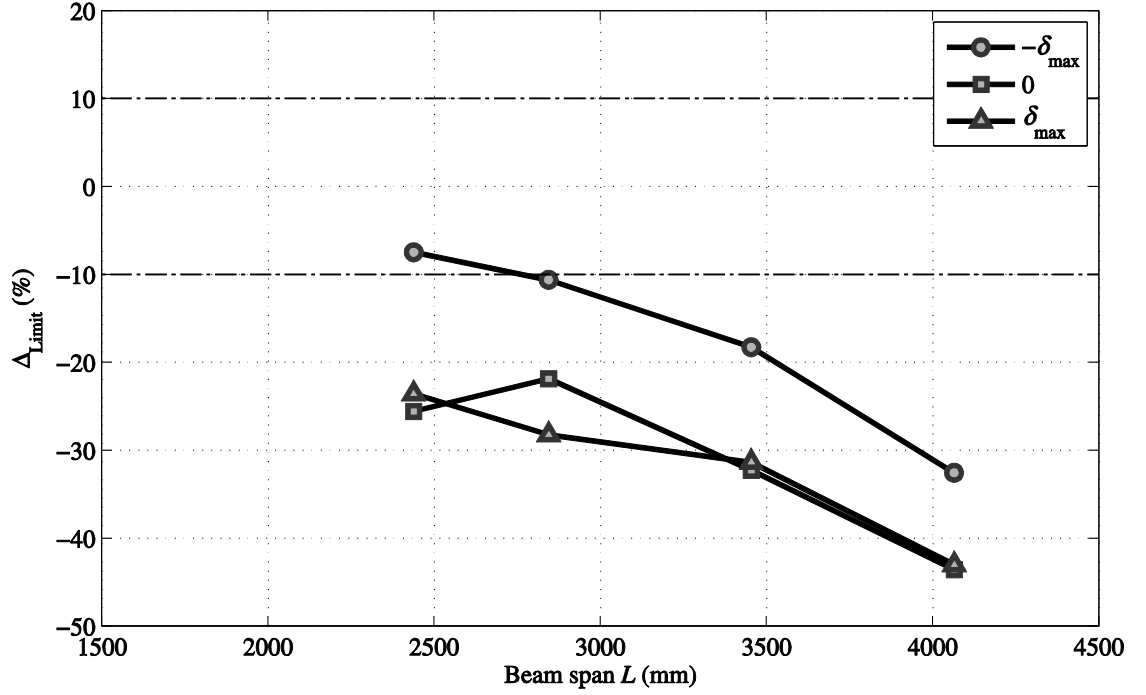
Figure 5.21 Plots of Δ_{Limit} vs. span L for BF_EC2

To compare $P_{\text{Limit,FEA}}$ with $P_{\text{Limit,e}}$ their difference is expressed, in percentage, by $\Delta_{\text{Limit}} = (P_{\text{Limit,e}}/P_{\text{Limit,FEA}}-1)\times 100\%$. Plotted in Figures 5.16 to 5.18 is Δ_{Limit} vs. L for loading case of TF, SC and BF and with EC1 end condition applied.

If it is assumed that a difference of $\pm10\%$ is for a good agreement, there are points (for each loading case) in the three figures that are within these limits. Equivalent plots with EC2 are presented in Figures 5.19 to 5.21. It is observed that the data point for EC2 cannot all lies within the good agreement limits.

Nonlinear analyses have shown that the LTB response is very sensitive to the magnitude of the initial geometric imperfection in the form of a minor axis half sine wave. Further investigations towards understanding the sensitivity of LTB resistance to changes in key parameters are presented in section 5.5.

5.5. Sensitivity analyses

These were carried out with a number of parameters to see how either $P_{cr,FEA}$ or $R_{Limit,FEA}$ changes. The parameters investigated are: 5.5.1 geometric shape of the section; 5.5.2 elastic constant; 5.5.3 geometric imperfection; 5.5.4 lateral load position; 5.5.5 vertical load height; 5.5.6 the overhang length.

5.5.1. Sensitivity of $P_{cr,FEA}$ with the geometrical modelling

It has been shown in Chapter 4 and Sub-section 5.2.3 that by modifying the mesh specification it is feasible to reliably compensate for the loss in torsional constant (I_t) when adopting the conventional constant thickness shell modelling. To investigate the sensitivity of $P_{cr,FEA}$ to the way a section is modelled, FE eigenvalue simulations have been carried out using the geometrical properties of the tested I-section.
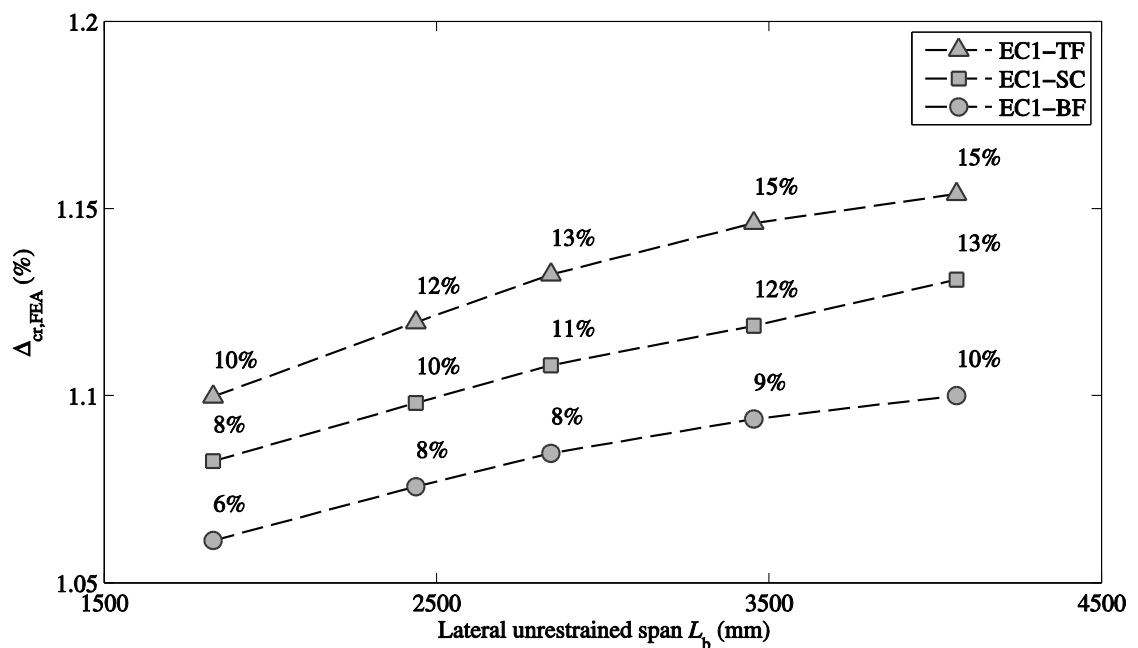
Figure 5.22 Sensitivity with geometrical modelling for EC1
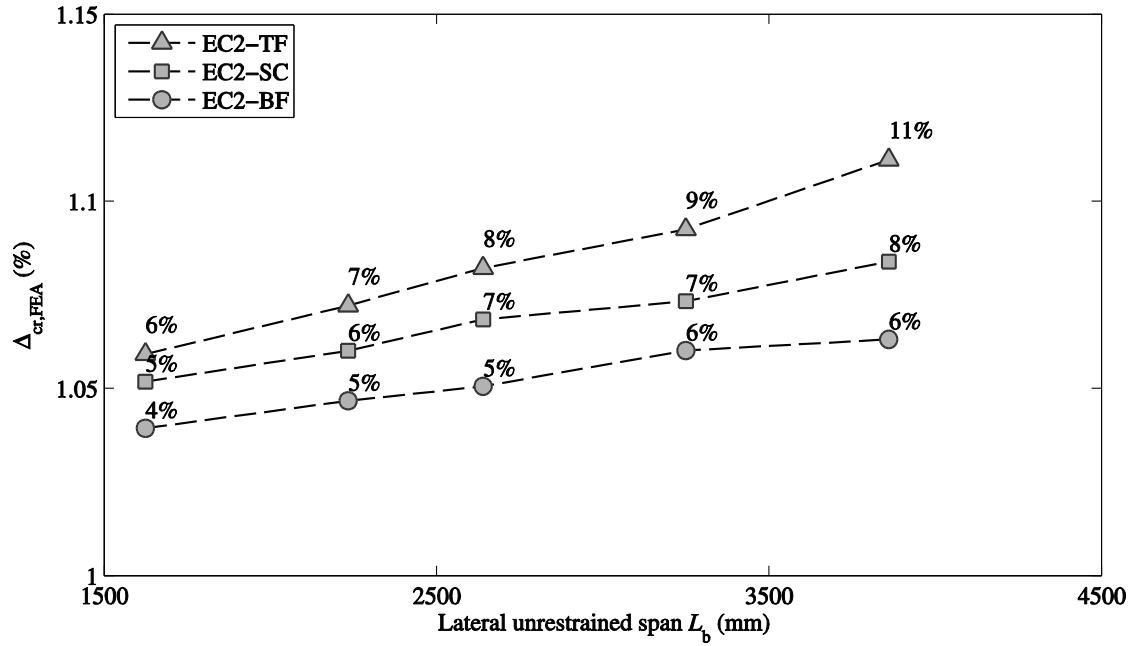
Figure 5.23 Sensitivity with geometrical modelling for EC2

In the first model adopted by Brooks and Turvey (1995), Turvey (1996), Qiao *et al.* (2003) and Shan and Qiao (2005) a section is formed from where the I-beams were built by three flat (constant thickness) panels. $P_{cr,FEA,1}$ is obtained from eigenvalue analysis with this model. In the second model that takes into account the fillet radius areas (Schleich *et al.*, 1998, Trumpf, 2006), the wall thickness local to the fillet regions is increased. This method is illustrated in Figure 5.1 and discussed in Sub-section 5.2.3. Critical buckling load from this improved model is given by $P_{cr,FEA,2}$ which is expected to be higher than $P_{cr,FEA,1}$ since the second model accounts for the additional resistance contribution from having fillet areas. The percentage difference between the two models is given by $\Delta_{cr,FEA} = (P_{cr,FEA,2} / P_{cr,FEA,1} - 1) \times 100\%$, and they are plotted in Figures 5.22 and 5.23 against the lateral unrestrained span L_b. For EC1 $L_b (= L)$ are 1828, 2438, 2844, 3454 and 4064 mm and with EC2 they ($L_b = L - 204$) are 1624, 2234, 2640,

3250 and 3860 mm. From the results in the figures, it is seen that the increase in $\Delta_{cr,FEA}$ is higher at longer spans. For changes to the vertical load height, the influence becomes more significant as the load moves from bottom flange to top flange. The effect of having EC1 is found to be higher than on having end conditions EC2. Differences for EC1 are from 6% to 15% while they are for EC2 between 4% and 11%.

This investigation shows that the way flange and web panels are modelled can have a significant effect on the prediction of LTB resistance. The second model is recommended should FEA be required to be validated by experimental results. When buckling resistances are generated for the purpose of design validation, it is proposed that the first modelling method be adopted, as it will give a lower numerical prediction, which will be conservative. The calculation of the three geometrical properties I_z, I_w and I_t in the closed-form equation (Eq. 2.1) is usually done with fillet areas ignored.

5.5.2. Sensitivity of $P_{cr,FEA}$ with elastic constant

The determination of G_{LT} is difficult for reasons discussed in Chapter 3. Values from 16 sources collated in Table 3.15 show its value can mostly lie in the range from 3 to 5 GPa. This sensitivity analysis focuses on changing G_{LT} with the assumption that other three in-plane elastic constants (E_L, E_T and ν_{LT}) remain unchanged and take the values given in Table 5.1. By changing G_{LT} in increments of 0.2 GPa, 11 $P_{cr,FEA}$s were obtained at each span. By changing the vertical load heights from BF to TF further $P_{cr,FEA}$s were generated.
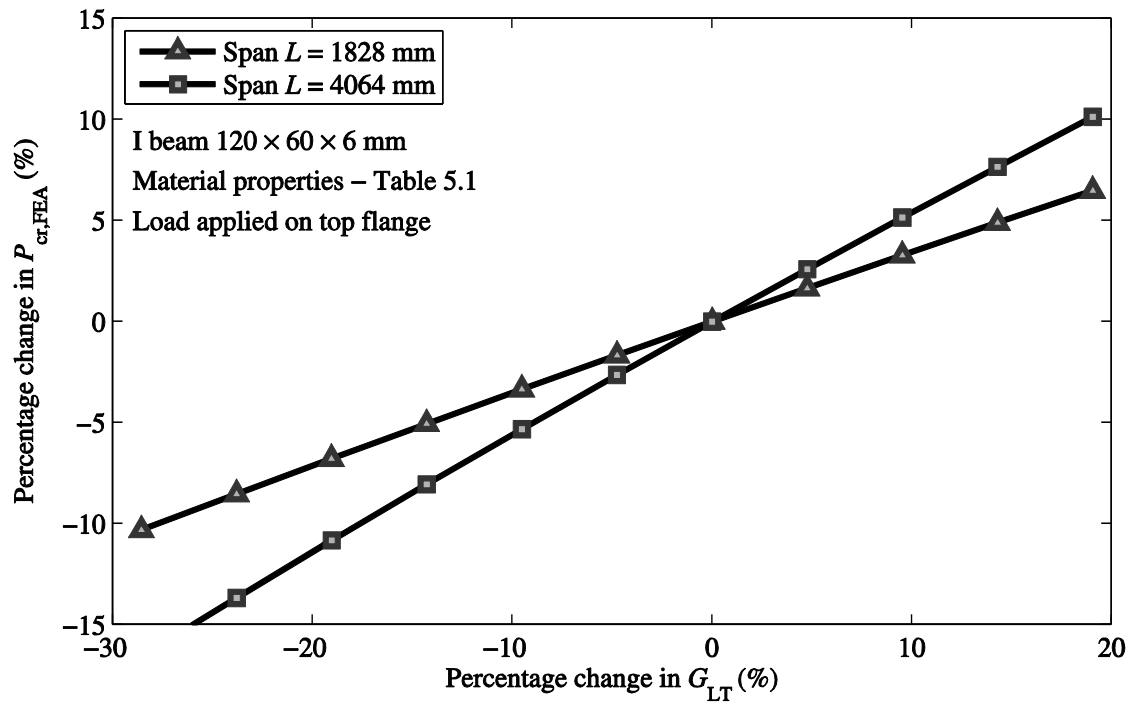
Figure 5.24 Change in $P_{cr,FEA}$ vs. G_{LT} for TF loading at two span lengths
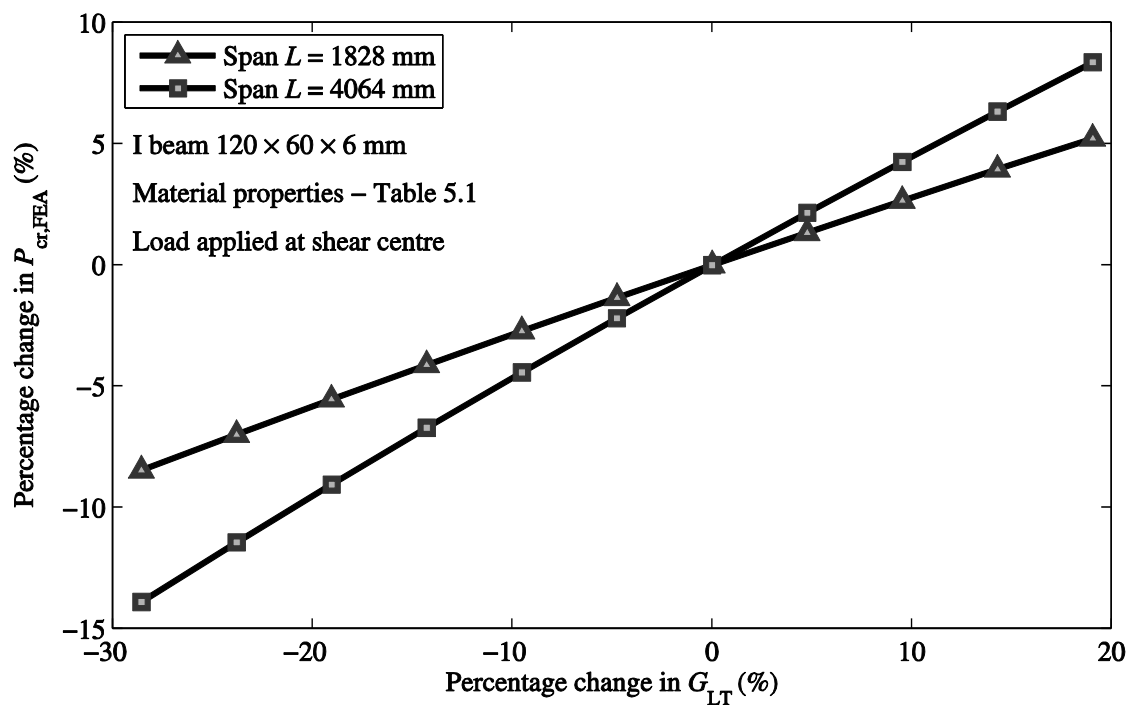
Figure 5.25 Change in $P_{cr,FEA}$ vs. G_{LT} for SC loading at two span lengths
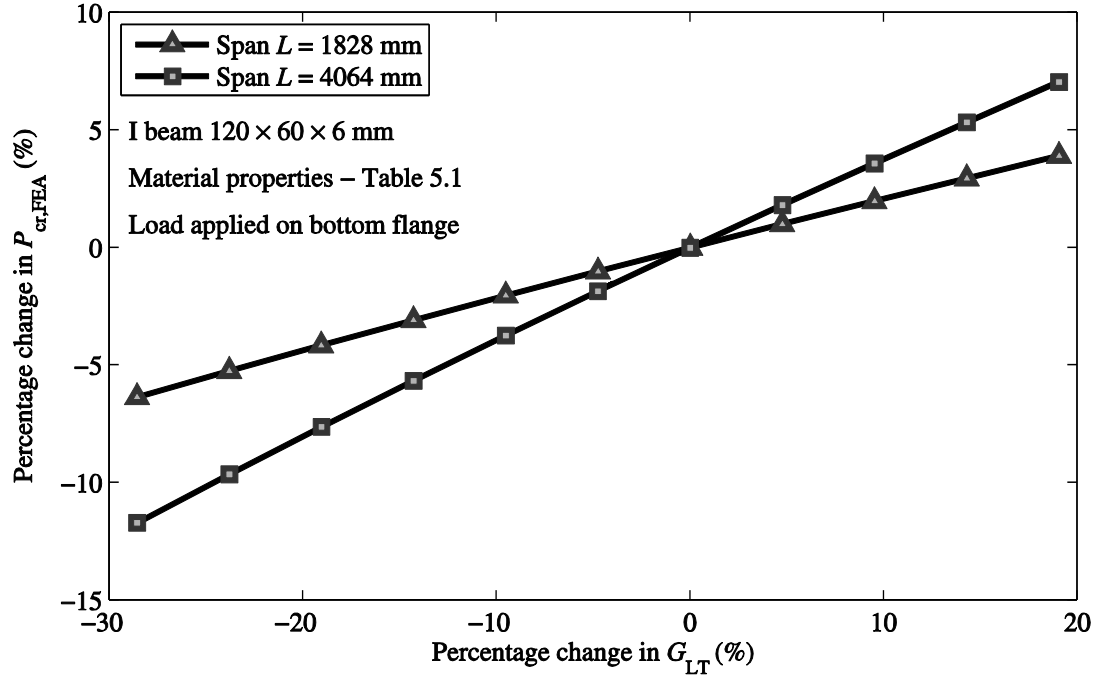
Figure 5.26 Change in $P_{cr,FEA}$ vs. G_{LT} for BF loading at two span lengths

To show the change with G_{LT} the percentage increases/decreases in $P_{cr,FEA}$ from $(P_{cr,FEA} / P_{cr,FEA,base} - 1) \times 100\%$ are plotted against the percentage change in G_{LT} from $(G_{LT} / G_{LT,base} - 1) \times 100\%$. The base value for $G_{LT,base}$ is 4.2 GPa which is the mean measured, and with this shear modulus the eigenvalue analysis gave $P_{cr,FEA,base}$. Figure 5.24 shows the plots for TF loading at the two spans of 1828 mm and 4064 mm. Figures 5.25 and 5.26 give the equivalent plots for SC and BF loading, respectively. Irrespective of the loading case it is found that the change in G_{LT} has a higher effect on LTB resistance at the shorter span. For TF loading, the change is -10 % to 7% at 1828 mm and is -17% to 10% at 4064 mm. Changing under loading case SC is -9% to 5% (1828 mm) and -14% to 8% (4064 mm). For BF it is -6% to 4% (1828 mm) and 12% to 7% (4064 mm). The change in $P_{cr,FEA}$ is also more significant as the load position moves from BF to TF. This parametric study shows that $P_{cr,FEA}$ is significantly influenced by

172

the choice of G_{LT}. Varying G_{LT} from 3 GPa to 5 GPa, it is revealed that the critical buckling load will increase by up to 17 % at $L = 1828$ mm and by up to 27% at the longer span. To validate FE predictions with test results, it is important to characterize the in-plane shear modulus properly.

5.5.3. Sensitivity of $P_{Limit,FEA}$ with geometric imperfection

To investigate the sensitivity of $P_{cr,FEA}$ with a change in the initial geometric imperfection, nonlinear analyses have been conducted with beam I-2500 having a point load applied at the shear centre. The δ_{max} is considered to be varying from 0 mm to 10 mm (or 0 to $L/250$). This imperfection was introduced into the FE's mesh with lateral initial deformation that would give the highest effect on LTB failure (i.e. the direction for $-\delta_{max}$ as shown in section 5.4).
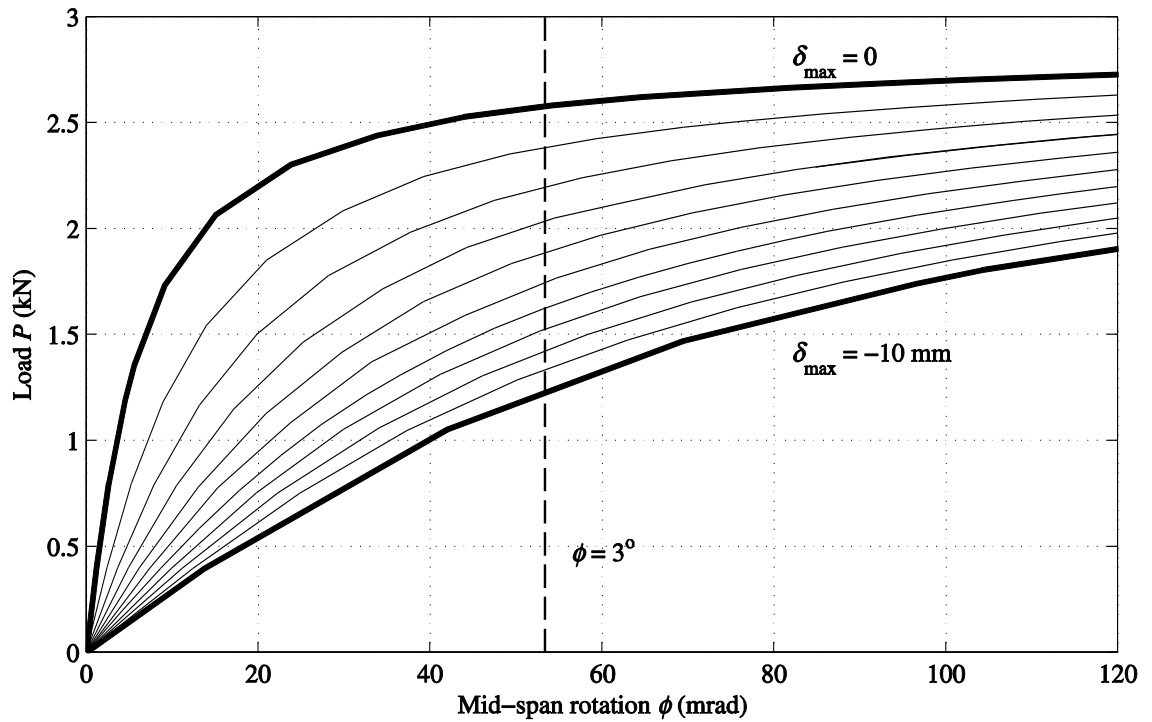
Figure 5.27 Load vs. mid-span rotation curves for I-2500_EC1_SC with δ_{max} changing
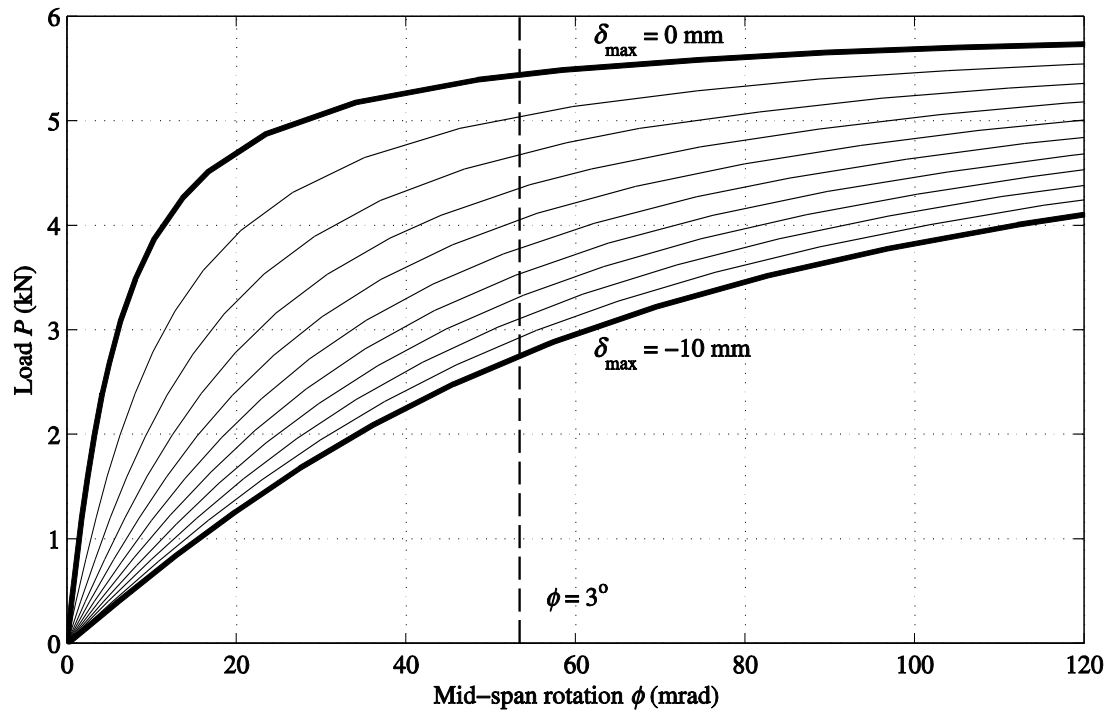
Figure 5.28 Load vs. mid-span rotation curves for I-2500_EC2_SC with δ_{max} changing
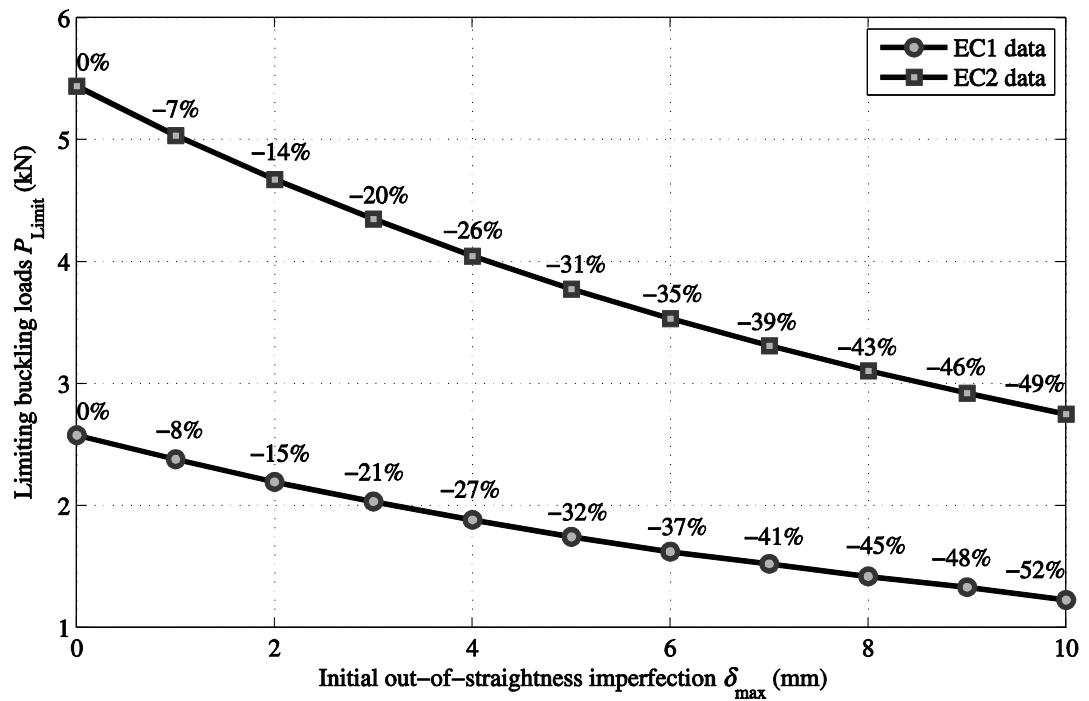
Figure 5.29 Limiting buckling loads of I-3500_SC for EC1 and EC2 with δ_{max} changing

Figures 5.27 and 5.28 show 11 curves for P vs. ϕ with end conditions EC1 and EC2. Moving from one curve to the next is for a 1 mm change in $\delta_{\max}$. The outer two curves for $\delta_{\max} = 0$ mm and -10 mm are highlighted using a bolder line. To establish what $P_{\mathrm{Limit,FEA}}$ is, the author takes P when the mid-span rotation attains 3 degrees. This limit for ϕ is given by a vertical dashed line in Figures 5.27 and 5.28. Figure 5.29 presents value of $P_{\mathrm{Limit,FEA}}$ vs. $\delta_{\max}$ for EC1 and EC2. Curve for EC1 uses a circular symbol whilst that for EC2 has a rectangular shape. The $P_{\mathrm{Limit,FEA}}$ is compared using the $\delta_{\max} = 0$ mm prediction and the percentage difference is written above the data point.

It is seen in Figures 5.27 and 5.28 that the beam's response will change significantly with an increase in $\delta_{\max}$, the variation is most stark at the lower loads. For example, P for the same mid-span rotation of 20 mrad (over 1 degree) with $\delta_{\max} = 0$ mm is found to be three times to that with $\delta_{\max} = -10$ mm. When ϕ is 60 mrad the change in P is double. As P increases, the curves are seen to be convergent.

The maximum initial out-of-straightness imperfection allowed by ASTM D3917 (ASTM, 2012a) is $D = L/240$ which is 10.4 mm for I-2500. This allowance (D) is slightly higher than the highest imperfection numerically investigated. It is found from Figure 5.29 that should a member in possesses this magnitude of geometric imperfection its LTB capacity decrease 50% compared to that without imperfection which is significant.

BS EN 13706-2 (BSI, 2002b) gives the allowance of $D = 0.0005L^2$ (D and span length L in metres) for this imperfection. Letting L be 2500 mm this standard allows $\delta_{\max}$ is 3.1 mm. It can be seen from Figure 5.29 that if a member possesses this imperfection, the LTB resistance would decrease 15% and this seems to be more appropriate as an

upper limit to this geometric imperfection. It is found from Figure 5.29 that the influence of the geometric imperfection is almost independent from the change for displacement boundary conditions for lateral flexure. It can be drawn from this investigation that the influence of $\delta_{\max}$ must be taken into account when analysing the LTB problem of PFRP beam.

5.5.4. Sensitivity of $P_{\text{Limit,FEA}}$ with change of lateral load position

When a beam is subjected to a point load that is offset laterally from the plane of the shear centre its response will be influenced by the introduction of an additional torque. This influence is evaluated by conducting nonlinear analyses with beam I-3000 having EC1 or EC2, and load applied on TF. The initial out-of-straightness geometric imperfection is for the Euler buckling shape with $\delta_{\max} = -1.95$ mm taken from Table 5.3 for the worst case.

Figure 5.30 shows numerical results from the nine lateral load positions on top flange. In this figure, the load applied on the vertical plane of Shear Centre (SC) is denoted as P_0. The other eight positions are offset by 3mm, 5 mm, 10 mm and 15 mm from P_0 in both directions and are labelled P_3, P_5, P_{10}, $P_{15,}$ P_{-3}, P_{-5}, P_{-10} and P_{-15}. The subscript defines the distance in millimeters from the SC plane. The figure also shows the positive directions for axis rotation UR_x and vertical and lateral deflections U_z and U_y. Labels for each flange outstand of I1-I4 are also presented. These flange outstands have the different value of longitudinal modulus of elasticity E_L listed in Table 5.1.
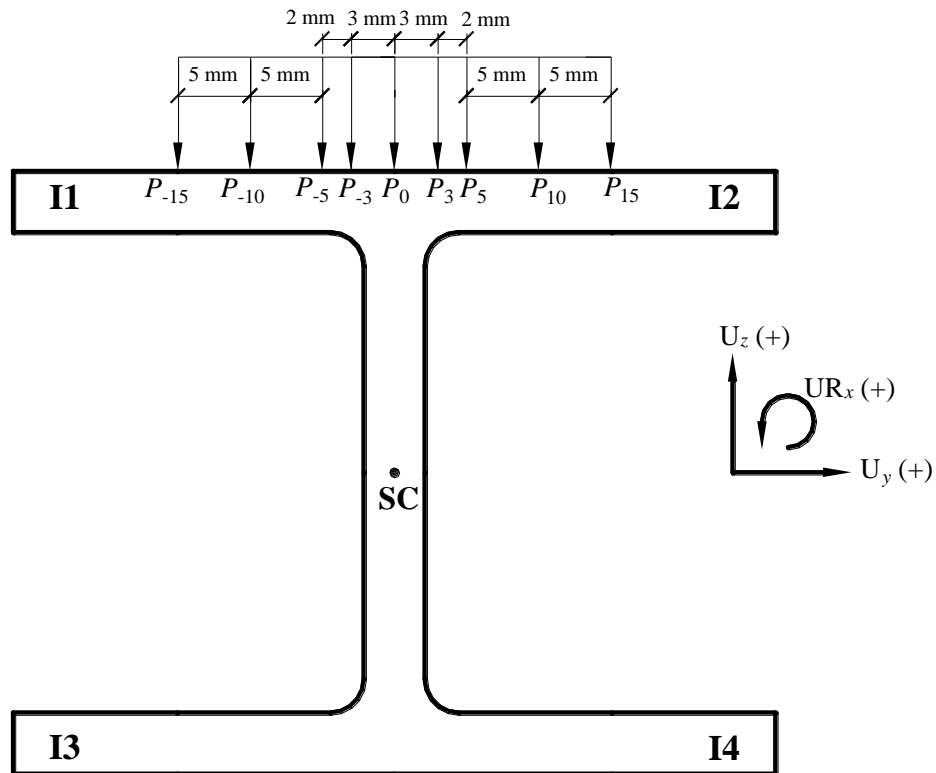
Figure 5.30 Lateral load positions on top flange for I-section (not to scale)
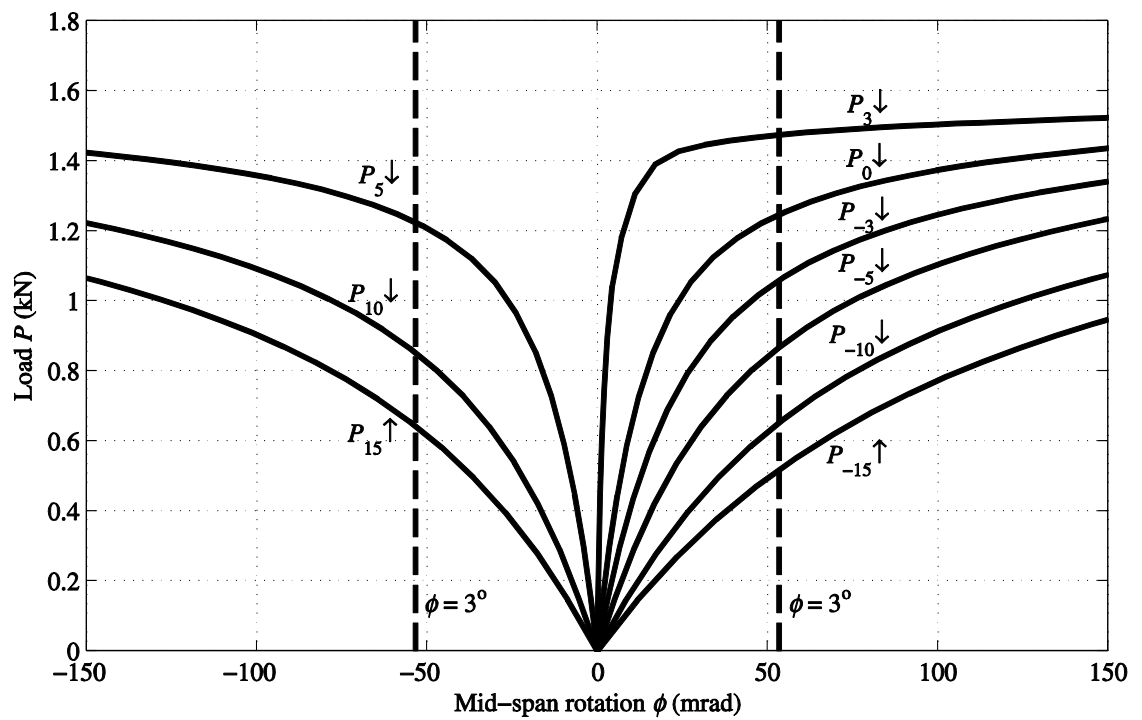
Figure 5.31 P vs. ϕ for I-3000-TF_EC1 with different lateral load positions
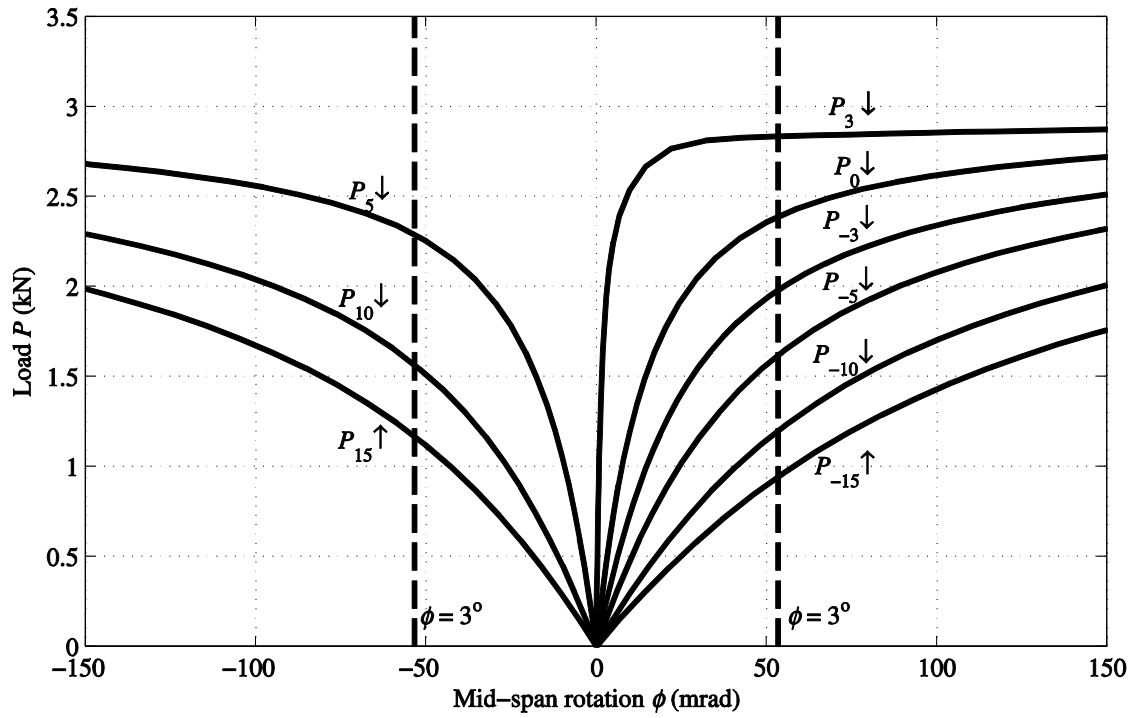
Figure 5.32 P vs. ϕ for I-3000-TF_EC2 with different lateral load positions

Figures 5.31 and 5.32 present the $P-\phi$ curves for the nine loading positions with end conditions EC1 and EC2, respectively. The load label (e.g. P_0) is given with an arrow pointing toward its $P-\phi$ curve. It is seen in both figures that for load position P_0 the beam twists to the left-side positive direction for ϕ (i.e. $UR_x > 0$) because the elastic constants are unsymmetrical in the flange outstands and the imperfection was introduced to the left-side. Beams with loads applied eccentrically on the right-side for P_{15}, P_{10} and P_5 deformed to the right (ϕ is negative). This shows that the effect of load eccentricity for these three loading cases outweighs the combined effect of geometric and material imperfections. At load eccentricity of 3 mm to the 'right' (i.e. P_3) beam started to fail to the 'left'. This indicates that the effect of lateral load eccentricity is now lesser than the combined geometric-material imperfections. From this loading point

178

towards the left beam will, of course, fail to the left. This is shown on the figure that

beams with P_{-3}, P_{-5}, P_{-10} and P_{-15} failed in the same direction with that for P_0.

It is observed that at the load eccentricity P_3, the beam has a response and resistance

that is the higest. Such a combination of imperfections, which can exist in reality, have

put the beam into a 'perfect' state where beam will fail at a significantly higher load

than expected or not go unstable. This finding explains what Mottram (1992a) has found

from 35 repeated LTB tests, on a single span PFRP I-beam, that they can have

significantly different buckling resistances with the highest nearly doubles the lowest.

This investigation could also (partly) explains there were five 'NO LTB' failure beam

configuration in Chapter 4. The presence of some test results that shown to be

significantly higher than the predictions might also due to this reason.
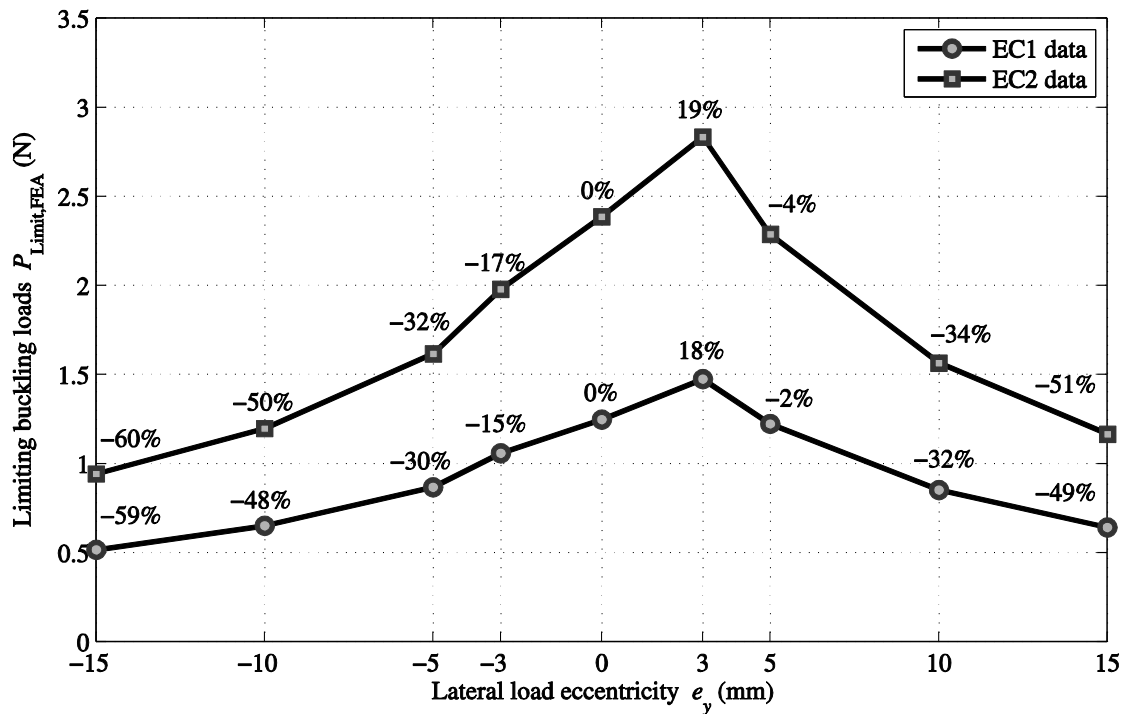
Figure 5.33 Influence of lateral load eccentricity on $P_{\text{Limit,FEA}}$ for I-3000-TF

The $P_{\text{Limit,FEA}}$s obtained at $\phi = 3^{\circ}$ are plotted against the lateral load eccentricities e_ys in Figure 5.33. Curve for EC1 has the circular symbol points and that for EC2 has the rectangular shape. Using $P_{\text{Limit,FEA}}$ for when $e_y = 0$ as reference, the $P_{\text{Limit,FEA}}$s can be given a difference value besides their symbol. It is found that the $P_{\text{Limit,FEA}}$ for load eccentricity P_3 is highest amongst nine loading cases. For the same magnitude of e_y, say ± 3 mm the beam has a different $P_{\text{Limit,FEA}}$. While the limiting buckling load for P_3 is 19% higher than P_0, that for P_{-3} is 15% lower. The shape of the two curves shows that change in Figure 5.33 show $P_{\text{Limit,FEA}}$ is not influenced by having end conditions of EC1 or EC2.

5.5.5. Sensitivity of $P_{\text{Limit,FEA}}$ with change of vertical load height

LTB resistance is influenced by the vertical distances of load (z_g) from the shear centre due to the additional torque about the longitudinal centroidal axis that is generated from the lateral movement of the vertical point load when instability happens. The investigation has been conducted using eigenvalue analysis (Nguyen *et al.*, 2013). This particular parametric study has showed that a change in load height had a more significant effect on resistance when a beam is of PFRP than if of structural grade steel.

This sub-section further the investigation by performing a nonlinear analysis with beam I-3500-EC1 having the point load moved from TF to BF in 12 equal increments. Figure 5.34 shows the $P - \phi$ relationships with EC1 and EC2 end boundary conditions. Curves for TF to BF with EC1 are plotted between the two curves labelled BF_EC1 (bottom flange loading for EC1) and TF_EC1, having thicker line width. Curves for TF to BF with EC2 are similarly presented.
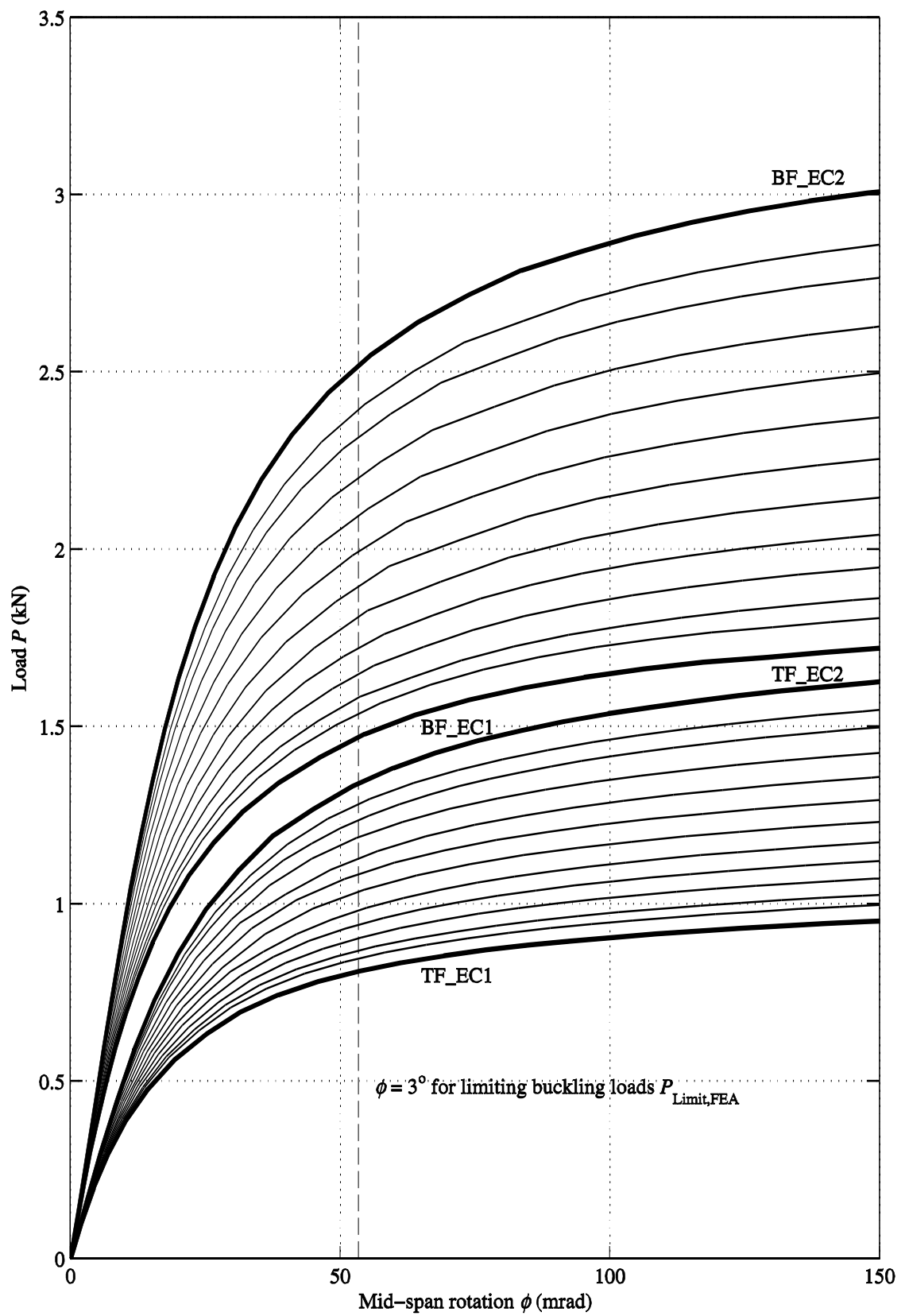
Figure 5.34 Load vs. mid-span rotation for I-3500 with EC1 and EC2
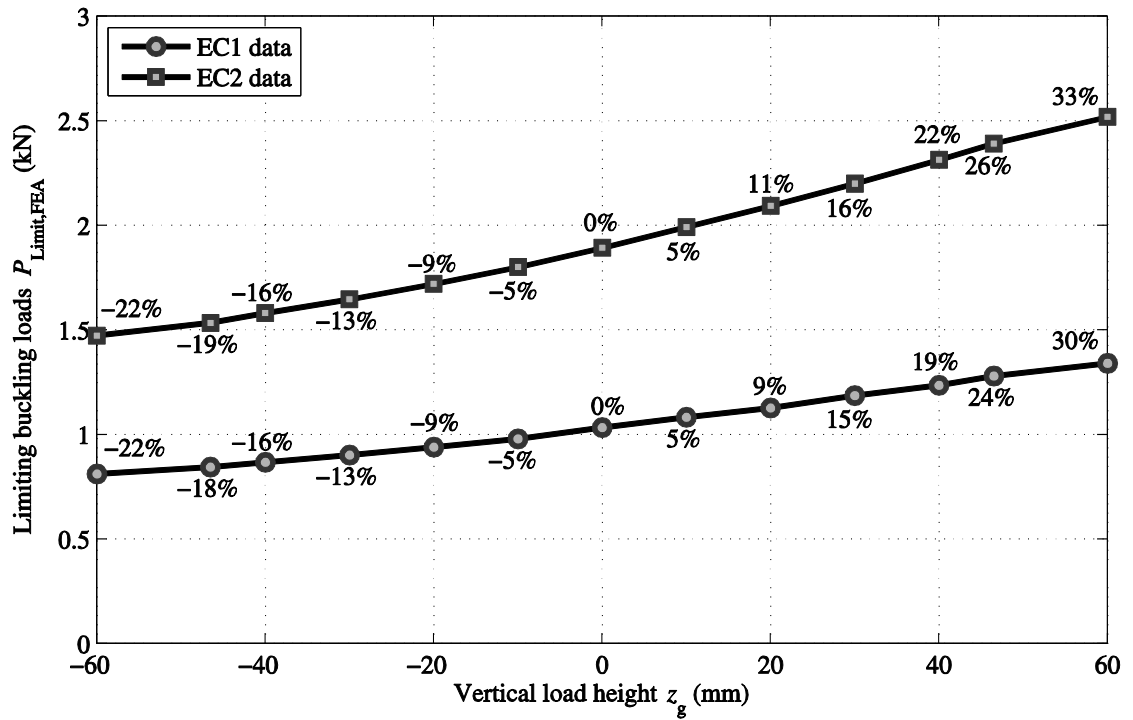
Figure 5.35 Limiting buckling load vs. vertical load height for I-3500 with EC1 and EC2

It is found that a load height change affects the deformation significantly. To investigate the influence of load height on the limiting buckling load, $P_{\mathrm{Limit,FEA}}$ was obtained using the same data analysis method of Section 5.4 and is why there is a vertical dashed line at $\phi = 3^{\circ}$ in Figure 5.34. Figure 5.35 reports $P_{\mathrm{Limit,FEA}}$ plotted against the vertical load height z_{g}. The percentage differences relative to the SC load height are given above the data points. $P_{\mathrm{Limit,FEA}}$ is found to reduce by 20% when load moves from SC to TF and increase by 30% when moving down from SC to BF. The curves in Figure 5.35 also show that the influence of load height does not seem to be affected by the change in end boundary conditions.

5.5.6. Sensitivity of $P_{cr,FEA}$ with overhang length

LTB resistance is influenced by the overhang length (Figure 5.36) that extends beyond the end supports. This change in response is due to an increase in the effective warping restraint as the overhang length grows (Stoddard, 1997). To investigate this influence eigenvalue analyses were conducted with the measured I section properties at a fixed span (L) of 1500 mm and with EC1 end conditions. The overhang length parameter ranged from 0 mm to 1250 mm, increasing in increments of 50 mm. This analysis gives 26 FE models having overall length $L_{Overall}$ from 1500 mm to 4000 mm.
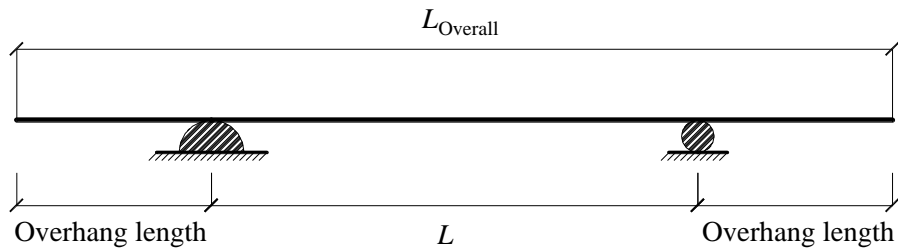
Figure 5.36 Illustration for test beam with overhang length
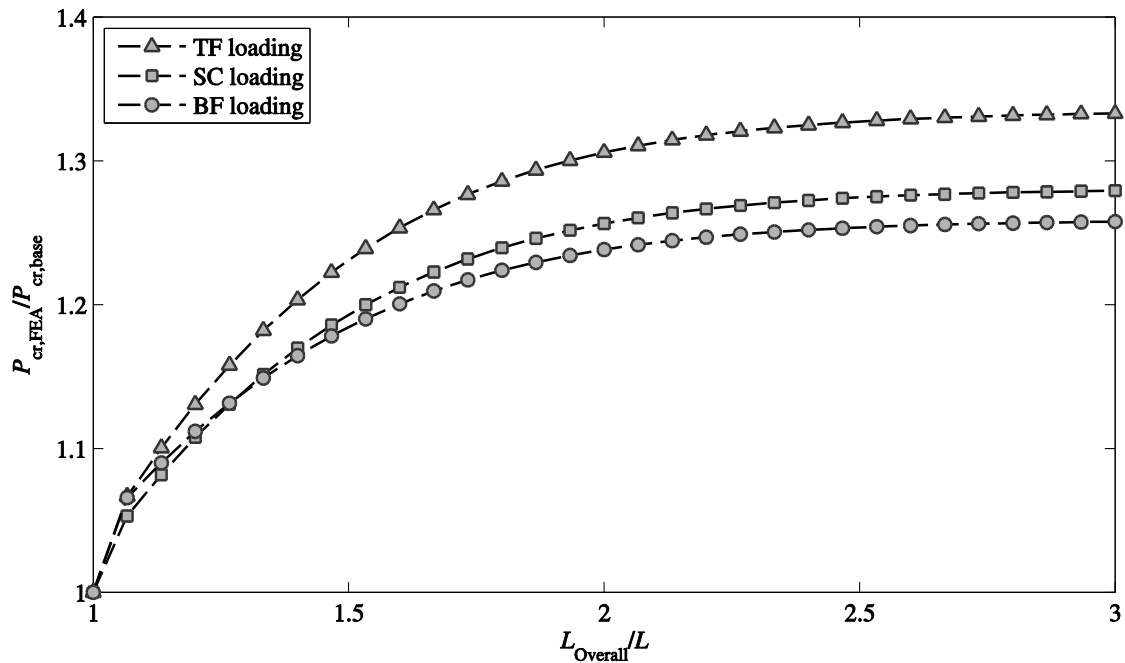
Figure 5.37 Sensitivity of $P_{cr,FEA}$ with the overhang length

This parametric study was implemented with the three vertical load heights of TF, SC and BF. Resistances were normalized using the ratio of $P_{\mathrm{cr,FEA}} / P_{\mathrm{cr,base}}$ where $P_{\mathrm{cr,base}}$ is the FE resistance for beam configuration without an overhang length (i.e. $L_{\mathrm{overall}} = L = 1500$ mm). $P_{\mathrm{cr,FEA}}$ is LTB resistance calculated by an FE model.

In Figure 5.37 this ratio is plotted against the non-dimensional length term L_{Overall} / L. The three curves are for the three loading positions, each having 26 numerical predictions. The plots show that the influence of overhang length is significant, with an increase of up to 33% for TF, 28% for SC and 26% for BF. It is found that the greatest increase in resistance is for the longest L_{Overall}. When $L_{\mathrm{Overall}} / L \geq 2$ this rate of increase is found to reduce significantly and almost disappears for $L_{\mathrm{Overall}} / L \geq 2.5$. In the plots this is shown by $P_{\mathrm{cr,FEA}} / P_{\mathrm{cr,base}}$ tending to a constant as the overall span increases. This observation gives evidence that the overhang is developing a restraint to warping beyond the end supports. The longer the overhang length the greater 'fixity' imposed until, at the end supports, warping is fully fixed. This numerical finding shows that the test results are, more or less, influenced by the overhang length. This finding is also important to know for design, since the overall length of a beam (L_{Overall}) is normally assumed to be the beam span and thus any increasing due to there being overhangs is ignored. This FE investigation has shown that what in standard practice is conservative and valid.

5.6.   Concluding remarks

Details of the FE modelling methodology with ABAQUS® for LTB instability on PFRP beams have been presented. The plates were treated as single layered transverse

isotropic materials. The 8-noded thick shell element (S8R) with side lengths of 15 mm or less was adopted. The fillet areas at flange-web junction were taken into account by assigning 'over-thickness' elements in these regions. As adopted in physical testing, the displacement boundary conditions were EC1 and EC2. Loading for C-sections was simulated by using a 'RIGID BODY' constraint. Linear eigenvalue and nonlinear analyses were conducted on I and C1 beams to gain knowledge and understanding of their LTB resistances.

Comparison between FE eigenvalue simulations and test results has shown a good agreement for EC1. The difference is in range of -9% to 14% for I and -22% to 2% for C1 beams. The FEA does not seem to give a good correlation with test results for EC2. It gives results that are all higher to significant higher with differences from -34% to -19% for I and -49% to -26% for C1 beams.

Nonlinear analyses were carried out considering the influence of initial out-of-straightness geometric imperfection. This imperfection was introduced into the FE model as a half sine wave shape with the maximum magnitude of δ_{max} located at mid-span. Other initial geometric imperfections were not included because they are believed to have a much lower influence on a beam's buckling resistance as there are no measured values for these imperfections. Comparison between FE nonlinear analyses and test results were made using a limiting buckling load, which is defined as the load when mid-span rotation reached 3 degrees. This approach was needed because the load-displacement responses do not show a clear buckling bifurcation due to the introduction of imperfections. Results are used to demonstrate a better correlation especially for EC1. It is found that the combination influence of geometric and material imperfection could

create a condition where beam has a better response under loading than when there is no geometrical imperfection (i.e. $\delta_{\max} = 0$).

Sensitivity analyses were implemented using six parameters to show how the LTB resistance is changing. These investigations showed the following:

(1) The modelling method that takes into account the fillet radius areas gives significantly (6-15% for EC1 and 4-11% for EC2) higher LTB resistance compared with the modelling option of constant thickness panels in the PFRP sections. The author finds that it is necessary to use this modelling feature when analysing the LTB phenomenon.

(2) The change in in-plane shear modulus G_{LT} from 3 GPa to 5 GPa increases LTB resistance by 17% for short span (e.g. $L = 1828$ mm) and up to 27% at a long span (e.g. $L = 4064$ mm). The characterization of G_{LT} is highly important for the LTB problem.

(3) A beam's LTB response is sensitive with the change in geometric imperfection. It is found that when the minor axis out-of-straightness imperfection increases from 0 mm to 10 mm, value of $R_{\text{Limit,FEA}}$ reduces more than 50%. The author makes the case that the allowance for this imperfection (D) in ASTM D3917 of $L/240$ is too high, and not appropriate. Although pultruders are likely to produce shapes that do not possess such a high out-of-straightness the author suggests that code writers ensure that the LTB mode of ultimate failure will occur after a SLS (Serviceability Limit State) has been attained. The author has found that equivalent allowance in (BSI, 2002b) of $D = 0.0005L^2$ is a more suitable practical limit for this tolerance in the pultrusion process.

186

(4) A beam's behaviour is significantly influenced by the lateral position of the vertical loading. In practice, a PFRP beam cannot always be subjected to gravity loading acting on the vertical plane of the shear centre. The most common case would be to have the loading applied with a lateral eccentrically. It is believed that an eccentricity up to 3 mm could have existed in the author's series of physical tests. The FE investigation has shown that for an eccentricity of 3 mm, the value of $P_{\text{Limit,FEA}}$ reduced by up to 17% or increased by up to 19%

(5) The influence of vertical load height is more significant in PFRP than in steel. Using nonlinear FE analyses and the limiting buckling load when mid-span rotation attained 3 degrees, it has been shown that, when compared to the shear centre situation, $P_{\text{Limit,FEA}}$ decreases by 20% for top flange loading and increases by 30% for bottom flange loading.

(6) As the overhang length increases the LTB resistance also increases from warping restraint

It is to be noted that the influence of geometric imperfection, vertical load height, and lateral load eccentricity have been evaluated using a limiting buckling load which value is highly influenced by how it is defined. The adoption of another buckling load definition will change the numerical results but will not alter the findings.

The FE model by the author can be further improved to give a more realistic prediction of the actual behaviour of beam in testing. The improvement could be carried out on the modelling of the loading disc with its pulley system rather than a simplified method as in this study. The modelling for end displacement boundary conditions EC1 and EC2 can also be improved by considering the frictional contact between the steel rods and the flange outstands.

CHAPTER 6

DESIGN PROPOSAL FOR BEAM IN BENDING

6.1. Introduction to design proposal

This chapter presents the preliminary investigation into the development of an approach for instability design check of PFRP beams in bending for inclusion in a future Eurocode. The calibration method adopts the general case 'strength' function in Eurocode 3 (BSI, 2005a) and follows the standard procedure in Eurocode 0 (BSI, 2002a) when calibrating the 'design model' to determine the partial factor γ_M for the LTB mode of failure. The design expression for resistance is given by dividing the strength function by γ_M. The starting point of the calibration process is the observation that the isotropic closed-form formula (Eq. 2.1) generally used to predict M_{cr} for steel can be used with PFRP. A number of items of information that have not been determined in the Ph.D. work are adopted either from Eurocode 3 (EC3) for steel or from previous research. A brief introduction to the LTB design methods that have been popular in steel structural design will be given prior to the calibration procedure. The calibration for PFRP beams is carried out with I- and C1-sections that have had their properties characterized in Chapters 3 and 4.

6.2. Lateral buckling checking methods in standards

Laterally unrestrained beams subjected to flexure about their major axis are required to have LTB failure checked in design. Each design standard had its own method to determine whether a structural member is acceptable. Briefed herein are the LTB check methods in the two design standards of Eurocode 3 (EN 1993-1-1:2005) and AISC 360-10 (AISC, 2010)

6.2.1. Procedure in American Standard AISC 360-10

The LTB check for steel beam in accordance with the specification for Structural Steel Buildings (AISC, 2010), hereafter referred to AISC, follows the Load and Resistance Factor Design (LRFD) approach is expressed by:

$$M_u \leq \phi_b M_n \tag{6.1}$$

In Eq.(6.1) M_u is the required design moment calculated using LRFD load combinations, M_n is the resistance moment and $\phi_b = 0.9$ is the resistance factor for flexure. The resistance factor ϕ_b can be said to be equivalent to the Eurocode partial factor for resistance (γ_M), and so from how Equation (6.1) is applied, $\gamma_M = 1.11$ for steel.

The nominal flexural strength is determined based on the lateral unsupported length L_b (Figure 6.1). If $L_b \leq L_p$ (determined by Eq. F2-5 in AISC), no LTB check is required. When $L_p < L_b \leq L_r$ (determined by Eq. F2-6 in AISC), the LTB check must take the inelastic behaviour of steel into account.
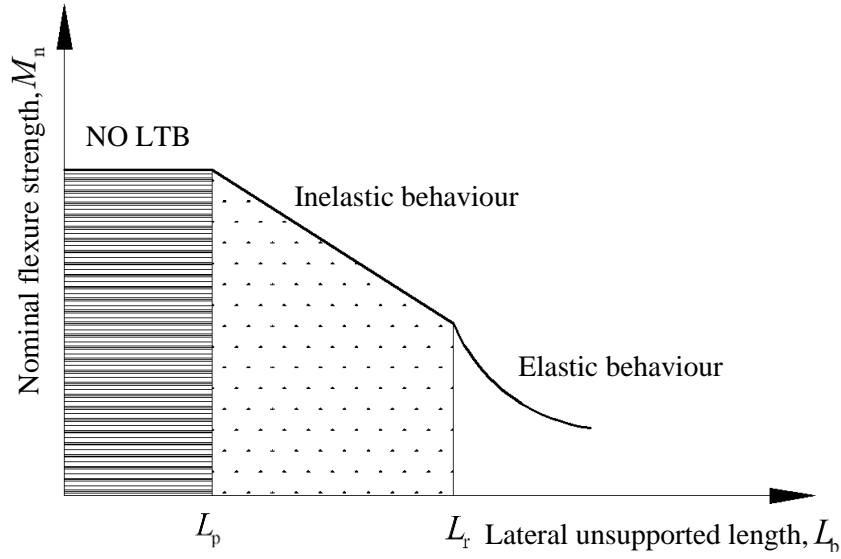
Figure 6.1 Lateral unsupported length for LTB check with American standard

When $L_b > L_r$ the nominal flexural strength $M_n = M_{cr}$. The critical elastic buckling moment M_{cr} can be determined from Eq. F2-4. This expression is identical with Eq. (2.1) (for EC3) when the lateral bending factor k and warping factor k_w have the same value. There is no consideration in AISC for the possibility of k being different from k_w; there is in EC3.

The LRFD function in the Pre-standard for LRFD of Pultruded FRP structures (ASCE, 2010) is somewhat different to that in AISC. It is expressed as:

$$M_u \leq \lambda \phi M_n \qquad (6.2)$$

Where λ is the time effect factor that is to account for when the design loading is applied long-term (to account for the creep in FRP materials), and for reduction in mechanical properties due to durability effects, such as occurs from long-term exposure to aggressive environments. λ is specified in Table 2.3-1 in the Pre-standard. The resistance factor ϕ is now taken to be 0.7 to reflect the greater uncertainty in

190

quantifying the 'true' behaviour and a higher target reliability factor (β) than if the material is steel. This resistance factor can be assumed to be equivalent to having $\gamma_M = 1.43$.

6.2.2. Procedure in Eurocode BS EN 1993-1-1:2005

EC3 provides three methods for checking the LTB resistance of laterally unrestrained steel beams subjected to flexure about their major axis. Procedures are detailed in *clause* 6.3.2 of the standard EN 1993-1-1:2005. The primary method adopts the LTB curves for two cases, the general case in *clause* 6.3.2.2 and special case in *clause* 6.3.2.3 for rolled sections and equivalent welded sections.
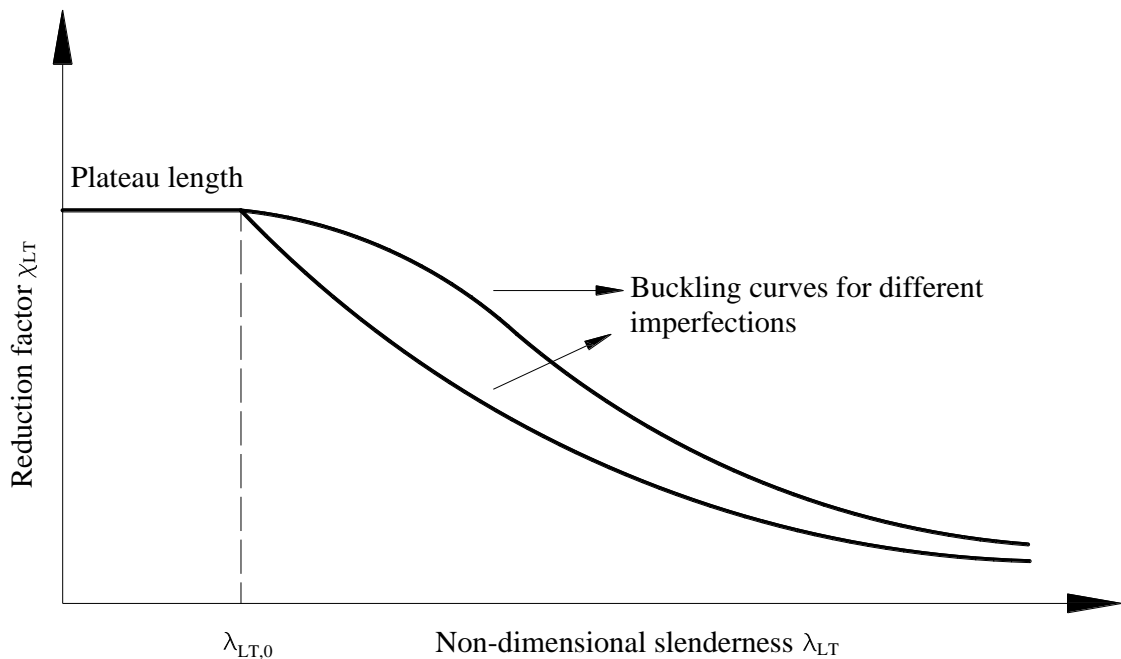
Figure 6.2 Buckling curves in Eurocode 3

For a beam to pass the LTB check, the design buckling resistance moment of the beam $M_{b,Rd}$ must be higher than the design value of the moment M_{Ed}.

$M_{b,Rd}$ is taken as (BSI, 2005a):

$$M_{b,Rd} = \chi_{LT} W_y \frac{f_y}{\gamma_M} \qquad (6.3)$$

The reduction factor χ_{LT} is the solution to the Ayrton-Perry Formula (APF) based LTB curve (Szalai and Papp, 2010). For the general case it is determined as:

$$\chi_{LT} = \frac{1}{\Phi_{LT} + \sqrt{\Phi_{LT}^2 - \lambda_{LT}^2}} \qquad (6.4)$$

where $\qquad\qquad \Phi_{LT} = 0.5\left[1 + \alpha_{LT}\left(\lambda_{LT} - \lambda_{LT,0}\right) + \lambda_{LT}^2\right] \qquad (6.5)$

In Eq. (6.5) $\lambda_{LT,0}$ is the plateau length in Figure 6.2.

Φ_{LT} can also be expressed in a form of a generalized imperfection factor η_{LT} as (Szalai and Papp, 2010):

$$\Phi_{LT} = 0.5\left(1 + \eta_{LT} + \lambda_{LT}^2\right) \qquad (6.6)$$

The non-dimensional slenderness λ_{LT} is given by:

$$\lambda_{LT} = \sqrt{\frac{W_y f_y}{M_{cr}}} \qquad (6.7)$$

The imperfection factor α_{LT} can take the value of 0.21; 0.34; 0.49 and 0.76 for different cross-sectional class of standard steel section.

As shown in Eq. (6.7) the determination of the non-dimensional LTB slenderness λ_{LT} requires the knowledge of the elastic critical buckling moment M_{cr}. Eurocode 3 (EC3) provides no expression or guidance on how M_{cr} should be calculated. Its calculation was considered by the code writers to be standard textbook material. Eurocode 3 only

mentions that this value should be determined based on gross cross-sectional properties and accounted for the loading conditions, the moment distribution and the lateral restraints (*clause* 6.3.2.2(2)). Discussion on the determination of M_{cr} has been given by the author in Chapter 2 and so will not be repeated here.

The LTB design check using EC3 procedure is straightforward, starting with the determination of M_{cr} for the calculation via Eq. (6.7) of the non-dimensional slenderness λ_{LT} of the member. The imperfection factor α_{LT} is selected based on cross-section type and the beam's h/b ratio. This follows with the calculation of the reduction factor χ_{LT} using Eq. (6.4). The next step is to calculate $M_{b,Rd}$ by Eq. (6.3). The last step in the general case procedure is to compare this value with the given M_{Ed}. The member is safe against LTB failure if the latter is smaller than the former.

6.3. Design proposal and the Eurocode 3 approach

To generate a LTB curve in accordance with EC3 for PFRP beams, four factors need to be characterized. These are developed in the sub-sections 6.3.1 for the plateau length $\lambda_{LT,0}$, 6.3.2 for the imperfection factor α_{LT}, and 6.3.3 for the safety partial factor γ_M.

6.3.1. Plateau length

The plateau length $\lambda_{LT,0}$ is the value of the non-dimensional slenderness for LTB below which no failure occurs. For beams with slendernesses $\lambda_{LT} \leq \lambda_{LT,0}$ only cross sectional resistance check is required. For $\lambda_{LT} \geq \lambda_{LT,0}$, LTB governs the design with partial safety

factor γ_M. EC3 for structural steel gives $\lambda_{LT,0} = 0.2$ for general case and $\lambda_{LT,0} = 0.4$ (maximum) for rolled sections and equivalent welded sections. It is worth noting that $\lambda_{LT,0}$ is influenced by how the cross-section ultimate mode of failure is defined. For steel it depends of section classification and is either the moment resistance at first yield M_y or the plastic moment of resistance $M_{pl,y}$. Having high relative strength-to-stiffness ratio, it is argued that the 'cross-section' mode of failure for PFRP beams is to be local buckling rather than materrial rupture. It can be seen that the cross-section ultimate mode of failure for steel sections (e.g. yielding strength) is well-defined. In PFRP the moment for local buckling failure will depend on the cross-section geometry, load application and end boundary conditions. Because it also depends of the rotational stiffness along the junctions between panels in the thin-walled section, its determination by either a closed-form equation or physical testing is not straightforward.

Trumpf (2006) proposed a plateau length of $\lambda_{LT,0} = 0.5$ for PFRP beam sections (from Fiberline Composites A/S), based on his Ph.D. work combining testing and numerical investigations. The author adopts Trumpf's value for the calibration in this chapter. It is noted that γ_M is not sensitive to the value of $\lambda_{LT,0}$.

Taking local buckling to be the cross-section ultimate mode of failure the non-dimensional slenderness λ_{LT} is defined as:

$$\lambda_{LT} = \sqrt{\frac{W_y \sigma_{Loc}}{M_{cr}}} \tag{6.8}$$

In Eq. (6.8) σ_{Loc} is the local buckling stress and W_y is the elastic section modulus. The elastic critical LTB moment M_{cr} can be determined using Eq. (2.1).

In this study σ_{Loc} is obtained by the author from a concentrically compression test on short column and is reported in sub-section 3.7. It is 134 MPa for I and is 100 MPa for C1. It is assumed that σ_{Loc} is constant over a flange outstand in a beam and so the calibration procedure neglects the presence of a stress gradient through the depth of the section.

6.3.2. Imperfection factor

In the APF based solution to account for member geometric imperfections the generalized imperfection factor η_{LT} is expressed by an expression using the mid-span minor axis out-of-straightness imperfection (v_0) and initial twist rotation (φ_0). η_{LT} is defined by (Szalai and Papp, 2010):

$$\eta_{\text{LT}} = v_0 \frac{W_{\text{y}}}{W_{\text{w}}} + \varphi_0 \frac{W_{\text{y}}}{W_{\text{z}}} - \varphi_0 \frac{GI_{\text{t}}}{M_{\text{cr}}} \frac{W_{\text{y}}}{W_{\text{w}}} \tag{6.9}$$

For the beam, $W_{\text{y}}, W_{\text{z}}$ and W_{w} are the elastic major axis, elastic minor axis and warping sectional moduli.

The warping sectional modulus can be expressed in a form of warping function Ψ as:

$$W_{\text{w}} = \frac{I_{\text{w}}}{\Psi_{\text{max}}} \tag{6.10}$$

where Ψ_{max} is the maximum of the warping function. This value is calculated using software ShapeBuilder (IES Inc, 2013). For the I-section in this study, it is 1.79×10^3 mm^2 and for C1, it is 1.91×10^3 mm^2.

The two imperfections of v_0 and φ_0 are assumed to satisfy the deformed shape for the first LTB mode, that is:

$$\frac{v_0}{\varphi_0} = \frac{M_{cr}}{N_{cr,z}} \quad (6.11)$$

In Eq. (6.11) $N_{cr,z}$ is the Euler buckling load. By taking the measured initial minor axis out-of-straightness imperfection δ_{max} in Section 4.4 to be v_0 the initial twist imperfection φ_0 can be determined using Eq. (6.11). Substituting these two geometric imperfections into Eq. (6.9) the generalized imperfection factor for the PFRP section is determined.

Table 6.1 gives in columns (1-7) the relevant data for the calculation of η_{LT} that is presented in column (8). It is found that for the I-section the factor has a range of values from 0.18 to 0.51 and for the C1-section the range is from 0.05 to 0.18.

From Eqs. (6.5) and (6.6) we have:

$$\eta_{LT} = \alpha_{LT}\left(\lambda_{LT} - \lambda_{LT,0}\right) = \alpha_{LT}\left(\sqrt{\frac{W_y\sigma_{Loc}}{M_{cr}}} - 0.5\right) \quad (6.12)$$

Table 6.1 Calculation of generalized imperfection factor η_{LT}

Beam	v_0 (mm)	φ_0 (rad)	W_y (mm^3)	W_w (mm^4)	W_z (mm^3)	M_{cr} (kN.m)	η_{LT}	α_{LT}
(1)	(2)	(3)	(4)	(5)	(6)	(7)	(8)	(9)
I-1828	0.78	0.013				1.62×10^6	0.18	0.11
I-2438	2.86	0.036	4.65×10^4	3.92×10^5	3.63×10^3	1.08×10^6	0.51	0.26
I-2844	1.95	0.021				8.87×10^5	0.31	0.14
I-3454	2.72	0.024				6.98×10^5	0.36	0.14
C1-1828	0.27	0.006				1.37×10^6	0.05	0.04
C1-2438	0.80	0.013	4.30×10^4	3.30×10^5	4.63×10^3	1.02×10^6	0.11	0.07
C1-2844	1.55	0.021				8.78×10^5	0.18	0.11
C1-3454	1.72	0.019				7.23×10^5	0.16	0.08

To obtain estimations for α_{LT} we substitute W_y, M_{cr} and η_{LT} from columns (4), (7) and (8), taking $\sigma_{Loc} = 134$ MPa for the I-section and $\sigma_{Loc} = 100$ MPa for the C1-section into Eq. (6.12). σ_{Loc} is given in sub-section 3.7.3 of Chapter 3. The value of α_{LT} at each beam span is reported in column (9) of Table 6.1. It is found that the maximum α_{LT} for the I-section is 0.26 and is 0.11 for the C1-section. These imperfection factors are relatively lower when compared to those in EC3. For the author's calibration study $\alpha_{LT} = 0.34$ is chosen for both sections. The reason for this choice is that it would be most convenient for structural engineering designers if the imperfection factor for LTB design with PFRP was one of the four recommended in EC3. The imperfection factor equal to 0.34 is for curve *b* in EN 1993-1-1:2005.

6.3.3. Partial factor for lateral-torsional buckling

Presented next is the standard procedure to generate the partial safety factor γ_M. The calibration is conducted with the I-section and C1-section as two separate sets of data. Each set of data includes results from 30 physical tests reported in Chapter 4. The calibration procedure follows the steps for the Standard Procedure in D8.2.2. of Eurocode 0 (BSI, 2002a). These are now presented and explained.

Step 1: *Establish a 'design model'*

The 'design model' is the theoretical prediction of the resistance r_t. The chosen strength function is Eq. (6.5) with λ_{LT} defined for PFRP to be Eq. (6.8). The expression that involves all the basic variables is:

$$r_t = g_{rt}(\underline{X}) = \chi_{LT}(I_t, I_w, I_y, E_L, G_{LT}, \sigma_{Loc}) \times M_{Loc}(W_y, \sigma_{Loc}) \tag{6.13}$$

197

This 'design model' includes seven basic variables of $I_t, I_w, I_y, E_L, G_{LT}, W_y$ and σ_{Loc}. It is a requirement that all the parameters to be measured for each individual test. Amongst the seven variables, I_t, I_w, I_y and W_y are the section geometrical properties calculated using the measured geometric dimensions reported in Table 4.1. Calculations do not account for the contribution of the fillet areas; they are ignored in EC3 too. This is an appropriate approach as the theoretical prediction for LTB resistance will be lower compared to that when the fillet areas are included. Mechanical properties E_L, G_{LT} and σ_{Loc} were not measured for each test specimen. The characteristic value of E_L or G_{LT} is assumed to be constant, and is taken from Table 3.14. Their Standard Deviation (SD) and Coefficient of Variation (CV) are computed based on data in Table 3.7 for E_L and Table 3.13 for G_{LT}. It is worth noting that EC3 does not consider any of these material properties as a variable. This may due to the modulus of elasticity E of structural steels being well-defined, and consistent for the different steel grades (e.g. S235 to S335). The situation is, however, different with PFRP material as mechanical properties are more difficult to characterize. Trumpf (2006) combined E_L with I_z (for flexural rigidity) and G_{LT} with I_t (for shear rigidity) when establishing the CV of I_z and I_t. There is no evident in his Ph.D. thesis to show that the material properties were determined for each test specimen.

σ_{Loc} is 134 MPa and 100 MPa for the I- and C1-sections. In the calibration process these strength values are assumed to be both the nominal and characteristic values. This approach is similar to EC3, in which only a nominal value (also assumed to be the characteristic value) for the yield stress f_y is given. The coefficient of variation for f_y is $V_{fy} = 7\%$ (Sedlacek *et al.*, 1989). The mean value (f_{ym}) of f_y is taken as the 2.3% fractile value from:

$$f_{ym} = f_y \exp\left(-1.64 V_{fy} - 0.5 V_{fy}\right)^{-1} \qquad (6.14)$$

By assuming that the mean value of σ_{Loc} can also be taken as the 2.3% fractile value, Eq. (6.14) can also be adopted for a PFRP material. It is assumed that the CV of σ_{Loc} is $V_{\sigma Loc} = 10\%$, which is higher than $V_{fy} = 7\%$ for steel. This assumption is appropriate because as yield stress of steel is better defined than σ_{Loc}, it variability should be smaller. By applying Eq. (6.14) the mean local buckling stress is $\sigma_{Locm} = 166$ MPa for the I-section and $\sigma_{Locm} = 124$ MPa for the C1-section.

Assuming that Eq. (6.14) can also be adopted for E_L and G_{LT} we have:

$$E_{Lm} = E_{Lm} \exp\left(-1.64 V_{EL} - 0.5 V_{EL}\right)^{-1} \qquad (6.15)$$

and
$$G_{LTm} = G_{LTm} \exp\left(-1.64 V_{GLT} - 0.5 V_{GLT}\right)^{-1} . \qquad (6.16)$$

Table 6.2 Basic variables and their CVs

Specimen	I_t (mm^4)	I_w (mm^6)	I_z (mm^4)	W_y (mm^3)	E_L (N/mm^2)	G_{LT} (N/mm^2)	σ_{Loc} (N/mm^2)
(1)	(2)	(3)	(4)	(5)	(6)	(7)	(8)
I-1828	1.71×10^4	7.03×10^8	2.18×10^5	4.95×10^4			
I-2438	1.68×10^4	7.00×10^8	2.17×10^5	4.97×10^4			
I-2844	1.73×10^4	7.05×10^8	2.19×10^5	4.99×10^4	30600	4200	134
I-3454	1.72×10^4	7.06×10^8	2.19×10^5	4.95×10^4			
I-4064	1.68×10^4	6.99×10^8	2.16×10^5	4.97×10^4			
Mean	1.70×10^4	7.03×10^8	2.18×10^5	4.97×10^4	32000	5000	166
SD	210	3.21×10^6	1.14×10^3	180	700	340	13.4
CV (%)	1.2	0.46	0.53	0.36	2.17	8.09	10
C1-1828	1.52×10^4	6.46×10^8	2.83×10^5	4.43×10^4			
C1-2438	1.52×10^4	6.36×10^8	2.74×10^5	4.27×10^4			
C1-2844	1.49×10^4	6.34×10^8	2.78×10^5	4.38×10^4	31600	4800	100
C1-3454	1.52×10^4	6.43×10^8	2.76×10^5	4.27×10^4			
C1-4064	1.52×10^4	6.37×10^8	2.77×10^5	4.31×10^4			
Mean	1.51×10^4	6.39×10^8	2.78×10^5	4.32×10^4	34060	5100	124
SD	140	4.48×10^6	3.58×10^3	530	1100	140	10.0
CV (%)	0.91	0.76	1.29	1.24	3.50	2.91	10

Table 6.2 reports the data for the variables in Eq. (6.13). Column (1) is used to give beam labelling in a form of section's name (i.e. I or C1) and span L (e.g. 1828 mm). Columns (2-5) list the measured geometric parameters of I_t, I_w, I_z and W_y . By substituting values of E_L and G_{LT} from Table 6.2 into Eqs. (6.15) and (6.16), their means can be determined. Given in columns (6-7) are the characteristic values for E_L and G_{LT}. Their SDs and CVs are presented below the mean. It is observed that the CVs of geometrical properties for the I-section are in range of 0.36% to 1.2% and for the C1 section they are between 0.76% and 1.29%. For I-section Trumpf (2006) presents, CVs for geometrical properties from 0.79% to 1.81%. EC3 (Sedlacek *et al.*, 1989) reports 3% for the four properties in columns (2-5) in Table 6.2.

The CVs for the mechanical properties in Table 6.2 at 2.17% to 8.09% for the I-section and at 2.91% to 3.50 % for the C1-section are significantly higher.

Step 2: *Compare test results and theoretical predictions*

The theoretical moment resistances r_t (i = 1 to n, where n is number of test) are obtained by substituting the variable data listed in columns (2-8) in Table 6.2 with the loading height and end displacement boundary conditions into the resistance function Eq. (6.13). The experimental moment resistances, for r_e , are acquired using:

$$r_e = \frac{P_{cr,e} \times L}{4} \tag{6.17}$$

In Eq. (6.17) $P_{cr,e}$ is the experimental buckling load reported in Tables 4.5 and 4.6 for the five spans, two displacement boundary conditions of EC1 and EC2 and three load heights.

Table 6.3 r_e and r_t for the I-section

Beam	TF (Top Flange)		SC (Shear Centre)		BF (Bottom Flange)	
	r_e (kN.m)	r_t (kN.m)	r_e (kN.m)	r_t (kN.m)	r_e (kN.m)	r_t (kN.m)
(1)	(2)	(3)	(5)	(6)	(7)	(8)
I-1828_EC1	1.73	1.23	2.80	1.85	4.17	2.71
I-2438_EC1	1.26	0.89	1.77	1.27	2.40	1.79
I-2844_EC1	1.17	0.78	1.49	1.07	1.84	1.46
I-3454_EC1	0.93	0.65	1.11	0.85	1.39	1.12
I-4064_EC1	0.73	0.55	0.91	0.70	1.13	0.89
I-1828_EC2	2.87	1.87	-	3.18	-	4.82
I-2438_EC2	2.03	1.32	2.76	2.14	3.68	3.34
I-2844_EC2	1.49	1.15	2.30	1.78	3.19	2.71
I-3454_EC2	1.27	0.95	1.74	1.40	2.27	2.04
I-4064_EC2	1.05	0.81	1.36	1.14	1.71	1.60

Table 6.4 r_e and r_t for the C1-section

Beam	TF (Top Flange)		SC (Shear Centre)		BF (Bottom Flange)	
	r_e (kN.m)	r_t (kN.m)	r_e (kN.m)	r_t (kN.m)	r_e (kN.m)	r_t (kN.m)
(1)	(2)	(3)	(5)	(6)	(7)	(8)
C1-1828_EC1	1.51	1.27	2.53	1.96	3.46	2.84
C1-2438_EC1	1.11	0.94	1.85	1.37	2.58	1.97
C1-2844_EC1	1.03	0.81	1.39	1.16	1.88	1.63
C1-3454_EC1	0.86	0.69	1.29	0.93	1.52	1.26
C1-4064_EC1	0.66	0.60	0.81	0.79	1.13	1.03
C1-1828_EC2	2.29	1.84	3.86	3.06	5.80	3.99
C1-2438_EC2	2.00	1.34	3.00	2.21	4.46	3.23
C1-2844_EC2	1.33	1.16	2.48	1.88	3.05	2.82
C1-3454_EC2	1.26	0.99	1.74	1.50	-	2.21
C1-4064_EC2	1.03	0.87	1.28	1.26	1.62	1.80

Table 6.3 presents in column (1) the I-section labelling and in columns (2-3) r_e and r_t for TF loading height for the ten test listed in rows (1-10). Results for SC and BF loading cases are given in columns (5-6) and (7-8). The equivalent r_e and r_t values for the C1 beams are reported in Table 6.4.
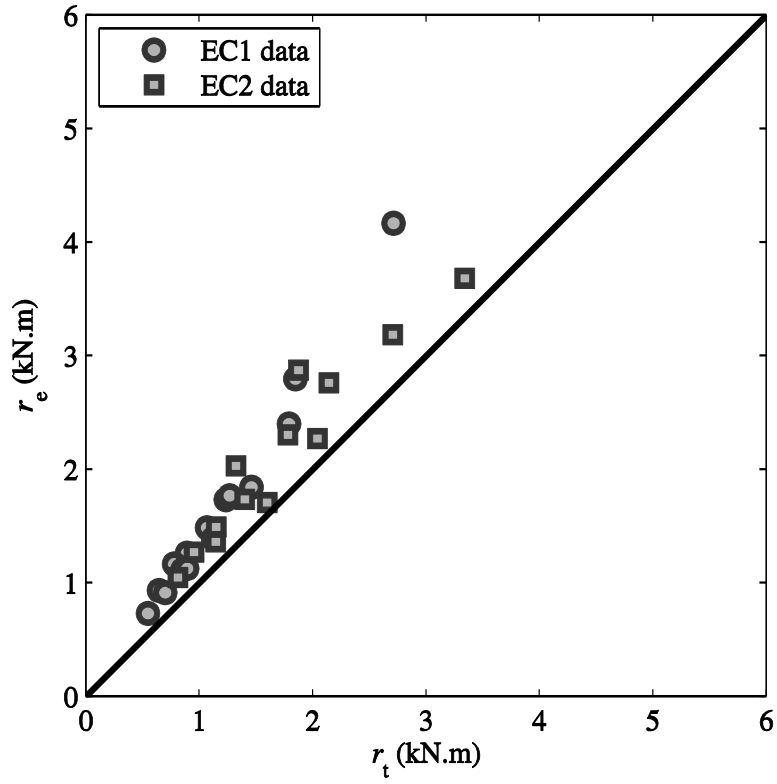
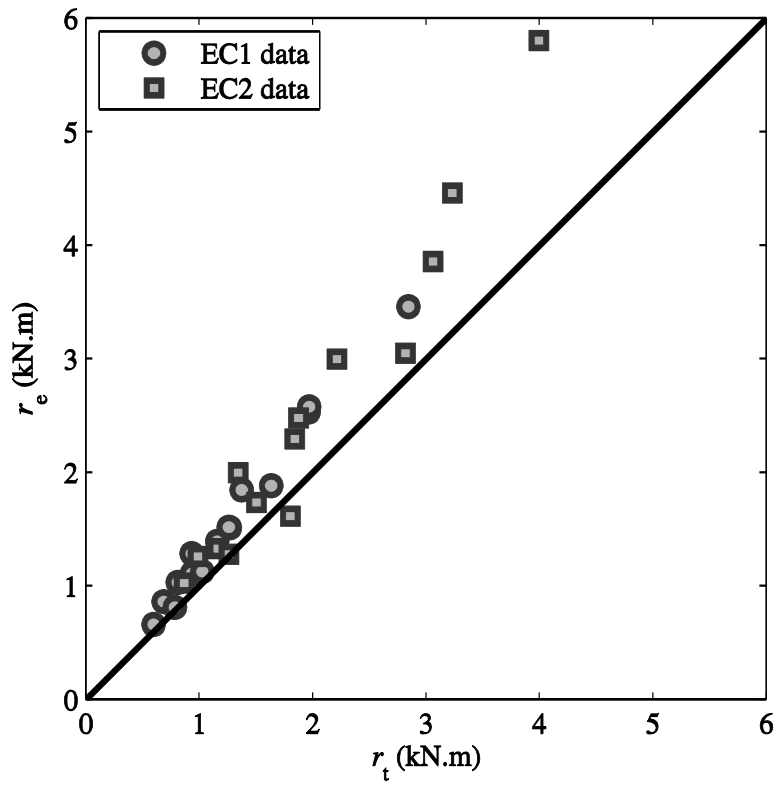Figure 6.3 Plot of r_e vs. r_t for I-section

Figure 6.4 Plot of r_e vs. r_t for C1-section

Figures 6.3 and 6.4 are plots of r_e vs. r_t using the data presented in Tables 6.3 and 6.4. In the figures the data points for EC1 are given by the circular shaped symbol and those for EC2 have a rectangular symbol. A linear line for $r_e = r_t$ is plotted to show that, if the 'design model' is exact, and complete, all the data points would lie on this line. As is normal found in practice there is some scatter and r_e (measured) is generally higher than r_t (theoretical).

Step 3: *Calculate the mean correction factor b_m*

The mean correction factor b_m can be estimated using:

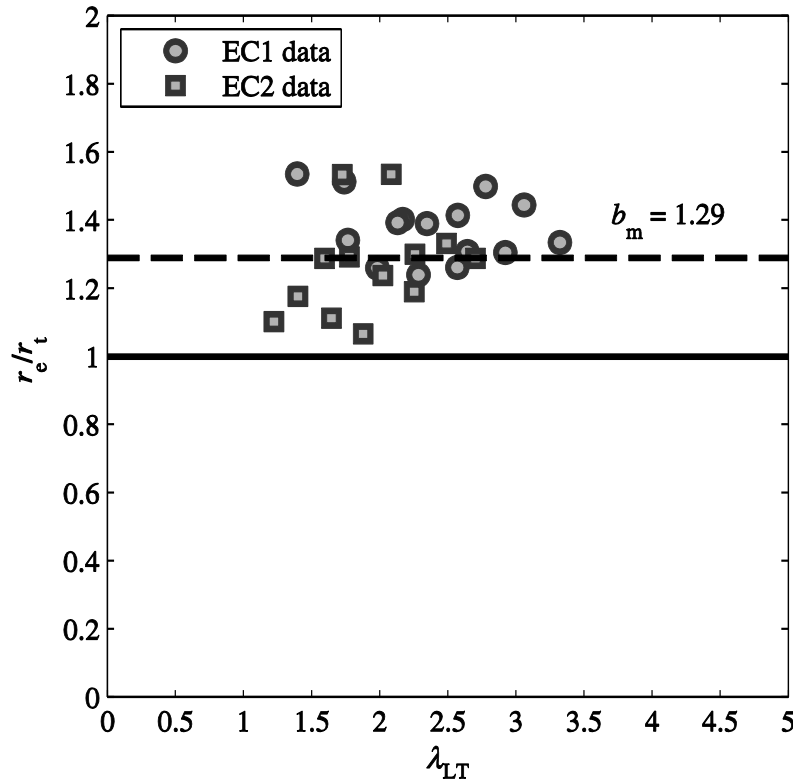$$b_m = \frac{\sum r_e r_t}{\sum r_t^2} \tag{6.18}$$

Figure 6.5 r_e / r_t vs. non-dimensional slenderness λ_{LT} for I-section
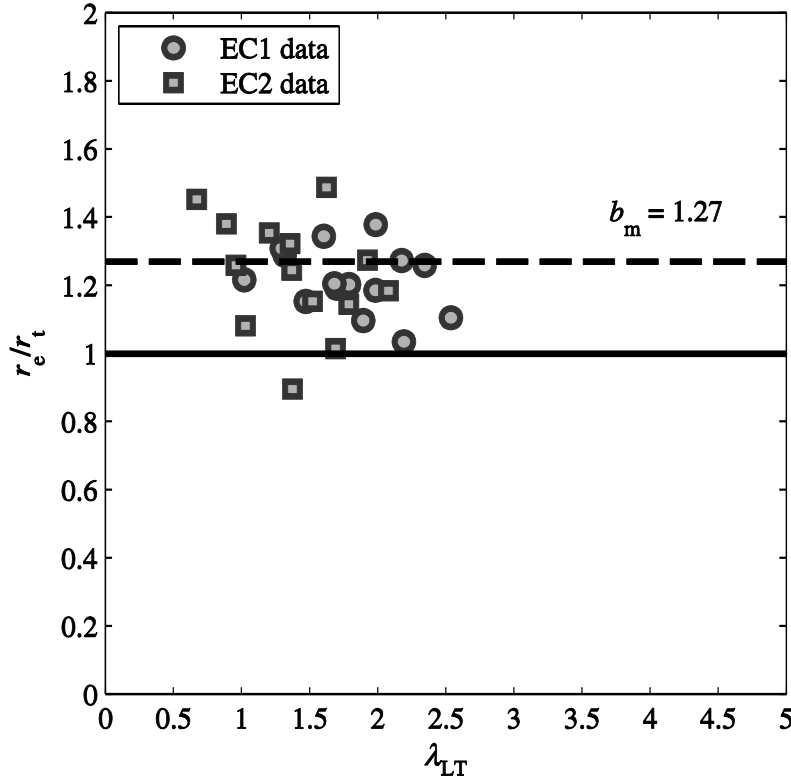
Figure 6.6 r_e / r_t vs. non-dimensional slenderness λ_{LT} for C1-section

The test results given in Tables 6.3 and 6.4 give the mean correction factor $b_m = 1.29$ for I-section and $b_m = 1.27$ for C1-section. Figures 6.5 and 6.6 are for plots of r_e / r_t with λ_{LT} for the I-section and C1-section. It is seen that only for I beams does all the data points locate above the line $r_e / r_t = 1$, which means the expression for r_t gives 'safe' results. Test results using the C1-section give a higher scatter, especially with the EC2 displacement boundary conditions. The EC2 data points in Figures 6.5 and 6.6 are highlighted by having a rectangular symbol.

Step 4: *Determine of the coefficient of variation for the error terms*

The error term δ_i ($i = 1 \rightarrow n$) for each test results r_{ei} is calculated from:

$$\delta_i = \frac{r_{ei}}{b_m r_{ti}} \tag{6.19}$$

Estimation for the coefficient of variation for the error V_δ can be obtained by:

$$V_\delta = \sqrt{\exp\left(s_\Delta^2\right) - 1} \tag{6.20}$$

where

$$s_\Delta^2 = \frac{1}{n-1} \sum_{i=1}^{n} \left(\Delta_i - \overline{\Delta}\right)^2 \tag{6.21}$$

In Eq. (6.21) , $\Delta_i = \ln(\delta_i)$ and $\overline{\Delta} = \frac{1}{n} \sum_{i=1}^{n} \Delta_i$

Reported in Tables 6.5 and 6.6 are δ_i and Δ_i for the two beam sections, calculated using Eqs. (6.19) and (6.20). The error terms and Δ_i are presented in columns (2-3) for TF, (4-5) for SC and (6-7) for BF loading. V_δ is obtained by substituting these tabulated parameters into Eqs. (6.21) and (6.20). V_δ is 0.101 for the I-section and 0.112 for the C1- section. It has been shown that the coefficient of variation for the error terms is close to 10%.

Table 6.5 δ_i and Δ_i for I-section

Beam	TF (Top Flange)		SC (Shear centre)		BF (Bottom Flange)	
	δ_i	Δ_i	δ_i	Δ_i	δ_i	Δ_i
(1)	(2)	(3)	(4)	(5)	(6)	(7)
I-1828_EC1	1.08	-0.081	1.17	-0.157	1.19	-0.172
I-2438_EC1	1.09	-0.089	1.08	-0.074	1.04	-0.036
I-2844_EC1	1.16	-0.148	1.08	-0.072	0.97	0.026
I-3454_EC1	1.12	-0.111	1.01	-0.011	0.96	0.042
I-4064_EC1	1.03	-0.031	1.01	-0.009	0.98	0.025
I-1828_EC2	1.19	-0.170	-	-	-	-
I-2438_EC2	1.19	-0.171	1.00	0.004	0.85	0.160
I-2844_EC1	1.01	-0.005	1.00	0.001	0.91	0.094
I-3454_EC2	1.03	-0.030	0.96	0.044	0.86	0.150
I-4064_EC2	1.00	0.004	0.92	0.083	0.82	0.193

Table 6.6 δ_i and Δ_i for C1-section

Beam	TF (Top Flange)		SC (Shear centre)		BF (Bottom Flange)	
	δ_i	Δ_i	δ_i	Δ_i	δ_i	Δ_i
(1)	(2)	(3)	(4)	(5)	(6)	(7)
C1-1828_EC1	0.94	0.065	1.01	-0.013	0.96	0.045
C1-2438_EC1	0.93	0.070	1.06	-0.055	1.03	-0.029
C1-2844_EC1	1.00	-0.001	0.95	0.056	0.91	0.098
C1-3454_EC1	0.99	0.010	1.08	-0.080	0.95	0.054
C1-4064_EC1	0.87	0.140	0.81	0.206	0.86	0.148
C1-1828_EC2	0.98	0.022	0.99	0.010	1.14	-0.133
C1-2438_EC2	1.17	-0.157	1.06	-0.063	1.09	-0.082
C1-2844_EC2	0.90	0.106	1.04	-0.039	0.85	0.162
C1-3454_EC2	1.00	-0.002	0.91	0.098	-	-
C1-4064_EC2	0.93	0.072	0.80	0.226	0.70	0.350

Step 5: *Examine the compatibility*

The purpose of this step is to examine the compatibility of the test results with the assumptions in the 'design model'. It is suggested that if the scatter of the (r_e, r_t) pairs is too high, it can be lowered by either adjusting the design model to accounts for the ignored variables or to separate the test results into sub groups, in which the contribution of those additional variables can be considered constant. In this investigation, all the influencing factors have been considered. It is found that the data points of the I-section spread evenly and the scatter is not too high. There are data points of the C1-section that show a larger scatter. Because of the preliminary nature of the study to calibrate γ_M it was decided not to alter the design model.

Step 6: *Calculate the coefficients of variation for the basic parameters*

The coefficient of variation V_{Xi} for the seven basic parameters in the resistance function have been determined and presented in Table 6.2.

Step 7: *Determine the characteristic value of the resistance* r_k

To determine this value, it is required that the coefficient of variation for V_r be calculated using:

$$V_r = \sqrt{V_\delta^2 + V_{rt}^2} \, . \tag{6.22}$$

V_{rt} should be calculated using:

$$V_{rt} = \frac{1}{g_{rt}^2\left(\underline{X}_m\right)} \times \sum_{i=1}^{j} \left(\frac{\partial g_{rt}}{\partial X_i}\sigma_i\right)^2 \tag{6.23}$$

where j is the number of basic parameters and $\underline{X}_m$ is the mean of the basic parameters, as given in Table 6.2.

Eq. (6.23) is computed using Matlab (Mathworks Inc, 2013). The V_{rt}s resented in column 2 of Tables 6.7 and 6.8 are for the two sections. It is seen that these CVs are very small having a maximum value of 0.003 for the I-section and 0.003 for the C1-section. When substituting V_δ and V_{rt} into Eq. (6.22) to determine V_r, the contribution of V_{rt} can be ignored for the I-section since:

$$V_r = \sqrt{V_\delta^2 + V_{rt}^2} = \sqrt{0.101^2 + 0.003^2} = 0.10105 \cong 0.101 = V_\delta \, .$$

Similarly, for the C1-section we have:

$$V_r = \sqrt{V_\delta^2 + V_{rt}^2} = \sqrt{0.112^2 + 0.007^2} = 0.1122 \cong 0.112 = V_\delta$$

It is acceptable in the calibration procedure to treat $V_r = V_\delta$. A similar observation is given in Trumpf (2006), who found that when calibrating the design model for LTB the contribution of V_{rt} to V_r is small enough to be ignored.

Table 6.7 Calculation of safety partial factor γ_M for I-section

Specimen	$Q_{rt} = V_{rt}$	$Q_\delta = Q$	α_{rt}	r_k	r_d	γ_M
(1)	(2)	(3)	(4)	(5)	(6)	(7)
I-1828_TF_EC1	0.0010		0.0095	1.41	1.22	1.156
I-1828_SC_EC1	0.0007		0.0066	2.08	1.81	1.149
I-1828_BF_EC1	0.0006		0.0057	3.05	2.64	1.155
I-2438_TF_EC1	0.0012		0.0121	1.04	0.90	1.156
I-2438_SC_EC1	0.0008		0.0080	1.45	1.26	1.151
I-2438_BF_EC1	0.0006		0.0056	2.02	1.75	1.154
I-2844_TF_EC1	0.0014		0.0140	0.89	0.77	1.156
I-2844_SC_EC1	0.0009		0.0093	1.21	1.05	1.152
I-2844_BF_EC1	0.0006		0.0063	1.63	1.41	1.156
I-3454_TF_EC1	0.0015		0.0153	0.74	0.64	1.156
I-3454_SC_EC1	0.0011		0.0105	0.96	0.84	1.143
I-3454_BF_EC1	0.0007		0.0071	1.26	1.09	1.156
I-4064_TF_EC1	0.0016		0.0156	0.65	0.55	1.182
I-4064_SC_EC1	0.0011		0.0110	0.81	0.70	1.157
I-4064_BF_EC1	0.0008	0.101	0.0076	1.02	0.88	1.159
I-1828_TF_EC2	0.0009		0.0091	2.15	1.85	1.162
I-1828_SC_EC2	0.0008		0.0075	3.63	3.14	1.156
I-1828_BF_EC2	0.0026		0.0259	5.64	4.88	1.156
I-2438_TF_EC2	0.0013		0.0125	1.54	1.33	1.158
I-2438_SC_EC2	0.0008		0.0075	2.46	2.13	1.155
I-2438_BF_EC2	0.0007		0.0074	3.81	3.30	1.155
I-2844_TF_EC2	0.0015		0.0149	1.32	1.14	1.158
I-2844_SC_EC2	0.0009		0.0088	2.02	1.75	1.154
I-2844_BF_EC2	0.0006		0.0061	3.03	2.63	1.152
I-3454_TF_EC2	0.0017		0.0166	1.10	0.95	1.158
I-3454_SC_EC2	0.0010		0.0101	1.60	1.38	1.159
I-3454_BF_EC2	0.0006		0.0062	2.29	1.98	1.157
I-4064_TF_EC2	0.0017		0.0170	0.95	0.83	1.145
I-4064_SC_EC2	0.0011		0.0107	1.32	1.14	1.158
I-4064_BF_EC2	0.0007		0.0066	1.82	1.58	1.152

Table 6.8 Calculation of safety partial factor γ_M for C1-section

Specimen	$Q_{rt} = V_{rt}$	$Q_\delta = Q$	α_{rt}	r_k	r_d	γ_M
(1)	(2)	(3)	(4)	(5)	(6)	(7)
C1-1828_TF_EC1	0.0006		0.0055	1.35	1.16	1.164
C1-1828_SC_EC1	0.0008		0.0074	2.11	1.81	1.166
C1-1828_BF_EC1	0.0023		0.0206	3.13	2.68	1.168
C1-2438_TF_EC1	0.0006		0.0049	1.01	0.86	1.174
C1-2438_SC_EC1	0.0007		0.0060	1.49	1.28	1.164
C1-2438_BF_EC1	0.0009		0.0082	2.17	1.86	1.167
C1-2844_TF_EC1	0.0005		0.0048	0.87	0.75	1.160
C1-2844_SC_EC1	0.0006		0.0058	1.25	1.07	1.168
C1-2844_BF_EC1	0.0009		0.0076	1.77	1.51	1.172
C1-3454_TF_EC1	0.0005		0.0048	0.73	0.63	1.159
C1-3454_SC_EC1	0.0006		0.0055	1.00	0.86	1.163
C1-3454_BF_EC1	0.0008		0.0069	1.37	1.17	1.171
C1-4064_TF_EC1	0.0005		0.0048	0.64	0.54	1.185
C1-4064_SC_EC1	0.0006		0.0053	0.84	0.72	1.167
C1-4064_BF_EC1	0.0007	0.112	0.0065	1.11	0.95	1.168
C1-1828_TF_EC2	0.0007		0.0060	1.98	1.69	1.172
C1-1828_SC_EC2	0.0034		0.0303	3.41	2.91	1.172
C1-1828_BF_EC2	0.0069		0.0615	4.67	3.99	1.170
C1-2438_TF_EC2	0.0006		0.0050	1.45	1.24	1.169
C1-2438_SC_EC2	0.0009		0.0078	2.45	2.09	1.172
C1-2438_BF_EC2	0.0047		0.0421	3.72	3.18	1.170
C1-2844_TF_EC2	0.0005		0.0048	1.26	1.07	1.178
C1-2844_SC_EC2	0.0007		0.0064	2.04	1.74	1.172
C1-2844_BF_EC2	0.0021		0.0190	3.13	2.68	1.168
C1-3454_TF_EC2	0.0005		0.0049	1.06	0.91	1.165
C1-3454_SC_EC2	0.0006		0.0058	1.63	1.39	1.173
C1-3454_BF_EC2	0.0010		0.0090	2.44	2.09	1.167
C1-4064_TF_EC2	0.0005		0.0048	0.93	0.79	1.177
C1-4064_SC_EC2	0.0006		0.0055	1.36	1.16	1.172
C1-4064_BF_EC2	0.0008		0.0075	1.96	1.68	1.167

It is required that if the number of individual tests is limited ($n < 100$) the characteristic resistance r_k should be determined by:

$$r_k = b_m g_{rt}(\underline{X}_m)\exp(-k_\infty \alpha_{rt} Q_{rt} - k_n \alpha_\delta Q_\delta - 0.5Q^2) \tag{6.24}$$

with:
$$Q_{rt} = \sigma_{\ln(rt)} = \sqrt{\ln(V_{rt}^2 + 1)} = V_{rt} \tag{6.25}$$

$$Q_\delta = \sigma_{\ln(\delta)} = \sqrt{\ln(V_\delta^2 + 1)} \tag{6.26}$$

$$Q = \sigma_{\ln(r)} = \sqrt{\ln(V_r^2 + 1)} = Q_\delta \tag{6.27}$$

$$\alpha_{rt} = \frac{Q_{rt}}{Q} \tag{6.28}$$

$$\alpha_\delta = \frac{Q_\delta}{Q} = 1 \tag{6.29}$$

In Eq. (6.25) k_n is the characteristic fractile factor from Table D1 on page 108 of BS EN 1990:2002 for "V_X unknown". For this calibration with $n = 30$, k_n is 1.73; k_∞ is the value of k_n when $n \rightarrow \infty$, it is 1.64.

Listed in Table 6.7 for the I-section and Table 6.8 for the C-section are parameters Q_{rt}, $Q_\delta = Q$, α_{rt} and r_k in columns (2-5).

Steps 1 to 7 are explicitly found in BS EN 1990:2002, whilst the following Steps 8 and 9 of the calibration procedure for γ_M are not numbered.

Step 8: *Obtain the design value of the resistance r_d*

The design value r_d for the the test polulation that has less than 100 tests should be calculated by:

$$r_{\mathrm{d}} = b_{\mathrm{m}} g_{\mathrm{rt}}(\underline{X}_{\mathrm{m}}) \exp(-k_{\mathrm{d},\infty}\alpha_{\mathrm{rt}}Q_{\mathrm{rt}} - k_{\mathrm{d,n}}\alpha_{\delta}Q_{\delta} - 0.5Q^2) \tag{6.30}$$

In Eq. (6.31) $k_{\mathrm{d,n}}$ is the design fractile factor from Table D2 on page 108 in Eurocode 0 (BSI, 2002a) for "V_{X} unknown". In this study, $k_{\mathrm{d,n}}$ is equal to 3.13. $k_{\mathrm{d},\infty}$ is the value of $k_{\mathrm{d,n}}$ for $n \rightarrow \infty$ and is 3.04 from Table D2.

Step 9: *Determine the safety partial factor* γ_{M}

The partial safety factor for resistance γ_{M} accounts for material property and for model uncertainties and dimensional variations. It can be determined by:

$$\gamma_{\mathrm{M}} = \frac{r_{\mathrm{k}}}{r_{\mathrm{d}}} \tag{6.31}$$

Given in columns (6-7) of Tables 6.7 and 6.8 are r_{d} and γ_{M}. To three significant figures it is found that γ_{M} is in range of 1.14 to 1.18 for the I-section and 1.16 to 1.19 for the C1 section. Taking into account the degree of uncertainties for the seven variables and to provide for a safer design, the author suggests, for PFRP members in bending, the partial factor is 1.3 for the LTB mode of ultimate limit state failure.

6.4. The lateral-torsional buckling curves

Plotted in Figures 6.7 and 6.8 are the LTB curves for the two sections having $\alpha_{\mathrm{LT}} = 0.34$ and $\gamma_{\mathrm{M}} = 1.3$. In the figures the solid line is the unfactored LTB curve for χ_{LT} vs. λ_{LT}.
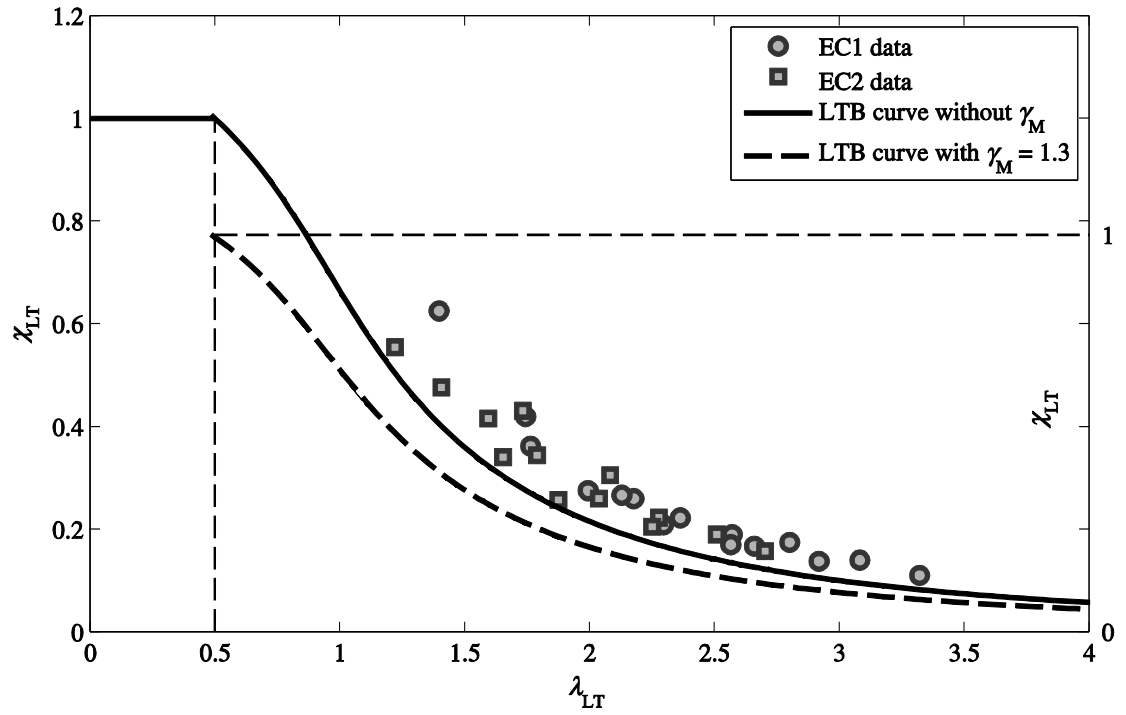
Figure 6.7 LTB curve for I-section with $\alpha_{LT} = 0.34$ and $\gamma_M = 1.3$
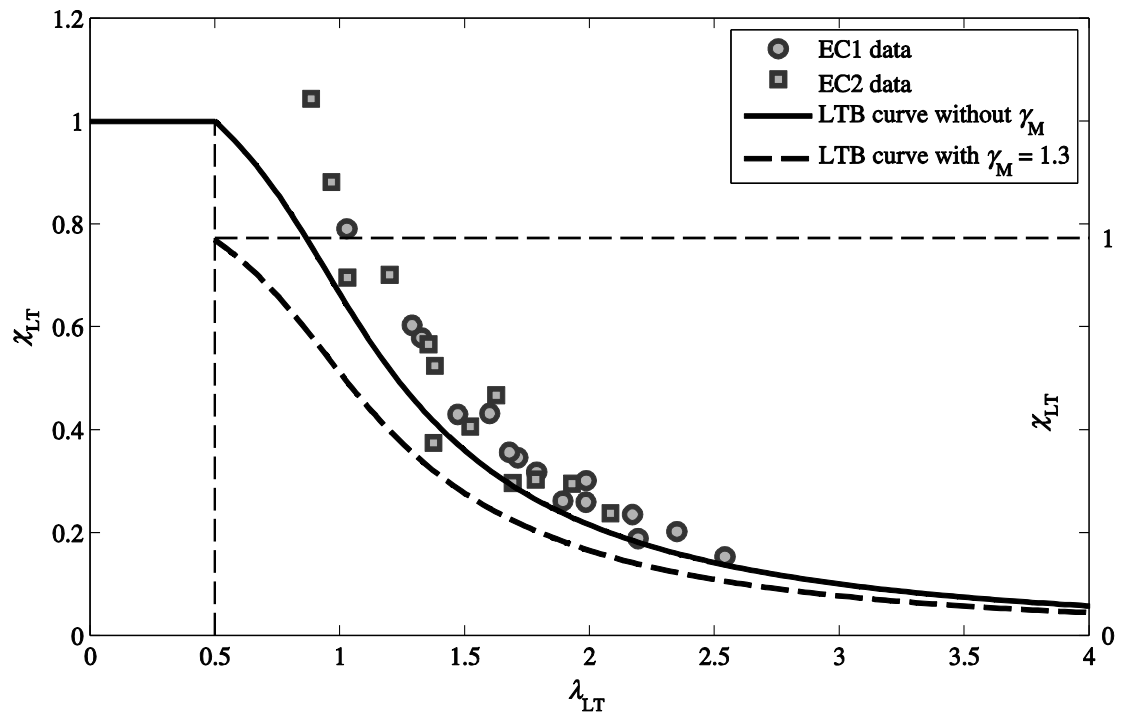
Figure 6.8 LTB curve for C1-section with $\alpha_{LT} = 0.34$ and $\gamma_M = 1.3$

To show the effect of the partial factor (γ_M) the solid curve is scaled down by a factor of 1.3 and is presented in the figures by the dashed line curve. The ordinate axis scale for this factored curve is given on the right side. It is noted that should such a plot be given in a design standard, this dashed line would not exist. It is seen in Figures 6.7 and 6.8 that all the test data points lie above the factored curve. This means design is safe and reliable. The results presented in these two figures provide strong evidence that $\alpha_{LT} = 0.34$ and $\gamma_M = 1.3$ would be appropriate for the two sections.

To take a step further, the author incorporates all the data from the test programme in Chapter 4 into one LTB curve to find out if the proposed curve would be okay. By assuming $\sigma_{Loc} = 134$ MPa is for the 'second' ultimate failure stress (to define $\chi_{LT} = 1.0$), the non-dimensional slenderness λ_{LT} and reduction factor χ_{LT} for the tested beams of I, C1, C2 and C3 sections can be constructed. This universal curve is plotted in Figure 6.9. The results in this figure give further evidence that the proposed LTB curve would be reliable when calibrated against all 114 test results in this study.
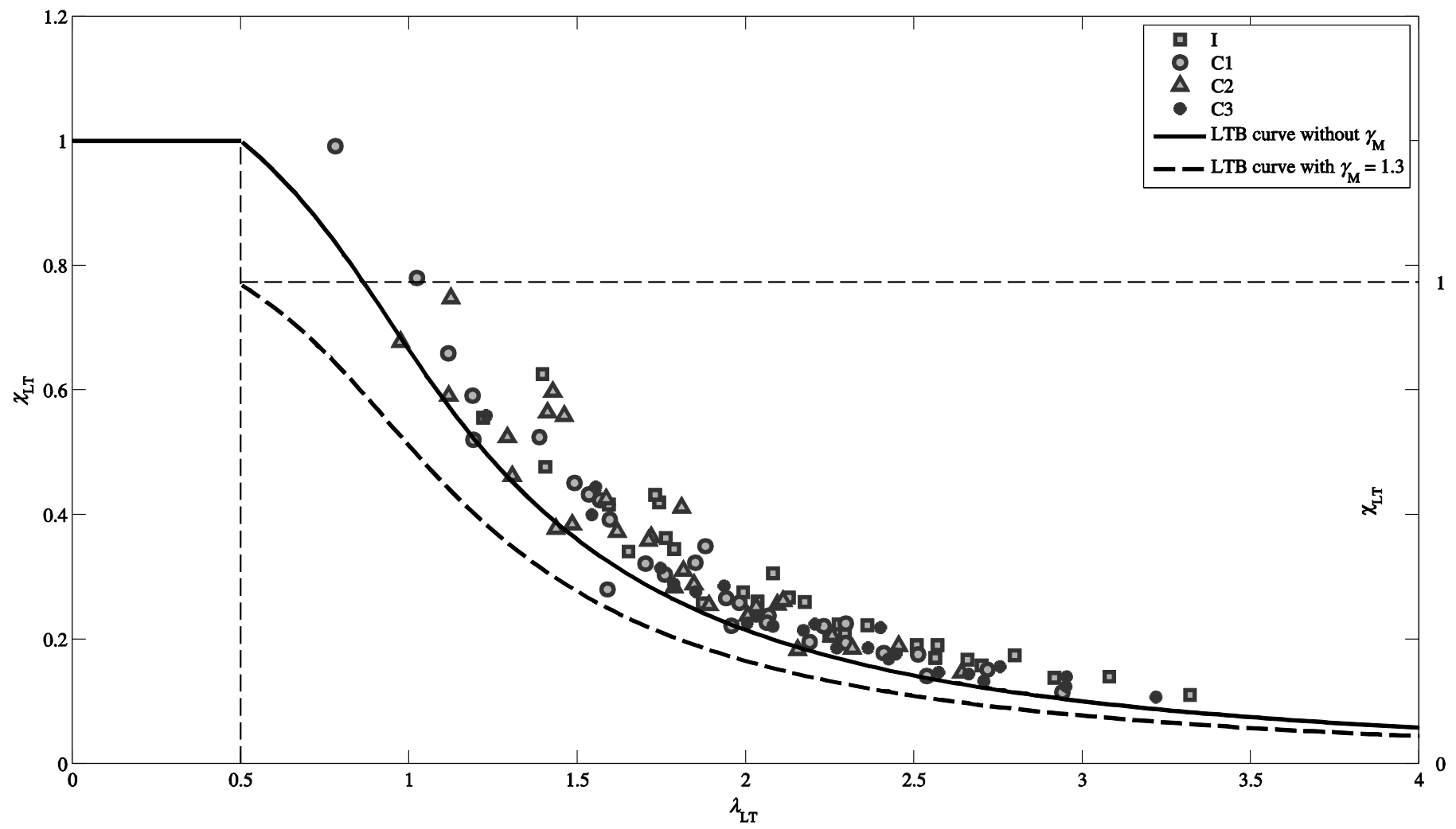
Figure 6.9 LTB curves for PFRP beams

6.5. Concluding remarks

A brief introduction to the two popular approaches for a LTB resistance check in Europe (Eurocode) and American (AISC) has been presented. A design proposal in accordance with the Eurocode 3 approach is developed. For the LTB curve a plateau length of $\bar{\lambda}_{\mathrm{LT},0} = 0.5$ is assumed, after Trumpf (2006) proposed this value based on physical testing and numerical simulations. Based on measured section geometries and the Ayrton-Perry Formula solution for LTB strength an imperfection factor of $\alpha_{\mathrm{LT}} = 0.34$ is found to be acceptable. The calibration procedure for γ_{M} followed the steps in Annex D in BS EN 1990:2002. It is conducted using data for the I- and C1-sections in the test programme of Chapter 4. Each calibration involves one section with 30 tests, for five span lengths, three vertical load positions and two displacement boundary conditions. A number of justified assumptions had to be made during the calibration process, in terms of obtaining the nominal and mean values to the seven basic variables. These are the same assumptions that had to be made when γ_{M} was calibrated for steel in BS EN 1993-1-1:2005. A fair assumption was also made that the coefficient of variation for the local flange buckling stress was 10%.

From the calibration process it is found that γ_{M} for the I-section is in range of 1.14 to 1.18 and for the C-section the range is from 1.16 to 1.19. To take into account the level of uncertainty in the geometrical dimensions and the LTB test results, and emanating from the assumptions made, the author is recommending a γ_{M} of 1.3 for PFRP beams. It can also be recommended that there might be a need to adopt a higher imperfection factor to cover the possible practical range of initial geometry imperfections with pultruded beam sections. This is not scoped in this Ph.D. thesis.

For a comparison with another design factor for PFRP beams, it is noteworthy that in the ASCE pre-standard (2010) the resistance factor (ϕ) for LTB failure is 0.7, which is equivalent to having $\gamma_M = 1.43$. The fact that 1.43 is higher than the proposed 1.3 shows that the test results and calibration assumption presented in this thesis are more reliable than those available when ϕ was determined.

The study in this chapter to establish a partial factor of resistance for the LTB mode of failure has shown that the Eurocode calibration approach is suitable when the material is PFRP.

CHAPTER 7

CONCLUSIONS AND FURTHER WORKS

7.1. Research summary

Before conclusions, in the form of a number of findings from the Ph.D. work are given, there is a summary of the research contributions presented in Chapters 2 to 6. The author has combined computational simulations using the Finite Element (FE) code ABAQUS$^{®}$ with physical testing to investigate the Lateral-Torsional Buckling (LTB) behaviour of pultruded FRP beams. 94 coupon tests were carried out to determine the material properties of four sections (one I and three channels) in the series of physical tests. Elastic constants for the orthotropic material were needed for the predictions of resistance by a closed-form formula and by Finite Element Analysis (FEA). In the 114 tests a beam was subjected to a mid-span point load and the vertical height of the loading was one of: Top Flange (TF); Shear Centre (SC); Bottom Flange (BF). At the ends of the simply supported beam (for major-axis bending) the lateral flexure was free (EC1) or fixed (EC2), whilst warping is always free (both EC1 and EC2). To demonstrate the sensitivity of LTB resistance to changing a number of the several key design parameters the FEA work was essential. A good agreement with difference in range of -22% to 14% between test measurements and FEA elastic buckling loads was established when the end displacement boundary conditions were EC1. The agreement

was poorer for the EC2 conditions, and the physical reasons for this divergence are presented. A design curve has been constructed for PFRP beams in bending in accordance with the approach adopted in the Eurocode suite of standards for design of civil engineering works.

A brief introduction to the contents of the research is presented in Chapter 1. Examples of PFRP structures are given along with reasons for why there should be a future Eurocode for the newer structural material of FRP.

Provided in Chapter 2 is the general review that is used to inform the research reported in the thesis. The review mainly focuses on the testing by previous researchers. Because of the low number of previous individual tests and weaknesses in the boundary conditions the authors found that there is need for more test results that can be used in the procedure to calibrate design equations; for a factor towards ensuring safety. There is a discussion on the closed-form formulae that have been formulated to predict the resistance of structural steel and information to show how they can be simply modified to be suitable for beams of Pultruded FRP (PFRP) material.

Chapter 3 presents 54 coupon tests (with specimens cut from flange and web panels) to determine the longitudinal modulus of elasticity (E_L) and the Major Poisson's ratio. 20 coupon tests (cut from web panels) are used to characterize the transverse modulus of elasticity E_T and 20 coupons (from web panels) for 10° off-axis tests are evaluated to establish the in-plane shear modulus (G_{LT}). To have numerical predictions for LTB resistances these elastic constants are needed in both the closed-form formulae and FEA work. This chapter has a section on the testing of short columns to determine the local buckling load. The resistances for this different thin-walled buckling mode are used to define the non-dimensional slenderness for PFRP beams in Chapters 4 and 6.

Chapter 4 is used to report the results of 114 LTB tests using four sections at five span lengths (i.e. 1828, 2438, 2844, 3454 and 4064 mm), three vertical load positions (i.e. TF, SC and BF) and two end displacement boundary conditions (EC1 and EC2). To minimize any restraint against LTB deformation occurring as assumed in the theoretical formulation the loading fixture was specifically made in accordance with a disc system designed and commissioned by Flint (1948), for his Ph.D. research with thin gauged steel sections. The loading system adopted dead weights when failing slender beams and a tension jack was required when the beam configuration was too stockier for dead weights.

Each LTB resistance was determined either from the 'peak load' method (when the load vs. mid-span rotation curve gives the 'bifurcation-like' failure) or by the Southwell plot method, when the load-lateral displacement curve gave the 'displacement-amplification-like' response. By having the elastic constants from the coupon testing presented in Chapter 3 the new test results were compared against theoretical predictions using a closed-form formula that could be included in a future Eurocode design standard for FRP materials (to be equivalent to BS EN 1993-1-1:2005 for structural steel).

Chapter 5 covers the computational simulations by modelling and solving with the FEA code ABAQUS®. Both linear and nonlinear buckling analyses were conducted on the I- and C1-sections. An imperfection shape was successfully introduced into the FE modelling in form of an Euler buckling shape. The maximum initial minor axis out-of-straightness imperfection is located at mid-span and takes the measured value for the section reported in Chapter 4. Sensitivity analyses were carried out to study the influence of geometric imperfections, lateral load eccentricities, loading height and overhang lengths on failure by LTB. When appropriate to do so comparisons are made between simulation outputs and measured test results. Another new contribution is that

a modelling technique to accounts for the contribution of the radius fillet areas is developed and proposed as being suitable for the most effective numerical predictions.

Chapter 6 offers a preliminary study towards the development of a robust design method for PFRP beam in bending. The calibration procedure to generate a partial safety factor for resistance is carried out following the standard procedure given in EN 1990:2002.

7.2. Conclusions

The following bullet points describe the main findings:

(1)   *Material properties*

- Because elastic constants in PFRP materials are influenced by fibre architectures and layer distributions in the thin-walled panels it is a challenge to obtain, for numerical analysis, the characteristic values for the moduli of elasticity, especially the in-plane shear modulus (G_{LT}). It would be expected that the four outstand flanges in an I-section shape would possess the same stiffnesses. By way of coupon testing it is found that the longitudinal modulus of elasticity (E_L) in opposite flanges differs by 13.3%. This finding implies that the flexural response under loading is going to be influenced by this material imperfection.

- The measured $E_L(29.2-31.6\,\text{GPa})$ and $G_{LT}(4.2-4.8\,\text{GPa})$ are 30% to 60% higher than those tabulated, for the purpose of engineering design, in the Fiberline Composites Design Manual. This implies that it will be safe, if not too

conservative should the designer adopt the mechanical properties for PFRP beam members recommended by the pultruder.

- Using the 10° off-axis tensile coupon test method for the determination of G_{LT}, for each of the four pultruded sections, gave consistent results. Because this shear test approach has advantages, such as size of a relatively high volume in pure shearing, and a simpler specimen preparation and loading procedure, the author recommends that the 10° off-axis tensile test method be adopted for the characterization of in-plane shear properties.

(2)   *Local buckling*

- The determination by testing of the uniform stress for the onset of local buckling is difficult. One of the reasons would be due to the limited number of tests. More importantly, the buckling load is influenced by many factors, such as cross-section geometry, loading distribution, end conditions, rotational stiffness along the web-flange junction. The thesis adopted the lowest value amongst testing, FEA and theoretical prediction. It would be expected that this choice is safe for design. Furthermore, the role of that value in this Ph.D. as a reference for the definition of the non-dimensional slenderness has no effect on the key findings and conclusions drawn from this study.

(3)   *LTB resistance by testing*

- The test rig designed in accordance with the principles developed by Flint (1948) worked successfully and the disc system applying the mid-span loading enabled the influence of load height on LTB resistance to be realized. The test programme showed that the dead weight loading approach is the best for

221

establishing LTB resistance. Although the tensile jack loading approach introduced a horizontal restraining force it is shown to be effective also.

- The LTB failure in the 114 beam configurations was mostly of the 'displacement-amplification like' form, rather than the 'bifurcation like' form. The former dominated the beams' deformation because it is influenced by a complex combination of the imperfections, emanating from geometric, loading, material and test set-up. On occasions the combination created a 'perfect condition' when the beam did not failed with LTB instability mode. As expected there is not a one-to-one correlation between the closed-form predictions (using measured moduli) and LTB test data; this finding is the same for LTB resistances with 'off-the-shelve' steel sections. As a result it is essential to perform a calibration procedure to be able to have design guidelines that can be demonstrated to be safe, reliable and relevant.

(4)   *Numerical simulations*

- A finite element modelling methodology that additionally accounts for the fillet radii present in I- and C-sections is shown to be appropriate when predicting the LTB response of PFRP beams. Its inclusion is found to be essential if FEA is to be used to establish relevant buckling resistances for the beam configurations that had been tested. The simpler modelling assumption of using geometric properties that ignore the fillet radii area is applicable should the FE output be used for calibration of a design resistance formula. The justification of this guidance is that a lower numerical LTB resistance is obtained, and this is for a safer design.

- It is observed that the influence of G_{LT} (ranging from 3-5 GPa) on LTB resistance is 17-27%. This finding highlights the importance for us to have a test method that can reliably characterize this key elastic constant.

- FEA simulations are used to show that the LTB response of PFRP beams is going to be sensitive to changes in the geometric imperfections. It is shown that the allowance ($L/240$) in ASTM D3917 for the minor axis out-of-straightness geometric imperfection is too high and not appropriate. The allowance ($0.005L^2$) in BS EN 13706-2 is more suitable, and based on geometrical measurements of the tested sections is practically accepted.

- It is shown numerically that resistance is highly influenced by the lateral position of the vertical loading. To represent what could exist in practice it can be assumed that loading is applied at the top flange height with a lateral offset for a load eccentricity. If this eccentricity is taken to be 3 mm, it is found that the limiting LTB buckling load can reduce by 17% or increased by 19%.

(5)   *Proposal for a design procedure*

- By making a number of justified assumptions the author successfully applied the Eurocode 0 approach to establish the partial factor for the modified Eurocode equation (it is Eq. (6.56) in BS EN 1993-1-1:2005) for LTB resistance by the general curve method. It is established that a LTB curve for the safe and reliable design for PFRP beam, having the imperfection factor $\alpha_{LT} = 0.34$ (this is equivalent to curve b in Table 6.3 of BS EN 1993-1-1:2005), requires a partial safety factor for resistance (γ_M) of 1.3. This major new contribution was verified using all 114 results from the author's series of physical tests. The higher equivalent value of γ_M is 1.43 (inverse of a calibrated LRFD resistance

factor of 0.7) from the ASCE pre-standard of 2010 indicates that the LTB test data information presented in this thesis is more relevant than was available in 2010.

- There might be a need to adopt a higher imperfection factor to cover the possible practical range of initial geometry imperfections found in PFRP beam sections. To make it easy for steel designers to design with PFRP the adopted α_{LT} will match a Eurocode 3 value, such as 0.49 for curve *c* or 0.76 for curve *d*.

7.3. Further work

The work reported in this thesis makes an important contribution to the design of PFRP beams in bending that can eventually be given in a future Eurocode. To obtain more knowledge that can be analysed to provide designers with guidance that will be the most reliable, economical and relevant, there are particular areas that require further work. They are listed in what follows:

- To be confident in the predictions of LTB resistance, there is a need to ensure appropriateness and reliability of test methods to determine the mechanical properties of the PFRP material. Particular attention should be given to the measurement of the in-plane shear modulus. There is currently no consensus towards a standard test method. The author recommends that the 10° off-axis test method be properly characterized by undertaking test series with different specimen sizes and PFRP materials.

- The stress for the onset of local flange buckling, which is required in the expression for the non-dimensional slenderness (λ_{LT}) of a beam member, is

not well-defined. The author suggests that more compression (stub column) tests with a range of PFRP sections and specimen heights (relative to the buckling half-wave length) should be conducted to establish the local buckling stresses. It is recommended that further consideration be given to what constitutes a robust expression for λ_{LT}.

- Physical testing with the EC1 end displacement boundary conditions gave buckling loads in good agreement with the theoretical predictions; the agreement being better for an I-section than for a C-section. It is recommended that when carrying out further LTB test with C-section that the position of the vertical point-load is gradually moved laterally so that shear centre loading can be obtained.

- For the buckling loads test results and numerical predictions are not in a good agreement when the beam configurations had the EC2 end displacement boundary conditions. An investigation is required to understand exactly what EC2 condition was in the test series. A new approach to impose the EC2 condition in testing is to be recommended. It is worth noting that prior to the author's work there had been no previous LTB testing with EC2. Testing and FE work for PFRP beam configurations having other displacement boundary conditions found in practice is needed for a comprehensive understanding of the LTB mode of failure.

- To obtain more reliable test results, and to minimise uncertainty in measurement due to the test set-up conditions, repetitive tests on every beam configuration is highly recommended.

- Further improvements in the FE modelling methodology are feasible through the actual modelling of the geometry and boundary conditions.

- Mode interaction between local and global (LTB) buckling can occur at intermediate spans at a buckling load that is either lower than both distinct mode. It is important to take the influence of mode interaction into consideration in a future research.

- The static loading considered is for short term only. The creep effect on the LTB response was not considered. The LTB behaviour under changing temperatures was not scoped also. It is recommended that these effects can be investigated in a future work.

REFERENCES

AFIFI, A. A. M. 2007. *Buckling of stiffened pultruded GRP plates and columns.* PhD, University of Lancaster.

AISC 2010. Specification for Structural Steel Buildings. *ANSI/AISC 360.* Chicago, IL, USA: American Institute of Steel Construction.

ALLEN, H. G. & BULSON, P. S. 1980. *Background to buckling,* London, McGraw-Hill.

ANON. 2004. The new and improved pultex pultrusion design manual of standard and custom fiber reinforced polymer structural profiles, Vol 4, rev 9. Alum Bank, PA, USA: Creative Pultrusions, Inc.

ANON. 2014a. Fiberline Design manual. Middelfart, Denmark: Fiberline A/S.

ANON. 2014b. Strongwell design manual. Bristol, VA, USA.: Strongwell Corp.

ASCE 2010. Pre-standard for load and resistance factor design (LRFD) of pultruded fiber reinforced polymer (FRP) structures. Arlington, VA,USA.

ASTM 2008. Standard test method for tensile properties of polymer matrix composite materials. *D3039 / D3039M.* West Conshohocken, PA, USA: ASTM International.

ASTM 2010. Standard test method for tensile properties of plastics. *D638.* West Conshohocken, PA, USA: ASTM International.

ASTM 2012a. Standard specification for dimensional tolerance of thermosetting glass-reinforced plastic pultruded shapes. *D3917*. West Conshohocken, PA, USA: ASTM International.

ASTM 2012b. Standard test method for shear properties of composite materials by the V-notched beam method. *D5379 / D5379M*. West Conshohocken, PA,USA: ASTM International.

ASTM 2012c. Standard test method for shear properties of composite materials by V-notched rail shear method. *D7078 / D7078M*. West Conshohocken, PA, USA: ASTM International.

ATTARD, M. 1983. Extrapolation Techniques for Buckling Loads. *Journal of Structural Engineering,* 109**,** 926-935.

BANK, L. C. 1987. Shear coefficients for thin-walled composite beams. *Composite Structures,* 8**,** 47-61.

BANK, L. C. 1990. Shear properties of pultruded glass FRP materials. *Journal of Materials in Civil Engineering,* 2**,** 118-122.

BANK, L. C. 2006. *Composites for construction: Structural design with FRP materials,* NJ, USA, John Willey & Sons.

BARROS DA S. SANTOS NETO, A. & LEBRE LA ROVERE, H. 2007. Flexural stiffness characterization of fiber reinforced plastic (FRP) pultruded beams. *Composite Structures,* 81**,** 274-282.

BROOKS, R. J. & TURVEY, G. J. 1995. Lateral buckling of pultruded GRP I-section cantilevers. *Composite Structures,* 32**,** 203-215.

BSI 1992. Eurocode 3: design of steel structures, Part 1.1 General rules for buildings. *DD ENV 1993-1-1*. London, UK: British Standards Institution.

BSI 1997. Plastics - Determination of tensile properties - Part 4: Test conditions for isotropic and orthotropic fibre-reinforced plastic composites. *BS EN ISO 527-4.* London, UK: British Standards Institution.

BSI 2002a. Eurocode - Basis of structural design. *BS EN 1990.* London, UK: British Standards Institution.

BSI 2002b. Reinforced plastic composites - Specificationa for pultruded profiles - Part 2: Method of test and general requirements. *BS EN 13706-2.* London, UK: British Standards Institution.

BSI 2005a. Eurocode 3: Design of Steel Structures - Part 1-1: General Rules and Rules for Buildings. *BS EN 1993-1-1.* London, UK: British Standards Institution.

BSI 2005b. Reinforced plastics - Determination of the in-plane shear modulus by the plate twist method. *BS EN 15310.* London, UK: British Standards Institution.

BSI 2012a. Plastics - Determination of tensile properties - Part 1: General principles. *BS EN ISO 527-1.* London, UK: British Standards Institution.

BSI 2012b. Plastics - Determination of tensile properties - Part 5: Test conditions for unidirectional fibre-reinfoced plastic composites. *BS EN ISO 527-5.* London, UK: British Standards Institution.

BUREAU, A. 2006. NCCI: Elastic critical moment for lateral torsional buckling. *SN003a-EN-EU.* Access Steel

CHAMBERS, R. E. 1997. ASCE design standard for pultruded fiber-reinforced-plastic (FRP) structures. *Journal of Composites for Construction,* 1**,** 26-38.

CHAMIS, C. C. & SINCLAIR, J. H. 1977. Ten-deg off-axis test for shear properties in fiber composites. *Experimental Mechanics,* 17**,** 339-346.

CHENG, J. & YURA, J. 1988. Lateral buckling tests on coped steel beams. *Journal of Structural Engineering,* 114**,** 16-30.

CLARK, J. W. & HILL, H. N. 1960. Lateral Buckling of Beams. *Journal of the Structural Divison-ASCE,* 86**,** 175-196.

CLARKE, J. L. 1996. *Structural design of polymer composites,—EUROCOMP design code and handbook, 1996,* London, UK, E & FN Spon.

CORREIA, J. R., BRANCO, F. A., SILVA, N. M. F., CAMOTIM, D. & SILVESTRE, N. 2011. First-order, buckling and post-buckling behaviour of GFRP pultruded beams. Part 1: Experimental study. *Computers & Structures,* 89**,** 2052-2064.

CRISFIELD, M. A. 1981. A fast incremental/iterative solution procedure that handles "snap-through". *Computers & Structures,* 13**,** 55-62.

DASSAULT SYSTÈMES SIMULIA CORP 2013a. Abaqus Analysis User's Guide, ver. 6.13. Providence, RI, USA.

DASSAULT SYSTÈMES SIMULIA CORP 2013b. ABAQUS/Standard Ver 6.13. Providenvce, RI, USA.

DASSAULT SYSTÈMES SIMULIA CORP 2013c. Theory manual, ver 6.13. Providence, RI, USA.

DAVALOS, J. F., QIAO, P. & SALIM, H. A. 1997. Flexural-torsional buckling of pultruded fiber reinforced plastic composite I-beams: experimental and analytical evaluations. *Composite Structures,* 38**,** 241-250.

DUMONT, C. & HILL, H. 1940. The lateral stability of equal-flanged aluminum-alloy I-beams subjected to pure bending. *NACA Technical Note 770,* 22**,** 31-36.

FLINT, A. R. 1948. *On the lateral stability of beams.* Ph.D, University of Bristol.

GOSLING, P. D. & SARIBIYIK, M. 2003. Nonstandard tensile coupon for fiber-reinforced plastics. *Journal of materials in civil engineering,* 15**,** 108-117.

HODGKINSON, J. 2000. *Mechanical testing of advanced fibre composites,* Cambridge, UK, Woodhead Publishing Limited.

HYER, M. W. & WHITE, S. R. 1998. *Stress analysis of fiber-reinforced composite materials,* Singapore, WCB/Mc Graw-Hill.

IES INC 2013. ShapeBuilder Ver 7.0. Bozeman, MT, US.

KOLLÁR, L. P. 2003. Local buckling of fiber reinforced plastic composite structural members with open and closed cross sections. *Journal of Structural Engineering,* 129**,** 1503-1513.

KOLLÁR, L. P. & SPRINGER, G. S. 2003. *Mechanics of composite structures,* Cambridge, University press.

LANE, A. 2002. *An experimental investigation of buckling mode interaction in PFRP columns.* PhD University of Warwick.

LEE, S. 2001. *Flexural-torsional buckling of pultruded T-sections.* PhD, Georgia Institute of Technology.

LINDNER, J. 1996. Influence of constructional details on the load carrying capacity of beams. *Engineering Structures,* 18**,** 752-758.

MANDAL, P. & CALLADINE, C. R. 2002. Lateral-torsional buckling of beams and the Southwell plot. *International Journal of Mechanical Sciences,* 44**,** 2557-2571.

MATHWORKS INC 2013. MATLAB release 2013 ed. Natick, Massachusetts, Unite States.

MEASUREMENTS GROUP INC 1983. Errors due to transverse sensitivity in strain gages. *Experimental Techniques,* 7**,** 30-35.

MECHATOOLS TECHNOLOGIES INC 2013. ShapeDesigner (SaaS). 2013 ed. Quebec city, Quebec, Canada.

MOTTRAM, J. T. 1992a. Lateral-torsional buckling of a pultruded I-beam. *Composites,* 23**,** 81-92.

MOTTRAM, J. T. 1992b. Lateral-torsional buckling of thin-walled composite I-beams by the finite difference method. *Composites Engineering,* 2**,** 91-104.

MOTTRAM, J. T. 2004a. Determination of critical load for flange buckling in concentrically loaded pultruded columns. *Composites Part B: Engineering,* 35**,** 35-47.

MOTTRAM, J. T. 2004b. Shear Modulus of Standard Pultruded Fiber Reinforced Plastic Material. *Journal of Composites for Construction,* 8**,** 141-147.

MOTTRAM, J. T., BROWN, N. D. & ANDERSON, D. 2003. Physical testing for concentrically loaded columns of pultruded glass fibre reinforced plastic profile. *Proceedings of the ICE-Structures and Buildings,* 156**,** 205-219.

MOTTRAM, J. T. & SHAW, C. T. 1996. *Using finite elements in mechanical design,* London, McGraw Hill.

NETHERCOT, D. A. & ROCKEY, K. C. 1973. Lateral buckling of beams with mixed end conditions. *Structural Engineer,* 51.

NGUYEN, T. T., CHAN, T. M. & MOTTRAM, J. T. 2013. Influence of boundary conditions and geometric imperfections on lateral–torsional buckling resistance of a pultruded FRP I-beam by FEA. *Composite Structures,* 100**,** 233-242.

NGUYEN, T. T., CHAN, T. M. & MOTTRAM, J. T. 2014. Lateral-torsional buckling resistance by testing for pultruded FRP beams under different loading and displacement boundary conditions. *Composites Part B: Engineering,* 60**,** 306-318.

OMIDVAR, B. 1998. Shear Coefficient in Orthotropic Thin-Walled Composite Beams. *Journal of Composites for Construction,* 2**,** 46-56.

PILKEY, W. D. 2005. *Formulas for stress, strain, and structural matrices*, John Wiley & Sons New Jersey.

PINDERA, M. J. & HERAKOVICH, C. T. 1986. Shear characterization of unidirectional composites with the off-axis tension test. *Experimental Mechanics,* 26**,** 103-112.

QIAO, P. Z., ZOU, G. P. & DAVALOS, J. F. 2003. Flexural–torsional buckling of fiber-reinforced plastic composite cantilever I-beams. *Composite Structures,* 60**,** 205-217.

RAZZAQ, Z., PRABHAKARAN, R. & SIRJANI, M. M. 1996. Load and resistance factor design (LRFD) approach for reinforced-plastic channel beam buckling. *Composites Part B: Engineering,* 27**,** 361-369.

RIKS, E. 1979. An incremental approach to the solution of snapping and buckling problems. *International Journal of Solids and Structures,* 15**,** 529-551.

ROBERTS, T. & AL-UBAIDI, H. 2002. Flexural and Torsional Properties of Pultruded Fiber Reinforced Plastic I-Profiles. *Journal of Composites for Construction,* 6**,** 28-34.

ROBERTS, T. M. 2002. Influence of shear deformation on buckling of pultruded fiber reinforced plastic profiles. *Journal of Composites for Construction,* 6**,** 241-248.

SAPKÁS, A. & KOLLÁR, L. P. 2002. Lateral-torsional buckling of composite beams. *International Journal of Solids and Structures,* 39**,** 2939-2963.

SCHLEICH, J. B., ESPIGA, F., ANZA, J., BUREAU, A., GALÉA, Y., CHABROLIN, B. & CHANTRAIN, P. 1998. Promotion of plastic design for steel and composite cross-sections(new required conditions in Eurocodes 3 and 4, practical tools for designers). *EUR(Luxembourg).*

SEDLACEK, G., UNGERMANN, D., KUCK, J., MAQUOI, R. & JANSS, J. 1989. Evaluation of test results on beams with cross-sectional classes 1-3 in order to obtain strength functions and suitable model factors. . *Background report to EUROCODE 3 - Common Unified Rules for Steel Structures.*

SHAN, L. Y. & QIAO, P. Z. 2005. Flexural–torsional buckling of fiber-reinforced plastic composite open channel beams. *Composite Structures,* 68**,** 211-224.

SINGER, J., ARBOZ, J. & WELLER, T. 1999. Buckling Experiments: Experimental Methods in Buckling of Thin Walled Structures. Volume 1 Basic Concepts, Columns, Beam and Plates. *Book Reviews,* 21**,** 883-886.

SONTI, S. S. & BARBERO, E. J. 1996. Material characterization of pultruded laminates and shapes. *Journal of reinforced plastics and composites,* 15**,** 701-717.

SOUTHWELL, R. V. 1932. On the analysis of experimental observations in problems of elastic stability. *Proceedings of the Royal Society of London. Series A,* 135**,** 601-616.

STEPHEN, R. E. 1998. *Behavior and design of fiber-reinforced polymeric composite equal-leg angle struts.* PhD, Georgia Institue of Technology.

STODDARD, W. P. 1997. *Lateral-torsional buckling behavior of polymer composite I-shaped members.* PhD, Georgia Institute of Technology.

SZALAI, J. & PAPP, F. 2010. On the theoretical background of the generalization of Ayrton–Perry type resistance formulas. *Journal of Constructional Steel Research,* 66**,** 670-679.

TIMOSHENKO, S. 1936. *Theory of elastic stability,* New York, McGraw-Hill

TIMOSHENKO, S. P. & GERE, J. M. 1961. *Theory of elastic stability,* New York, McGraw-Hill.

TRAHAIR, N. S. 1993. *Flexural -torsional buckling of structures,* London, UK, E & FN Spon.

TRAHAIR, N. S., BRADFORD, M., NETHERCOT, D. & GARDNER, L. 2007. *The behaviour and design of steel structures to EC3*, Taylor & Francis.

TRUMPF, H. 2006. *Local and global stability of plane frame works made of orthotropic FRP profiles.* PhD, University of Aachen, Germany.

TURVEY, G. J. 1996. Effects of load position on the lateral buckling response of pultruded GRP cantilevers —Comparisons between theory and experiment. *Composite Structures,* 35**,** 33-47.

TURVEY, G. J. 1998. Torsion tests on pultruded GRP sheet. *Composites Science and Technology,* 58**,** 1343-1351.

TUTTLE, M. E. 2012. *Structural analysis of polymeric composite materials*, CRC Press.

YOUNG, W. C. & BUDYNAS, R. G. 2002. *Roark's formulas for stress and strain*, McGraw-Hill New York.

ZAFARI, B. 2012. *Startlink building system and connections for fibre reinforced polymer structures.* PhD, University of Warwick.

ZUREICK, A. & SCOTT, D. 1997. Short-Term Behavior and Design of Fiber-Reinforced Polymeric Slender Members under Axial Compression. *Journal of Composites for Construction,* 1**,** 140-149.

APPENDIX A

PLOTS FOR COUPON TESTS

This appendix presents the plots for the coupon tests whose results are presented in Chapter 3. It has the plots from three test series for: (**A1**) Longitudinal tensile coupon tests; (**A2**) Transverse tensile coupon tests and (**A3**) 10-degree off-axis coupon tests. Appendix A1 has 54 plots for the relationship of longitudinal stress σ_L with longitudinal train ε_L. Figures A.1 to A.9 have six plots per page and they are numbered parts (a) to (f). The figure caption defines the coupon specimen for each plot in the group of six. Each plot presents the best least-squares straight line fits over the strain range of 0.1% to 0.5%, which is the range adopted to determine the longitudinal tension modulus of elasticity E_L. Both R^2 and E_L are given with the plot. Appendix A2 presents 20 plots in Figures A.10 to A.14 at five per page the relationship of Transverse stress σ_T with Longitudinal train ε_T. There are five plots per section type (e.g. I, C1, C2 and C3). The best least-squares straight line fit over the strain ranges of 0.05% to 0.25% is presented. Both R^2 and E_T are given with the plot. 40 plots for the 10-degree off-axis coupons are presented in pairs in Figures A.11 to A.21 in Appendix A3. One plot (part (a), (c) or (e)) shows the principal shear tress σ_{12} vs. principal shear strain γ_{12} throughout the test to material failure, and second plot (part (b), (d) or (f)) is for the same test results over the narrower strain range of 0% to 0.4%. The second plot had best least-squares straight line fit used to determine a value for G_{LT}.

A. 1   Plots for longitudinal tensile coupon tests

Figure A.1 σ_L vs. ε_L for (a) I1-1-1; (b) I1-1-2; (c) I1-1-3; (d) I1-2-1; (e) I1-2-2; (f) I1-2-3
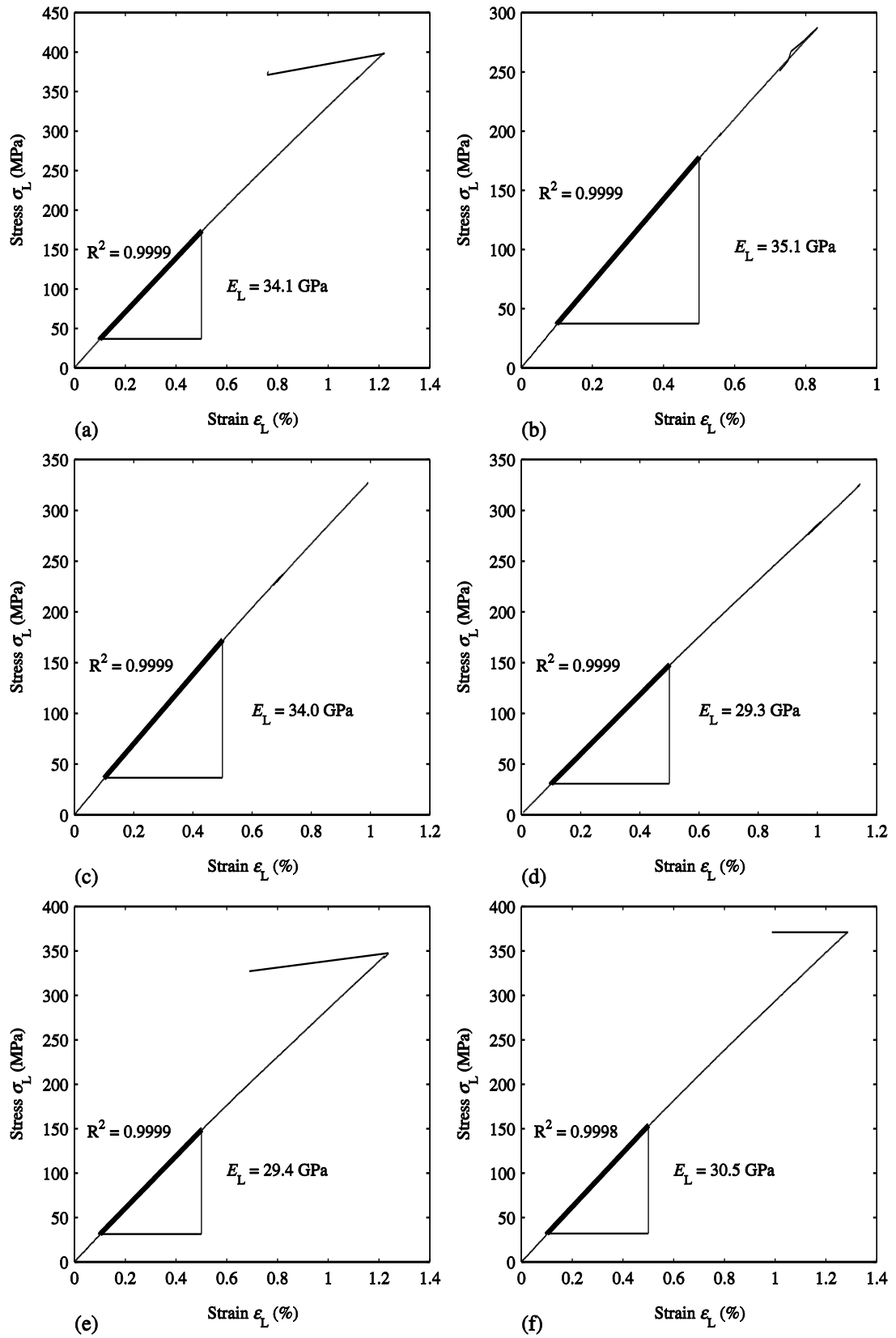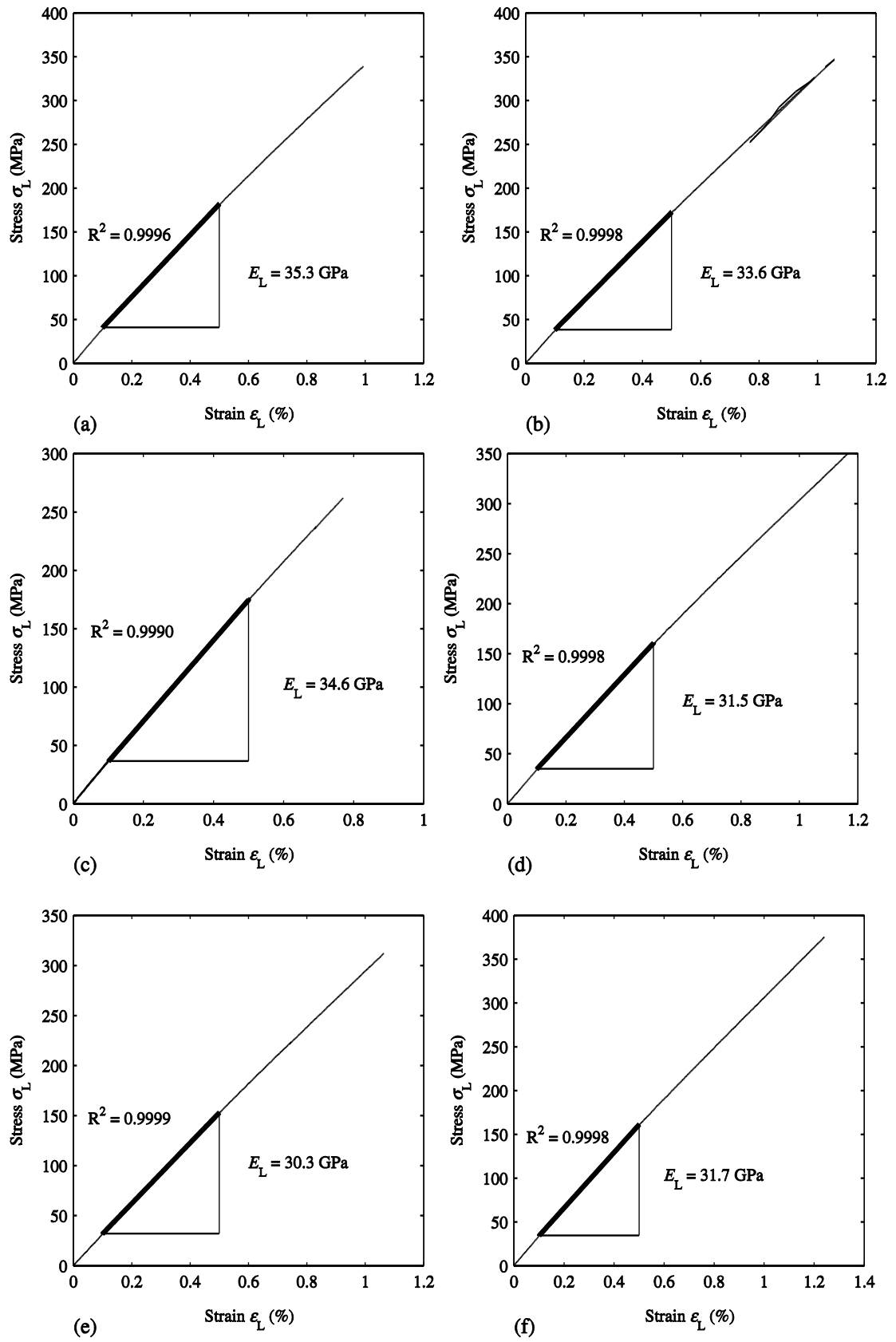
Figure A.2 σ_L vs. ε_L for (a) I1-3-1; (b) I1-3-2; (c) I1-3-3; (d) I1-4-1; (e) I1-4-2; (f) I1-4-3
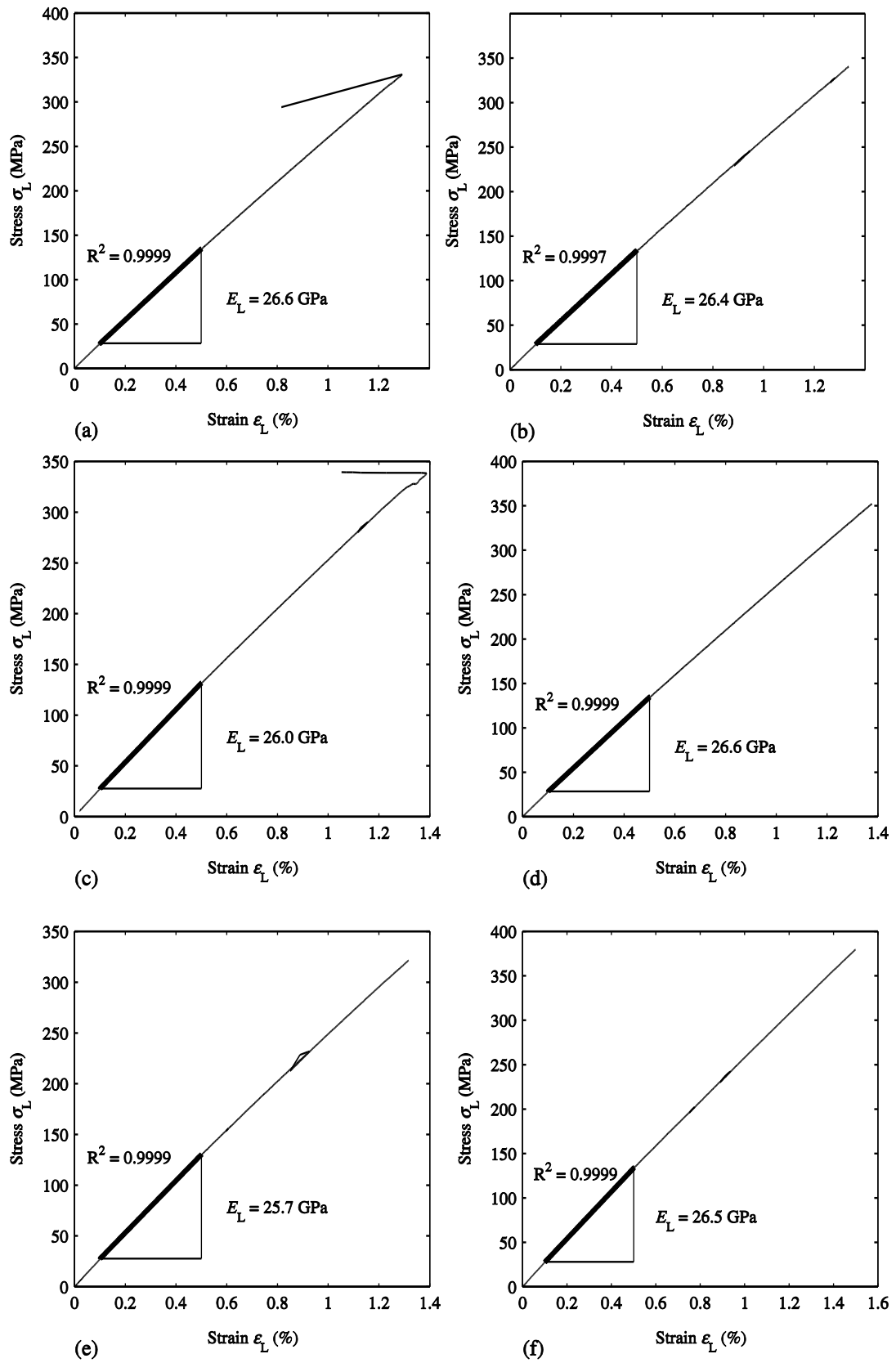
Figure A.3 σ_L vs. ε_L for (a) I1-5-1; (b) I1-5-2; (c) I1-5-3; (d) I1-6-1; (e) I1-6-2; (f) I1-6-3

239
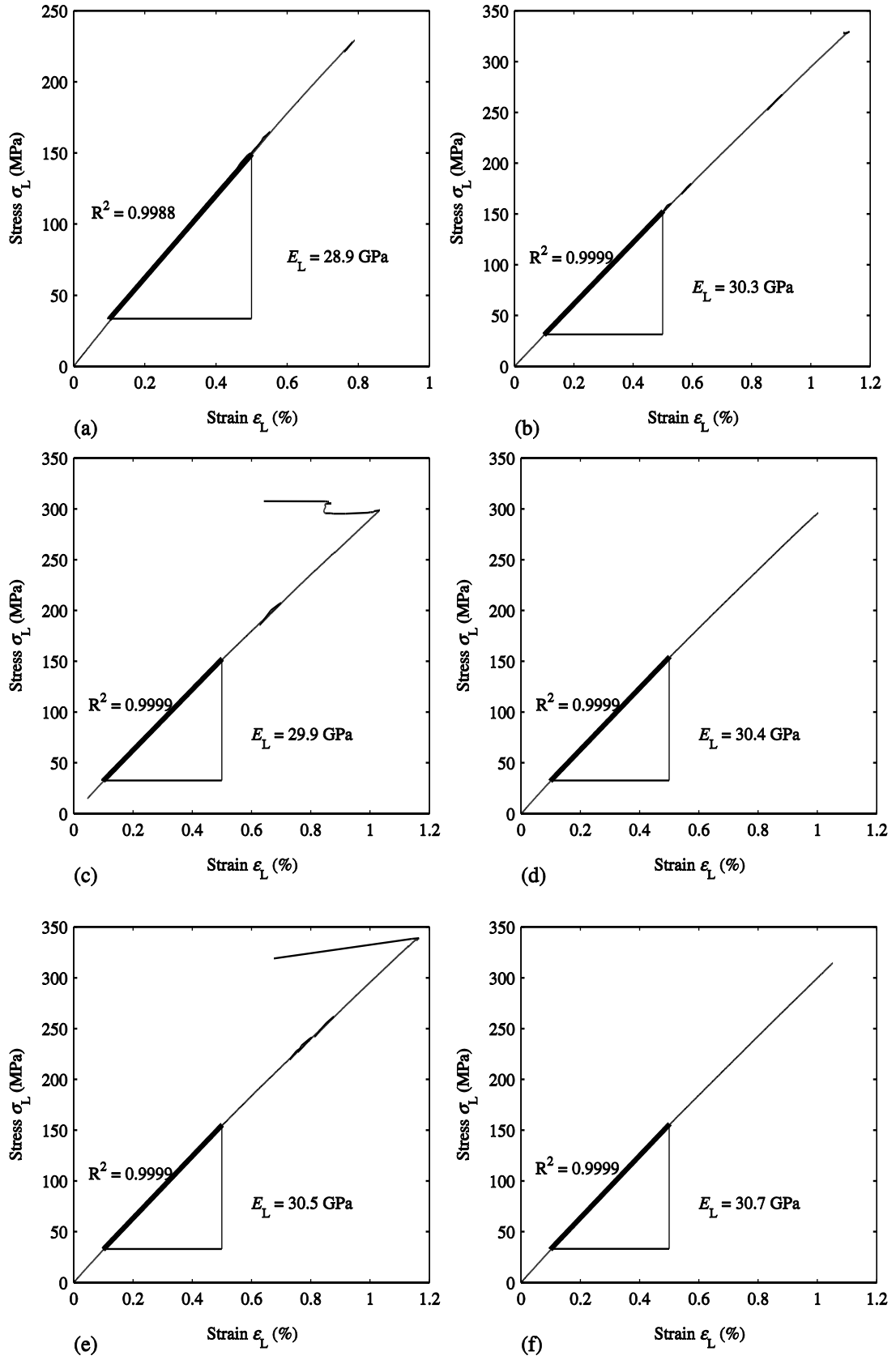
Figure A.4 σ_L vs. ε_L for (a) C1-1-1; (b) C1-1-2; (c) C1-1-3; (d) C1-2-1; (e) C1-2-2; (f) C1-2-3
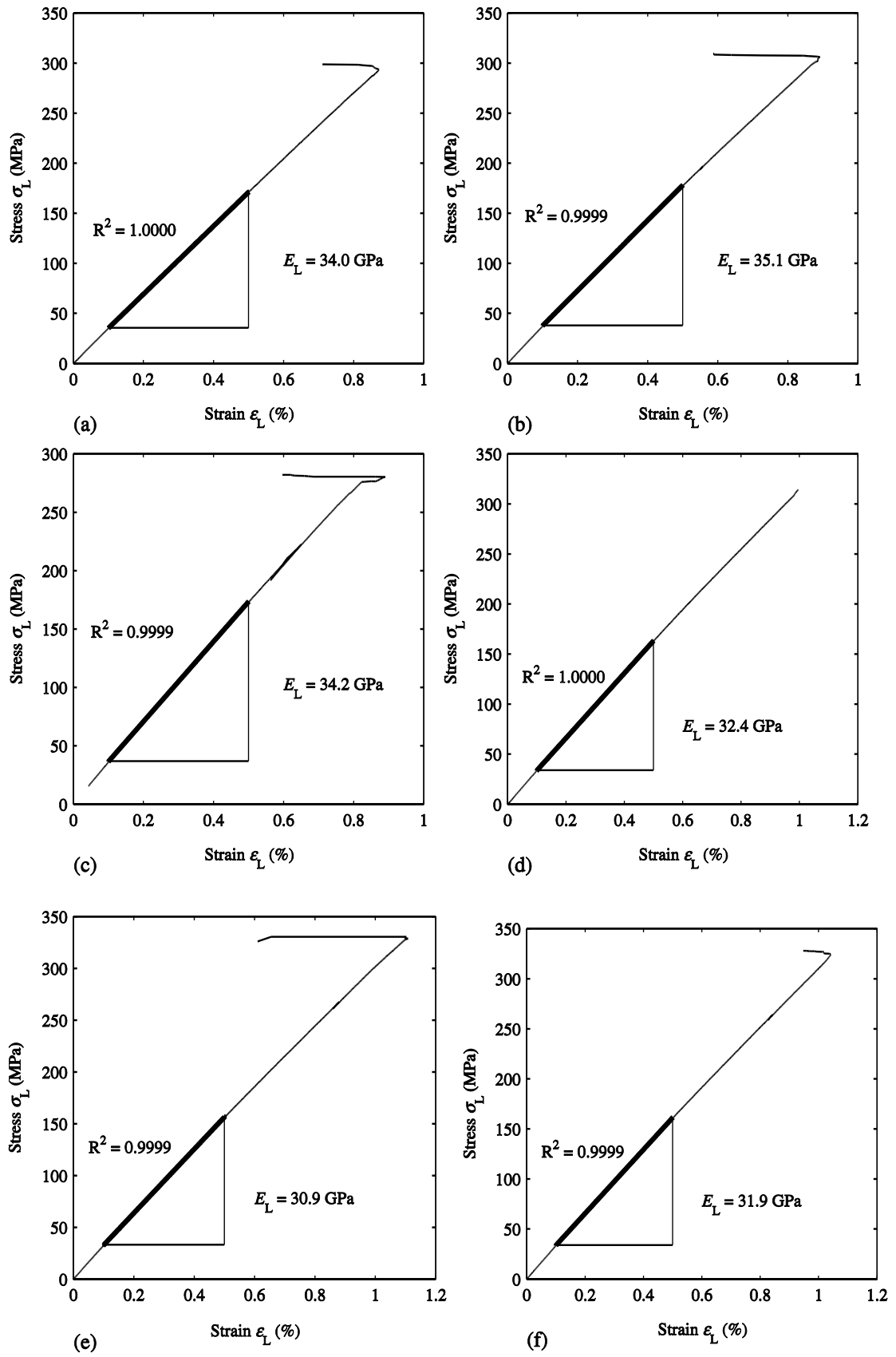
Figure A.5 σ_L vs. ε_L for (a) C1-3-1; (b) C1-3-2; (c) C1-3-3; (d) C1-4-1; (e) C1-4-2; (f) C1-4-3
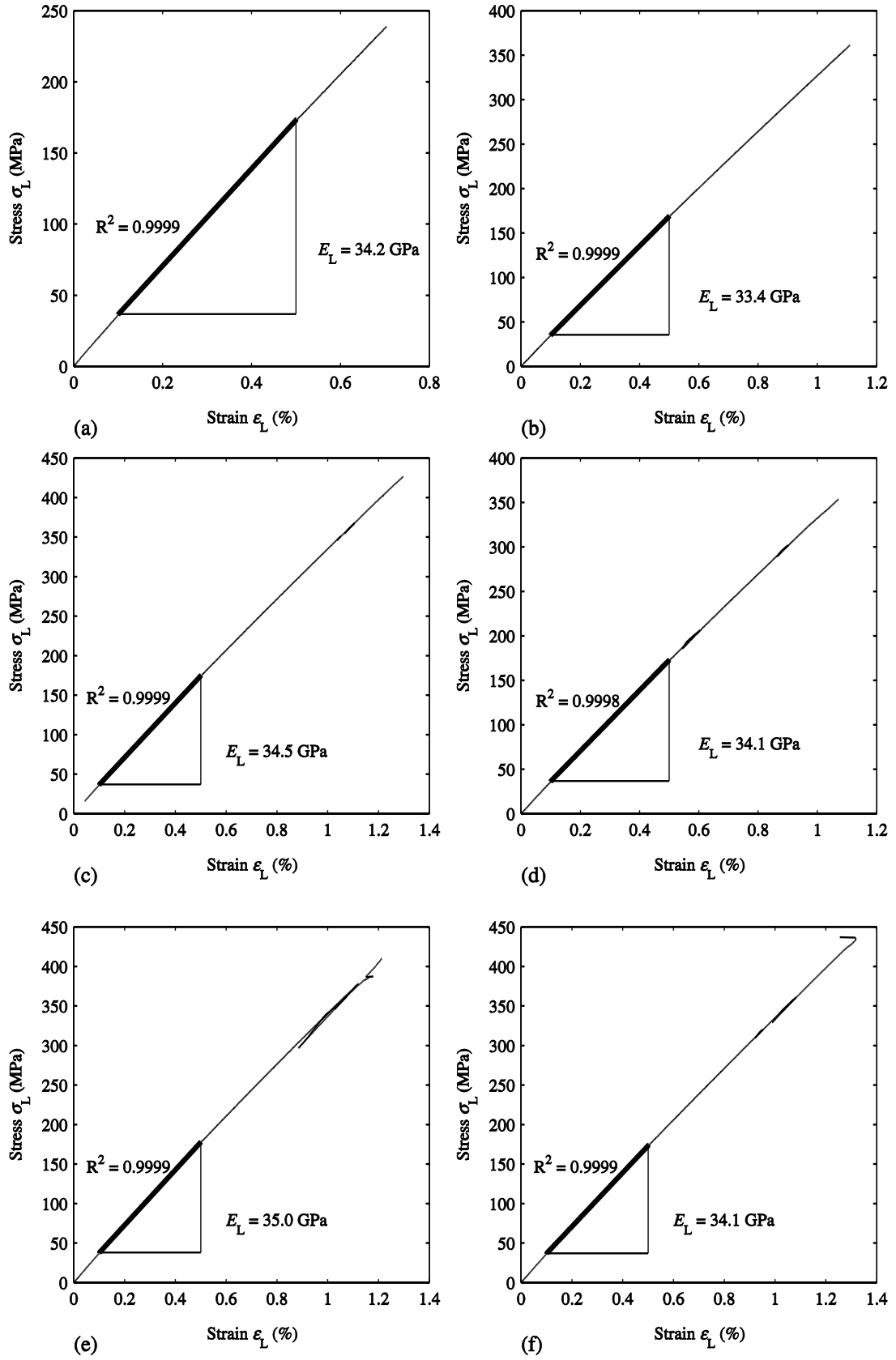
Figure A.6 σ_L vs. ε_L for (a) C2-1-1; (b) C2-1-2; (c) C2-1-3; (d) C2-2-1; (e) C2-2-2; (f) C2-2-3
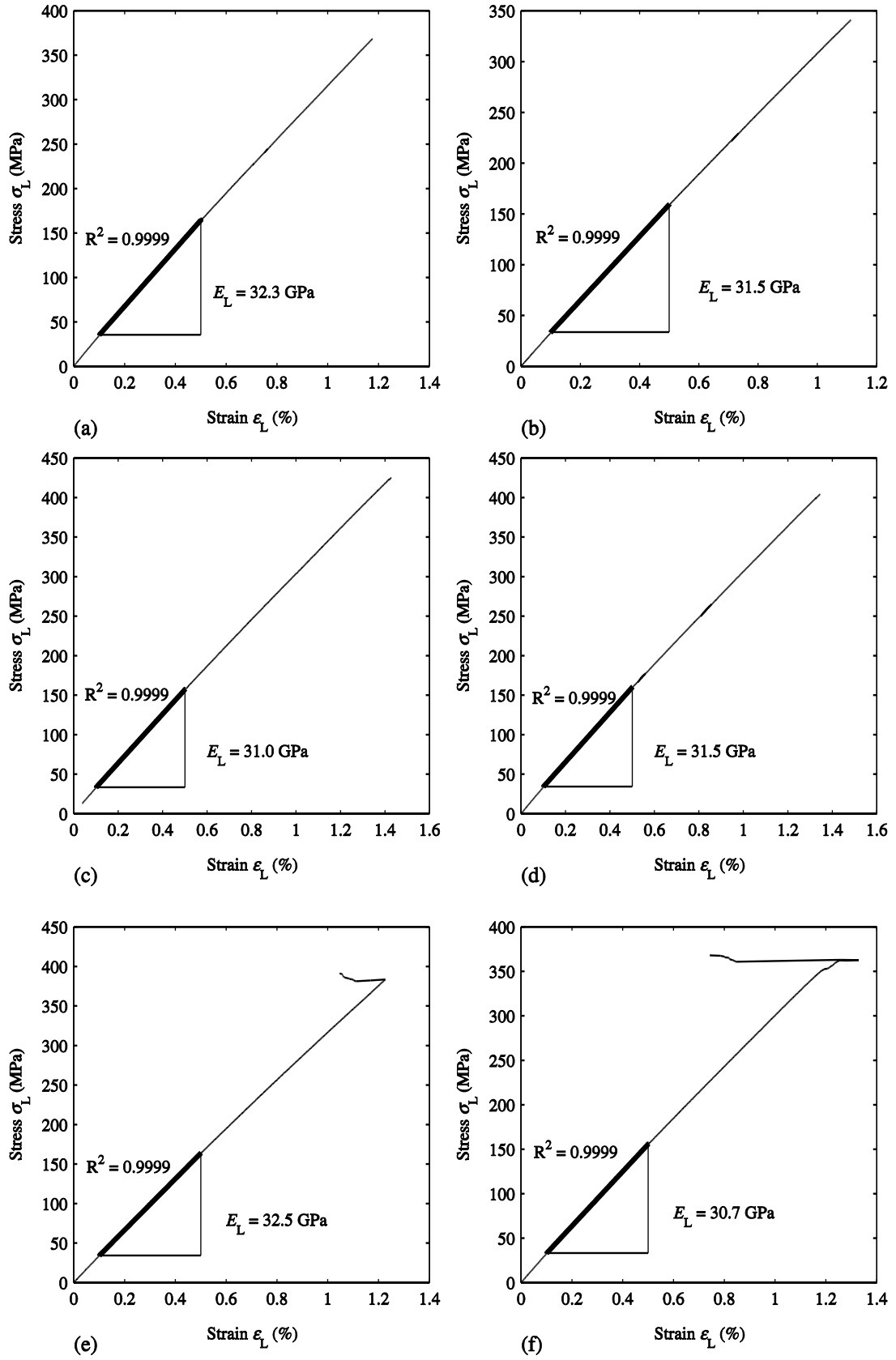
Figure A.7 σ_L vs. ε_L for (a) C2-3-1; (b) C2-3-2; (c) C2-3-3; (d) C2-4-1; (e) C2-4-2; (f) C2-4-3
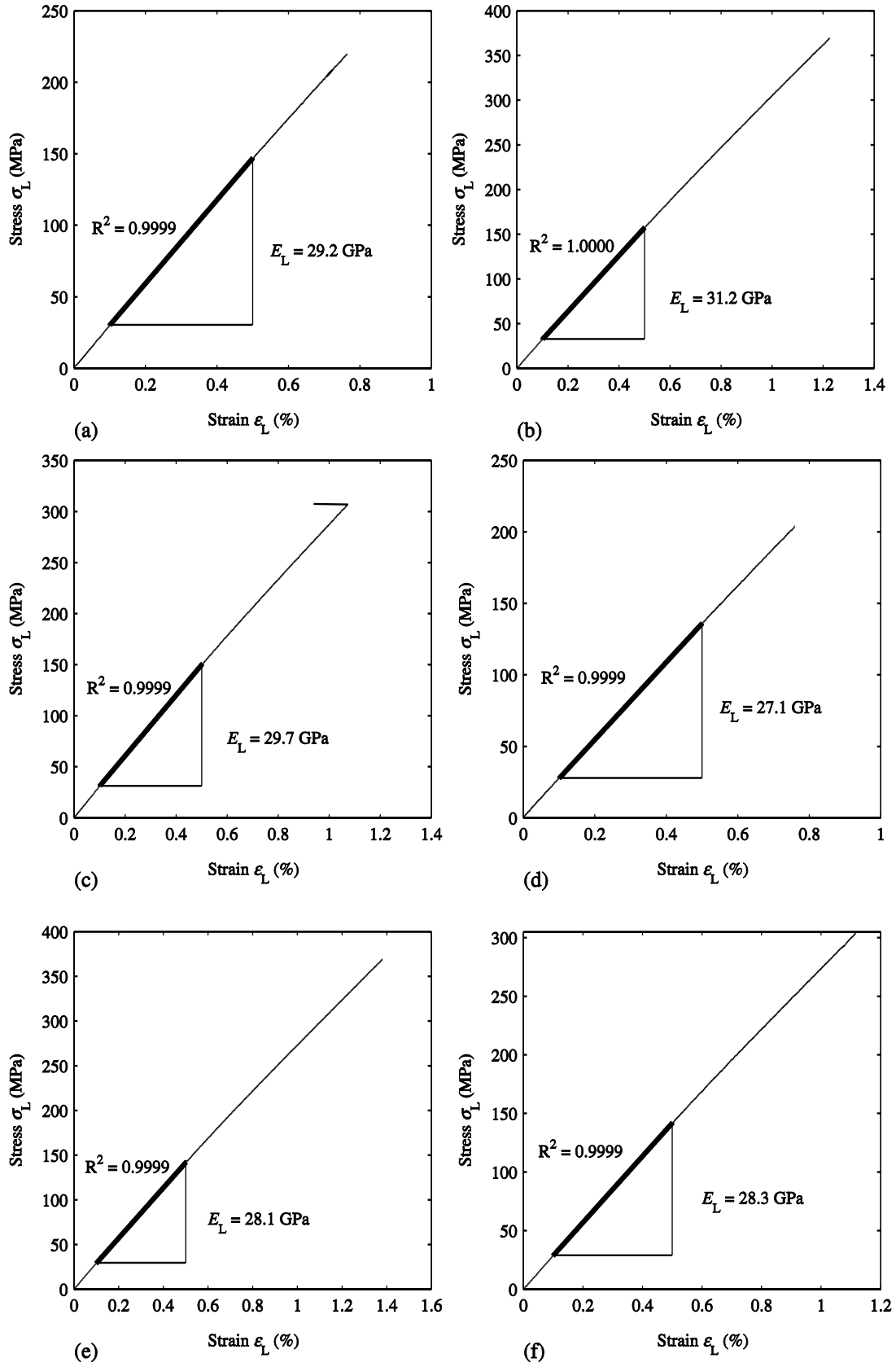
Figure A.8 σ_L vs. ε_L for (a) C3-1-1; (b) C3-1-2; (c) C3-1-3; (d) C3-2-1; (e) C3-2-2; (f) C3-2-3

244
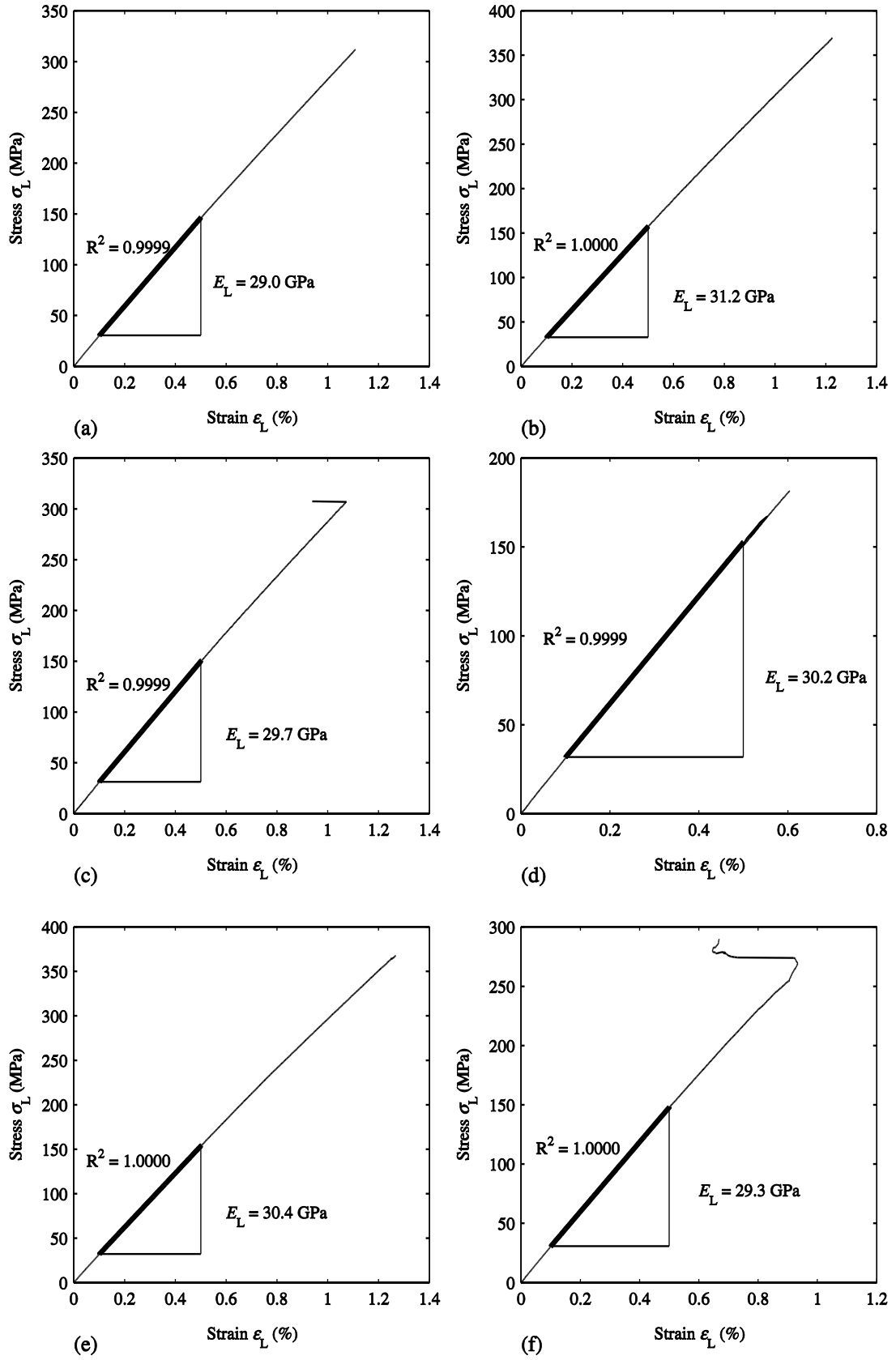
Figure A.9 σ_L vs. ε_L for (a) C3-3-1; (b) C3-3-2; (c) C3-3-3; (d) C3-3-1; (e) C3-3-2; (f) C3-3-3

245

A. 2 Plots for transverse tensile coupon tests
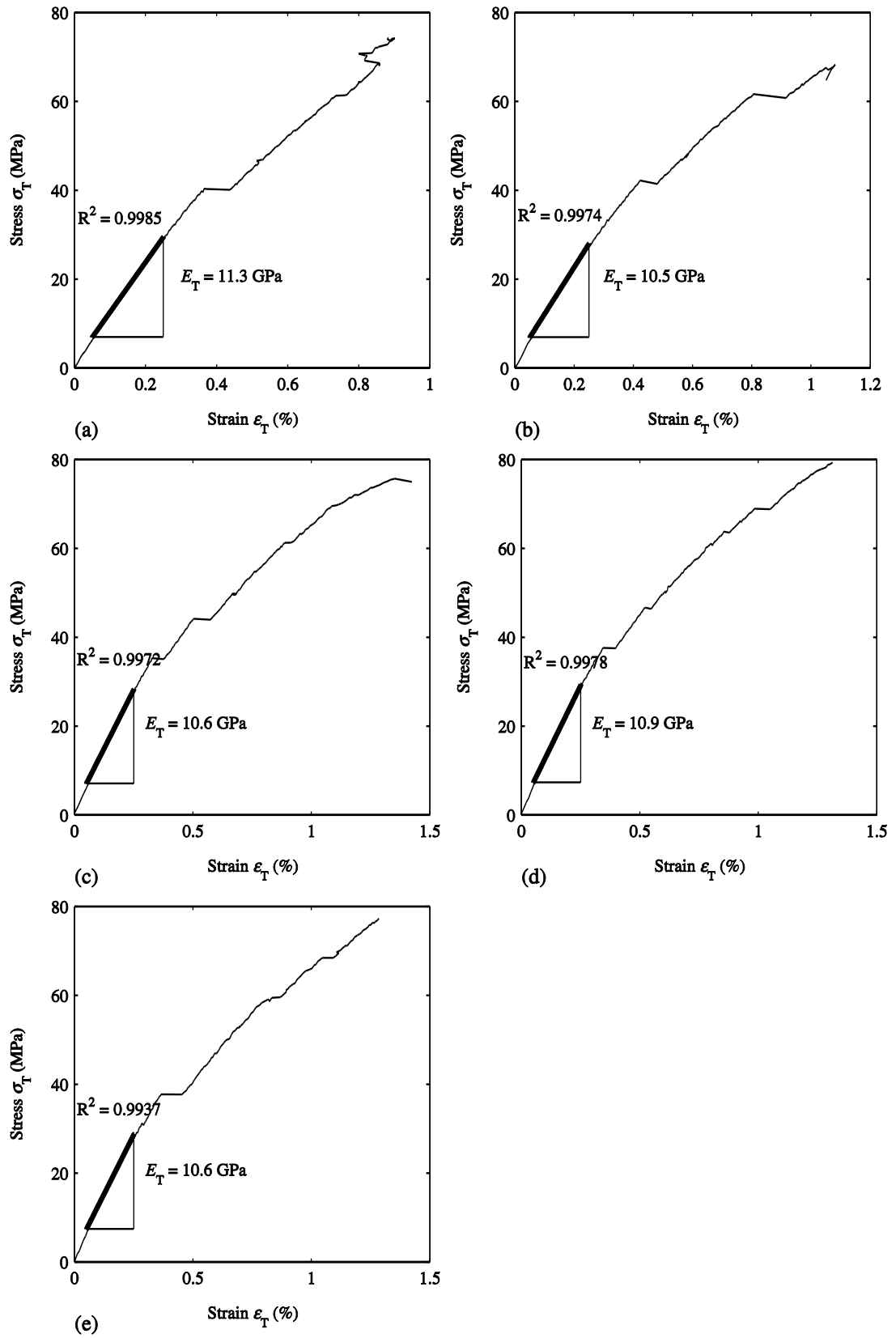
Figure A.10 σ_T vs. ε_T for (a) T-I-1; (b) T-I-2; (c) T-I-3; (d) T-I-4; (e) T-I-5
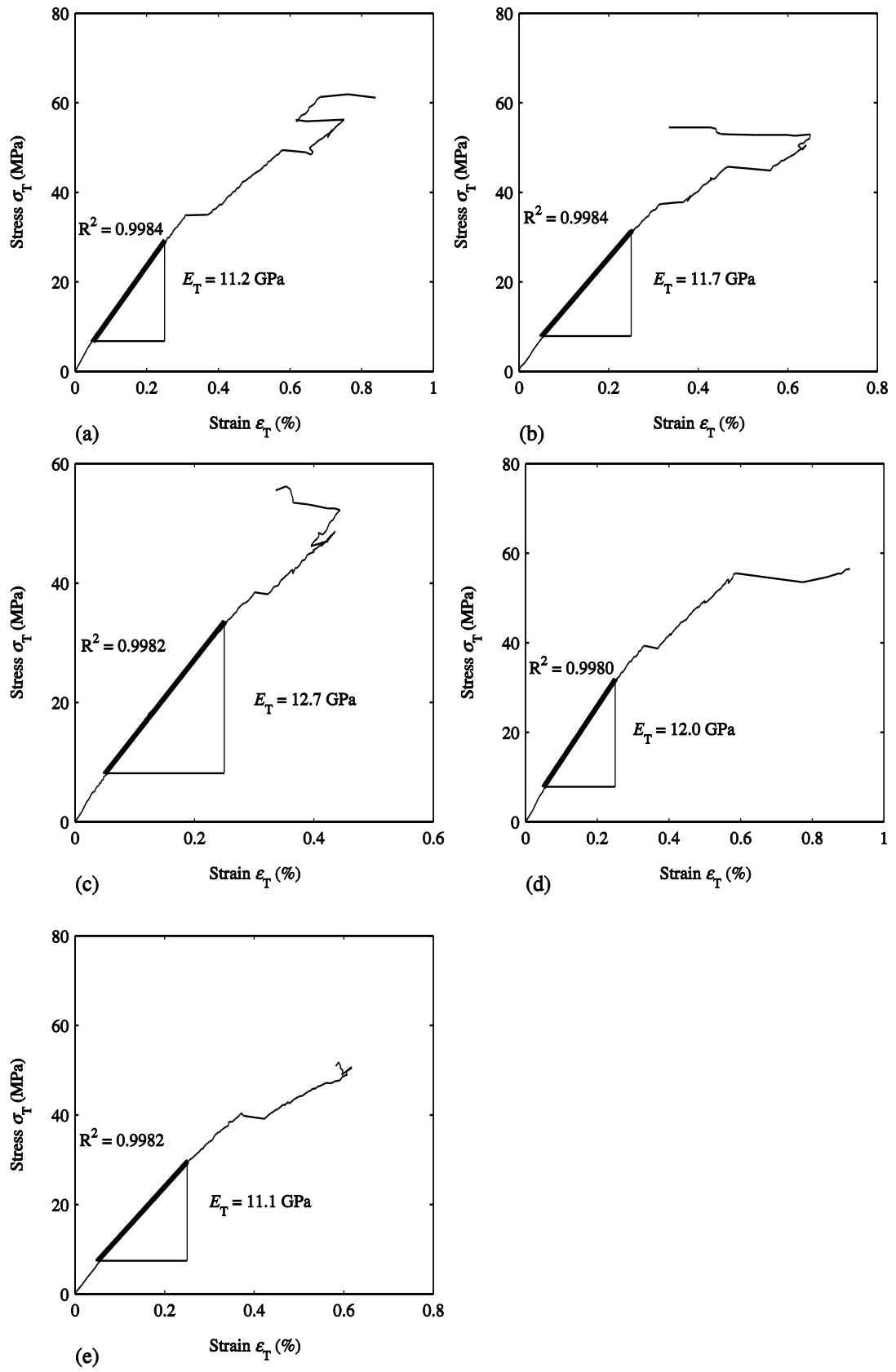
Figure A.11 σ_T vs. ε_T for (a) T-C1-1; (b) T-C1-2; (c) T-C1-3; (d) T-C1-4; (e) T-C1-5
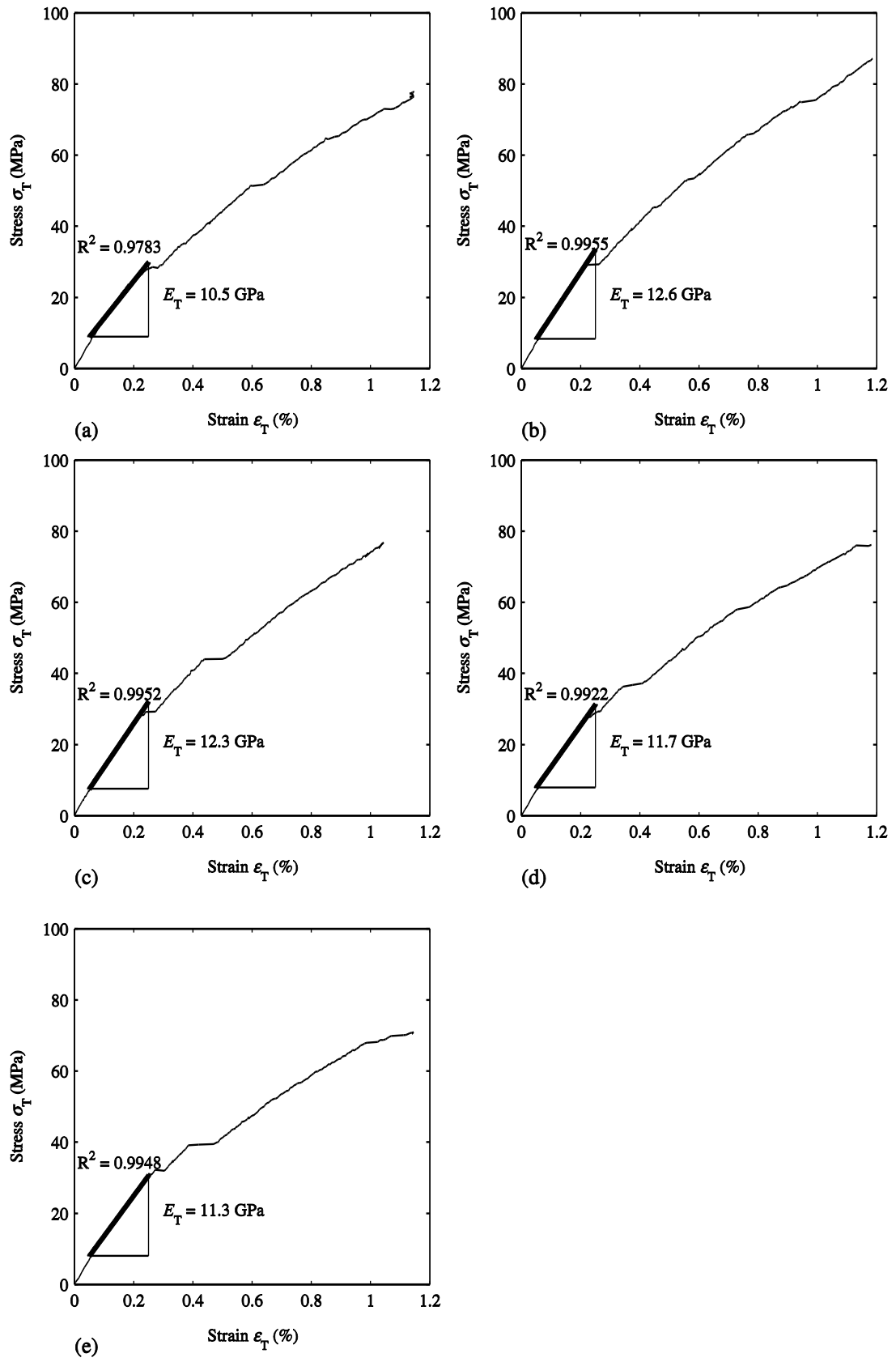
Figure A.12 σ_T vs. ε_T for (a) T-C2-1; (b) T-C2-2; (c) T-C2-3; (d) T-C2-3; (e) T-C2-5
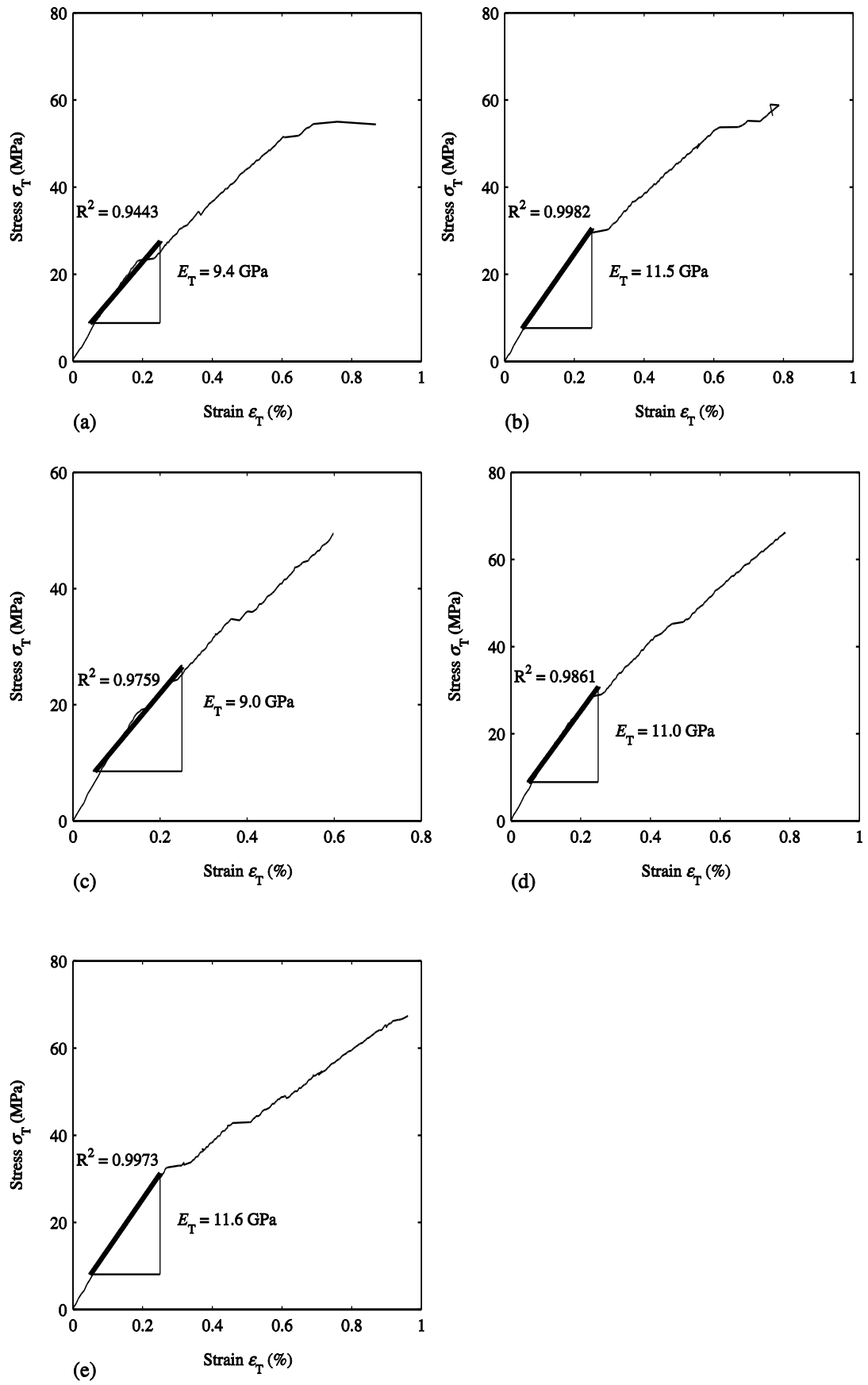
Figure A.13 σ_T vs. ε_T for (a) T-C3-1; (b) T-C3-2; (c) T-C3-3; (d) T-C3-3; (e) T-C3-5

A. 3   Plots for 10° off-axis tensile coupon tests
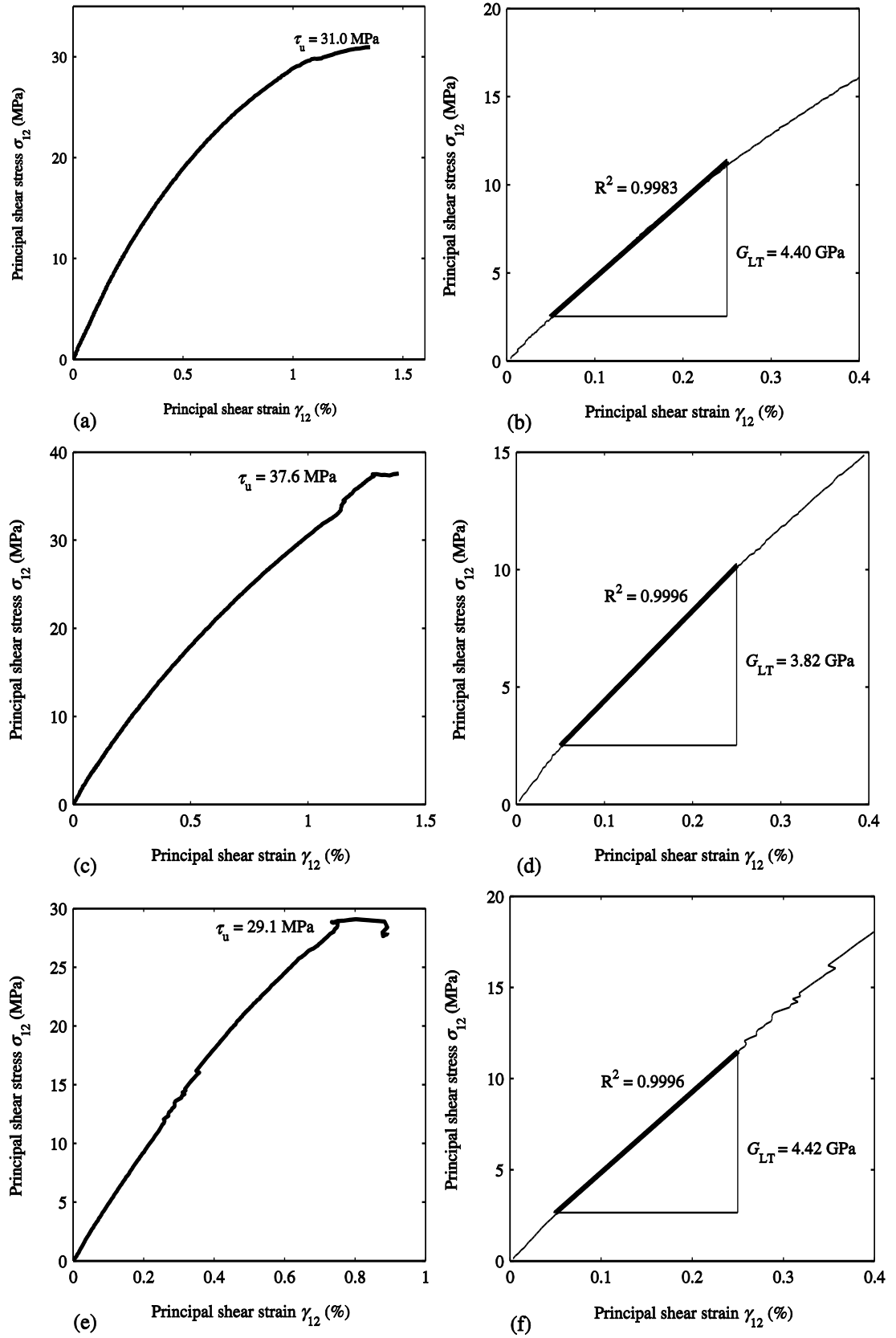
Figure A.14 σ_{12} vs. γ_{12} for: (a), (b) S-I-1-1; (c), (d) S-I-2; (e), (f) S-I-3
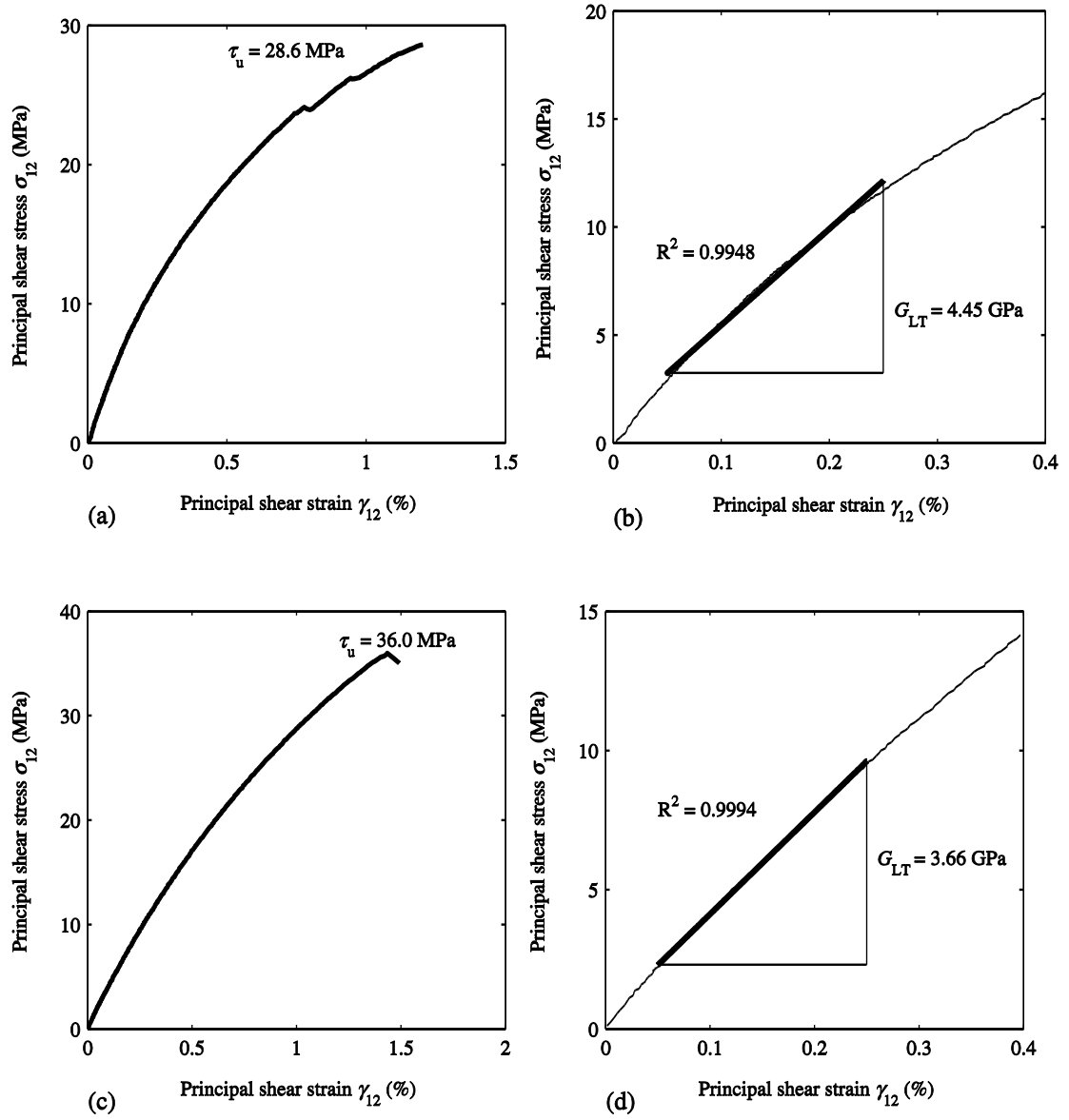
Figure A.15 σ_{12} vs. γ_{12} for (a), (b) S-I-4; (c), (d) S-I-5
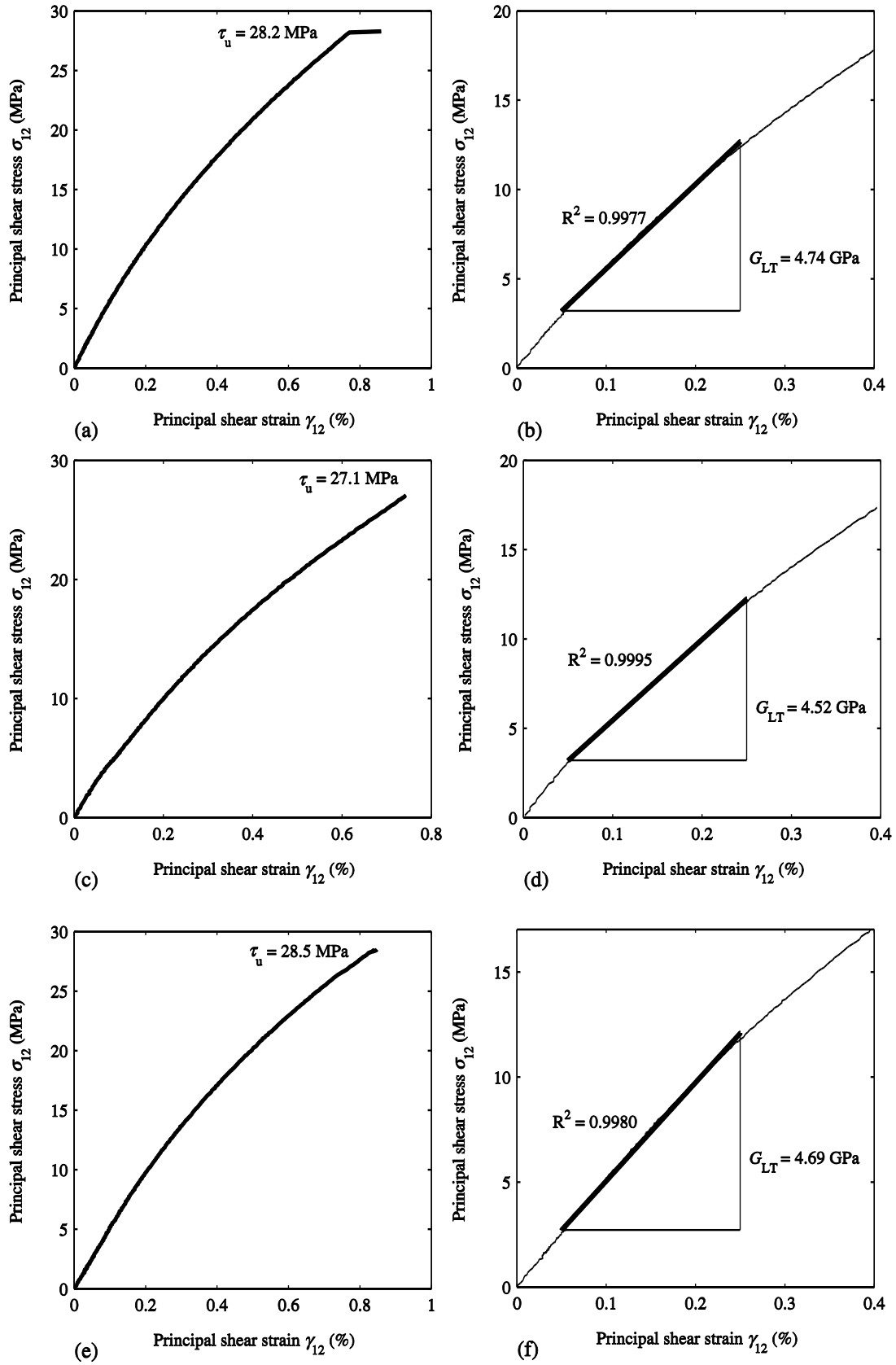
Figure A.16 σ_{12} vs. γ_{12} for: (a), (b) S-C1-1; (c), (d) S-C1-2; (e), (f) S-C1-3
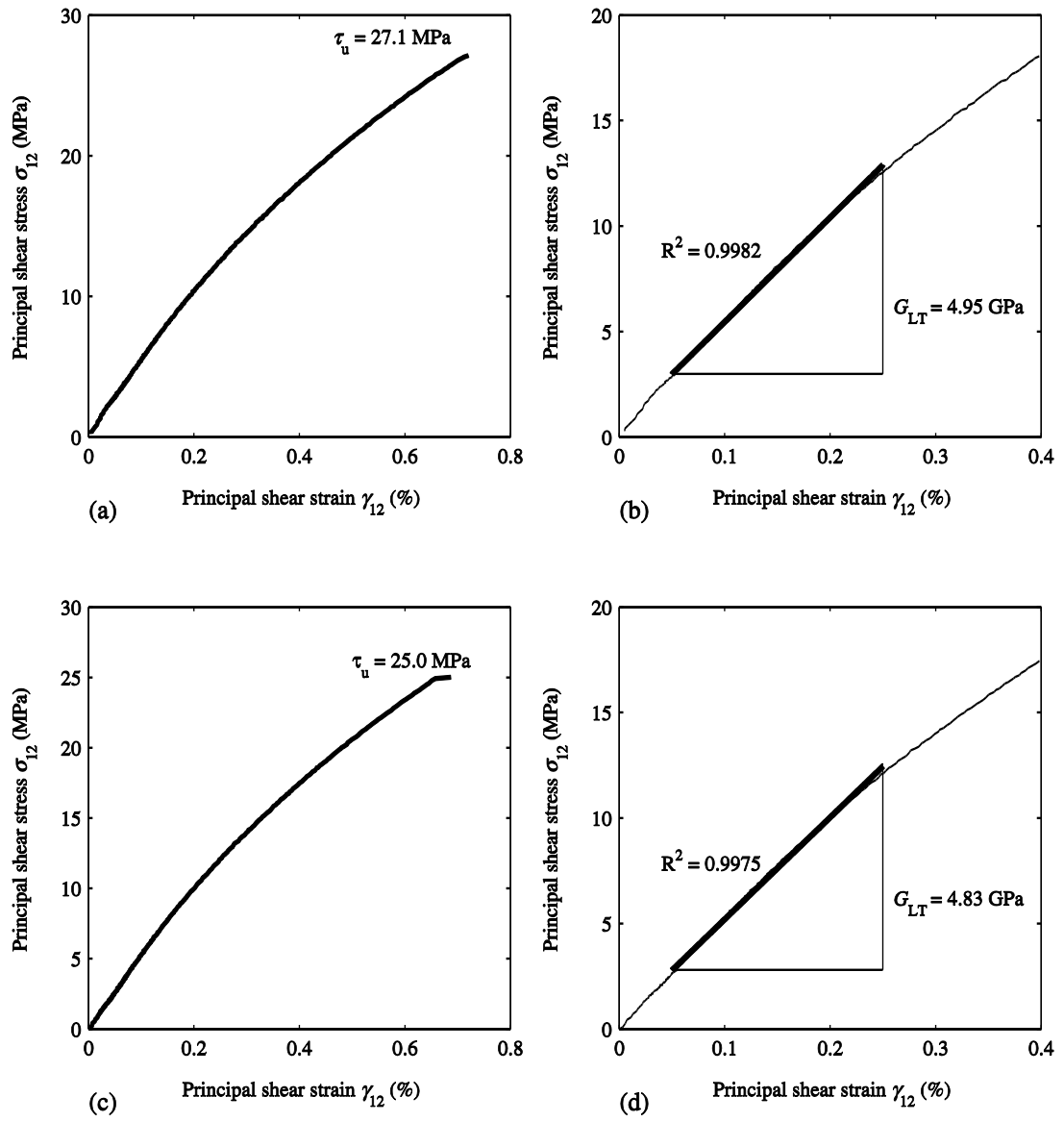
Figure A.17 σ_{12} vs. γ_{12} for (a), (b) S-C1-4; (c), (d) S-C1-5
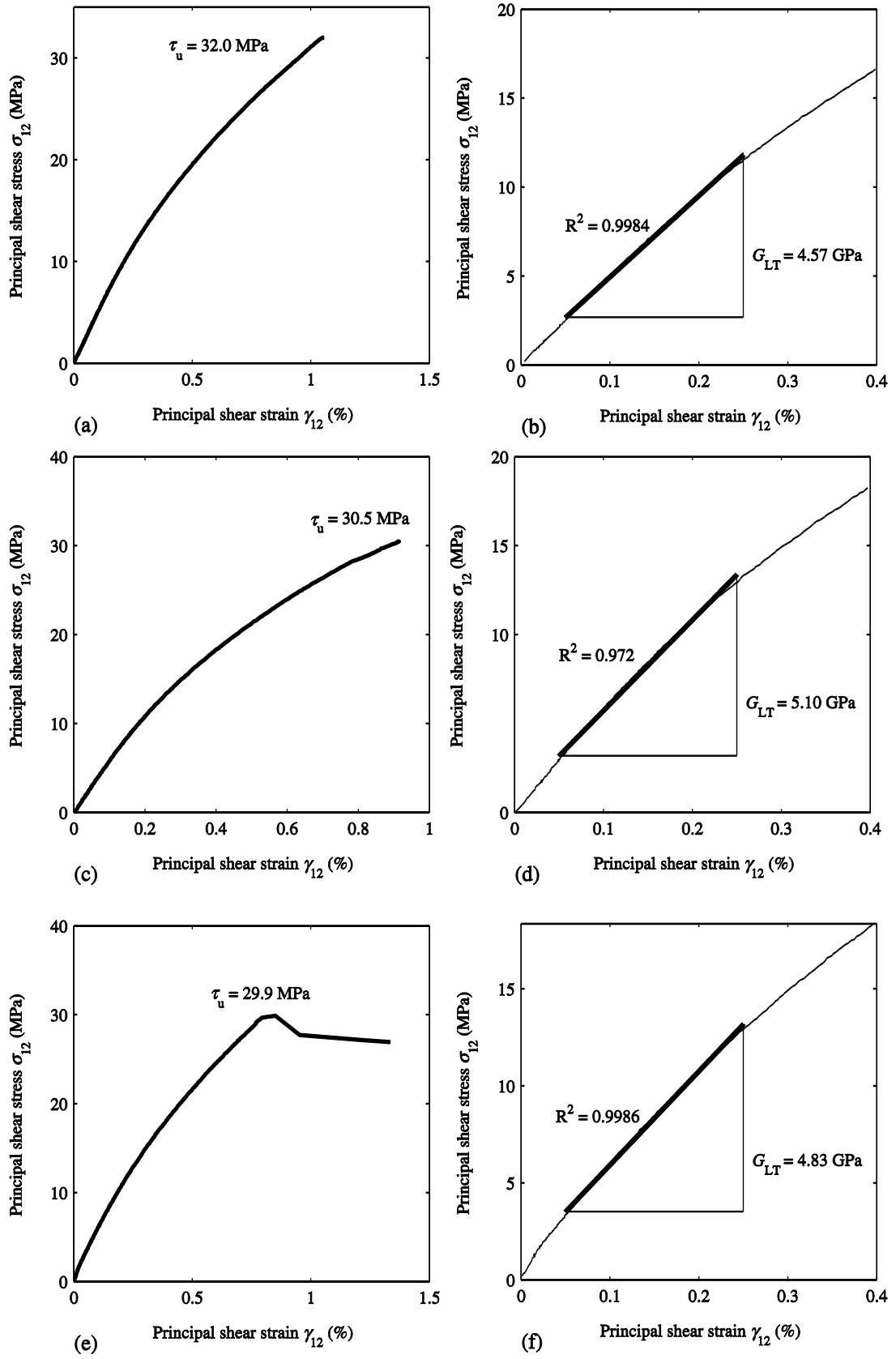
Figure A.18 σ_{12} vs. γ_{12} for: (a), (b) S-C2-1; (c), (d) S-C2-2; (e), (f) S-C2-3
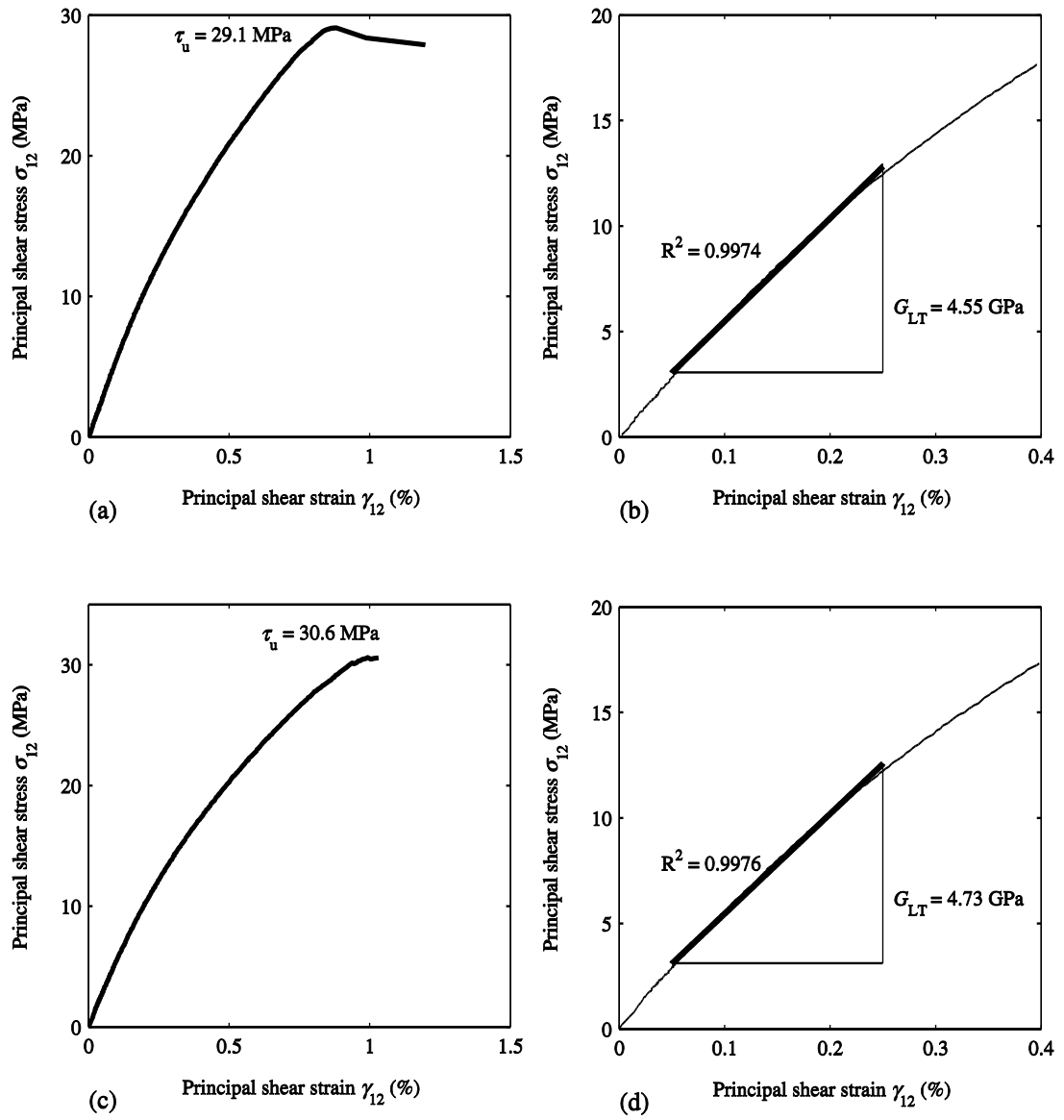
Figure A.19 σ_{12} vs. γ_{12} for (a), (b) S-C2-4; (c), (d) S-C2-5
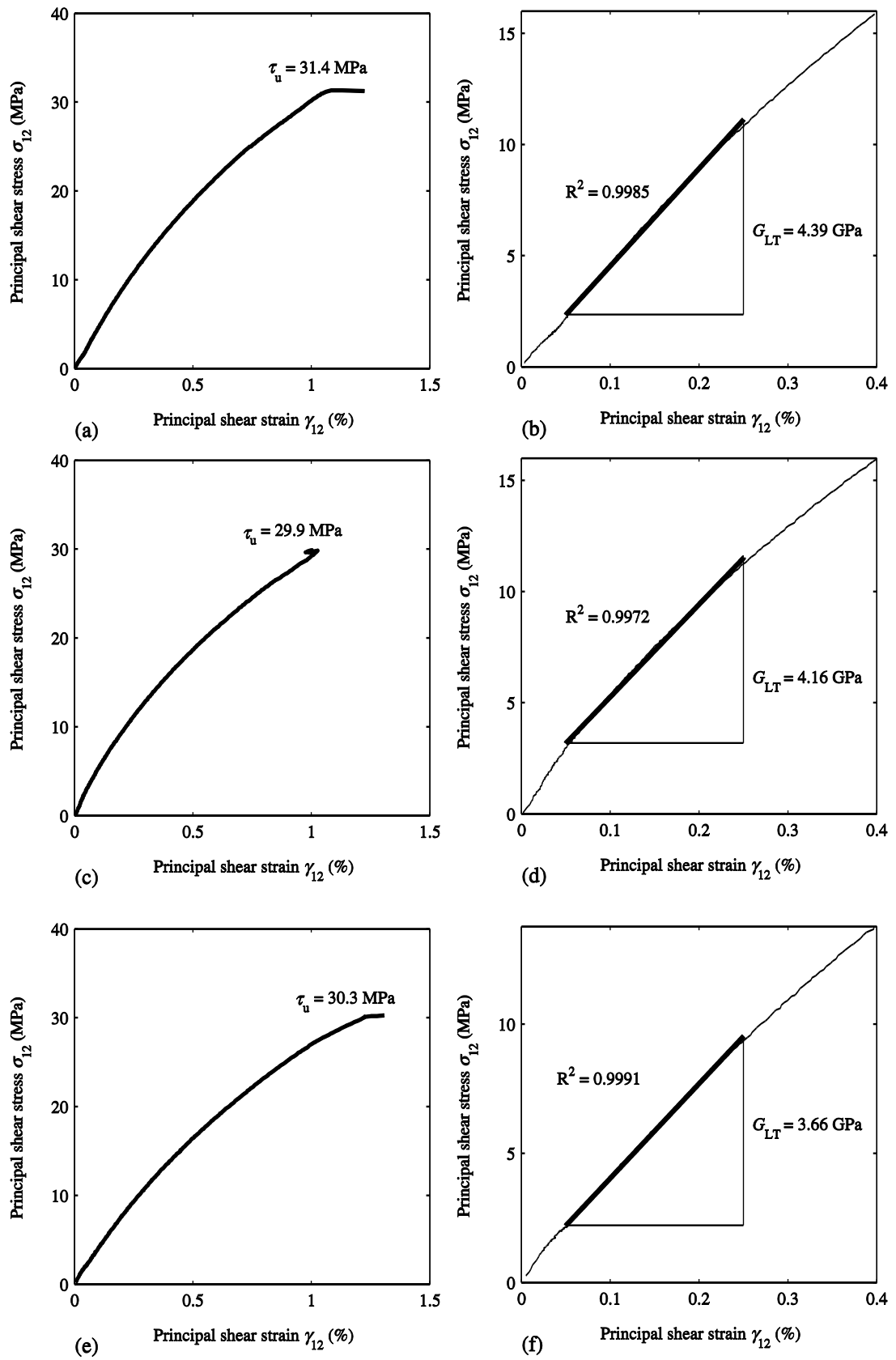
Figure A.20 σ_{12} vs. γ_{12} for: (a), (b) S-C3-1; (c), (d) S-C3-2; (e), (f) S-C3-3
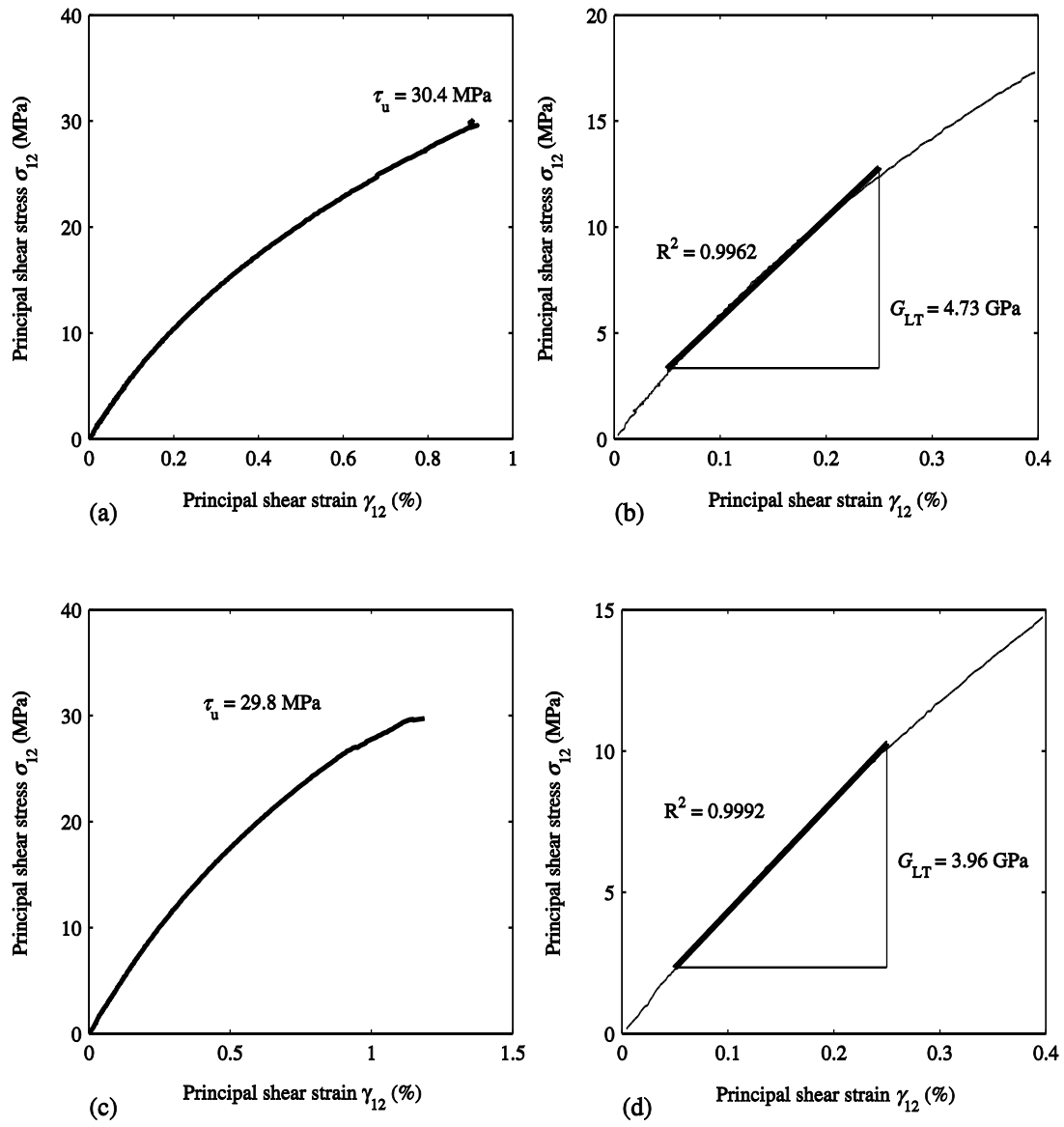
Figure A.21 σ_{12} vs. γ_{12} for: (a), (b) S-C3-4; (c), (d) S-C3-5

APPENDIX B

PLOTS FOR LATERAL BUCKLING TESTS

This appendix B includes two categories for: (B1) plots for the measurement of initial out-of-straightness imperfection and (B2) plots for the LTB tests. Appendix B1 presents 16 plots in Figures B.1 to B.4 at four per page. Each page is the the measurement of initial minor axis out-of-straightness imperfection vs. beam length for each section of I, C1, C2, C3 at span of 1828mm, 2438mm, 2844mm and 3454 mm. Each plot presents two curves for the measurement on two sides of a beam. The maximum of imperfection $\delta_{\max}$ of each side are given with the plot.

Plots for the LTB tests are presented in Figures B.5 to B.17 in Appendix B2. Each figure generally has 6 plots for part (a) to (f). Each plot in Figures B.5 to B.11 presents three curves for Load P vs. mid-span rotation ϕ for tests on a same span with different vertical load positions. The solid curve is for loading on Top Flange (TF). The dashed curve and dot-dashed curve is for Shear Centre (SC) and Bottom Flange (BF) loading, respectively. For LTB test where beam was failed by "bifurcation-like" failure, the buckling load was marked as the 'peak' load in testing and this value is given above the curve. There will be no Southwell plot for these tests. Each plot in Figures B.12 to B.17 presents the Southwell plot of ϕ / P vs. ϕ to determine the critical buckling load P_{cr}. The polyfit line for each test was presented with the same type of line that represents TF,

SC and BF loading in Figures B.5 to B.11. On these lines, the data point was also shown with circular symbol for TF, rectangular shape for SC and triangle marker for BF loading. The fitting equation for $y = ax + b$ and the critical buckling load that is determined by $P_{cr} = 1/a$ was also given on the figure.

B. 1   Measurements of out-of-straightness initial imperfection
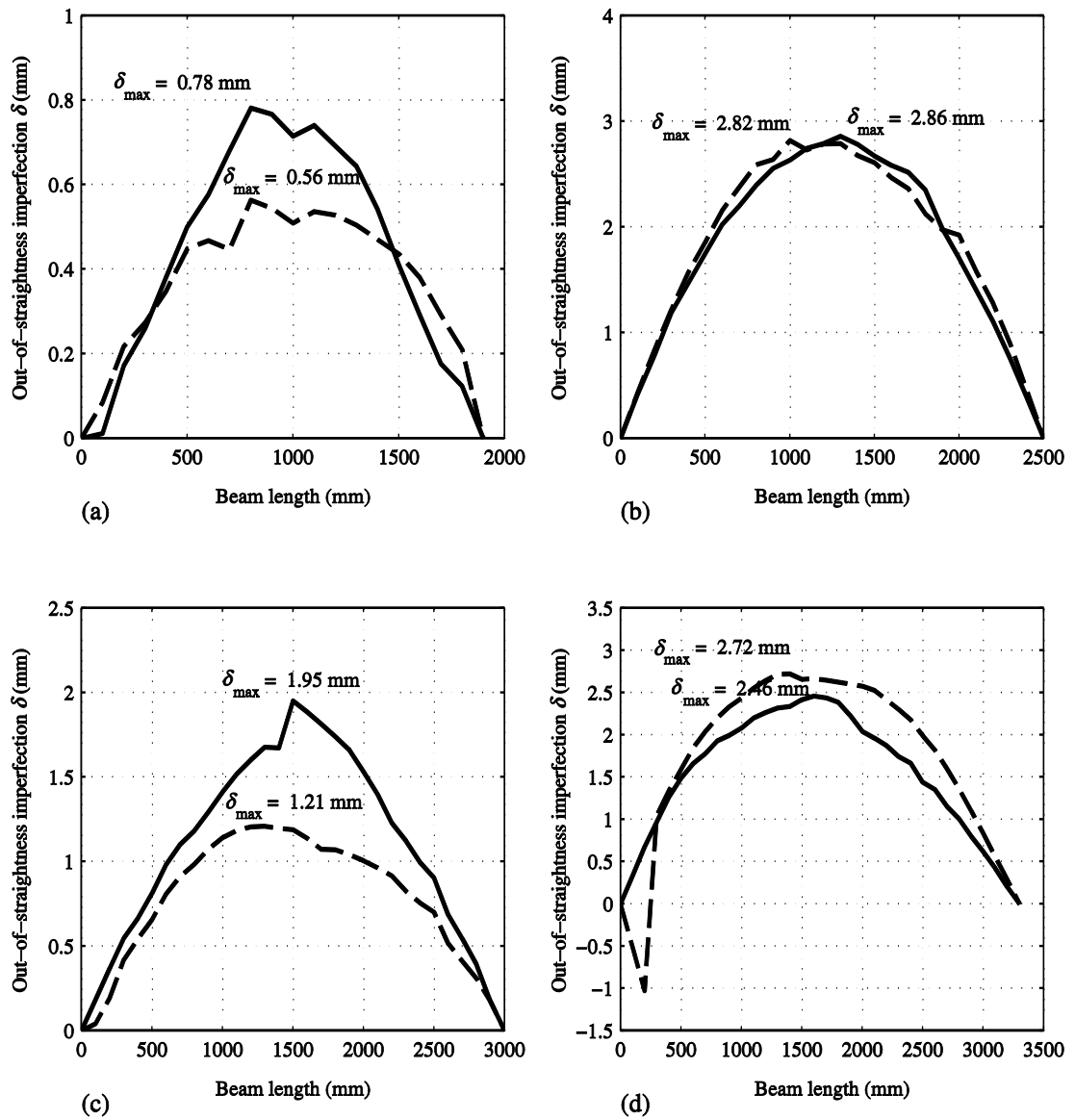
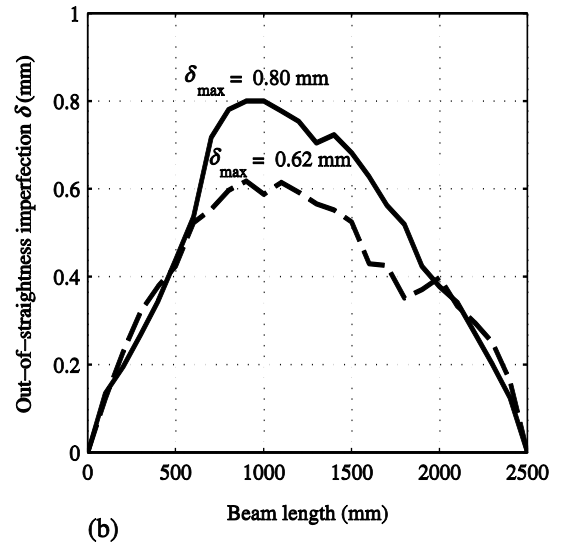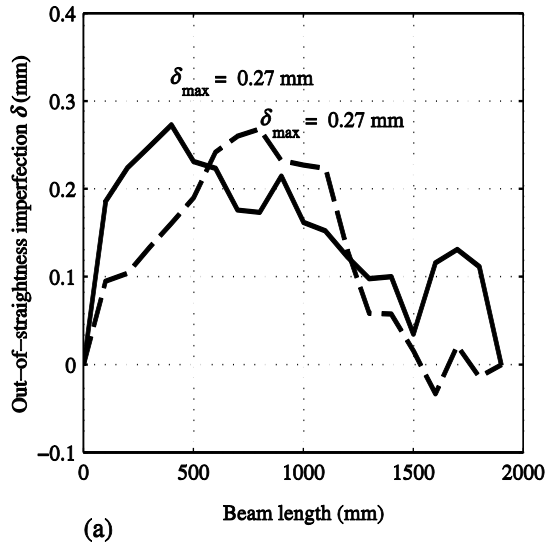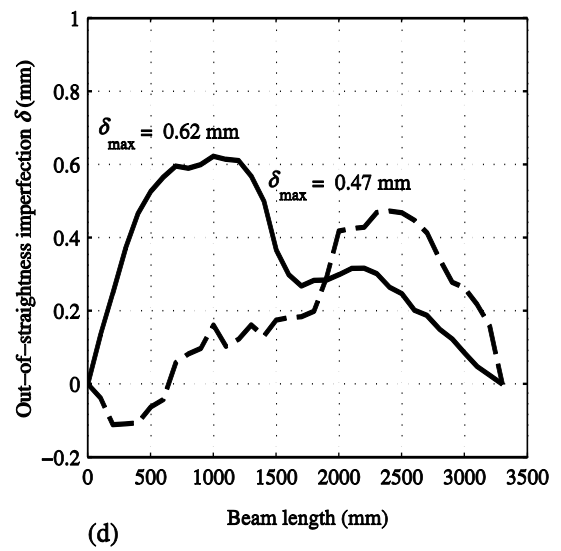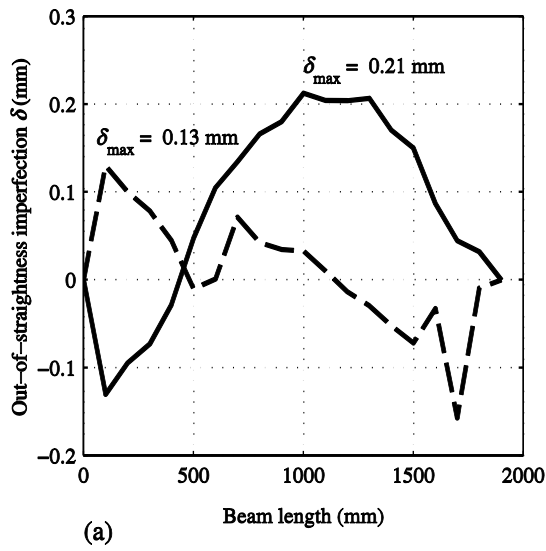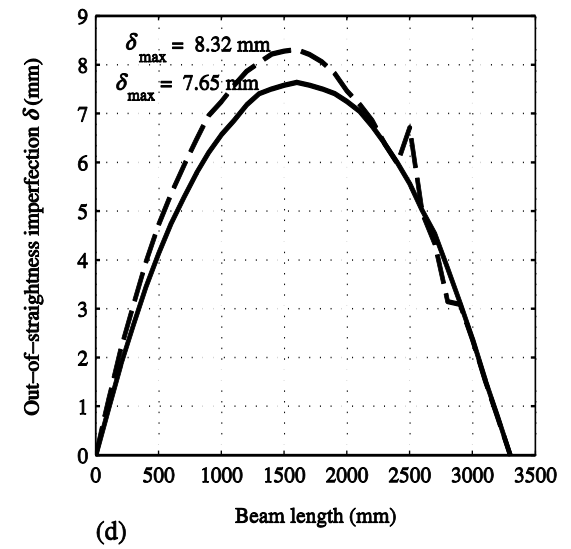Figure B.1 Out-of-straightness along the length of beams: (a) I-1828; (a) I-2438; (a) I-2844; (a) I-3454
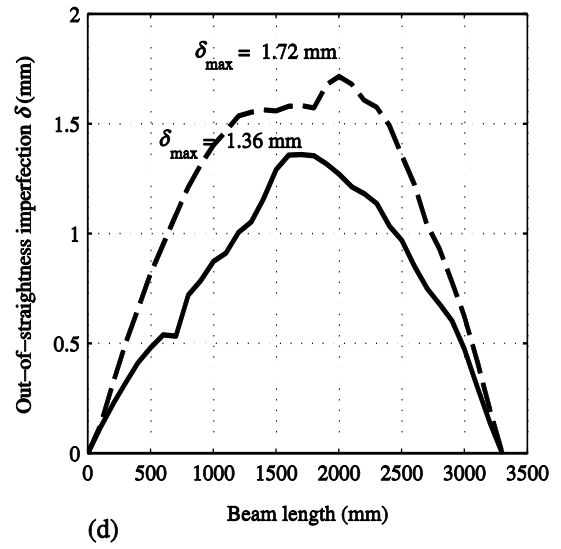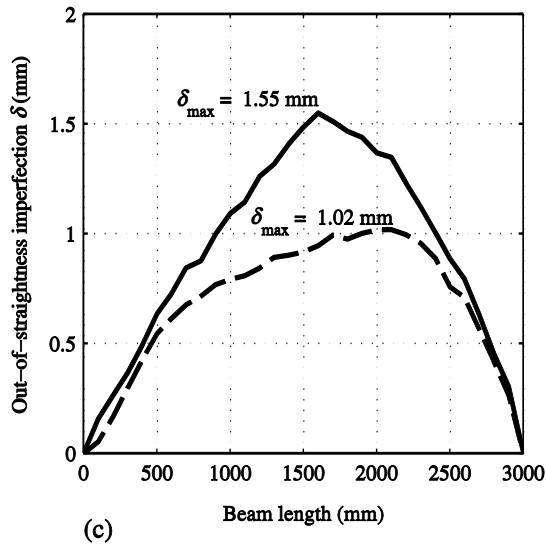
Figure B.2 Out-of-straightness along the length of beams: (a) C1-1828; (a) C1-2438; (a) C1-2844; (a) C1-3454
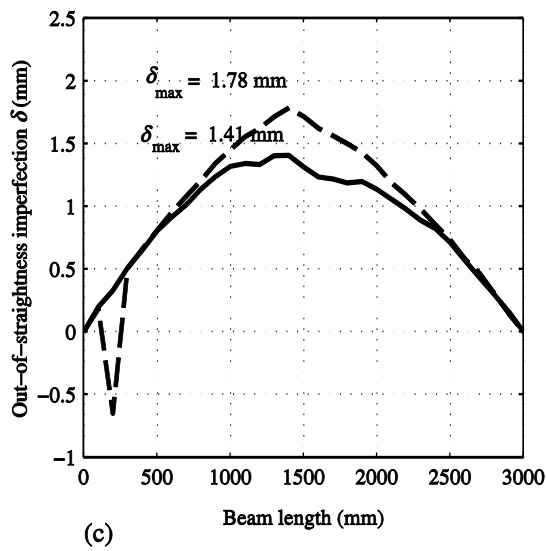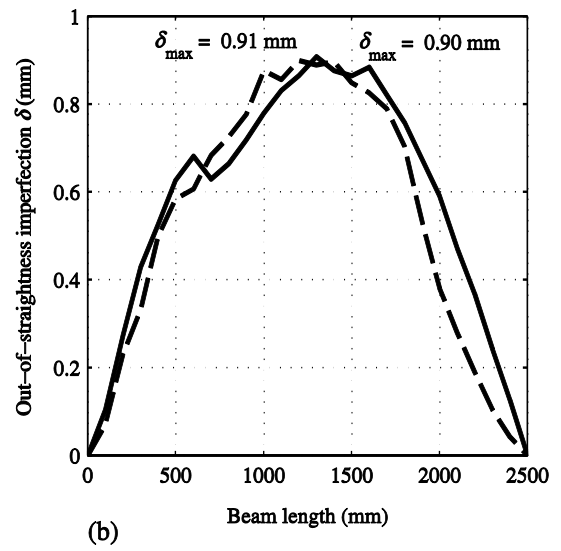
Figure B.3 Out-of-straightness along the length of beams: (a) C2-1828; (a) C2-2438; (a) C2-2844; (a) C2-3454
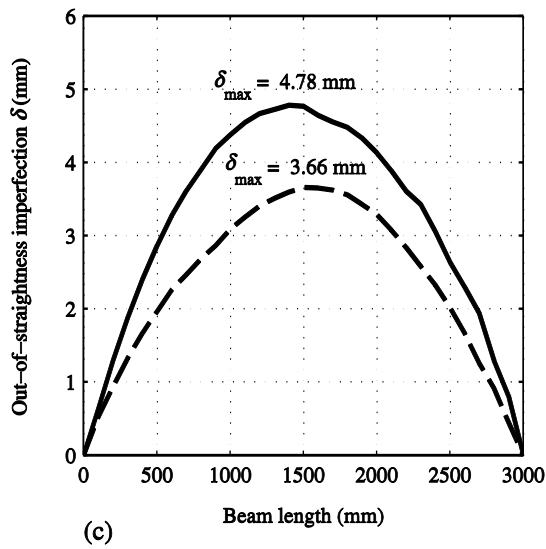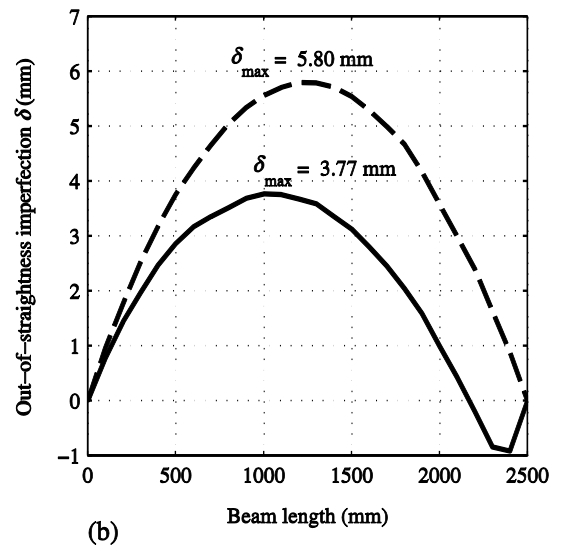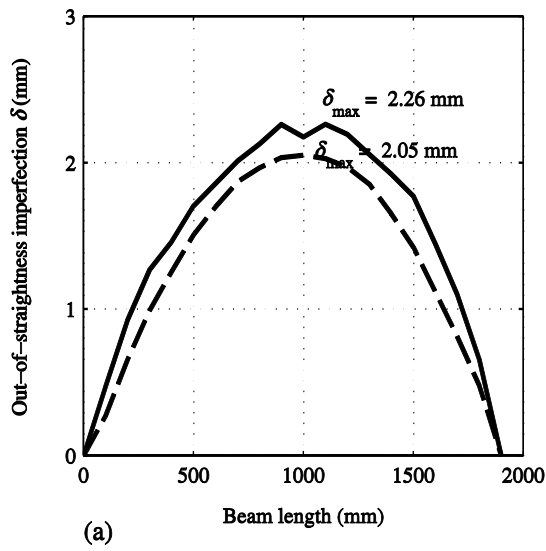
Figure B.4 Out-of-straightness along the length of beams: (a) C3-1828; (a) C3-2438; (a) C3-2844; (a) C3-3454

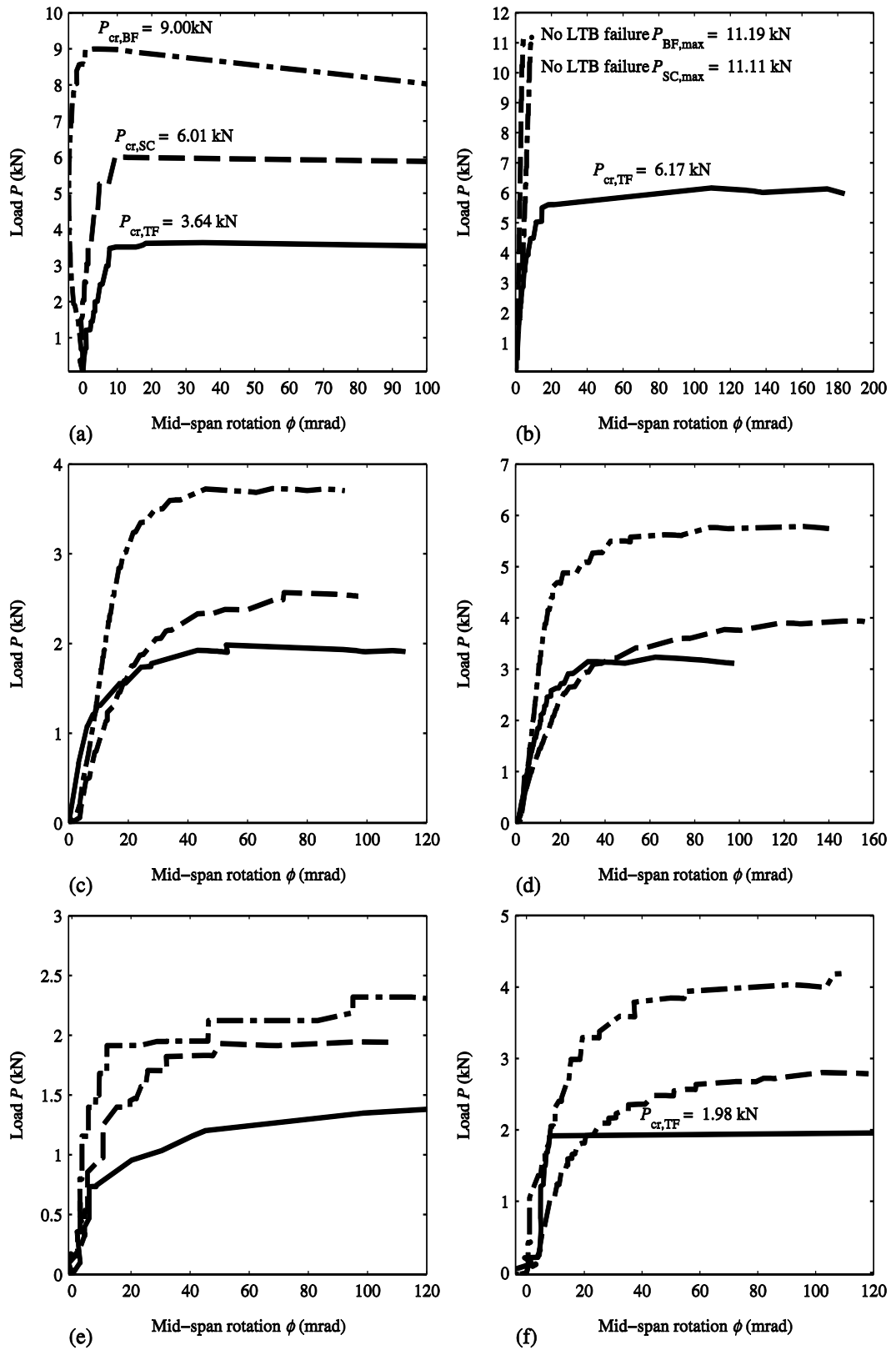## B. 2   Lateral-torsional buckling tests

Figure B.5 P vs. ϕ for (a) I-1828-EC1; (b) I-1828-EC2; (c) I-2438-EC1; (d) I-2438-EC2; (e) I-2844-EC1; (f) I-2844-EC2
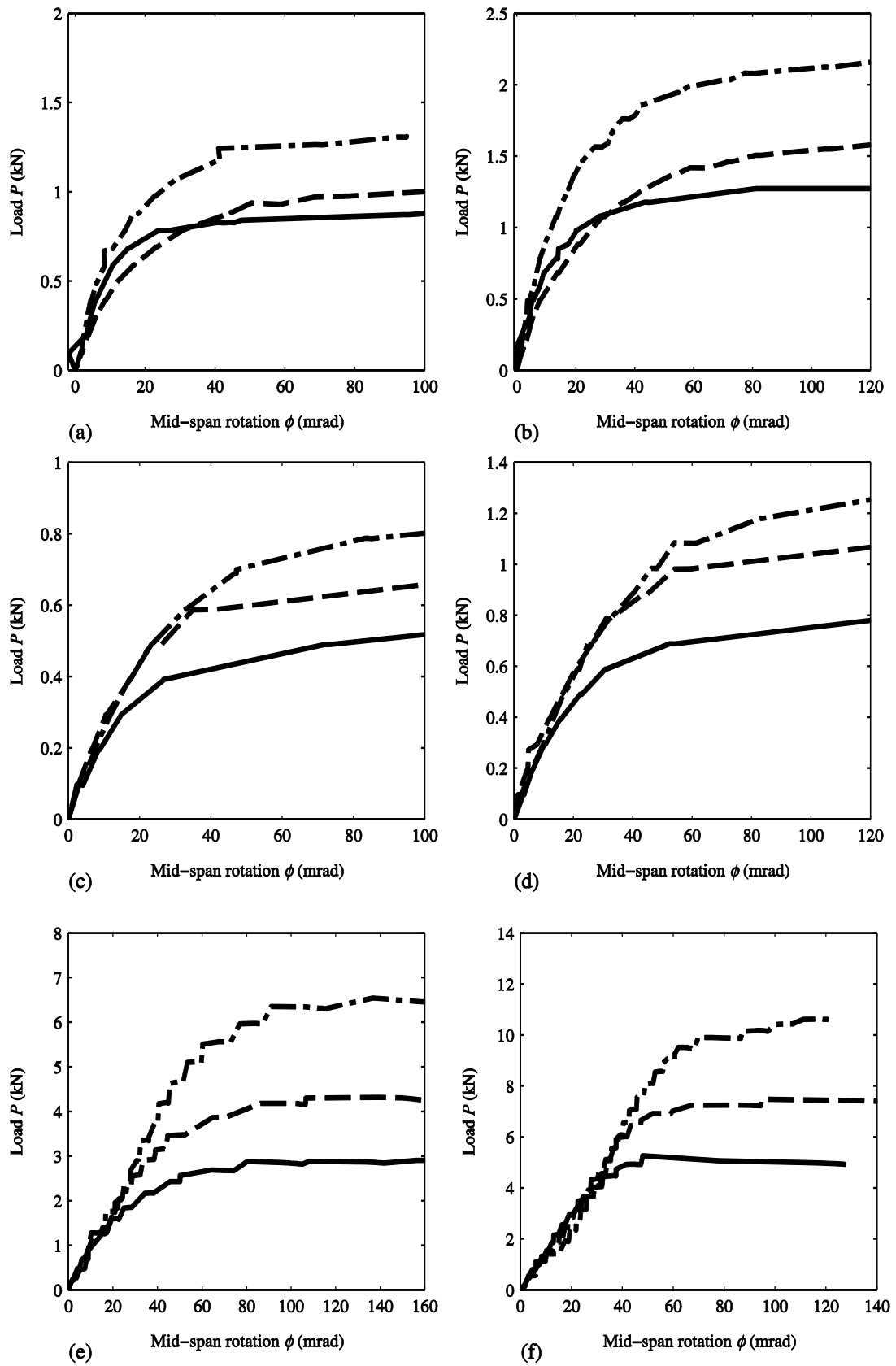
Figure B.6 *P* vs. ϕ for (a) I-3454-EC1; (b) I-3454-EC2; (c) I-4064-EC1; (d) I-4064-EC2; (e) C1-1828-EC1; (f)C1-1828-EC2
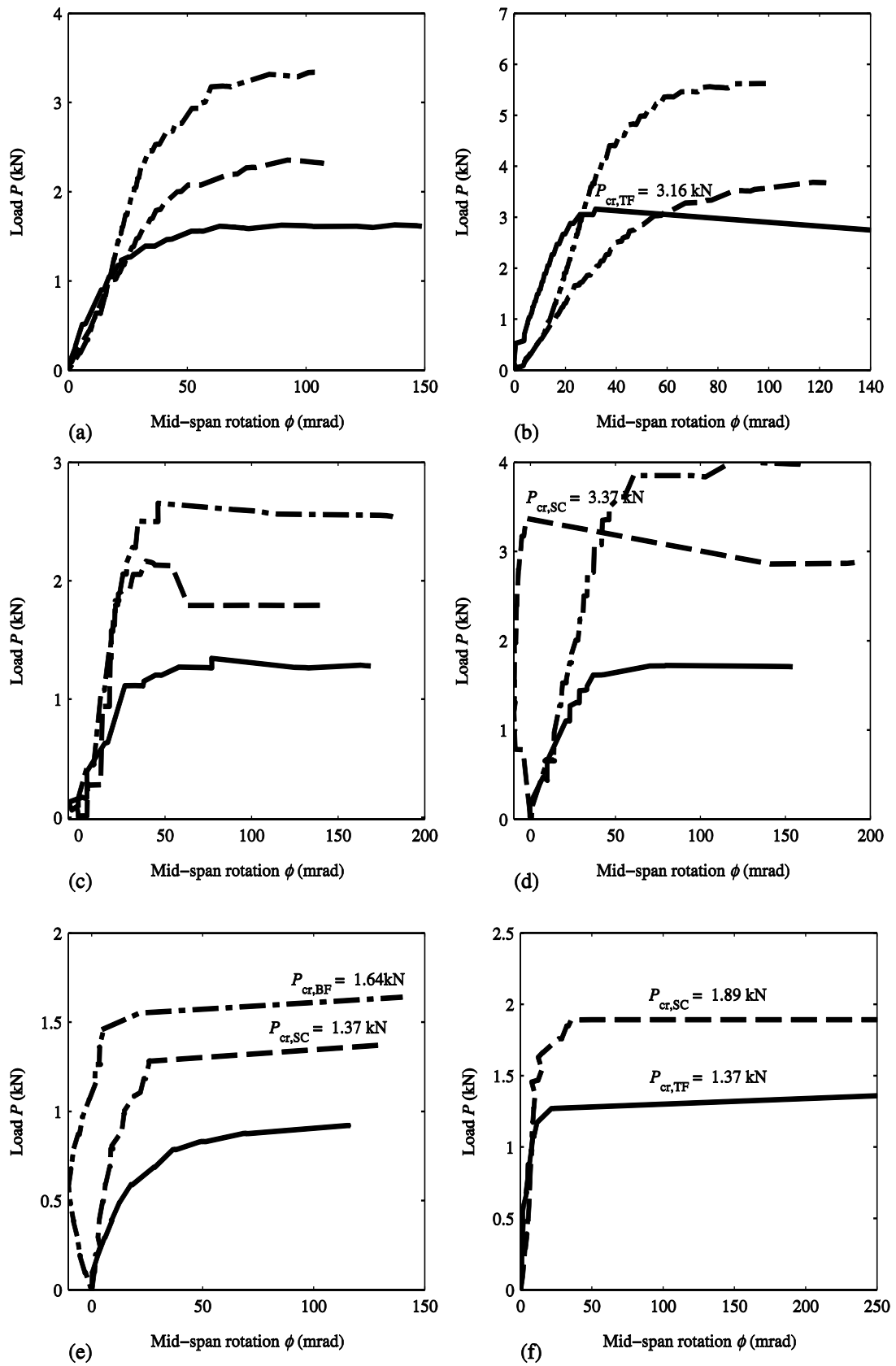
Figure B.7 P vs. ϕ for (a) C1-2438-EC1; (b) C1-2438-EC2; (c) C1-2844-EC1; (d) C1-2844-EC2; (e) C1-3454-EC1; (f) C1-3454-EC2
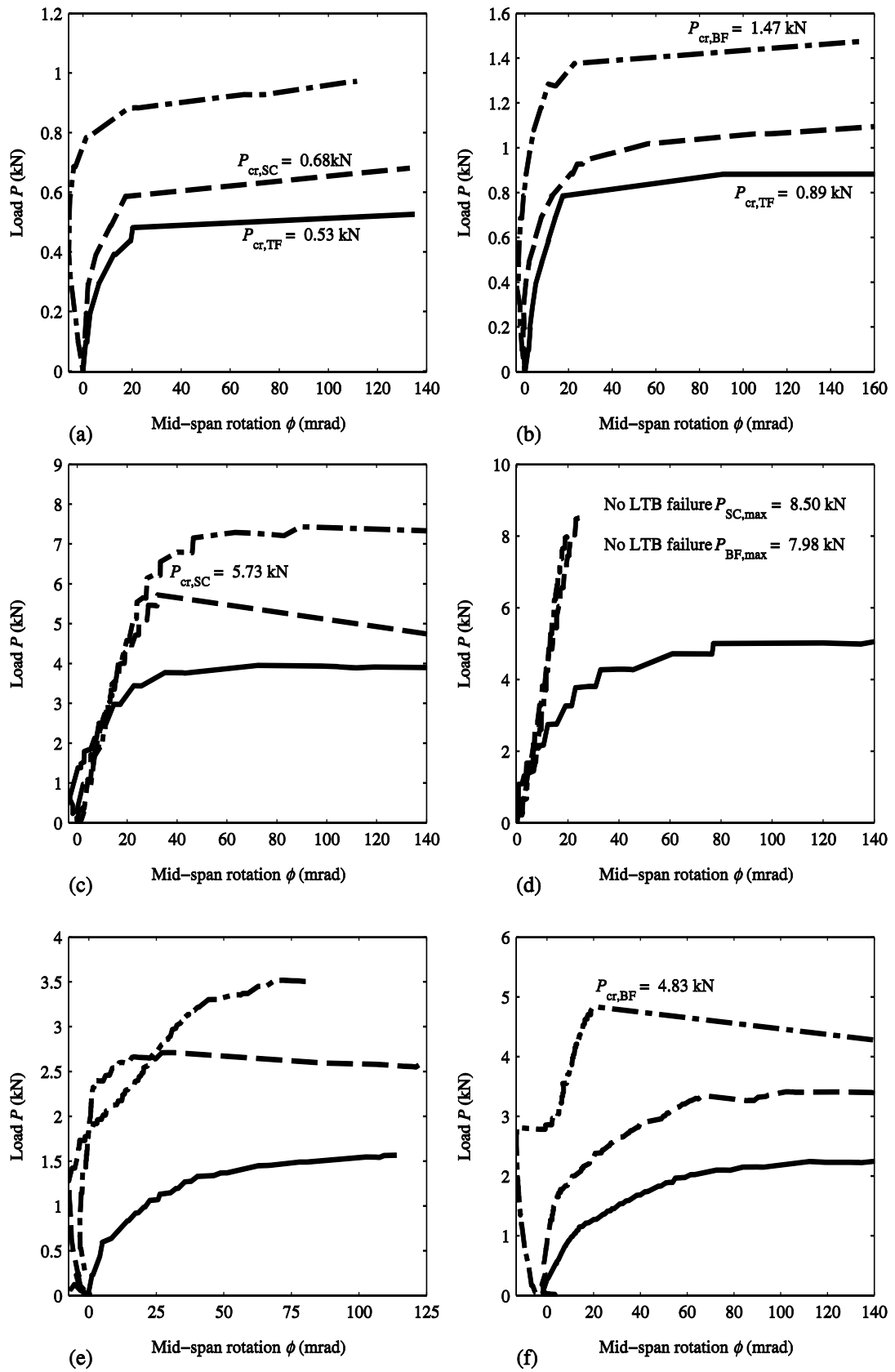
265

Figure B.8 P vs. ϕ for (a) C1-4064-EC1; (b) C1-4064-EC2; (c) C2-1828-EC1; (d) C2-1828-EC2; (e) C2-2438-EC1; (f) C2-2438-EC2
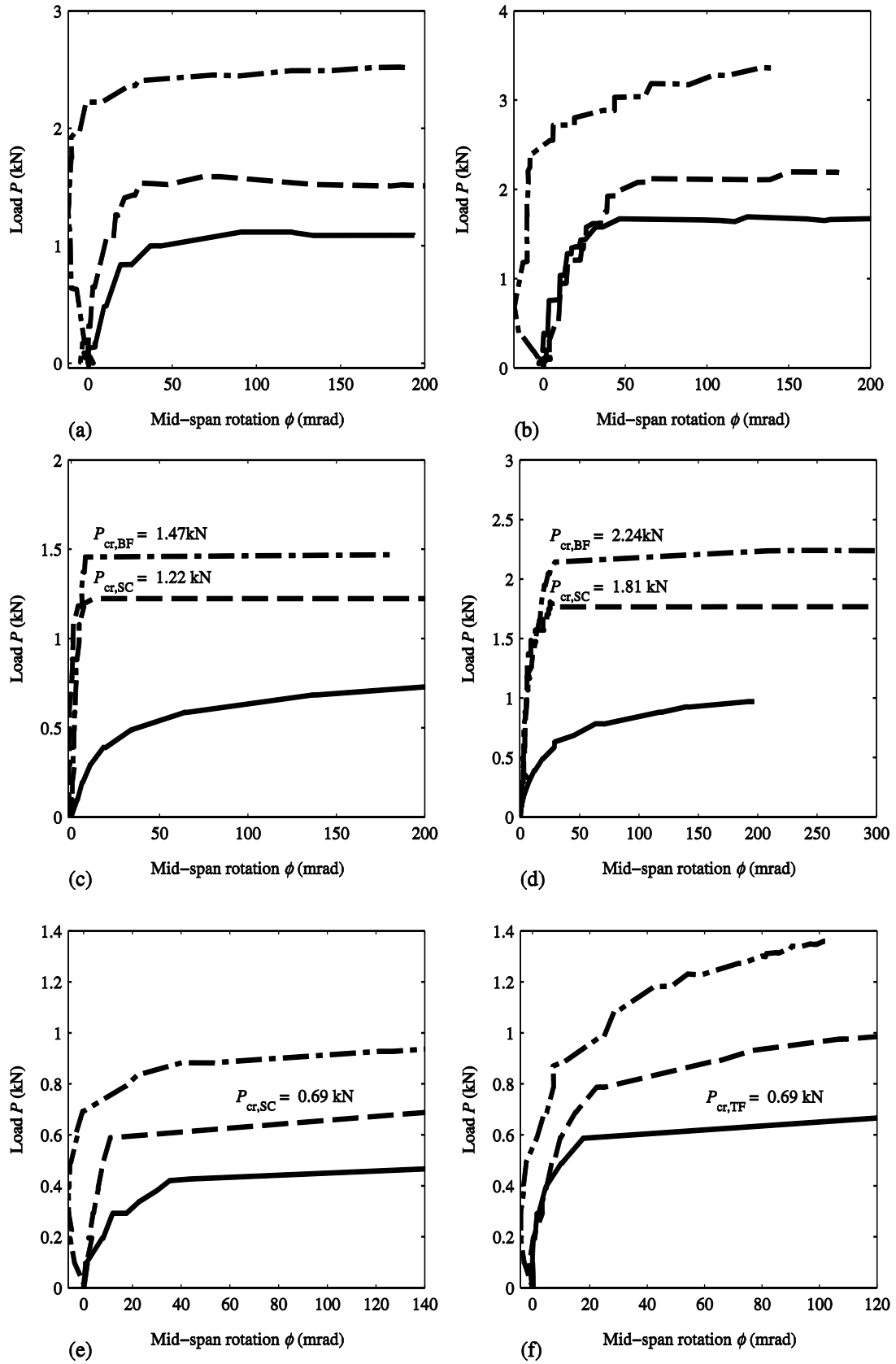
266

Figure B.9 *P* vs. ϕ for (a) C2-2844-EC1; (b) C2-2844-EC2; (c) C2-3454-EC1; (d) C2-3454-EC2; (e) C2-4064-EC1; (f) C2-4064-EC2
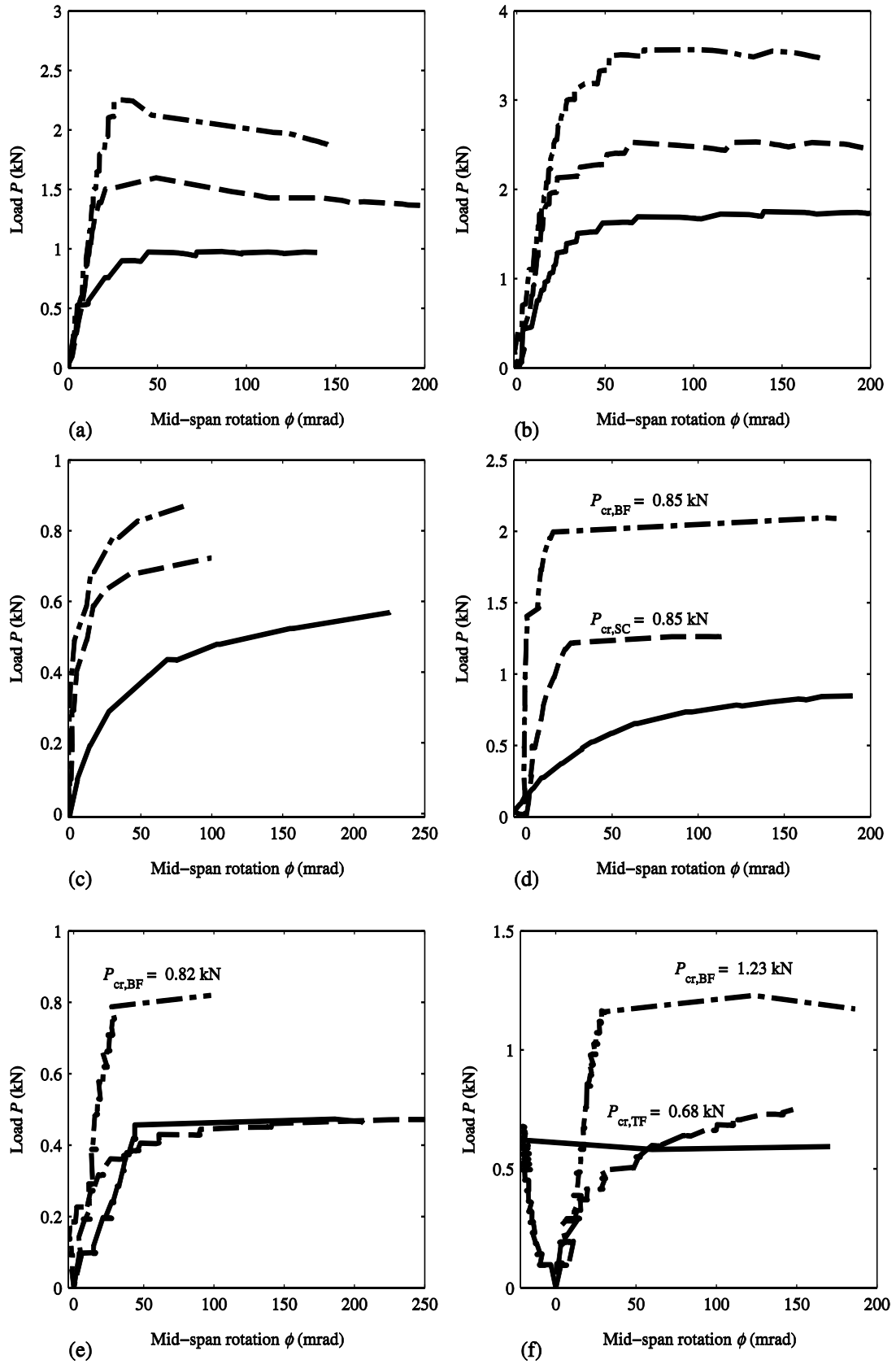
Figure B.10 P vs. ϕ (a) C3-1828-EC1; (b) C3-1828-EC2; (c) C3-2438-EC1; (d) C3-2438-EC2; (e) C3-2844-EC1; (f) C3-2844-EC2
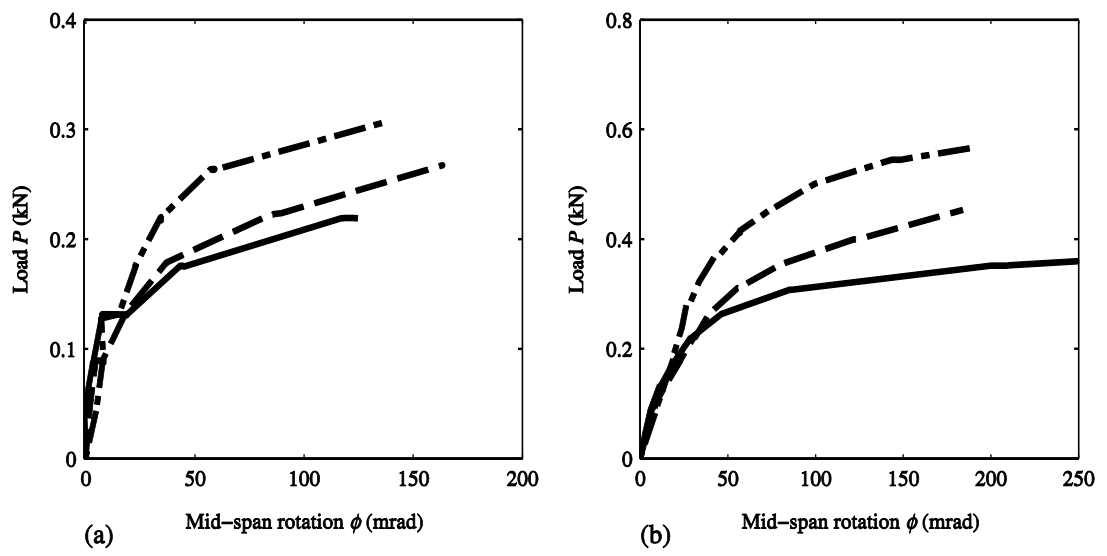
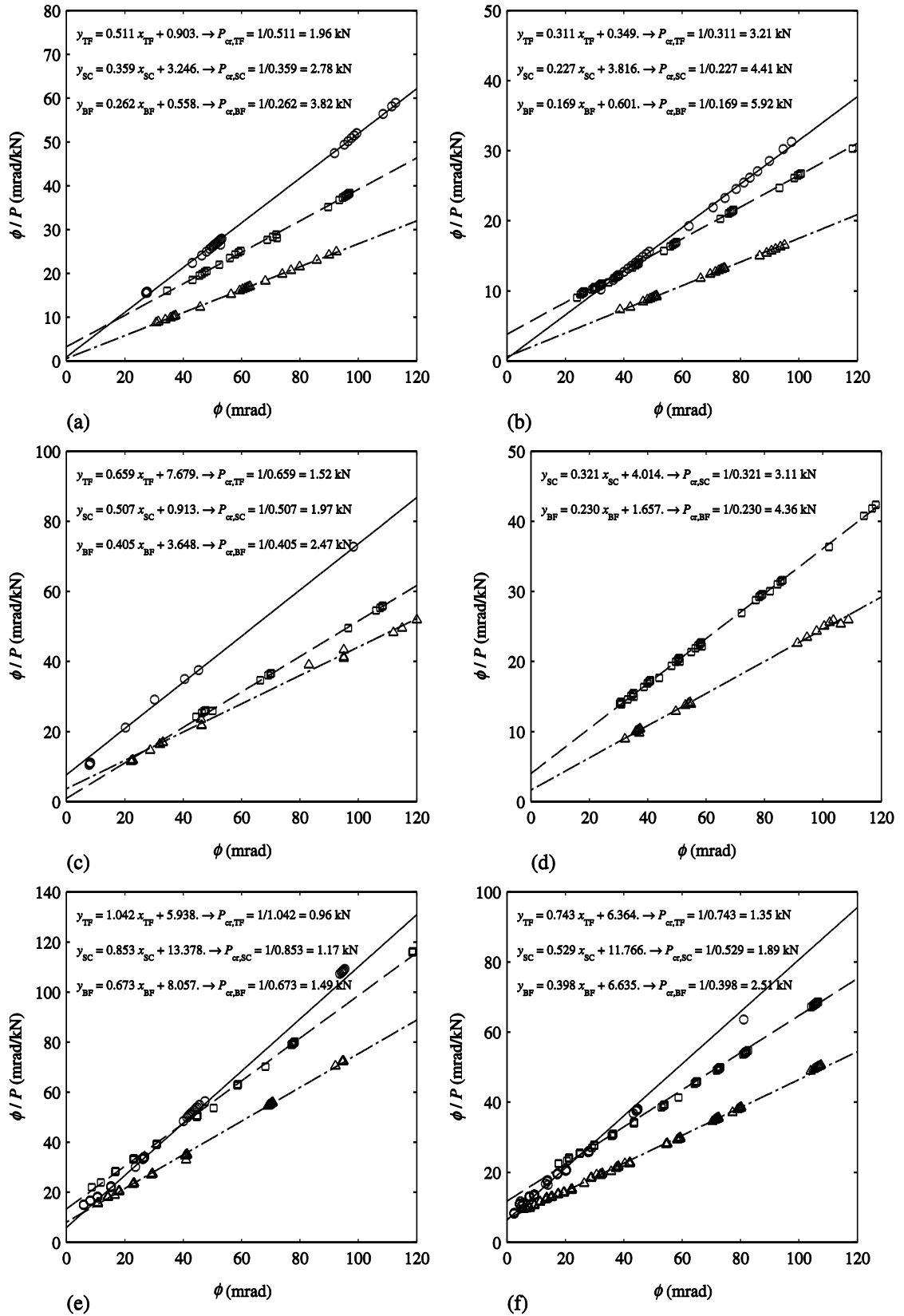Figure B.11 *P* vs. ϕ for (a) C3-3454-EC1; (b) C3-3454-EC2

Figure B.12 Southwell plot with test results from (a) I-2438-EC1; (b) I-2438-EC2; (c) I-2844-EC1; (d) I-2844-EC2; (e) I-3454-EC1; (f) I-3454-EC2.
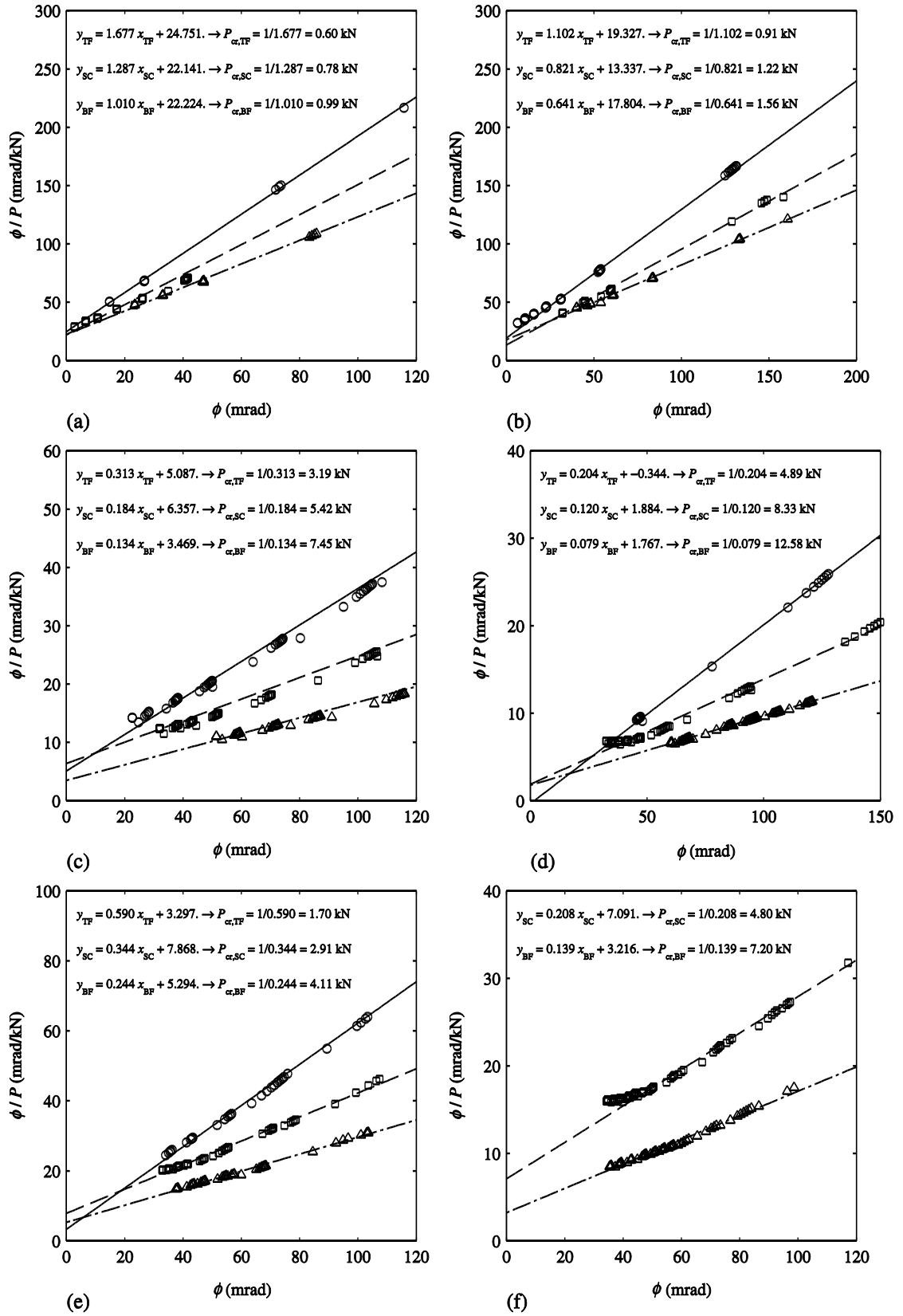
(a)

$y_{TF} = 1.677\,x_{TF} + 24.751. \rightarrow P_{cr,TF} = 1/1.677 = 0.60$ kN

$y_{SC} = 1.287\,x_{SC} + 22.141. \rightarrow P_{cr,SC} = 1/1.287 = 0.78$ kN

$y_{BF} = 1.010\,x_{BF} + 22.224. \rightarrow P_{cr,BF} = 1/1.010 = 0.99$ kN

(b)

$y_{TF} = 1.102\,x_{TF} + 19.327. \rightarrow P_{cr,TF} = 1/1.102 = 0.91$ kN

$y_{SC} = 0.821\,x_{SC} + 13.337. \rightarrow P_{cr,SC} = 1/0.821 = 1.22$ kN

$y_{BF} = 0.641\,x_{BF} + 17.804. \rightarrow P_{cr,BF} = 1/0.641 = 1.56$ kN

(c)

$y_{TF} = 0.313\,x_{TF} + 5.087. \rightarrow P_{cr,TF} = 1/0.313 = 3.19$ kN

$y_{SC} = 0.184\,x_{SC} + 6.357. \rightarrow P_{cr,SC} = 1/0.184 = 5.42$ kN

$y_{BF} = 0.134\,x_{BF} + 3.469. \rightarrow P_{cr,BF} = 1/0.134 = 7.45$ kN

(d)

$y_{TF} = 0.204\,x_{TF} + -0.344. \rightarrow P_{cr,TF} = 1/0.204 = 4.89$ kN

$y_{SC} = 0.120\,x_{SC} + 1.884. \rightarrow P_{cr,SC} = 1/0.120 = 8.33$ kN

$y_{BF} = 0.079\,x_{BF} + 1.767. \rightarrow P_{cr,BF} = 1/0.079 = 12.58$ kN

(e)

$y_{TF} = 0.590\,x_{TF} + 3.297. \rightarrow P_{cr,TF} = 1/0.590 = 1.70$ kN

$y_{SC} = 0.344\,x_{SC} + 7.868. \rightarrow P_{cr,SC} = 1/0.344 = 2.91$ kN

$y_{BF} = 0.244\,x_{BF} + 5.294. \rightarrow P_{cr,BF} = 1/0.244 = 4.11$ kN

(f)

$y_{SC} = 0.208\,x_{SC} + 7.091. \rightarrow P_{cr,SC} = 1/0.208 = 4.80$ kN

$y_{BF} = 0.139\,x_{BF} + 3.216. \rightarrow P_{cr,BF} = 1/0.139 = 7.20$ kN

Figure B.13 Southwell plot with test results from (a) I-4064-EC1; (b) I-4064-EC2; (c) C1-1828-EC1; (d) C1-1828-EC2; (e) C1-2438-EC1; (f) C1-2438-EC2
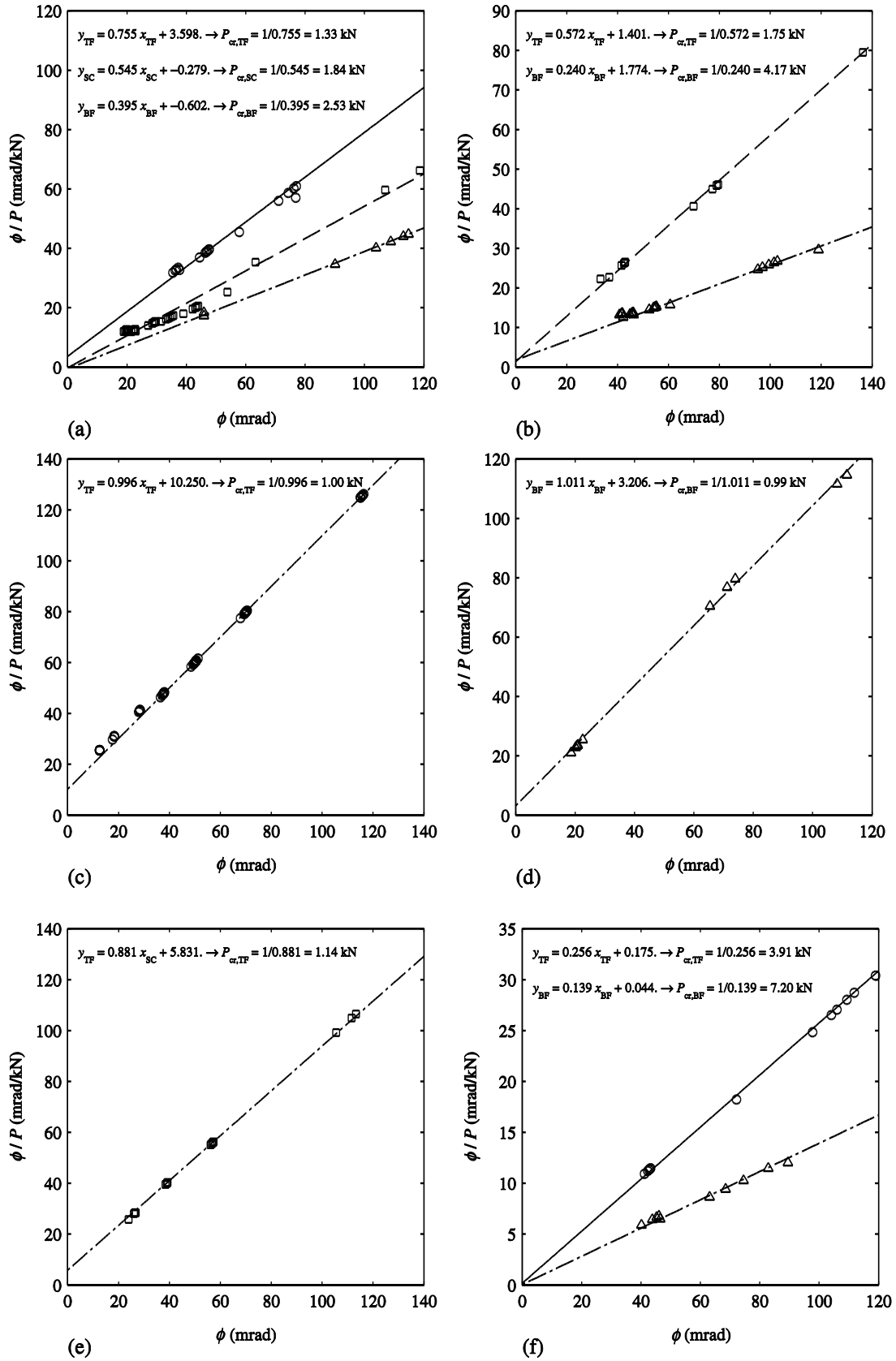
271

Figure B.14 Southwell plot with test results from (a) C1-2844-EC1; (b) C1-2844-EC2; (c) C1-3454-EC1; (d) C1-4064-EC1; (e) C1-4064-EC2; (f) C2-1828-EC1
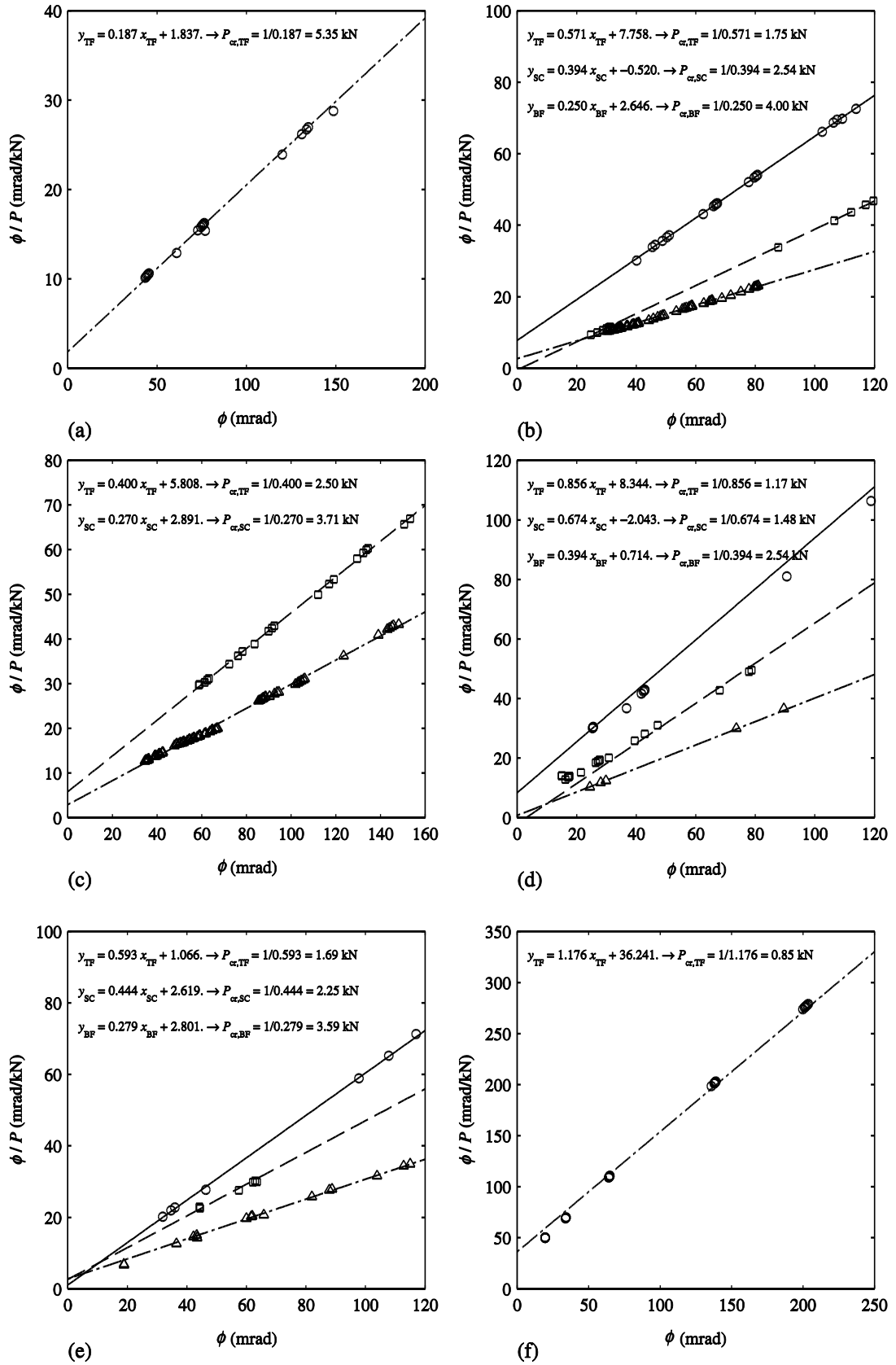
Figure B.15 Southwell plot with test results from (a) C2-1828-EC2; (b) C2-2438-EC1; (c) C2-2438-EC2; (d) C2-2844-EC1; (e) C2-2844-EC2; (f) C2-3454-EC1
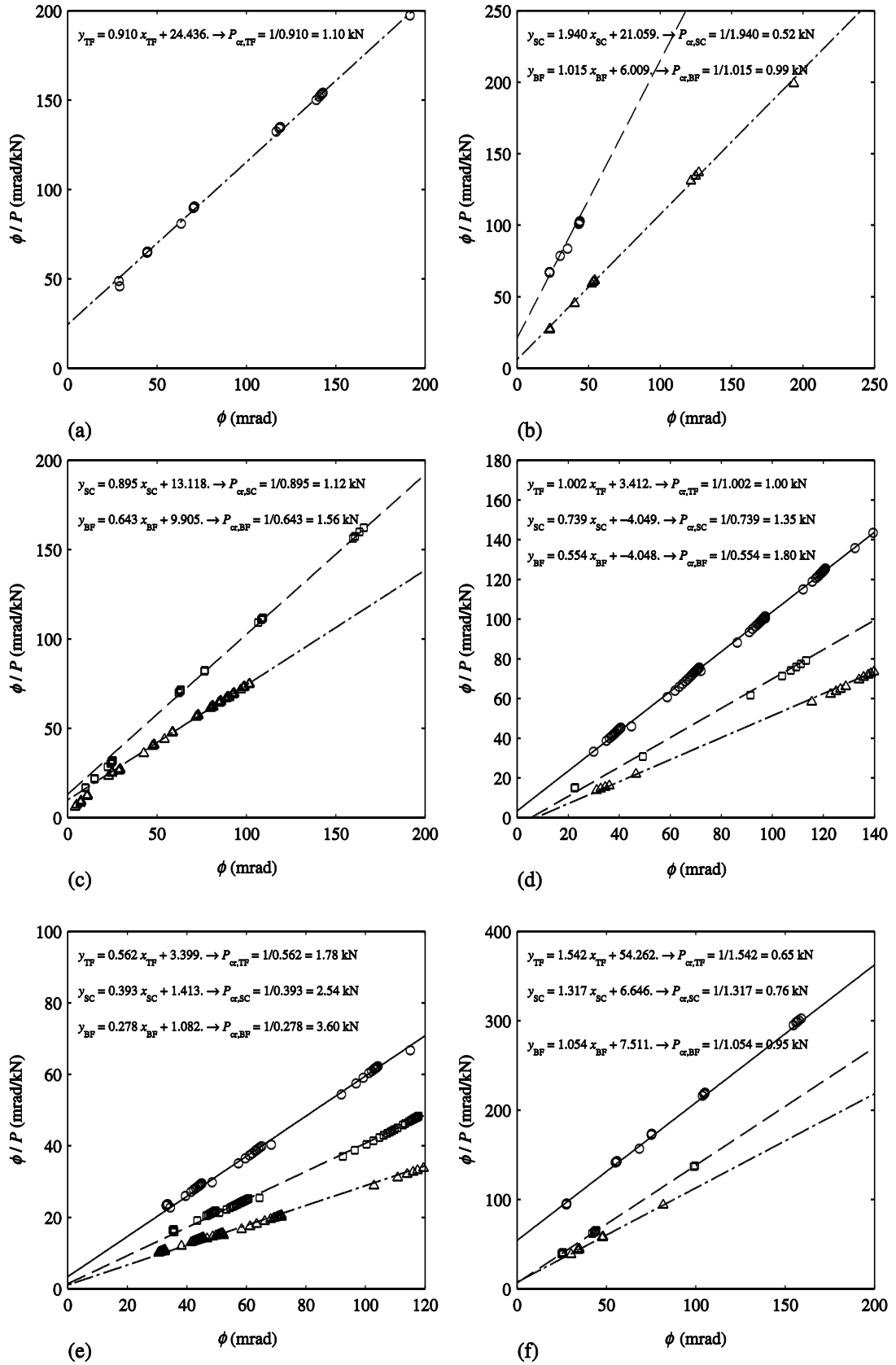
273

Figure B.16 Southwell plot with test results from (a) C2-3454-EC2; (b) C2-4064-EC1; (c) C2-4064-EC2; (d) C3-1828-EC1; (e) C3-1828-EC2; (f) C3-2438-EC1
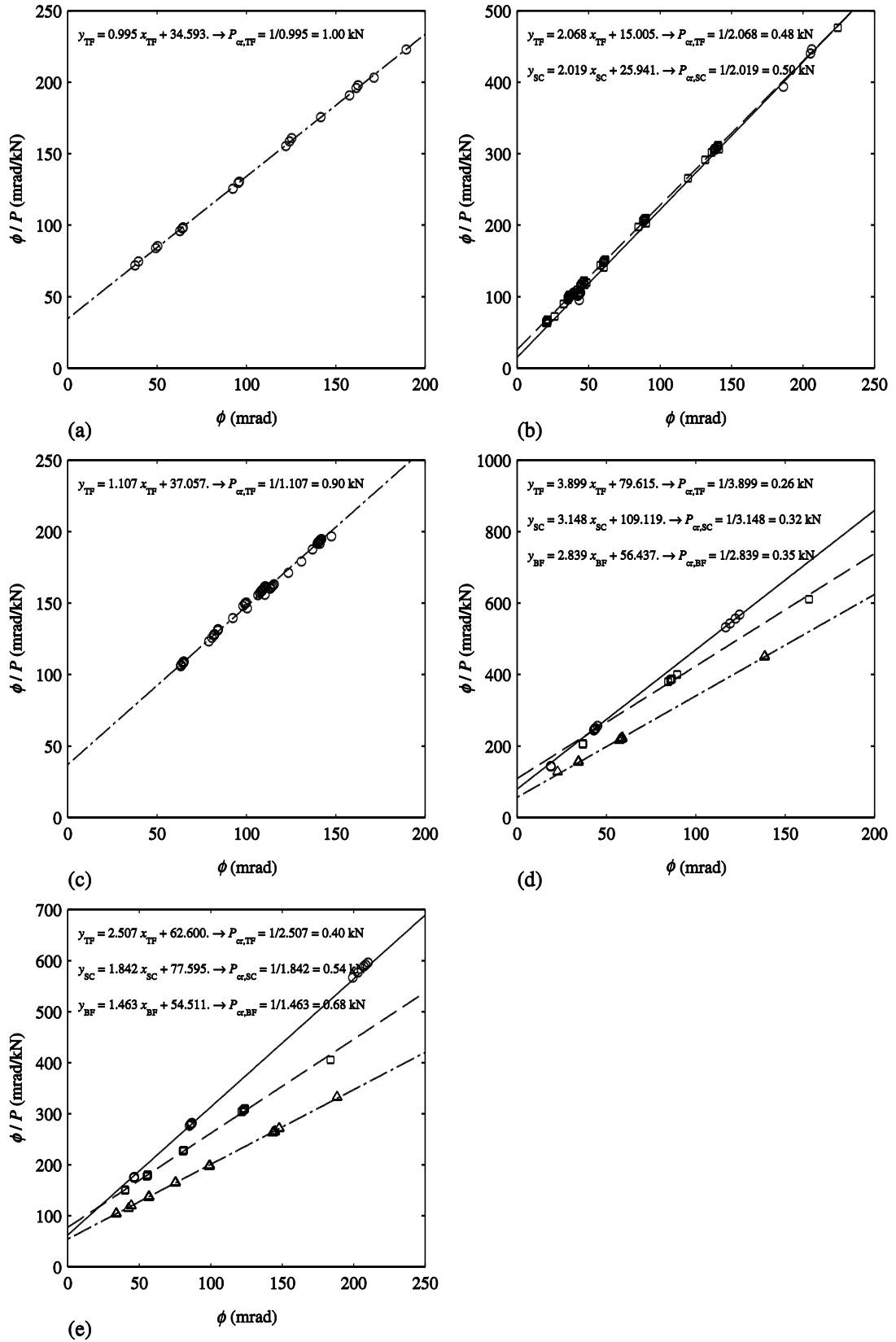
Figure B.17 Southwell plot with test results from (a) C3-2438-EC2; (b) C3-2844-EC1; (c) C3-2844-EC2; (d) C3-3454-EC1; (e) C3-3454-EC2